Air charge system emulation for diesel engine

Zhang, Kai

Award date:
2010

Awarding institution:
University of Bath

Air Charge System Emulation for Diesel Engine

Kai Zhang

A thesis submitted for the degree of Doctor of Philosophy

University of Bath

Department of Mechanical Engineering

May 2010

Abstract

The work presented in this thesis details a novel engine evaluation approach utilising real-time simulation and advanced engine testing systems for general applicability to new generations of air charging systems. A novel engine air charging system including a charge air handling unit (CAHU) has been developed which is connected to an engine to emulate advanced boosting system conditions. Significant analytical and development work has focused on generating a real-time turbocharger model such that the CAHU can be effectively controlled to emulate the turbocharger performance under both steady and pulsating conditions.

Experimental work was carried out to evaluate this new engine air charge testing system against a production turbocharged baseline engine. The accuracies with respect to the boost pressure, turbocharger speed, mass air flow, and fuel consumption in the steady state tests are above 95%, and the level of confidence for the engine back pressure is approximately 90%. The difference of turbocharger speed between the steady turbocharger model and the pulsation model is also identified. In engine transient tests, the boost pressure and engine torque have shown fast response characteristics similar to that of the baseline engine. While general transient trends were achieved, some issues were identified with the high speed control of the CAHU interacting with the dSPACE real time turbocharger model. It is proposed that future improvement can be achieved via applying new control algorithms to improve the accuracy and tracking the CAHU control without increasing the system instabilities.

Acknowledgement

The author is deeply indebted to Professor Frank Wallace, whose sad death in January 2009 was a great loss to his family and to his colleagues in the department. It was my pleasure of working closely with Professor Wallace for two and half years as his last student. I am always grateful for his kind guidance, valuable contribution and devoted support throughout this work.

I would like to thank Dr Sam Akehurst for his overall direction, ingenious solutions in all simulation and experimental work, and approachability throughout. I would like to express my sincere gratitude to Prof Gary Hawley for conceiving the project, and his continuous support and constructive suggestions.

Thank you to all the technical support staff for assistance on the test facilities and instrumentation. These include Sam Hurley, Don Blake and Vijay Rajput.

I am grateful to Dr Ricardo Martinez-Botas at Imperial College London, for his kind guidance on turbine analytical models. I also would like to thank Peter Dowell for the use of compressor data and discussions on engine and turbocharger simulations. Many thanks to all of my colleagues for their support and contribution: Dr Chris Brace, Dr Chris Bannister, Allan Cox, Yiping Tan, Pengfei Wang, Shifei Ye, Carlos Finol, Mitch Piddock, Adrian Hunt, Hasan Ali, Richard Burke, Edward Chappel, Andy Lewis, Joseph Moyers, Apiwat Suyabodha, Adam Rose, Xiaoling Chen, and Prof. Yumei Liu.

Finally, I would like to thank all of my family and friends for their faith in me and unconditional support, especially Uncle Bao Lixin for the financial support of my Msc study, and Jinwen Yang for her continuous encourage and support.

谨以此文献给我亲爱的父母:张治成和李健。 感谢你们长久以来的支持和鼓励.

Contents

List of Figures

List of Tables

Notation

Abbreviation	Meaning	Units (if available)
AFR	Air Fuel Ratio	-
At (A)	Area of Throat	m^2
b	Depth of Rotor Passage	m
BMEP	Break Mean Effective Pressure	bar
BP	Break Power	kW
BSFC	Break Specific Fuel Consumption	g/kWh
C(V)	Absolute Velocity	m/s
CFD	Computational Fluid Dynamics	-
C_p	Specific heat at constant pressure	kJ/kgK
d	Diameter	m
E	Energy	J
EGR	Exhaust Gas Recirculation	-
FGT	Fixed Geometry Turbocharger	-
h	Static Enthalpy	J/mol
h0	Stagnation (or total) Enthalpy	J/mol
HP	High Pressure Stage	-
I	Inertia	kgm^2
IMEP	Indicated Mean Effective Pressure	bar
J	Radial Velocity Ratio = (axial velocity component at exit)/(radial velocity componentat entry)	-
KE	Kinetic Energy	J
LP	Low Pressure Stage	-
l_{th2}	The Length of the Throat Formed by Two Adjacent Nozzle Blades	m
$\dot{M}$	Mass Flow Rate	kg/h
Mach	Mach Number	-

MAF	Mass Air Flow	kg/h
MAP	Inlet Manifold Pressure	bar
N	Turbocharger speed	rpm
n	Number of Nozzle blades	-
NOx	Nitrogen oxides	ppm
P	Pressure	bar
PE	Potentiel Energy	J
Pmax	Maximum Cylinder Pressure	bar
PR	Pressure ratio	-
Q	Heat transfer	J
T	Static Temperature	K
T0	Stagnation (or total) Temperature	K
TQ	Torque	Nm
TURB	Turbine	-
VGT	Variable Geometry Turbocharger	-
U(u)	Peripheral velocity (Rotor tip speed)	m/s
U/C	Turbine Blade Speed Ratio	
W(V_R)	Relative velocity	m/s
WAVE	Ricardo WAVE Simulation	-

Symbol	**Meanings**	**Units**
α	Absolute gas angle	◦
β	Relative gas angle	◦
γ	Ratio of specific heats	-
τ	Turbine torque (shock torque + rotor torque)	Nm
ρ	Density	kg/m^3
η	Efficiency	%
ω	Angular velocity	m/s
$\dot{\omega}$	Angular acceleration	m/s^2

Suffix	**Meaning**
01	Upstream stagnation
2	Nozzle exit condition
3	Interspace condition
4	Entry of the rotor
4’	Post shock condition
5	Rotor exit condition
actual	Actual Number
air	Ambient Air
comp	Compressor
corr	Corrected Number
f	Friction
in	Inlet
N(crit)	Critical Condition
n	Turbine Nozzle
out	Outlet
r	Turbine Rotor
turb	Turbine
t/s	Total to Static
t/t	Total to Total
ref	Reference Condition

Chapter 1 INTRODUCTION

1.1 Background

The exhaust emissions from automotive vehicles have been widely recognised as one of the major factors to cause air pollution and the climate change [1]. Legislation to reduce vehicle emissions has become more and more stringent during the last decade. The European Economy Community (EEC), for instance, have regulated the toxic emissions of nitrogen oxides (NOx), total hydrocarbon (THC), non-methane hydrocarbons (NMHC), carbon monoxide (CO) and particulate matter (PM) for most vehicle types [2]. Recently emissions of carbon dioxide (CO_2) by passenger cars sold in Europe have also been voluntarily limited by the European Automobile Manufacturers Association (ACEA) and European Commission (EC) [3]. Additionally, the reduction of vehicle fuel consumption has become of great importance, as the fossil fuel is considered a valuable resource.

Diesel engines currently dominate over half of the new European passenger vehicle market because of their inherent high efficiency. Moreover, in an effort to achieve the tightening emission legislation and CO_2 reduction targets as well as better fuel economy, a number of advanced diesel powertrain technologies have become available. Examples of such technologies are common rail fuel injection systems, variable geometry turbochargers, two-stage turbocharger, exhaust treatment systems, bio-diesel fuel, etc. Among these technologies, air charging systems to provide high levels of air boost in the engine inlet manifold are considered to be an effective solution in reducing CO_2, improving engine efficiency as well as leading to engine downsizing. The adoption of compressed air with greater mass flow rate in the engine cylinder allows more fuel to be burned, and hence the power output and fuel

efficiency is increased without excessively increase the engine weight. Downsizing will reduce the weight without compromising engine performance.

Historically, high pressure air charging system of diesel engine has been pursued over the last three decades [4].The existing engine air charging technologies normally include supercharger, turbocharger, variable geometry turbocharger, multi-stage supercharger or turbocharger, etc. Although each of these technologies is proposed to offer potential benefits to engine performance, the turbocharger has been widely used in the diesel engine applications due to its high efficiency and the ability to achieve to high level of boost. The turbocharger is a type of exhaust-driven compressor designed for charging reciprocating internal combustion engine. It consists basically of a compressor and a turbine coupled on a common shaft. The exhaust gas is used in the turbine to drive the compressor which compresses the air and supplies the air to the engine with higher density [5]. In recent research into two-stage turbochargers [4], the level of boost pressure possible was 6 bar, and the maximum in-cylinder pressure could reach 260 bar during the combustion.

Although these air charging technologies have the potential to answer the emission and power output requirement of future diesel engine, the hardware of the air charging system needs to match the engine performance, since the diesel engine is designed for variable speed and load operations. Therefore, the adoption of an air charging system increases the degree of complexity of powertrain functionality as well as the number of variables the engine strategy has to control. Additionally, any new air charging system has to be incorporated into the overall engine control strategy and subsequently its operation can compromise other engine sub-systems. Thus a significant optimisation procedure is required; this results in a very resource intensive work program both in time and in cost. Furthermore, testing prototypes for extreme parameters can also lead to hardware breakdown [6].

1.2 Aim and objectives

The aim of this work is to experimentally emulate, simulate and control a charge air handling unit to allow new turbocharger concept to be designed without extensive prototype engine development and testing.

Specific objectives in order to achieve the aim are:

1. To conduct a literature survey on air charging systems, real time simulation and hardware-in-the-loop systems, with a focus on turbocharger modelling techniques and the benefits of charge air handling systems emulation as appropriate to this study.
2. To undertake a detailed investigation of numerical and analytical approaches to predict compressor and turbine performance based on data supplied by the turbocharger manufactures.
3. To develop a turbocharger model to operate in a real time environment in conjunction with a hardware-in-the-loop system to control a charge air handling unit (CAHU) which emulates advanced boosting systems.
4. To carry out a detailed investigation and to design a model to simulate the turbine characteristics under pulse conditions.
5. To develop the hardware-in-the-loop system, to be used as a platform to test the engine with the CAHU emulating the turbocharger performance
6. To undertake an experimental programme of work to validate the new engine testing approach by benchmarking a engine with CAHU to emulate the air charging system against a baseline engine with production turbocharger, under both steady state and transient conditions.

1.3 Scope of thesis

This thesis is divided into following chapters:

Chapter 2. Literature Survey

This chapter gives an overview of engine boosting systems, especially the turbocharger, with a focus on the compressor and turbine simulation methods including the characteristics maps and energy losses models. Software (real time simulation) and hardware in hardware-in-the-loop (HIL) systems are also reviewed; followed by a detailed survey of existing applications in the automotive research. Finally previous attempts to develop air charge systems for development work are highlighted.

Chapter 3.Turbocharger Architecture

This chapter is dedicated to describing the architecture of a turbocharger including the turbine and compressor parameters, dimensionless representations, mass flow and energy equilibrium, temperature-entropy diagram and velocity triangle analysis for every stage of the flow.

Chapter 4. Software: Approaches to real-time turbocharger simulation

A thorough investigation of the numerical and analytical approaches to predict the compressor and turbine performance is performed to increase the density of the compressor and turbine maps based on the limited number of data points supplied by the manufacture. In addition, a turbocharger shaft model and a gas property model are described. This chapter also demonstrates the real-time turbocharger model in Matlab Simulink as a powerful tool for simulation in real-time environment.

Chapter 5. Simulating turbine characteristics under pulse conditions.

This chapter details a new approach to simulating the turbine characteristics under unsteady flow conditions from the engine exhaust pulsating flow, by constructing the mass flow and temperature pulsation based on the pressure pulsation profile from the fast response pressure measurement.

Chapter 6. Hardware

This chapter highlights the hardware of the new engine testing system including the CAHU system, dSPACE platform for the real-time modelling and the CAN (Control Area Network) bus communication platform among different testing control systems.

Chapter 7. Experimental Procedure and Results

This chapter details the advanced testing facilities which were used within the Powertrain and Vehicle Research Centre in the Department of Mechanical engineering at the University of Bath, especially the transient dynamometers, fast response temperature and pressure measurement, CP engineering Cadet V12 host PC and data acquisition system. Additionally the engine test capabilities with regard to the steady state test and transient tests are also described.

Chapter 8. Discussion of Experimental Result

This chapter demonstrates and analyses the test results with regard to the comparison between the baseline engine with production turbocharger and the engine with CAHU system to emulate the turbocharger performance under both steady state and transient conditions. This chapter also benchmarks the new engine testing system using a comparison of steady and pulsating engine exhaust flow calculations. The factors that cause system oscillation are analysed, and the modifications as well as the relative improvements on the system stability are also discussed in this chapter.

Chapter 9. Conclusion

This chapter concludes the major findings from this work and introduces recommendations for future research.

Chapter 2 LITERATURE SURVEY

Overview

This chapter provides an overview of the existing engine air charging technologies for increasing the engine power output and hence the fuel efficiency. The structure and usage of these 'boosting' technologies are reviewed with a focus on their merits and drawbacks. Turbocharger modelling techniques are investigated to gain an understanding of existing approaches to simulate the turbocharger performance with limited number of test data provided by the manufacture. The charge air handling unit (CAHU) is also introduced; followed by the benefits for future engine development. Also a survey of real time modelling techniques in the automotive applications, with a focus on the benefits of hardware-in-the-loop systems for future engine development is presented.

2.1 Air charging technologies

2.1.1 Introduction

The general purpose of this literature survey is to gain a thorough understanding of the existing work and current state of the art within the field of air charging technologies. More specifically this will enable different air handling candidate technologies to be identified with a focus on the turbocharger due to the widespread usage in diesel engines. Several different air charging techniques are examined and their relative merits and drawbacks are compared, enabling a suitable target to be chosen when developing the real time model, which will be discussed in a greater detail in chapter 4.

2.1.2 Candidate air charging technologies

In order to improve the engine combustion efficiency and therefore reduce the toxic emissions, engine downsizing is becoming a serious focus [5]. This allows the engine with reduced capacity to produce the same power, so the fuel consumption can be reduced due to lower pumping losses. Furthermore gases-to-wall heat transfer and friction losses from smaller moving parts also act to improve the overall engine efficiency. However, NO_x emissions can go up 20% to 100% with engine downsizing if appropriate measures are not taken [117] (**Figure 2.1**). So the uses of exhaust gas recirculation (EGR), high pressure fuel injection and after treatments with NOx reduction technologies may be applied to reduce the NO_x emission.

The engine downsizing can be achieved by applying boosting (air charging) technologies to raise the engine inlet air pressure and thus increase the engine specific power output without adding excessive weight to the engine. Hence these emerging air charging technologies need to be investigated, and can be used as the object of the real time model in the new engine testing approach. This section reviews emerging air charging technologies that have been applied in a modern diesel engine.

Supercharging

Supercharging refers to boosting systems which introduce air into an engine cylinder at a density greater than ambient. This enables a proportional gain in the amount of fuel that can be burned in the cylinder chamber and therefore increase the potential power output. This idea of charging denser air into the engine can be achieved by fitting a compressor at the inlet of the engine, and the compressor is driven externally via a mechanical or electrical source:

a. Mechanical supercharging

Mechanical supercharging refers to a device which is driven by the engine crank shaft via a belt or chain. The compressor in this type of supercharger is often a positive displacement one, which means that the level of boost pressure remains nearly constant regardless of engine speed. Since this advantage provides good throttle response, as well as the ability to reach the maximum boost pressure almost instantaneously, mechanical supercharging can be found in petrol engines, such as the BMW Mini Cooper S [7]. However, since the boost pressure is fairly constant, when the engine is running under high load conditions, the inlet manifold pressure may exceed the air pressure coming from the supercharger, and this unbalanced pressure will cause a backflow from the engine to the compressor until the pressure reaches equilibrium. Hence this highly inefficient process makes the mechanical supercharger unsuitable when it is used at high boost levels.

b. Electrical assisted supercharging

Electrical assisted supercharging is the name given to systems in which the compressor is driven by an electrical motor. This type of supercharging system could also provide a nearly instantaneous boost rise due to the fast response from the battery. However, a supercharger with a high level of boost pressure requires high power from a number of batteries which might impose a serious weight penalty to the vehicle that takes away the initial advantage. Moreover, a complex control system is required to

allow the supercharger to operate under different engine conditions, and this may lead to an expensive implementation. Although the electrical assisted supercharger has these drawbacks, this type of system has attracted great interest in recent research [8, 9, & 10]. Since hybrid or electric vehicles have drawn lots of attention and have the benefit of less emissions in urban environment, the electrical assisted supercharger can be fitted in to the electric system.

Turbocharging

The basic turbocharging system comprises an exhaust gas turbine driven compressor. Turbomachines have a long history which can be derived from the 18th century, when Papin published descriptions of centrifugal pumps and blowers [5]. Radial inflow, axial and radial outflow machines were widely used particularly in France, and Great Britain during the industrial revolution and in California during the gold rush period [5]. In the 19th century, the next major application came with steam turbine for marine propulsion and electrical power generation [5]. In the 20th century, turbomachines have developed rapidly with applications in gas turbine and internal combustion engines. Around 1925, Buchi [70] first successfully used a turbine, which used the engine exhaust gas, to drive the compressor for supplying high pressure inlet air.

For automotive applications, the turbine is mounted within the exhaust manifold of the engine and the compressor is situated in the inlet manifold of the engine (Figure 2.2). The turbine and compressor are coupled on a common shaft, in which the bearing is cooled and lubricated by engine oil. The operating range of the turbocharger shaft is from 100,000 rpm to 200,000rpm [4]. Similar to the supercharger, the main benefit of this system is to improve the output of the engine with a slight increase in weight. Furthermore, the turbocharger tends to be more efficient than the supercharger, since the energy in the hot exhaust gases that would normally be wasted can be utilised to drive the compressor. The level of boost can be controlled by either a waste gate controller on a fixed geometry turbocharger (FGT) or a nozzle vane position controller on a variable geometry turbocharger (VGT).

The Variable Geometry Turbocharger (VGT) was first emerged onto the marketplace in 1989 and has evolved through the 1990's up to present day [5]. Although the flow range of a particular turbine is large, operation away from the design point results in a loss of efficiency [5]. Additionally, the boost level of the compressor is directly related with the turbine expansion ratio, which will vary greatly with mass flow rate. So the engines with fixed geometry turbocharger have insufficient boost at low engine speed and be over-boosted at high speed. VGT's with varying angle of nozzle vane can essentially extend the turbine operating region for different mass flow conditions to suit different engine operations without significant loss of efficiency. Due to this property, the engine can be controlled to make the best use of the torque and fuel economy using VGT in conjunction with direct fuel injection (DI) systems [11]. VGT's reduce NOx emissions by adjusting exhaust flow conditions and therefore better enabling the flow of EGR (Exhaust Gas Recirculation) system within the engine [12]. Compared with the supercharging system, the advantages of a turbocharger system (especially VGT) can be summarised as:

a. Higher efficiency due to the use of energy from hot exhaust gas that would normally go to waste.

b. Better control of the engine boost pressure and hence torque and fuel economy

c. Potential to manage NOx emission when operating with an EGR system by controlling exhaust back pressure and boost pressure [120].

In the turbocharged engine applications, diesel engines are superior compared to gasoline engines, due to advantages in terms of the fuel consumption, torque output and steady state emissions. Although diesel engines have benefitted immensely from turbocharging, there are still some minor drawbacks:

a. the lack of boost at low engine speed/load due to low exhaust energy

b. slow acceleration of the turbocharger during transient

c. adverse effect on emissions as a result of turbocharger lag

Since the turbine is driven by the exhaust gases, the initial acceleration of turbocharger from low speed is limited by the lack of sufficient exhaust gas mass flow under low engine speed conditions. This could dramatically impact the vehicle drivability as well as the emissions due to the lack of oxygen in the air supplied to the engine. Since the engine is designed for variable speed and load conditions, the matching of a correct turbocharger to a diesel engine is of great importance, in order to obtain the best over-all performance from [5].

Two-stage turbocharging

Two-stage turbocharging refers to an air charging system where two turbochargers are arranged in parallel or series. Parallel 'twin-turbo' refers to a turbocharging system in which two identical turbochargers are equally split in the engine exhaust system, and each turbine serves half of the exhaust manifolds with both turbines functioning simultaneously. Hence the two smaller turbines improve the transient performance (less turbo lag) than a larger single turbine [4].

In a series (sequential) two-stage turbocharging system (Figure 2.3), a smaller turbocharger is closer to the engine and is termed the high pressure stage turbocharger (HP). A larger turbocharger further away is the lower pressure stage turbocharger (LP). When the engine operates at a low speed condition, the exhaust gas only expands across the HP turbine, and this provides better transient performance due to its lower inertia. However, at engine high speed conditions, the larger turbine (LP) will start to be partially active until maximum power output is achieved. The LP turbine is used for maximum power and greater efficiency than the high pressure turbine. Therefore the system operating region can be further extended, since varying the geometry of the nozzle vane in VGT can only be effective up to the point when performance is eventually limited by the size of a single turbocharger.

The benefits of two-stage turbocharging systems are:

a. Higher pressure ratio can be achieved through a series of compressions

b. Better transient performance at low speed (less turbo lag)

The series arrangement of a multi-turbocharger system can significantly increase the level of boost pressure and hence raise the engine specific power output. Alain [14] suggests that a two-stage turbocharging system is possible to increase engine specific power to 70kW/L (BMEP: 22bar), whereas a single turbocharging system only supports an engine specific power of 55-60kW/L (BMEP 17-19bar). Wallace et al [13] apply various types of turbochargers to a compound diesel engine used for heavy vehicle applications. The arrangement of two-stage turbocharging system shows that the level of boost pressure can achieve 6 bar absolute pressure and the BMEP can reach 33 bar. Although the initial research with regard to two-stage turbocharging system focuses on the heavy duty vehicle or racing car applications, this high boosting technology has also drawn more interest to improve the performance of passenger cars. BMW's two stage turbocharger system has been applied in a series of saloons (e.g. 335i) [15]. A 3.0 litre engine with two fixed geometry turbochargers for HP and LP is shown to provide a maximum torque of 560NM at 2000rpm. Renault has also investigated the possibility of using a two-stage turbocharging system to increase torque and power output of a 1.5 litre engine to match the performance of a 2.0 litre engine.

Although the two-stage turbocharger could potentially increase both the transient and the maximum power outputs, there are still some inherent shortcomings:

a. two turbochargers require extra space that could cause packaging problems.

b. The additional size of system could increase the thermal inertia in the exhaust system, such that the exhaust aftertreatment systems have a delayed warm up period [16].

In conclusion, the turbocharger is chosen to be the fundamental object for further investigation in this work. The turbocharger can be treated as a specific method of supercharging with the attempt to use hot exhaust gas of the engine to drive the supercharger compressor, and the multi-stage turbocharging system can be seen as a device with two or more turbochargers to be connected and work together

2.1.3 Turbocharger modelling

Among these existing air charging technologies, the turbocharging system has been widely applied for diesel engine applications due to its high efficiency and wide range of mass flow rates. However, in order to increase the engine power output and the fuel economy as well as the transient performance, matching of a correct turbocharger to a diesel engine is of great importance. For example, if a diesel engine is fitted with too small a turbocharger, the required level of boost could not be achieved. On the other hand, if a large turbocharger is coupled on a small engine, the high inertia from the turbocharger shaft will impact on the engine transient performance which may lead to a significant turbo lag. Therefore modelling programs to simulate the turbocharger performance in conjunction with an engine model allows the engine to be matched with the correct turbocharger.

Watson & Janota [5] cover the area of turbocharging in depth. It is suggested that the engine can be matched using calculations of the turbine and compressor powers under different flow conditions (pressure ratio, mass flow rate, and turbocharger speed). The relative turbocharger characteristics are normally represented by the turbine and compressor maps. In order to avoid excessive length in the literature review, the turbocharger architecture including parameters, dimensionless representations, energy and flow equations, and turbocharger maps are detailed in chapter 3.

Empirical model

Watson & Janota [5] point out that compressor and turbine simulations can be split into two types: empirical and analytical models. The compressor and turbine empirical models apply various curve fitting methods to interpolate and extrapolate the testing data to predict the compressor and turbine performance. However, the empirical models relay heavily on the availability of large quantities of testing data either provided by the turbocharger manufacture or tested on a specific turbo-

dynamometer (Figure 2.4). Moraal P., et al [17] assess a number compressor empirical models on three different types of compressors. These compressor empirical models include Jensen & Kristensen's model [19], Mueller's method [21], Zero Slope Line method [20] and Neural networks [22]. Among these modelling techniques, Moraal P., et al [17] claims that the Jensen & Kristensen's model provides better prediction of the compressor performance when the supplied testing data is not sufficient. Dowell P., et al [18] also suggest that the use of spline functions and Jensen & Kristensen's model to interpolate and extrapolate the compressor test data can generate a full compressor map. The detailed compressor model is discussed in chapter 4.

Analytical model

Although the compressor can be simulated using empirical models, the turbine is difficult to apply similar curve fitting methods due to the complex flow characteristics. The turbine normally works under pulsating conditions because of the exhaust valve opening and closing. The pressure wave resulting from blowdown propagates through the engine exhaust manifold. In addition, due to the effect of variable geometry of nozzle vanes, the direction of the flow varies at different nozzle positions, and the turbine empirical model therefore needs a vast number of testing data that the manufacture would not normally supply [5]. Hence the analytical model will provide an alternative solution which represents the processes more fundamentally and hence is less reliant on data sourcing. Turbocharger analytical models can be divided into two categories:

1) One-dimensional models which do not include complex geometric details
2) Three-dimensional models e.g. Computational Fluid Dynamics (CFD) with a high degree of spatial discretisation.

The turbine analytical model involves modular approaches to predict the turbine performance as a series of discrete components based on the moment of momentum, steady flow energy, mass flow continuity and thermodynamic equations. The gas flow in the channels of rotor and nozzle is viscous, three-dimensional, and unsteady when the turbine is connected with an internal combustion engine. So a turbine model with

analysis of three-dimensional flow can give a useful insight into the flow performance in the turbine. Katsanis [23] proposes a streamline curvature method applying inviscid flow in the hub-to-shroud and blade-to-blade analysis. Barnard and Benson [24], Benson et al.,[25] and Cartwright [26] also use similar methods. With the rapid development in computer processing power over recent decades, programs using computational fluid dynamics (CFD) are applied to analyse the flow in the turbulence. For example, Dawes [27] uses the 3D Renolds-averaged Navier-Stokes equations, and Baldwin-Lomax [28] applies two-layer mixing length model and uses vorticity to determine the boundary layer.

Although the flow in the turbine is actually three-dimensional, the 3-D solutions, CFD (Computational fluid dynamics) for instance, attempts to replicate the actual process, so three-dimensional models are very time consuming and processer-intensive. Moreover, the 3-D models lead to the requirement for the detailed geometry information that needs to be either supplied by the manufacture or measured by specific laser measuring devices. Therefore simple models with one dimension flow analysis are widely applied in the initial design of turbine components [5].

Wallace F.J., [34] and Wallace F.J., et al [35] provide a turbine analytical model for both the design and off-design conditions. The turbine design condition refers to the state that the relative velocity of the turbine flow leaving the nozzle matches the rotor speed. So under this condition, the turbine tends to be more efficient due to the lack of incidence loss. The essential feature of the off-design treatment is the postulation of an irreversible deflection at constant pressure of the flow leaving the nozzle to produce a relative velocity vector at entry to the rotor in conformity with the rotor blade angle at entry [35]. In Wallace's turbine model, the entropy and temperature changes at each stage of the turbine could be calculated by an iterative loop of the pressure in the nozzle-rotor interspace satisfying energy and mass flow continuity across the nozzle and the rotor. For supersonic gas flow conditions, the Mach number exceeds unity and choking happens either in the rotor or in the nozzle. In the analytical model, the critical pressure and relative isentropic turning are introduced,

so the gas flow in the nozzle or in the rotor passage does not permit the establishment of the supersonic velocities

Energy losses

In the one-dimensional turbine analytical model, no detailed account has been taken of energy losses, beyond the introduction of an all-enveloping efficiency term [5]. However, the actual fluid flow in the radial turbine is extremely complex since it is viscous and highly three-dimensional. Consequently, in the simple one-dimensional analysis, the energy losses calculation in terms of various empirical loss coefficients has been widely applied. Since the coefficients are empirical, they should not be applied to all classes of turbine with any expectation of great accuracy. However the data points from the calculations, especially at off-design conditions, can be useful to increase the data size to fill the lookup tables in the real-time turbine model. The energy losses can be sub-divided into following categories in terms of the source of energy loss:

a. Nozzle loss
b. Rotor incidence loss
c. Rotor losses in the passage
d. Disc friction loss
e. Clearance loss
f. Bearing loss

Nozzle loss refers to the energy loss in the inlet casing and the nozzle ring. This are usually obtained from tests on a 'blowing rig'. Benson [32] suggests that using a function of Mach number as the calculation of nozzle loss could be fitted with small automotive turbochargers.

The rotor incidence loss tends to be dominant in the pure radial turbine [5], which is caused by incorrect gas angle at rotor entry. After entering the rotor, the gas is constrained to have a purely radial relative velocity, and this irreversible deflection

results in energy loss. The Wallace model [34, 35] contains the calculation of incidence loss by assuming the gas deflection happens at constant pressure with corresponding entropy increase. The NASA model proposed by Futral S.M., and Wasserbauer C.A.,[29] is based on the assumption that the complete tangential component of the relative kinetic energy is destroyed. The incidence loss is then represented as the loss of tangential kinetic energy as the flow turns from its approach flow angle to the blade angle. This angle of flow turn in a sinusoid function is then introduced, so this allows the coefficient of this equation to be found by fitting the best efficiency point into the equation.

The passage loss in the rotor channel is assumed to account for blade and end wall friction losses and the secondary flow loss [31]. These losses in the rotor passage are not separated, because their individual contributions cannot be estimated from the test data. In the NASA model, the passage loss is expressible as a function of the mean passage kinetic energy. Bains N.C., [31] refines this passage loss equation by adding three terms to represent the frictional loss, hydraulic length and the secondary flow losses.

Since the loss models are one-dimensional, the clearance for the rotor tip cannot be simulated in detail. There are various formulations for the tip clearance loss. The NASA model provides a function of the ratio of the tip clearance to the exducer blade height to calculate the energy loss. Bains N.C., [31] assumes that the tip clearance acts as an orifice, so that shear flow exists in the clearance gap, with a velocity varying linearly from zero at the wall to the blade speed. The disc friction and bearing loss in the turbocharger shaft are also hard to measure. Therefore various empirical equations are proposed to represent these energy losses.

In conclusion, the turbine analytical model can be achieved by using various methods. Among existing modelling techniques, Wallace's one-dimensional approach provides an useful insight into the turbine flow by using the equations of thermodynamics, moment of momentum, steady flow energy and mass flow continuity. Additionally,

the aid of semi-empirical energy loss equations can help improve the accuracy of the model.

Pulsating flow in turbine

The aim of the turbocharger for the engine is to make maximum use of the high pressure and temperature flow which exists in the cylinder at the moment of exhaust valve/port opening. Therefore the flow to the turbine is not constant due to the exhaust valve/port opening and closing, and the propagation along the exhaust manifold. Watson & Janota **[5]** point out that using mean values for the turbine inlet pressure and temperature will lead to errors in the turbine energy and mass flow rate calculations. Chen et al [31] also claim that the pulsating flow contains higher isentropic energy than the constant one. Although various researches focus on experimental facilities to test the turbine under pulsating flow, there is little literature on how to simulate this phenomenon. Therefore a unique approach to construct the pulsating temperature and mass flow rate based on the measured pressure profile is developed in this work (chapter 5).

2.1.4 Charge air handling unit (CAHU)

The aforementioned air charging technologies all increase the air density charged into the engine cylinder, and hence raise the engine power output and thermal efficiency. However, the air charging device incorporated into the engine system will increase the degree of complexity with regard to engine controls. For example, the nozzle vane positions on a variable geometry turbocharger needs to be calibrated for different engine operating conditions as well as against other control sub-systems such as the EGR valve, and fuel injection system. This optimization process is extremely time consuming and labour intensive. Additionally, due to the limit of the operation of the air charging system, the engine cannot be examined completely for different air charging conditions (i.e. engine boost pressure, mass air flow, engine back pressure).

So this requires an air pressure control device to investigate the engine performance at different pressure and mass flow conditions.

Merola S. S., [116] applies a boost device in conjunction with a partially transparent single-cylinder SI engine to investigate the effect of boosting on combustion process under various intake pressures. The flame diagnostics in this research is achieved with the range of absolute intake air pressure from 1 bar to 1.6 bar. However, this was under steady state tests.

Akehurst S., and Piddock M., [36] designed an air charge emulation device which is called charge air handling unit (CAHU) that can be used to test multi-cylinder engines for various air charging conditions. This hardware emulates the air handling side of the engine (i.e. boost pressure, back pressure and intercooler outlet temperature). Furthermore, the CAHU provides a much wider pressure and mass flow operational region beyond the envelope of typical production turbochargers. It is therefore capable of emulating a variety of current and future boosting strategies.

Piddock M., [114] investigated a novel experimental approach of using the CAHU in conjunction with various simulation methods that enables the engine optimization for maximum torque and improved fuel consumption to be achieved in a shorter time frame and with reduced cost. In Piddock's research [114], the CAHU handles the intake air pressure up to 3 bar absolute irrespective of engine speed for a production diesel engine, and with reduced compression ratio engine and uprated gaskets the pressure that the CAHU supplies can reach 4 bar.

Akehurst S., and Piddock M., [36] proposed that instead of examining the engine performance at different charging conditions, the CAHU could also be used to emulate any air charge device, a turbocharger for instance, and allow tesing of the engine without prototype hardware. This described the same CAHU configuration

used for current research. The hardware and control system of CAHU is described in greater detail in chapter 5.

2.2 Hardware-in-the-loop and real time simulation

2.2.1 Introduction

Currently, when new enabling technology is adapted to an internal combustion engine to reduce fuel consumption and harmful emissions, the relative control algorithm needs to be integrated to the engine control system. Therefore, during engine development, there are several steps for introducing the new embedded control system including design, development, verification and validation, and excessive testing will be involved in the last two processes. The verification of the control algorithm on any level due to additional or refinement requirement may change the whole test schedule, and this tends to generate a huge amount of validation tests and usually comes very late in the process of the vehicle development. Traditionally, this real testing for validating the engine control unit (ECU) is done with open-loop test benches (with signal generators and PCs to record the resulting output), powertrain dynamometers, and real vehicles [37]. But there are several limitations for the conventional approach [6]:

1. Extensive testing of ECU with increased complexity (of electronics & software) during the development phase is not feasible.
2. Increased time to adapt new ECU in test bed.
3. Limited knowledge and control (over the system)
4. Hardware failure stops the testing/validation process
5. Reusability of existing ECU for new variants consumes more time
6. Automated testing and reproducible tests are difficult / impossible
7. Difficult to identify controller deficiencies which may occur only under certain circumstances.

8. Testing in the real hardware prototypes for extreme parameters can lead to hardware breakdown.

These shortcomings have forced the automotive industry to investigate better methods, such as the hardware-in-the-loop. This means that complex control systems can be tested using competitively efficient, cheap and accurate closed-loop testing approaches. For this purpose, a literature survey with regard to these new testing approaches needs to be conducted to gain a thorough understanding of the system structure, components, applications, merits and drawbacks.

2.2.2 Hardware-in-the-loop system

The hardware-in-the-loop (HIL) system can be seen a special form of real time simulation [38]. Compared with a pure model based simulation (i.e. software-in-the-loop), the real hardware component is involved in the HIL system. The hardware can be tested in this system with a greater accuracy, whilst the complex plants are simulated using real time models. In the automotive applications, the hardware component may be the engine control unit (ECU) or a real engine [38].

Figure 2.5 and 2.6 show the structure of a typical HIL system, where the real component is the ECU and the engine (plant) is simulated in a real time model. The purpose of this system is to provide all of the electrical stimuli needed to let the ECU 'think' that it is connected with a real plant. In this system (Figure 2.5), the real time simulation needs to catch the engine behaviour and send and receive synchronizing signals to the hardware [39]. Hence the ECU hardware can be fully examined without connecting to a real engine, and this allows the tests to be done at the early stage of the ECU development without building up the prototype engine.

In the literature survey of existing work (Table 2.1), the usage of HIL system can be divided into two groups [38]:

a. To test diagnostic code in the ECU (i.e. fault detection)

b. To develop new enabling control algorithm in ECU against simulated plant before taking to the real vehicle.

These applications mainly focuses on the engine control system evaluation and fault detection such as the TPS (Throttle Position Sensor), ABS (Anti-lock Brake System), ESP Electronic Stability Program), transmission system, knock detection, and etc.

Park S., et al [39] show that the electrical throttle control system can be verified using hardware-in-the-loop system and automated test program. In this test, most of sensor signals from vehicle are generated in the model except throttle position signals. A circuit error simulator is incorporated into the system to generate electrical and physical faults. Kim D., et al [41] describe a HIL system to test the electronic stability program (ESP). The engine and vehicle are simulated using real time models. Steiber J., et al [42] present a virtual vehicle test environment in HIL system by using a motor to simulate the engine behaviour and a transmission control unit. Therefore the transmission control system can be tested without implementing on a real vehicle.

Compared with other testing platforms (such as software-in-the-loop or the vehicle), the main advantages of the HIL system can be summarised as:

- Reduced need for prototype engine or vehicles
- Reproducibility and consistent test procedures
- Closed loop test for engine ECU
- Operation of the controller in critical operating range

Since the engine control system can be tested without a real engine or vehicle, the experimental work can be done by using an automated test program to achieve uninterrupted testing. The engine ECU is also a dynamic system that needs to communicat with sensors and actuators with synchronised signals. So the conventional open-loop vehicle tests could not achieve the full excises of the ECU.

Additionally, the hardware-in-the-loop system can also test the critical conditions without damaging the hardware.

2.2.3 Structure of hardware-in-the-loop system

Since both real time simulation and real hardware are involved in the hardware-in-the-loop system, the HIL system includes [39]:

Hardware components:

- Processor boards
- I/O (Inlet/Output) fulfilling specific HIL requirements
- Simulation of automotive busses (such as CAN (Control Area Network) bus)
- Signal conditioning for level adaptations to automotive voltages
- Electrical failure simulation
- Load simulation

Software Components:

- Implementation software
- Real-time models
- Software to establish and monitor bus communication
- Test software to program and administrate automated tests

In the literature survey of existing work (Table 2.1), there are several different hardware platform used in the HIL system including the MATT (The Mobile Advanced Technology Testbed) system by Shidore et al [43], the CAPPESS (Computer-controlled Automatic, Powertrain Electrical System Simulator) system by Wang et al [44, 37], the CARTS (Computer Aided Realtime Test system) system by Winsel et al. [45], the FPGA (Field Programmable gate array) system by Viele et al. [46], RT-LAB system by Jin et al. [47] and the Pi-AutoSim system by Sandiford et al. [48]

However, the dominant hardware platform adapted for HIL systems is the dSPACE simulation system. This off-the-shelf dSPACE simulation system includes: digital signal processor, I/O boards, loading boards and failure insertion units (FIU). Therefore the following discussion with regard to the hardware in HIL system is mainly focused on the dSPACE system.

Real time Processor

The real time processors are available in a wide range, from single board industrial computers to VME (Virtual Machine Environment). For HIL system, the model must be computed at a fixed time step. Kohl et al [39] indicated that the fixed time step for normal vehicle models should be less than 1 millisecond and for Formula One applications the time should be between 0.25 and 0.5millisecond. Jin et al [47] claimed that the step size between 100μs and 1 millisecond is needed for real-time automotive simulations. Table 2.2 shows the result of running a complex truck simulation with different processors [47]. However, for tests on engine combustion control units and angular based models, the in-cylinder pressure is measured every single degree crank angle. In this case, Hunt et al [49] described an in-cycle model with a fixed time size, which is less than 33.3μs with the maximum engine speed at 5000rpm. (Table 2.3)

I/O board and Conditioning Box

I/O boards play an important role, to connect the real hardware component (ECU or real engine) with the real time model, the sensors and actuators. They fulfil the specific HIL requirement (algorithm and waveform-based signal generation, angle-based measurement of injection and ignition pulses, etc) [39]. The I/O board provides the necessary functions and is capable of parallel I/O subsystems for complex automotive simulation of faster throughput. For adaptations to different levels automotive voltages (12V, 24V, 36V, 42V) from various components, a conditioning box is required to connect with the I/O boards, sensors and actuators which act as an adaptation in the HIL system.

The dSPACE I/O board DS2210, for example, is in widespread use in the automotive applications. It combines the I/O boards and the conditioning features, which provides the following capabilities [50]:

1. Support for up to 8 cylinder engine simulation, which is fully synchronized through an angular processing unit (APU) time base

2. Automation of the data capturing process for injection and ignition signals

3. Many additional I/O channels for various switch, sensor, and actuator simulation

Load Box and Failure Insert Unit (FIU)

Other components in the hardware-in-the-loop system consist of load boxes and failure insert units. The load box simulates the different kinds of loads, such as real loads, I-to-V (current to voltage) conversion for current controlled valves, etc. [39]. It could generate proper load which applies on the output of ECU signal to prevent the diagnostics errors during various kinds of tests [50]. If necessary, the load box could provide the interface for the connection to the real components, such as throttle, acceleration pedal, injectors and so on.

In order to simulate electronic failures, ECU output pins are wired to the load and HIL input channels via relays on a failure insertion unit. The failure insertion unit (FIU) simulates the following error conditions: open circuit, short to ground, short to battery voltage, and short between different ECU pins [39]. In the diagnostic test, the load (equivalent or real) is necessary to remain connected throughout the failure simulation. Meanwhile, the FIU is not only applied to the output of the ECU, but it is also necessary to simulate any failures occurring on the bus and sensors signal. Failure gateway, for example, is a good way to simulate the failure occurring on the network signal manipulation for a complex application including more than one ECU.

Apart from the hardware components, the commercial dSPACE simulation system also provides software functions to execute the real time model which simulate the

complex plant, and test software to program automated testes. Therefore the real time simulation is the most important component in the HIL system that needs to be developed.

2.2.4 Real time simulation

The real time computing refers to a software and hardware system, for which there is an operational deadline from event to system response. By contrast, a non-real-time system is one for which there is no deadline, even if the simulation operates in a high performance and fast response environment [51]. For example, a series of supercomputers running for solving a scientific problem may not be in real-time. However, the current usage of real time simulation normally implies the 'fast response' or 'fast computation' in terms of the program executing time. Because the real time system refers to the simulation that proceeded at a rate (time step), which is critical to match the real process in the hardware. In the automotive applications, for instance, the engine control system is required to operate in real time, since a delayed signal may cause engine failure or damage.

Because testing the ECU in real vehicles is time-consuming and labourer intensive, and it occurs very late in the engine development process, the prototype vehicle test in the early stage of design is increasingly being replaced by laboratory tests using HIL system which allows the engine ECU (prototype) to operate in conjunction with a real time simulation system emulating the plant (engine, vehicle dynamics, transmission, etc) or the whole vehicle [39]. By contrast, a conventional software-in-the-loop system, which is purely based on the simulation method, is limited by the insufficient insight of the engine behaviour, where the engine internal parameters are difficult to measure and simulate. It is therefore necessary to apply the real time modelling technique and hardware-in-the-loop system in the early stage of the engine development.

The modelling techniques can be classified into several categories depending on different concepts. In terms of the mathematical principle of the model, Brace [52] divides it into two types: analytical models and empirical models. Analytical models contain several equations including differential and algebraic equations, which are based on the laws of physics, chemistry, and thermodynamics. Those equations are based on either temporal discretization (time step) or spatial discretization (volume size), or even both of them. Empirical models apply look-up tables or fitted polynomials which are derived from empirical results. Empirical models could be very precise if the empirical data are measured accurately. However, the lack of predictive capability tends to limit the empirical model to a specific engine. On the other hand, analytical models may cause a speed problem for calculating those differential equations and the accuracy of the model is impacted by the complexity of the engine. However, most of the current models especially in the engine simulation are a combination of analytical and empirical models [53].

Fidelity and operational speed requirements

The real-time simulation required to provide a precise prediction, and programs for processing the simulation needs to be constantly operational to synchronise with the hardware within a specified time span. Therefore this trade-off between the simulation fidelity and execution speed is the critical task when developing a real time model to simulate complex plant.

In the literature (Table 2.1), the real-time model mainly focuses on the engine simulation, such as the linear engine models (e.g. LabVIEW [46,54] and Pi Autosim[48]), which are the analytical solution with simple combinations of several transfer functions; The mean value model which is also an analytical model and has been used widely, including Labcar [39], GT-Power [55], emmeskay's [56], TESIS [41,57] Univ.Kassel[58] , VDNAL [59] and ECUTEST [60]. Mean value models are mainly adapted as a part (engine) of a vehicle model in the research of vehicle dynamics such as TPS (Throttle Position Sensor), ABS (Anti-lock Brake System), knock detection, and etc. In terms of the computation speed, the mean value method

can be equivalent to (or faster than) a 'real-time' simulation but cannot provide detailed crank angle based prediction.

In order to improve the simulation accuracy as well as the operational speed, another type of engine model with the aid of empirical equations can be found in the GT-Power [55], RAPTOR-RT from SwRI [47], and some in-house engine simulations from University of Kassel [61,62] and Darmstadt University of Technology [63]. These engine real-time simulations apply a neural network to fit the experimental data, so it can fulfil both the speed and fidelity requirement. Hunt G., et al [49] also proposes a engine model using a series of simplified zero dimensional model to simulate the ducts and make up the air and exhaust path via lookup tables based on experimental data, so this model could be run in less than 33.3 μs (time for one crank angle at 5000rpm).

Model development tools

In order to develop the real time turbocharger simulation, software needs to be selected as platform tools. Therefore the application of Ricardo WAVE and the Matlab/Simulink will be discussed in this section.

a. Ricardo WAVE

The Ricardo WAVE model is not able to run in real-time due to its complexity (Hunt et al [49] from Ricardo declares that WAVE is 100-1000 times slower than real-time). However, WAVE is a satisfactory engine simulation with regard to predictive accuracy, which has already been validated both in steady and transient conditions by previous researchers in university of Bath [4]. Therefore, WAVE could provide data generation for the pre-processing work. Turbine data provided by the manufacturer, for instance, are usually limited to a small range of running conditions and have to be extrapolated to cover the full range.

WAVE follows the gas dynamics method to analyze the dynamics of pressure waves, mass flows and energy losses in ducts, plenums and the intake and exhaust manifolds.

The combustion process is simulated by a rate of heat release analytical model (Wiebe, Diesel jet and Profile models). The turbocharger (including VGT) is represented by steady state maps based on interpolation and extrapolation of the empirical data provided by the manufacture.

b. Matlab/Simulink

Matlab (**Mat**rix **Lab**oratory) provides a powerful mathematical tool to generate denser maps for the compressor and turbine based on the experimental data supplied by the manufacture. Various curve fitting methods and parametrical model can be executed in the Matlab environment. The iterative analytical model for predicting the turbine performance can be operated in the Matlab M-file.

The Simulink® toolbox in Matlab provides an environment for simulation and model-based design of dynamic and embedded systems, the turbocharger real-time model in this case. It provides a customizable set of block libraries that allows designing, simulating, implementing, and testing a variety of simulation programs. The real time simulation in Simulink can also be compiled from the matlab blocks into real time program code (RTC) with a simple mouse click. This RTC code is based on the C language which has higher operating speed and compactable with dSPACE platform to execute the real time program.

2.3 Conclusion

The literature review has provided an insight into the air charging systems, hardware-in-the-loop options and the real time modelling approaches.

1) Among existing air charging systems, the turbocharger is preferred as the device for emulating the engine air charge, since the turbocharger has been widely applied on diesel engines. Moreover, the compressor and turbine models can be used as the fundamental components for other air charging systems.

2) Empirical models for compressor and turbine may provide good prediction based on a large number of test data supplied by the manufacture. However the analytical model tends to represent the processes more fundamentally and is hence less reliant on data sourcing.

3) The charge air handling unit (CAHU) has the advantage that it allows testing engines without the time, financial and packaging constraints of developing prototype hardware

4) Most of the research shown in the literature survey applies to commercial products such as dSPACE simulator as the platform to form the hardware-in-the-loop system. Therefore this off-the-shelf platform is chosen in this work to investigate the new air charging testing approach.

5) The difficulty faced in real time simulation is the trade-off between the model accuracy to predict the turbocharger behaviour and the execution speed for communicating with the hardware in real time.

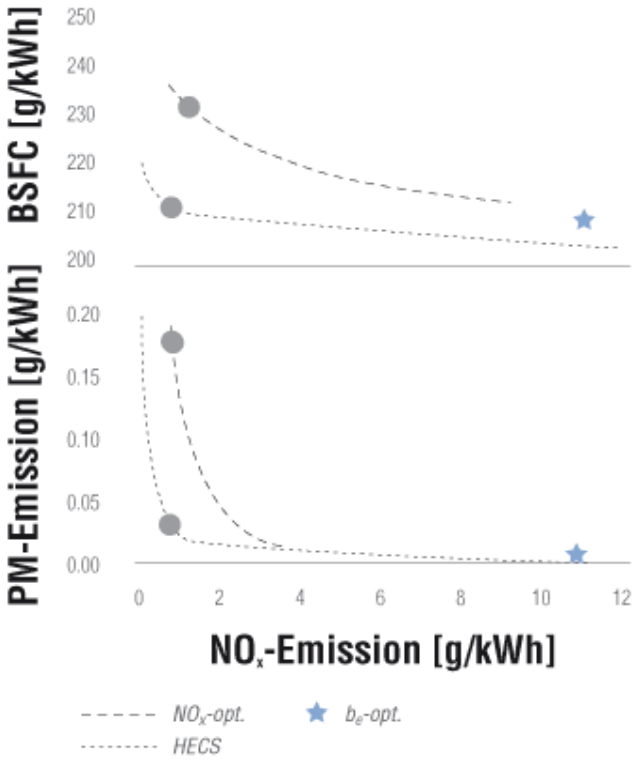

Figure 2.1 Trade-off between NOx and BSFC

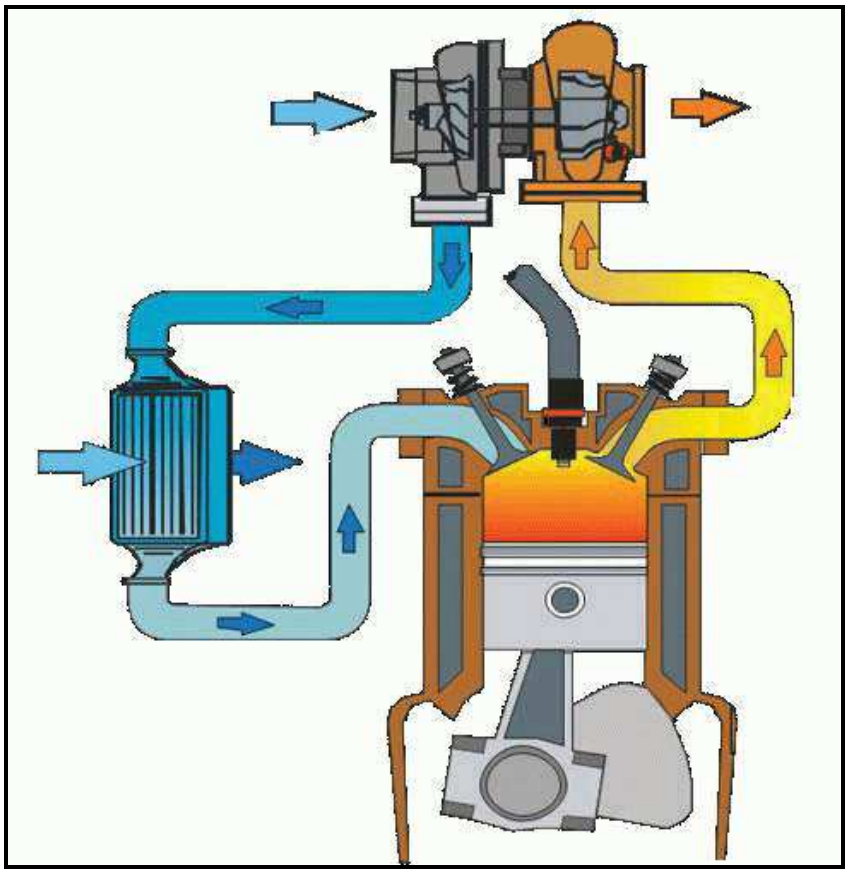

Figure 2.2 Turbocharger [4]

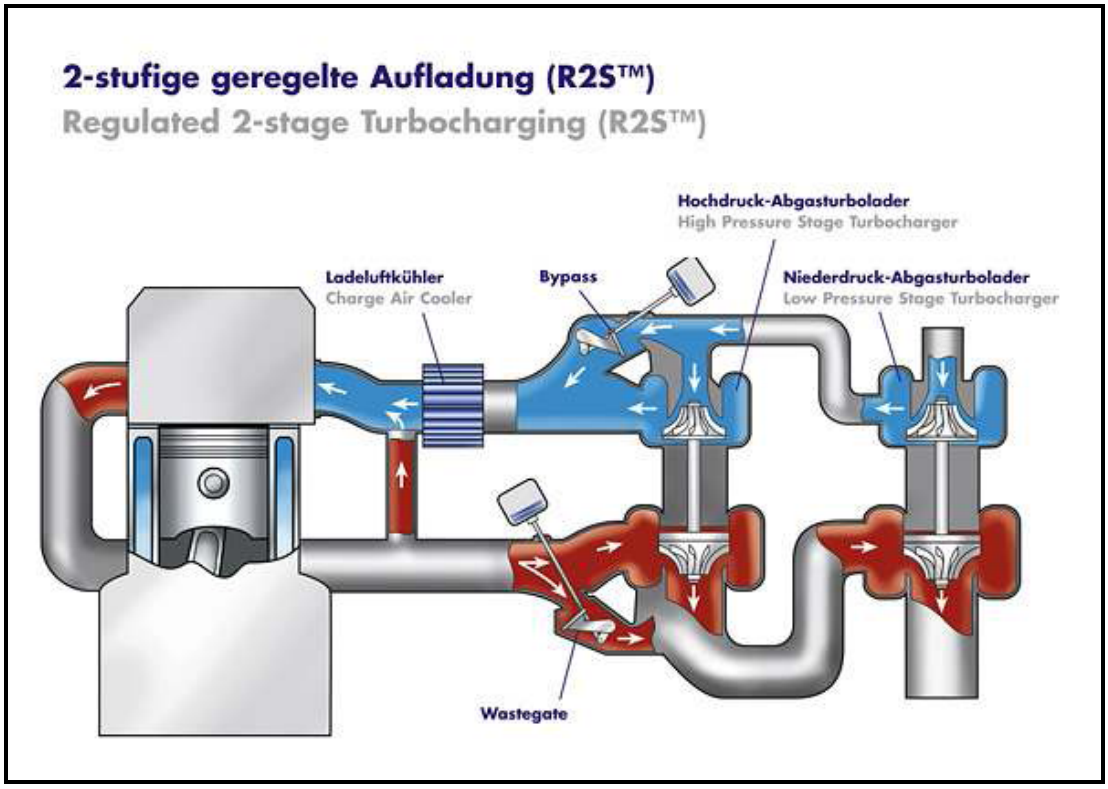

Figure 2.3 BorgWarner Two-stage turbocharging (R2S) [112]

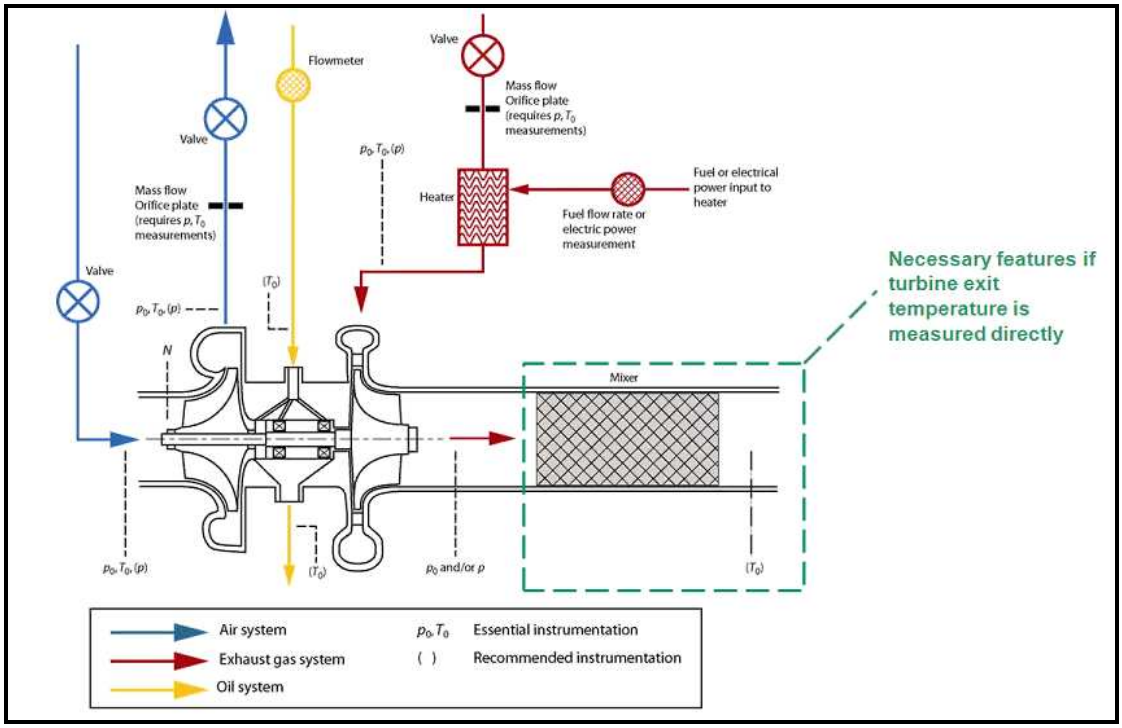

Figure 2.4 the schematic of a turbocharger gas stand [103]

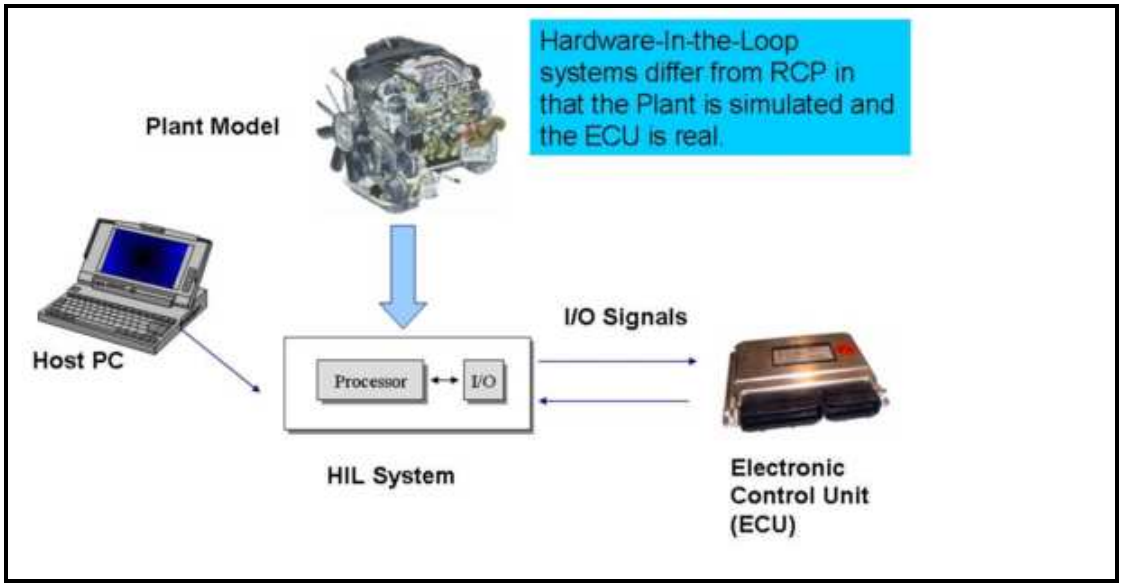

Figure 2.5 Hardware-in the loop system [38]

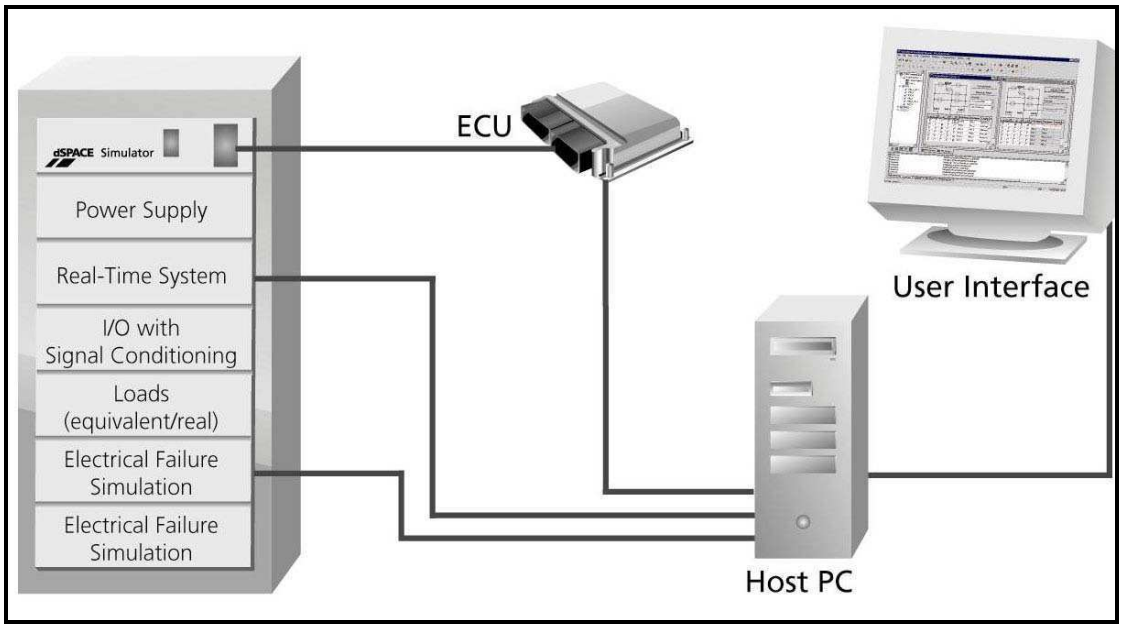

Figure 2.6 Structure of a typical hardware-in-the-loop system [39]

Table 2.1 Literature survey on real time model and hardware-in-the-loop system

Ref []	Instituation	Hardware	Software	Model	Real Sensor	Virtual Sensors	Test	Engine type
73	Unv. Huazhong S&T		VxWorks					
74	Scania CV AB, dSPACE	Scania truck/bus						
75	Lear Corp.							
	dSPACE GmbH							
	ETAS K.K.	Hybrid Electric Vehicle (HEV)						
	Horiba, Ricardo	HEV						
	ZF Friedrichshafen AG. Etc							
76	Unv. Parma & FIAT		QSF, F&E				RT model	Diesel Engine
40	Hyundai Motors		Labcar		TPS	Others	APS Failure	
45	Unv. Kassel. Etc	CARTS (Computer Aided Realtime Test system)					Cold start, warm-up VVT	4 Cylinder 1.6 L SI engine

Ref []	Instituation	Hardware	Software	Model	Real Sensor	Virtual Sensors	Test	Engine type
79	Unv.National Taipei	Matlab, xPC, PCI-6024E, Motorola MC 68376 Controler			None	All Sensors	MAP, Imep, Fmep	Scooter Engine (Yamaha XC125)
56	TATA Motors Ltd, ect	COTS,dSPACE's compact size simulator		Emmesk ay's				55KW(75PS) Four stroke,SII
44	Ford Motors & MIT	CAPPESS, VPACS-HIL simulator						
	IMECHE		Targetlink					
	Unv. Czech Tecl in Prague	LOLIMOT	GT-Power,					DI diesel engine for a small truck
77	Unv.Nottingham & Jaguar	dSPACE(S2210), Genix box and ECU/EMS	NuSim		Inj,VGT ,EGRv,IAT	MAP,MAF, Tem,APP, RPv,		V6 Turbo-charged Diesel Engine
6	TATA							4 Cylinder small car engine
80	Unvi. Parma			MVM model				Diesel Engine
43	Argonne National Lab	MATT, ANL-developed PSAT						
81	TESIS DYNAware GmbH							
65	Politecnio di Torino	dSPACE, vaccum booster, wheel cliper			8 pressur e		ABS, ESP	
37	Ford Motor	VPACS-HIL					ECU test	

Ref []	Instituation	Hardware	Software	Model	Real Sensor	Virtual Sensors	Test	Engine type
50	Ford Motor Co.						ECU test	
	KSAE	COTS, RTW of MATLAB						
	CSAE							
39	dSPACE GmbH	dSPACE						
82	Tech Univ. Hamburg-Harburg						Drive-Line	
83	STMicroelectronics	ROHR						
	IMECHE							
72	Univ. Salerno .Etc							Common-Rail, Multi-Jet diesel
	Elasis S.C.p.A							EVO Engine with VVT
	Elasis S.C.p.A .Etc							
78	Univ. Tsinghua							
85	DaimlerChrysler	dSPACE AutoBox ControlDesk		14DOF Veh			Chassis control	
84	Visteon, dSpace Inc	dSPACE, PC, IOBoard, Conditioning board, load, COTS						

Ref []	Instituation	Hardware	Software	Model	Real Sensor	Virtual Sensors	Test	Engine type
66	Univ.Tsinghua	Advantech. Co.		Math model			ESP, ABS	
49	Ricardo Consulting	dSPACE, PowePC 750 480Hz,		In-cycle	ET,Inj, VVT,VI,	Collant tem,MP,IAT,etc	Debug ECU	4cylinder,BMW, VVT, CR,DI, SI
86	BMW Group .Etc		PROMO	NN				
46	Woodward Governor. Etc	FPGA	LabView			cam, knock, Map. Etc		
55	Univ.Kassel. Etc		GT-Power,	NN	IMP,tem ,	others	cal cold start, warm-up	PFI /SI V6, manual,
48	Pi Technology. Etc	Pi AutoSim	Matlab				Angular model	
87	Elasis, TESIS		veDYNA				Real time model	
41	Mando Corpporation		ADAMS,Labcar				ESP	
42	Southwest Research Ins.Etc	AC motor, RT Lab, RAPTOR	ACSYSdyne				Transmission	
67	Southwest Research Ins.Etc	Ac motor (engine)					Transmission	
88	BMW Group	dSPACE		Physical, NN			RT model	

Ref []	Instituation	Hardware	Software	Model	Real Sensor	Virtual Sensors	Test	Engine type
47	Opal-RT Tech, Inc. Etc	RT-LAB	RAPTOR-RT					
68	Univ. Shanghai Jiao Tong	dSPACE (I/O)					ABS	
89	Univ. Tampere Tech						Control of Valvetrain	
57	dSPACE GmbH	dSPACE		Physical			ECU network	
90	Ent S.r.l-Italy	Texas Instruments CPU, DSP						
91	AVL List GmbH		Powertrain test bed					
54	San Diego State Univ		LabView					
69	Infineon Tec, dSPACE	dSPACE, Tricore CPU architecture					Knock detection	
58	Univ. Kassel, Volkswagen AG	CARTS (Computer Aided Realtime Test system)					Engine Calibration	CR Diesel engine
92	Ricardo, ETAS & Co.KG	LabCar					ECU software	
59	Systems Technology		VDNAL/RT				driving simulator	

Ref []	Instituation	Hardware	Software	Model	Real Sensor	Virtual Sensors	Test	Engine type
61	Univ. Kassel			MVM, NN				SI engine
63	Darmstadt Univ of Tech						RT model	Mecedes series 500 &900
60	KadraCons ultants	ECUTEST, VME/VXI		MVM				
62	Univ Kassel	CARTS (Computer Aided Realtime Test system)		NN			cylinder pressure	
93	Mforschung szentrum Inf		SPIN UPPAAL					
94	Univ Alberta		TKM				Ignition-timing	HCCI

Table 2.2 Benchmark results – running a complex truck simulation on different processors [28]

Processor	Calculation Time per Step
Intel Pentium III, 1GHz with PC-133 memory	4.4ms
AMD XP 2100, 1.73GHz with PC-2100 memory	2.6ms
Intel Pentium 4, 2.8 GHz with DDR memory	1.1ms

Table 2.3 Time step requirement for HIL processor at 5000rpm

Engine speed	**Engine speed**	**Frequency**	**Time step (per cycle)**	**Time step (per 1^{o} crank angel)**
5000 rpm	0.012 s/rad	83.3Hz	0.012s	33.3μs

Chapter 3 Turbocharger Architecture

3.1 Introduction

This chapter explains various analytical and experimental approaches that define the fundamental architecture of turbocharger operation. This is a detailed investigation of the turbocharger, its structure, components, dimensionless representations, and gas flow thermodynamics. Additionally, the gas flow energy and velocity triangle at each stage of the compressor and turbine are examined, so the physical principle can be applied in the research of real time turbocharger model which will be discussed in chapter 4.

3.2 Compressor

Through the history of turbo-machinery, there are two main flow types of compressor: radial flow and axial flow. Although the axial flow compressor has a higher efficiency, it has never been reached the production stage for an automotive engine due to the economic consideration [5]. Especially in the automotive application, the radial flow (centrifugal) compressor dominants the market, because of its simple design and wide operation range with a relatively high pressure ratio.

The radial flow (centrifugal) compressor consists of four basic components: [71]

1) stationary inlet casing (in some case provide with an air filter and noise reducing baffles)
2) rotating impeller (rotor)

3) stationary diffuser of the vaneless or vaned (preceded by a vaneless gap) type

4) collector or volute

Among these components, the rotating impeller and the stationary diffuser (vaneless or vaned) are usually called rotor and stator respectively in the TS (Temperature-Entropy) diagram which represents the gas thermo-properties while passing through the compressor. (Figure 3.3 shows the TS diagram of a typical radial flow compressor)

Inducer duct (Inlet Casing)

The function of the inducer duct is to deliver the air flow into the impeller with stable flow velocity. Therefore the property of the gas flow at the impeller inlet (impeller eye) is dependent upon the inducer duct design. According to the structure of the compressor, the configuration of the inducer duct tends to be categorised into different shapes: straight inlet duct, curved inlet duct, or a curved return passage of a multistage compressor [71]. However, the inducer duct should be designed to maintain as steady an inlet air flow velocity as possible. Otherwise, the circumferential and radial distortions of the flow could lead to a restraining effect on the unstable flow [72]. In this work, in order to simplify the turbocharger model for real-time running purposes, although there is an energy loss in the inlet casing while the turbocharger is mounted with outboard bearing [5], the process in the inlet casing would be considered as no energy transfer and the stagnation enthalpy remains constant (Figure 3.3), which is expressible as:

$$Q = KE$$

$$\dot{m}\,Cp(T_{01} - T_1) = \frac{1}{2}\dot{m}\,C_1^{\,2}$$

$$\therefore T_1 = T_{01} - \frac{C_1^{\,2}}{2Cp} \text{ and } P_1 = P_{01}\left(\frac{T_1}{T_{01}}\right)^{\frac{r}{r-1}}$$

Impeller (rotor)

The flow velocity triangle in the compressor impeller (rotor) is shown in

Figure 3.4, where V_1 is the axial entry velocity, U_1 is the rotor peripheral velocity (tip speed or rotational speed of the impeller), V_{R1} is the relative velocity, V_2 is the exit velocity, U_2 is the exit peripheral velocity, and V_{R2} is the exit relative velocity

So in this case (with stationary pre-whirl for the inlet), both inlet and exit:

$$V_R{}^2 = V^2 + U^2 - 2UV_\theta$$

3.1

The torque of the impeller is equal to the rate of change of angular momentum. Since the rate of change of angular momentum is given by the product of mass flow rate ($\dot{m}$), multiplied by the radius (r), and multiplied by the tangential component of actual velocity (V_θ).

$$TQ = \dot{m}\,(r_2 V_{\theta 2} - r_1 V_{\theta 1})$$

3.2

So the energy transfer in the rotor is given by the product of torque and angular velocity (ω):

$$E = \dot{m}\,\Delta h = \omega TQ = \omega\,\dot{m}(r_2 V_{\theta 2} - r_1 V_{\theta 1}) = \dot{m}(U_2 V_{\theta 2} - U_1 V_{\theta 1})$$

3.3

Because $U = \omega r$

From equation 3.1 and 3.3, the energy transfer expression gives:

$$-\dot{W} = E = \frac{1}{2}\dot{m}[(V_2^2 - V_1^2) + (U_2^2 - U_1^2) + (V_{R1}^2 - V_{R2}^2)]$$

3.4

The first term on the right hand side of equation **3.4** represents the change in absolute kinetic energy in the impeller. The second term represents the change of energy due to

moment of the rotating air from the inner radius of rotor to the outer radius of the rotor, where the centrifugal energy raises the static air pressure in the impeller. The third term represents the change in kinetic energy due to the change of relative velocity, resulting in a further change of static pressure within the rotor [5].

Because the majority of turbocharger compressors are designed without stationary pre-whirl vanes, the tangential component of inlet axial velocity could be neglected. So $V_{\theta 1} = 0$

Hence equation **3.3** could be rewritten as:

$$E = \dot{m}\Delta h = \dot{m}U_2 V_{\theta 2}$$

From the steady flow energy equation (SFEE):

$$\dot{Q} - \dot{W} = \Delta h + \Delta PE + \Delta KE \qquad 3.5$$

$\dot{Q} = 0$ $\dot{W} = \dot{E}$, and $\Delta PE = 0$

Hence equation **3.5** would be changed to

$$-\dot{W} = Cp(T_2 - T_{01}) + \frac{1}{2}V_2{}^2 \qquad 3.5a$$

Where T_2 is the static temperature at outlet of the impeller

T_{01} is the stagnation temperature for the impeller

Cp is the heat capacity at constant pressure for the air in the impeller.

$$-\dot{W} = \frac{1}{2}\{[V_2{}^2 - V_1^2] + [u_2^2 - u_1^2] + [V_{R1}{}^2 - V_{R2}{}^2]\}$$

$$\therefore Cp(T_2 - T_{01}) = [u_2^2 - u_1^2] + [V_{R1}{}^2 - V_{R2}{}^2]\}$$

Assuming isentropic condition when the air pass through the impeller,

$$\frac{T_2}{T_{01}} = \left(\frac{P_2}{P_{01}}\right)^{\frac{\gamma-1}{\gamma}}$$

$$V_{R2}{}^2 = 2CpT_{01}[1-\left(\frac{P_2}{P_{01}}\right)^{\frac{\gamma-1}{\gamma}}] + U_2^2$$

3.5b

The rotor mass flow with radial relative outlet velocity could be written as:

$$\dot{m} = V_{R2}\rho_2 A_2$$

3.6

Because the air flow during the rotor is considered as an isentropic process, the following equation could be deduced:

$$\rho_2 = \rho_{01}(P_2 / P_{01})^{\frac{1}{\gamma}}$$

And from the gas state equation;

$$\rho_{01} = \frac{1}{v_{01}} = \frac{P_{01}}{RT_{01}} = \frac{P_{01}}{CpT_{01}{}^{\frac{\gamma-1}{\gamma}}}$$

Equation **3.6** could be rewritten as:

$$\dot{m} = \sqrt{2c_pT_{01}\left[1-(p_2/p_{01})^{\frac{\gamma-1}{\gamma}}\right] + u_2^2}\ \left[p_{01}/(c_pT_{01})\right](\gamma/\gamma-1)A_2\left(\frac{p_2}{p_{01}}\right)^{\frac{1}{\gamma}}$$

3.6a

Therefore,

$$\left(\dot{m}\sqrt{c_pT_{01}}\right)/(p_{01}A_2) = \left[1-(p_2/p_{01})^{\frac{\gamma-1}{\gamma}} + u_2^2/2c_pT_{01}\right]^{1/2}[\gamma/(\gamma-1)](p_2/p_{01})^{1/\gamma}\sqrt{2}$$

3.7

The left hand side of equation **3.7** is the dimensionless mass flow number, which is possible to be deduced from turbine application as well. In the compressor, the rotor exit area A_2 is usually replaced by the square of the exit diameter d_2^2. Therefore the LHS of the equation **3.7** could be changed to $N\left(\dot{m}\right) = \dot{m}\sqrt{c_p T_{01}}/\left(p_{01} d_2^2\right)$

$$\left(\dot{m}\sqrt{c_p T_{01}}\right)/\left(p_{01} d_2^2\right) = \left[1-\left(p_2/p_{01}\right)^{\frac{\gamma-1}{\gamma}} + u_2^2/2c_p T_{01}\right]^{1/2}\left[\gamma/(\gamma-1)\right]\left(p_2/p_{01}\right)^{1/\gamma}\sqrt{2}$$

3.7a

Because the outlet rotor peripheral velocity term $u_2/\sqrt{2c_p T_{01}}$ is already dimensionless, the dimensionless speed number could be derived as following relationship:

$u_2 = \pi N d_2/60$

$$u_2\sqrt{c_p T_{01}} = \left[(\pi N d_2)/60\right]/\left(c_p T_{01}\right)$$

$$N(N) = N d_2/\sqrt{c_p T_{01}}$$

3.8

The third dimensionless is the pressure ratio:

$$N(p) = p_2/p_{01}$$

3.9

Again, assuming isentropic flow through the diffuser, these dimensionless numbers from the impeller calculation could be extended to the diffuser. As a result, the compressor map could be constructed with the overall pressure ratio p_3/p_{01} (eqn.**3.9**), the mass flow number $N\left(\dot{m}\right)$ (eqn. 3.7a) and the speed number $N(N)$ (eqn.**3.8**) as the variables.

In practice, the dimensionless mass flow and speed numbers, equations **3.7** and **3.8** are invariably replaced by their quasi-dimensionless equivalents, applicable to a particular machine and a particular working fluid.

The new quasi-dimensionless groups become:

For mass flow

$$N'\left(\dot{m}\right) = \dot{m}\sqrt{T_{01} / p_{01}} \qquad 3.7b$$

and for speed

$$N'(N) = N / \sqrt{T_{01}} \qquad 3.8a$$

which now replace their fully dimensionless equivalents, equations **3.7** and **3.8**.

The units employed are:

For the mass flow number

$$\dot{m}\sqrt{T_{01} / p_{01}} = (kg / s)\sqrt{K} / \left(N / m^2\right)$$

For the speed number

$$N / \sqrt{T_{01}} = (rev / s) / \sqrt{K}$$

Finally, when constructing compressor maps it is even more convenient to reduce the quasi-dimensionless mass flow number, equation **3.7** to a 'straight' mass flow $\dot{m}$ by adopting a reference stagnation pressure $(p_{01})_{ref}$ and temperature $(T_{01})_{ref}$ with the abscissa now representing the mass flow rate directly, corrected to the assumed reference stagnation conditions.

Typically, in SI units

$$(p_{01})_{ref} = 1 \text{ bar} = 100\ kN/m^2, \text{ i.e. } 1 \text{ bar}$$

and

$$(T_{01})_{ref} = 288\ ^\circ K, \text{ i.e. } 15\ ^\circ C$$

$$\left(\dot{m}\right)_{corr} = \left(\dot{m}\right)_{actual} \left(\sqrt{T_{01}/288}\right)/\left(p_{01}/100\right) \qquad kg/s \qquad \text{3.7c}$$

Similarly, the quasi-dimensionless speed criterion, equation (3.8a), may be replaced directly by speed, such that corrected speed becomes

In SI units

$$(N)_{corr} = (N)_{actual} / \sqrt{(T_{01,actual}/288)} \quad rev/s \qquad \text{3.8b}$$

Figure 3.1 is a typical compressor map, with the abscissa represented by the quasi dimensionless group $\dot{m}\sqrt{T_{01}} / p_{01}$, equation 3.7a.

Diffuser

The diffuser is a stationary component (stator) and is fitted directly around the impeller. The fluid discharges from the impeller with a high velocity (high kinetic energy). Consequently, the diffuser is required to convert the kinetic energy leaving the impeller tip into static pressure. The influence of the diffuser efficiency to convert the kinetic energy is important, since approximately half of the fluid energy at the impeller tip is kinetic energy [5]. The diffuser system of a centrifugal compressor is usually constructed of either a vaneless diffuser or a vaned diffuser.

The vaneless diffuser is often adopted because of its simplicity and inexpensive construction. The vaneless diffuser is constructed from two converging walls forming an open passage from the impeller tip to a specified discharge diameter [71]. The fluid leaving the impeller tip at high velocity (sonic absolute velocity) could be reduced to subsonic velocity with shock waves.

For vaneless diffuser, the long flow path leads to a high friction loss during the flow passing through the diffuser. But, this long flow path can not be easily reduced, because a long flow path is necessary to gain the required diffusion through the conservation of angular momentum [71]. Hence the vaned diffuser is often adopted to shorten the flow path, therefore reduce the diffuser loss and improve the overall efficiency, especially for a design of small compressor to produce the same amount of boost. However, compared with the vaneless diffuser, the main disadvantage of the vaned diffuser is the relatively small operating range. (Details would be discussed in the following section) In the automotive turbocharger application, a broad operating rage is required at different engine running condition. As a result, the vaned diffuser compressor is not generally used for the automotive turbocharger. However, in recent

research [119], variable geometry diffuser compressor has drawn attentions on potentially provide wider mass flow range and higher efficiency.

3.3 Turbine

Similar to the compressor, the turbine also has two basic designs at present in turbochargers: the radial flow turbine and axial flow turbine. The radial flow turbine is mainly used for small automotive or truck turbochargers; the axial type is commonly used for the large turbochargers applied to medium-speed stationary and railway traction engines and large marine engines [5]. Therefore, in this section, the discussion is mainly about the radial flow turbine which is suitable for automotive turbochargers. Because the radial flow turbine tends to efficiently deliver high pressure ratio (approaching 4:1) and is also more robust and cheaper than an axial turbine [5].

The turbine structure is similar to the centrifugal compressor, apart from the nozzle vanes replacing the diffuser vanes. So a typical turbine consists of these components: a inlet casing (a scroll), a set of inlet nozzles followed by a short vales gap, turbine wheel (rotor) and a exhaust diffuser in some cases [71, 5].

Stator

The inlet casing and nozzle are the stators in the turbine structure. The function of the stator is to deliver a gas flow as uniform as possible into the turbine rotor. Meanwhile, the gas would be accelerated and the pressure tends to be reduced when the exhaust flow is passing through the nozzle. Hence the kinetic energy of the gas increases before entering the turbine rotor. Some turbocharger turbines use a nozzleless casing to simplify and downsize the turbine design, and widen the turbine operating range. But considering a modern turbine design requirement, especially for the diesel engine turbocharger, variable geometry turbochargers (VGT) are necessary to provide

sufficient power when the engine is running at low speed condition. That means the geometry of inlet casing of the turbine could be varied via changing the nozzle vane position. For a fixed geometry turbocharger (FGT), the expansion ratio of the turbine will vary greatly with mass flow rate. Since the boost pressure (compressor pressure ratio) is related with the turbine expansion ratio. Compared with the engine speed range, the turbocharger could not operate with high efficiency at all engine running conditions. Hence the engine may have insufficient boost at low engine speed conditions and have over-boost at high engine speed. For a variable geometry turbocharger (VGT), at lower engine speed, the nozzle tends to close more (can drive EGR closed at very low engine speed) to deliver enough power for driving the compressor to provide sufficient boost pressure; at higher engine speed, the nozzle tends to open more to keep the turbine running with high efficiency, and prevent excessive pressure build up.

Rotor

The turbine inlet and outlet gas velocity triangles could be presented as Figure 3.6. In this case the fixed element (nozzle ring or nozzleless volute casing) precedes the impeller. Assuming the gas flow in the turbine is isentropic, the steady flow energy equation (SFEE) could be represented as:

$$v_2^2 = 2C_p T_{01}\left[1-\left(p_2 / p_{01}\right)^{\frac{\gamma-1}{\gamma}}\right] \qquad 3.10$$

If assuming that the turbine inlet flow to the rotor is radial, and the absolute outlet gas flow is axial, the velocity triangles could be presented as following equations:

$$v_{R_2}^2 = v_2^2 - u_2^2 \qquad 3.10a$$

$$v_{R_3}^2 = v_3^2 + u_3^2$$

3.10b

Substituting velocity relationship into SFEE applied to the impeller,

$$v_{R_3}^2 = v_{R_2}^2 + 2c_pT_2\left[1-\left(p_3/p_2\right)^{\frac{\gamma-1}{\gamma}}\right]+u_3^2-u_2^2$$

$$= v_2^2 - u_2^2 + 2c_pT_2\left[1-\left(p_3/p_2\right)^{\frac{\gamma-1}{\gamma}}\right]+u_3^2-u_2^2$$

with $T_{02}=T_{01}$ and $p_{02}=p_{01}$ for isentropic flow

$$v_{R_3}^2 = 2c_pT_{01}\left[1-\left(p_3/p_{01}\right)^{\frac{\gamma-1}{\gamma}}\right]+u_3^2-2u_2^2$$

3.11

With absolute outlet velocity v_3 given by equation 3.10b, the turbine rotor mass flow becomes:

$$\dot{m} = v_3.\rho_3.A_3$$

so that, substituting from equation **3.11** and with

$$\rho_3 = \rho_{01}\left(p_3/p_{01}\right)^{1/\gamma} = \left[p_{01}.\left(c_pT_{01}\right)\right]\left(\gamma/(\gamma-1)\right)\left(p_3/p_{01}\right)^{1/\gamma}$$

the rotor mass flow becomes

$$\dot{m}\sqrt{c_pT_{01}}/(p_{01}A_3)=\sqrt{\left[1-(p_3/p_{01})^{\frac{\gamma-1}{\gamma}}+u_2^2/(2c_pT_{01})\right]\left[(d_3/d_2)^2-2\right]}\left(\frac{p_3}{p_{01}}\right)^{\frac{1}{\gamma}}\sin\beta_3\frac{\sqrt{2}\,\gamma}{\gamma-1}$$

3.12

β_3 is the rotor outlet angle

Similar to compressor mass flow equation **3.7**, left-hand side of equation **3.12** is the dimensionless flow number. Thus the rotor velocity term $u_2^2/2c_pT_{01}$ under the square root on the right-hand side of equation **3.12** is again equivalent to the dimensionless speed criterion $Nd_2/\sqrt{c_pT_{01}}$.

The dimensionless groups arising from equation **3.12** are therefore as follows:

a) mass flow number $N\left(\dot{m}\right)=\dot{m}\sqrt{c_pT_{01}}/\left(p_{01}d_2^2\right)$

b) speed number $N(N)=Nd_2/\sqrt{c_pT_{01}}$

c) pressure ratio $N(p)=p_3p_{01}$

d) diameter ratio $N(d)=d_3/d_2$

and the dimensionless torque number would be:

e) $N(\tau)=\tau_t/\left(d_2^3p_{01}\right)$

The same with the case of compressors, for practical purposes, quasi-dimensionless numbers are more convenient for the turbine characteristics maps. So the quasi-dimensionless numbers and units are:

a) mass flow $N'\left(\dot{m}\right) = \dot{m}\sqrt{T_{01}} / p_{01} \quad (kg/s)\sqrt{K}/\left(kN/m^2\right)$

3.13

b) speed $N'(N) = N/\sqrt{T_{01}} \qquad (rev/s)/\sqrt{K}$

3.14

c) torque $N'(\tau) = \tau_t / p_{01} \qquad (Nm)/\left(kN/m^2\right)$

3.15

Turbine maps are constructed in an analogous manner to compressor maps, as described in previous section. The turbine specification, which is supplied by the manufacture, is usually based on a cold air test. So for further simplification, a reference pressure $(p_{01})_{ref}$ and temperature $(T_{01})_{ref}$ could be adopted in the turbine characteristic maps. The reference conditions are typically based on the following values:

$$(p_{01})_{ref} = 1 \text{ bar } = 100 kN/m^2$$

$$(T_{01})_{ref} = 288K \text{ i.e.} 15°C$$

giving corrected mass flow

$$\left(\dot{m}\right)_{corr} = \left(\dot{m}\right)_{actual} \sqrt{T_{01,actual}/288}\,/\left(p_{01,actual}/100\right) \quad kg/s$$

3.16

and corrected speed

$$(N)_{corr} = (N)_{actual} / \sqrt{T_{01,actual} / 288} \quad rev/s$$

3.17

3.4 Turbocharger Performance characteristics

3.4.1 Compressor and Turbine Efficiency

The definition for the compressor efficiency is the useful work divided by the actual work delivered by the compressor. From the second law of thermodynamics, the compressor efficiency is equal to the isentropic work divided by the actual work when the fluid passing through the compressor. According to the T-S diagram (Figure 3.3

), the total to total compressor efficiency could be represented as following equations:

$$(\eta_C)_{tt} = \frac{isentropic\_work}{actual\_work} = \frac{h_{03s} - h_{01}}{h_{03} - h_{01}} = \frac{|Cp(T_{03s} - T_{01})}{Cp(T_{03} - T_{01})} = \frac{T_{03s} - T_{01}}{T_{03} - T_{01}}$$

3.18

Since the engine benefits little from the kinetic energy of gas leaving the compressor, another definition of compressor efficiency (total to static) is more convenient and realistic [5].

The total to static compressor could be expressed as:

$$(\eta_c)_{t/s} = \frac{T_{01}\left[\left(\frac{p_3}{p_{01}}\right)^{\frac{\gamma_2}{\gamma}} - 1\right]}{T_3 - T_{01}}$$

3.19

Similar with the compressor, the turbine total to static efficiency is:

$$(\eta_T)_{t/s} = \frac{T_{01} - T_3}{T_{01}\left[1 - \left(\frac{p_3}{p_{01}}\right)^{\frac{\gamma_3}{\gamma}}\right]}$$

3.20

In the compressor specification, some manufactures quote total to total efficiency, because it is higher than total to static efficiency. Even worse, some manufactures quote total to total efficiency without declaring on what kind of efficiency is used for the calculation [5].

3.4.2 Turbine Blade Speed Ratio

The turbine blade speed ratio is the rotor tip velocity divided by the velocity that would be achieved by the gas following isentropic expansion from the inlet condition to the pressure at the exit from the turbine (total to static): [5]

$$\frac{U}{C_s} = \frac{U}{\sqrt{2(h_{01} - h_{3ss})}} = \frac{U}{\sqrt{2CpT_{01}\left[1 - \left(\frac{P_3}{P_{01}}\right)^{\frac{\gamma-1}{\gamma}}\right]}}$$

3.21

The term ‘blade speed ratio’ (BSR) was firstly used in impulse steam turbines where the enthalpy change in the rotor is zero. So the blade speed ratio refers to the blade speed divided by the gas jet speed [5]. The map of blade speed ratio against the turbine efficiency is very important for matching the compressor and represents the

turbines' own characteristics as well. With known inlet temperature and fixed pressure ratio (expansion ratio), the blade speed varies with the turbine speed, and the efficiency peak occurs at $\frac{U}{C_s} = 0.725$.

3.5 Turbocharger Maps

3.5.1 Introduction

As mentioned previously, there has been little research undertaken on a real time turbocharger model. Therefore the turbocharger model needs to be investigated firstly and the compatibility in a real-time environment can then be evaluated using the compiler in the Matlab real-time workshop (RTW).

With regard to the turbocharger simulation, especially for fulfilling the real-time requirement, the computation time and model accuracy need to be taken into consideration. As discussed in the previous section, the modelling techniques can be divided into two types: analytical model and empirical model. The analytical model is based on better understanding of the physical hardware, and it provides full range of the turbocharger operation where the experimental work cannot achieve. However the iteration loops or differential equations will dramatically reduce the speed of the model. On the other hand, the empirical model may have high fidelity and fast speed if the experimental data are accurate, but it can not provide any predicting capability, which is limited by the supplied database. Therefore the map based turbine and compressor models could solve these problem which apply both the analytical and empirical methods to predict the turbine and compressor performance in offline.

Hence an investigation of the turbine and compressor maps and their data limitation are presented in this section, whilst the numerical and analytical methods to improve the existing compressor and turbine maps will be detailed in chapter 4.

3.5.2 Compressor and turbine maps and data limitation

The conventional way to simulate the turbocharger performance is to plot (with data interpolation and extrapolation) compressor and turbine maps with dimensionless (or quasi-dimensionless) parameters. The compressor characteristics map is usually plotted in terms of pressure ratio $\left(P_{out} / P_{in}\right)$ against the mass flow parameter $\left(\dot{m}\sqrt{T_{01}} / P_{01}\right)$ with constant turbocharger speed line $\left(N / \sqrt{T_{01}}\right)$ (eqn.**3.8**) and compressor efficiency $\left(\eta_{CTT}\right)$. (Figure 3.1shows a typical compressor map)

In the compressor map (Figure 3.1), there are mainly three zones. The central zone is the stable operating zone which is separated from the other two unstable operation zones by a surge line on the left and choking limiting flow area on the right. At a constant pressure ratio, the efficiency decreases with the mass flow reduction but the compressor still runs in the stable area. However, with further mass flow reduction, this will relieve the adverse pressure gradient until a new flow regime at a lower pressure ratio is established. The flow will then build up again to the initial condition and thus flow instability will continue at a fixed frequency [65]. In practice, the vaned-type diffuser compressor tends to have the surge line closer to the maximum efficiency zone than the vaneless-type diffuser compressor. This is the reason why vaneless diffuser compressor has wider operation range. At the other extreme, the compressor operates at very high speed with high gas velocity with high boost and high mass flow. When the gas mass flow exceeds the ability of the diffuser to accept, the diffuser chokes. So the compressor speed would rises dramatically with a small mass flow rate increment. As a result, the compressor is running at an unstable condition. Hence, the compressor map needs to set up carefully; otherwise over-interpolation and extrapolation would lead to an unacceptable turbocharger performance simulation.

Compared with the compressor map, the turbine map could be plotted in the same way with pressure against mass flow rate with constant turbine speed lines and

isentropic turbine efficiency contours (Figure 3.2). However, calculations based on the pressure ratio/ mass flow parameter map are different. Because as in Figure 3.2, the efficiency contours tend to have a similar slope to the speed lines, leading to an inaccurate determination of the turbine efficiency. Hence a lookup table model based on this map may lead to a significant mistake while predicting the efficiency at different turbine running conditions. So this requires careful representations of the turbine map to fit in the real-time turbocharger model.

In both the turbine and compressor maps, the numerical data either are supplied by the manufacturer or tested by the experimental equipment (turbocharger dynamometer)

Manufacturers' data

The turbocharger data provided by the manufacture are normally measured on a gas stand (Figure 2.4), where the compressor and turbine are connected. From the compressor side, the blue line refers to the air drawn from the atmosphere, and P and T represent the pressure and temperature measurement at different locations. On the other hand, the red line passing through the turbine refers to the hot exhaust gas which needs to be heated by either a combustion chamber or a heat exchanger before entering the turbine.

The turbocharger manufacture data comes in the form of maps, usually as an image, as shown in Figure 3.1 and Figure 3.2. Therefore, the first difficulty in using this data is getting it from this image format into a set of data points. Another problem with compressor data supplied from manufacturers is the fact that it is measured at different operating conditions which is limited by the turbine flow rate and the shaft speed. The turbine map is also limited by the compressor performance and the shaft speed range. Although this data is often more accurate in the limited region it is taken in, the data points are sparse and require both interpolation and extrapolation in order to be useful. Understandably, this also makes comparison to experimental data difficult. Despite these faults, manufacturers' data is often more accurate than

experimental data and is still the most common source of data for modelling turbochargers.

Experimental data

The experimental data comes from the test on a turbocharger dynamometer. Figure 3.7 shows the schematic of a turbine dynamometer for measuring both the turbine performance under both steady state and pulsating conditions. Comparing with the gas stand (shown in Figure 2.4), the turbine can be measured separately in a wider flow range without the restriction from the compressor side. The difficulty of the turbo-dynamometer to measure the turbine or compressor performance is the indirect power measurement. Because the power of the turbine and compressor are calculated from the pressure and temperature ratio, the measurement of the temperature could introduce extra error since:

a. External heat transfer exists to the surroundings

b. Internal heat loss occurs across the turbocharger shaft

Although external heat loss could be controlled by lagging to isolate the compressor and turbine from the surroundings, the problem in terms of the internal heat loss in the bearing cannot be solved unless separate measurement are undertaken, and the separation could lead to additional errors. Additionally, the back to back test of turbine and compressor may restrict the compressor operating domain to match the turbine performance.

3.6 Conclusion

The architecture of turbocharger is described in this chapter including the turbine and compressor parameters, dimensionless representations, mass flow and energy equilibrium, temperature-entropy diagram and velocity triangle analysis for each stage of the flow. Furthermore, the use of compressor and turbine performance maps is also detailed in this chapter, with the focus on the modelling difficulties from insufficient testing data supplied by the manufactures or measured on the turbo-dynamometer. These analyses provide the fundamental principles of the flow characteristics in both the compressor and the turbine. These principles will be used in later chapters to describe the modelling of the performance of the compressor and turbine where appropriate.

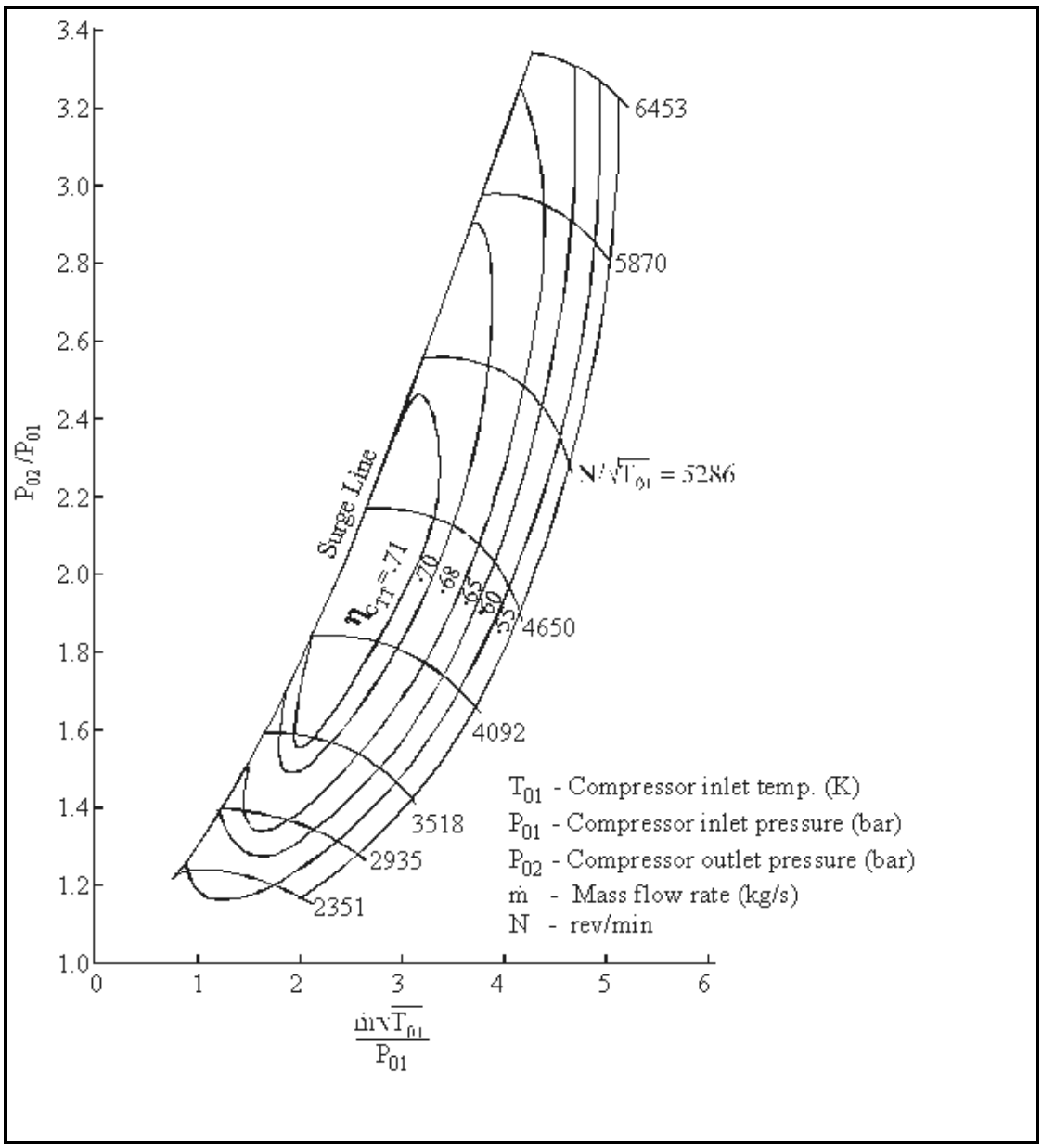

Figure 3.1 Compressor map [115]

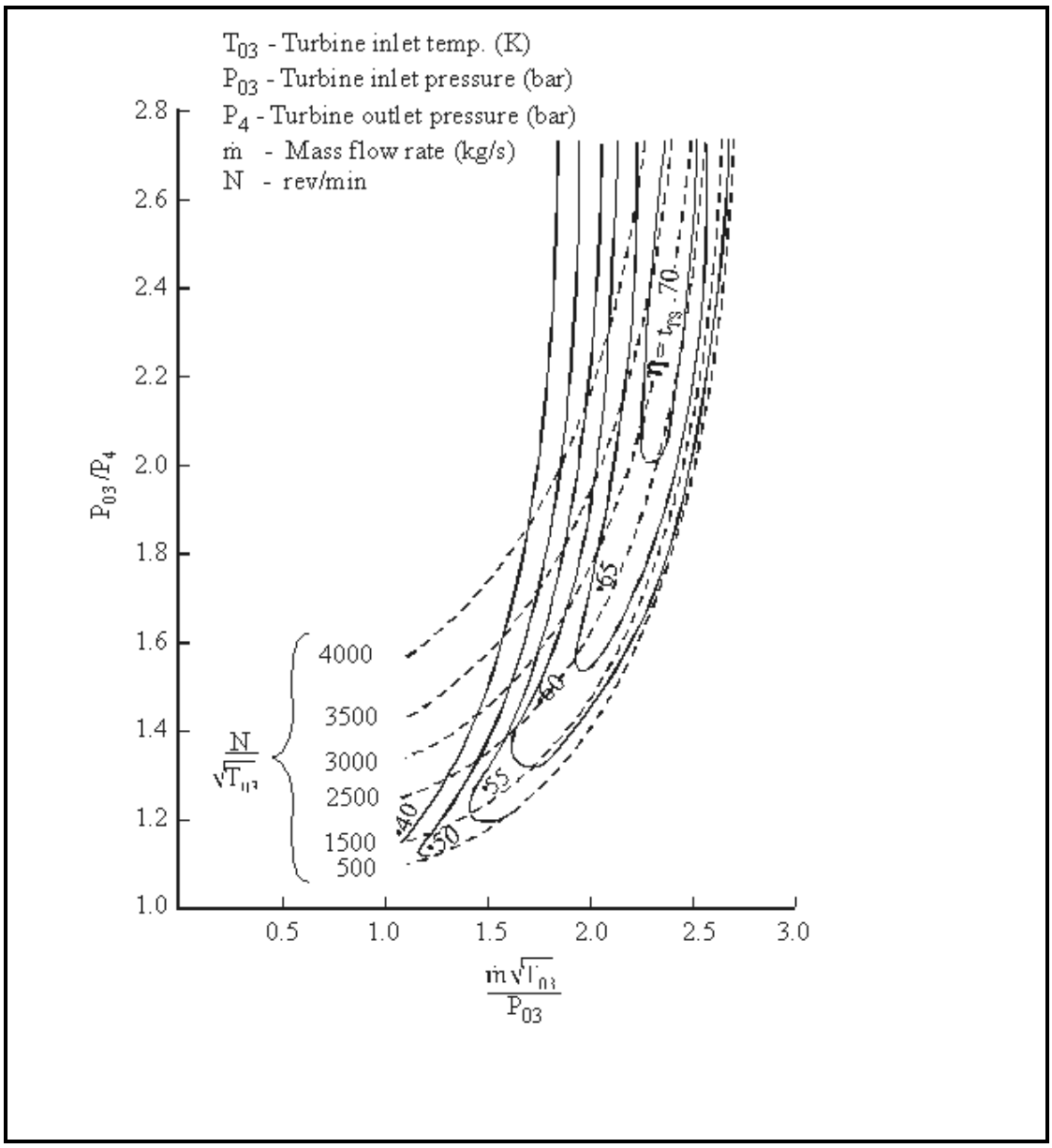

Figure 3.2 Turbine map [115]

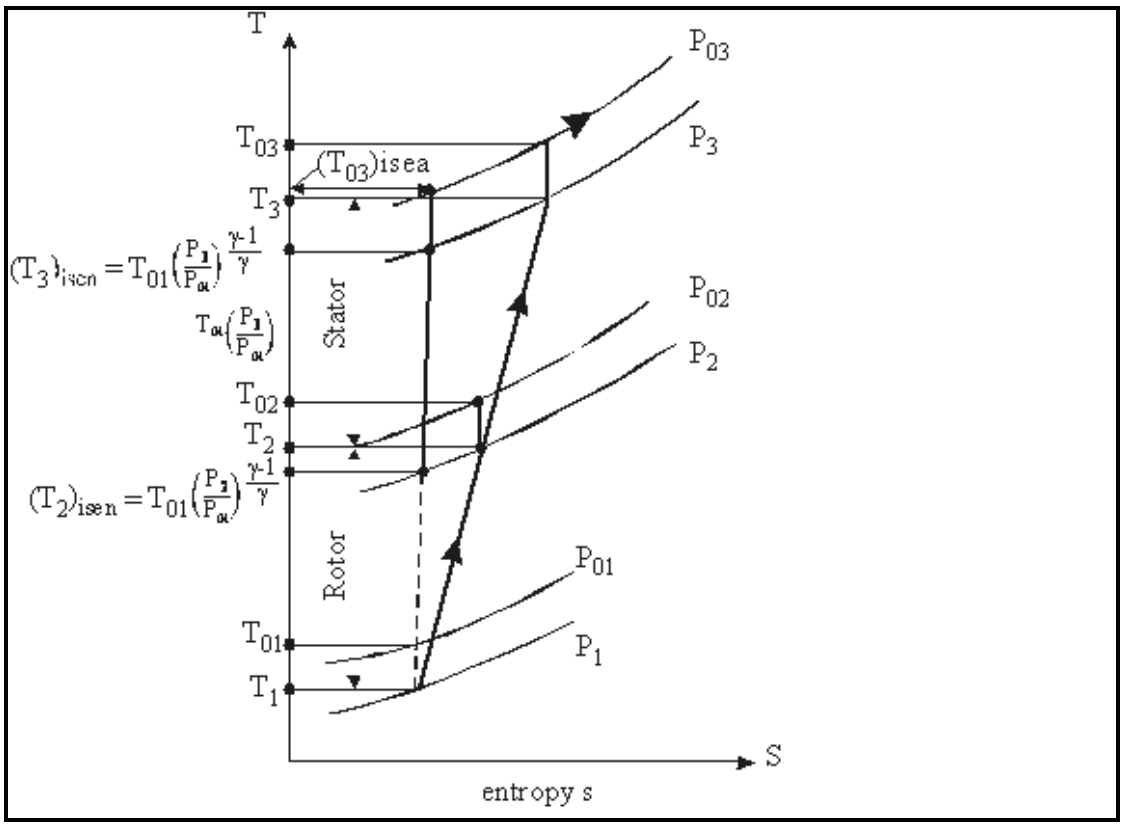

Figure 3.3 T-S diagram for compressor

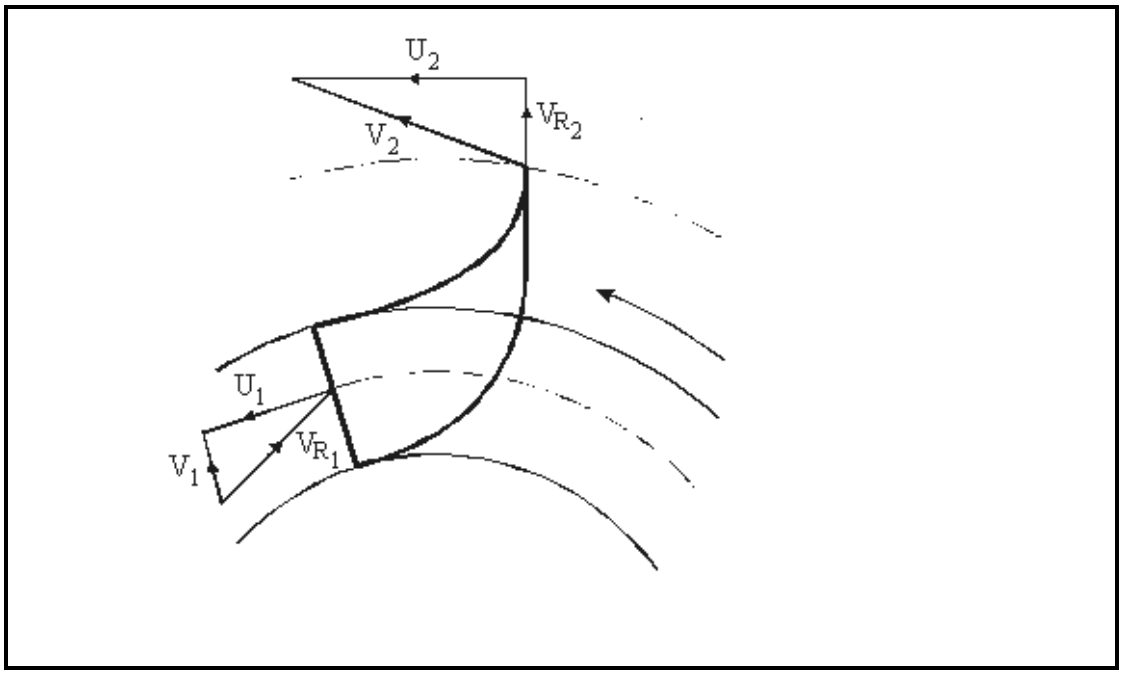

Figure 3.4 Velocity diagram for compressor

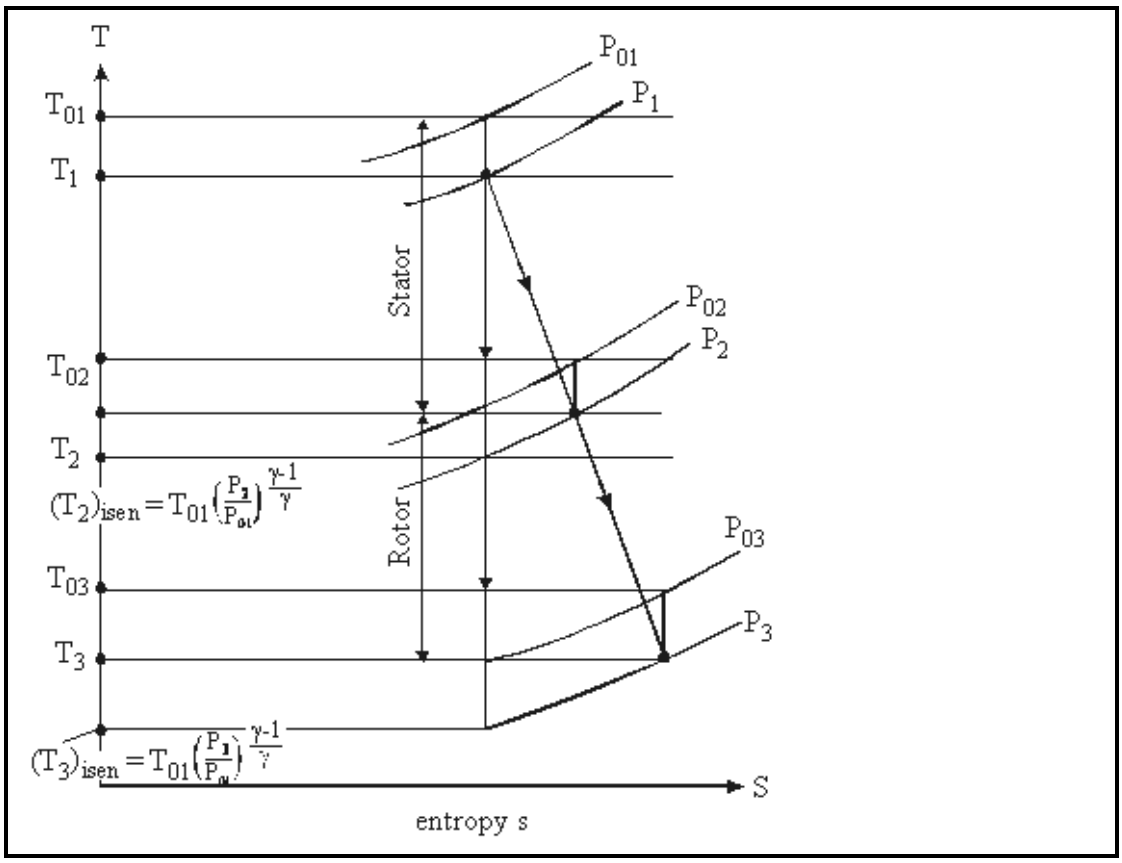

Figure 3.5 T-s diagram for turbine

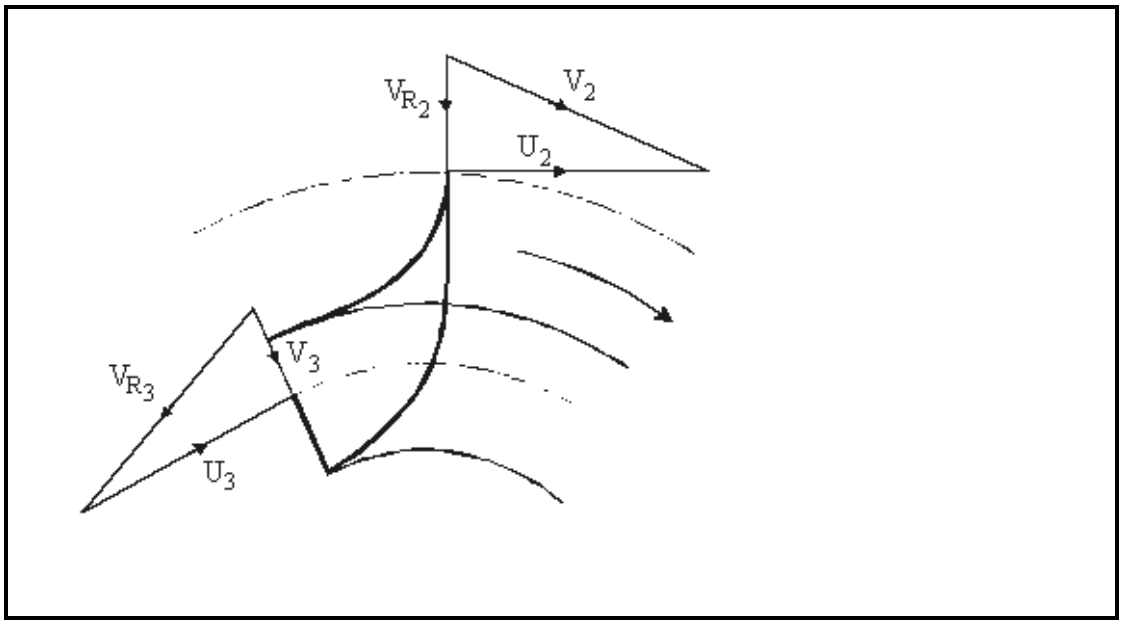

Figure 3.6 Velocity diagram for turbine

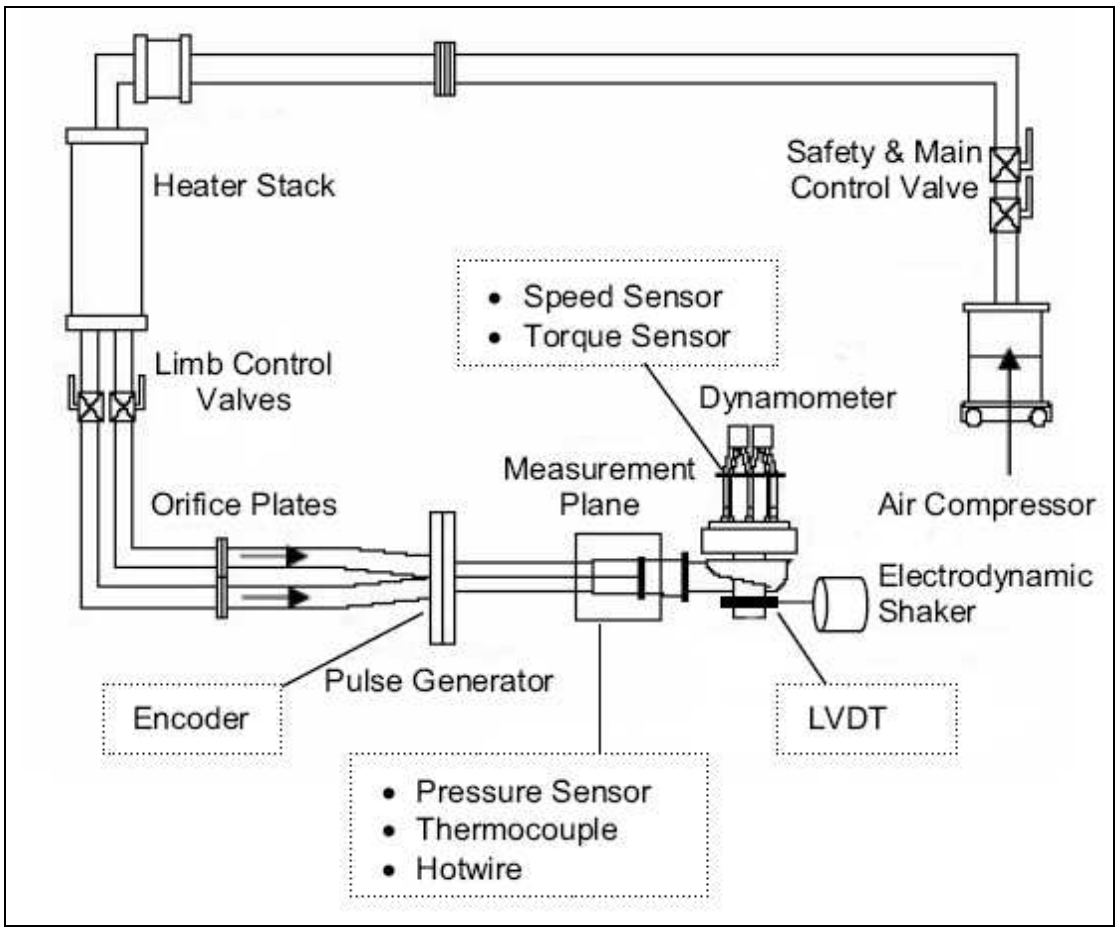

Figure 3.7 Schematic diagram of the turbine test rig [118]

Chapter 4 SOFTWARE: APPROACHES TO REAL TIME TURBOCHARGER SIMULATION

Overview

This chapter details the real-time turbocharger model as the software part in the hardware-in-the-loop testing system. Both the compressor and the turbine models are presented and different modelling techniques are discussed for the use in real-time models where the speed of execution is critical.

Section 1 covers the software environment of the real-time model. The reasons to choose Matlab/Simulink are discussed and the model structure as well as the inputs and outputs are detailed in this section.

Section 2 details the compressor model in the real-time turbocharger model. Since the compressor maps are typically presented in graphical form and do not cover the entire operating range of the engine, leading to difficulties in simulation, different modelling techniques are analysed in this section.

Section 3 details the turbine model with the effect of variable geometry nozzle vane positions. The analytical model is also presented and the outputs are discussed with the difficulty on lack of experimental data provided by the turbine manufacture.

Section 4 describes the turbocharger shaft model and the gas property model to calculate the specific heat capacity and the ratio of specific heat at different air-fuel ratio and temperature.

4.1 Software environment

4.1.1 Turbocharger model structure

The main objective of the software part of this HIL system is to allow the virtual simulation to operate in the real-time environment in conjunction with the communications between the software model and the hardware facilities. In this project, the communications between the CAHU and the turbocharger real-time model are handled by the dSPACE equipment (chapter 6). So the real-time turbocharger model is required to be built in the dSPACE authorised software which is the Matlab/Simulink. The turbocharger real-time model is originally created in the Matlab/Simulink software, and the model is then compiled by using the real-time workshop on the dSPACE hardware platform PC. During the compile process, the simulation program is transferred from Matlab code (file extension: .mdl) to C code (file extension: .swf) which increases the speed of the simulation to match the requirement of the real-time simulation. Hence the new form of the real-time model can be run on the dSPACE control desk.

The structure of the steady flow model in Matlab/Simulink is shown in Figure 4.1. The red block refers to the turbocharger sub-model, and the lines connected with the turbocharger model represent the input/output signals. The signals are connected with the real-time multi-message blocks (RTICANMM) from the integrated dSPACE workshop in the Simulink model library. In Figure 4.2, the turbocharger model is illustrated schematically, where

a. the red block is the turbine model;

b. the green block is the compressor model

c. the cyan block is the turbocharger shaft model

d. the yellow blocks are the input/output modules

e. lines represent the signals among individual modules

4.1.2 Model inputs and outputs

The I/O (input/output) module in compressor model was created based on the control requirements from the CAHU system point of view. Since the CAHU is designed to emulate the air charge of the engine, pressure setpoints from the compressor model are required to be sent to the CAHU system to control the valve for giving rise to the corrected boost pressure. It is therefore essential to let the real-time model generate outputs of pressure ratios across the compressor. Like the compressor model, the turbine model needs to provide the back pressure setpoints for the CAHU control system. Consequently, the exhaust gas expansion ratios have to be the output setpoints of the turbine model.

On the exhaust side of the engine, the Charge Air Handling Unit (CAHU) control system is designed to be set as pressure source or mass flow source, which means the control variable could be either pressure or the mass flow rate. However, in the turbine, the pressure ratio is built up mainly by the amount of gas passing through an orifice which refers to the blockage from the turbine stator and rotor. The orifice opening is controlled by the CAHU system. So the mass flow source method was selected to control the engine exhaust. Hence the mass flow rates on both the air and the exhaust gas are set to be the inputs for the turbocharger model. Although the model inputs and outputs are decided, the benefits and shortcomings of this selection will be discussed in the following sections.

In order to calculate the turbocharger speed, the torques in both the compressor and the turbine are required to be converged in the turbocharger shaft model. It is hence necessary to set the compressor/turbine isentropic efficiencies as the outputs from the compressor and turbine model respectively. The relative calculation will be detailed in section 4.4

4.2 Compressor model

4.2.1 Compressor maps

For matching the simulation requirement to allow the model to operate in real-time environment, simple calculation methods are preferred to be applied for increasing the speed of the simulation program. Therefore *lookup table* modules from the Simulink toolbox are widely utilized in the real-time model to calculate the compressor performance.

In the Matlab/Simulink tool box, the lookup table block uses an array of data set to map input values to output values, approximating a mathematical function. Given input values, the Simulink software performs a "lookup" operation to retrieve the corresponding output values from the table. If the lookup table does not define the input values, the block estimates the output values based on the interpolation between nearby table values [96]. Figure 4.3 illustrates the anatomy of a two-dimensional lookup table. Vectors or breakpoint data sets and an array, referred to as table data, constitute the lookup table. Each breakpoint data set is an index of input values for a particular dimension of the lookup table. The array of table data serves as a sampled representation of a function evaluated at the breakpoint values. Lookup table blocks use breakpoint data sets to relate a table's input values to the output values that it returns.

Since table lookups and simple estimations can be faster than mathematical function evaluations, using lookup table blocks results in speed gains when simulating a model. In the compressor model, it is considered using lookup tables in lieu of mathematical function evaluations, since

a. An analytical compressor expression is expensive to compute

b. No good analytical compressor expression exists, but the relationships have been determined empirically

The isentropic efficiency and pressure ratio across the compressor are derived from the lookup tables, which map the relationships between dimensionless variables:

Map I: Inputs: corrected turbocharger speed & corrected air mass flow rate

Outputs: pressure ratio

Map II: Inputs: corrected turbocharger speed & pressure ratio

Output: isentropic efficiency

The prediction of the compressor performance is dependent on the accuracy of the experimental data in the lookup tables. Consequently, in order to increase the size of the look-up tables, high density of the data points is required to be created based on:

a. Manufacturer's data
b. Experimental data.

From the previous analysis, the turbine and compressor data are limited to a small range, whereas the engine operates in a wider speed and load ranges [64]. Therefore, interpolation and extrapolation based on the test data are essential for covering all the turbocharger running condition.

4.2.2 Numerical methods for increasing the data size

From Figure 4.4, it can be observed that the manufacture's compressor data (blue dots) only contain limited number of operating points (49 points) along steady state speed curves. Red dots in Figure 4.4 are the compressor operating points from the baseline engine steady state tests. This means that although compressor manufacture's data might be more accurate, it cannot represent the whole engine operating conditions, especially when the turbocharger speed is low.

Due to the lack of data from the manufacture and experimental test, it is necessary to apply other methods to increase the density of the compressor data set:

a. Curve fitting method

b. Fully analytical solution

Curve fitting method

Curve fitting is the method of constructing a curve, or mathematical function, which has the best fit to a series of data points. Curve fitting can involve either interpolation, where an exact fit to the data is required, or extrapolation, which refers to the use of a fitted curve beyond the range of the supplied data, and is subject to a greater degree of uncertainty since it may reflect the method used to construct the curve as much as it reflects the observed data. Especially for the extrapolation, the curve fitting methods encounter significant errors due to the lack of data. There are different curve fitting methods, such as spline interpolation, Polynomial Least-Squares Regression, Gauss-Newton Method, etc. The spline interpolation will be discussed in the following section to predict the compressor performance on fixed speed lines.

Analytical model

An analytical compressor treatment refers to the simulation based on calculations of the gas dynamics and fluid mechanics in each part of the compressor. For a one-dimension analytical model, the geometric data of the compressor is essential which are rarely provided by the manufacture. Additionally, for a more accurate expression,

3-dimension model in terms of CFD (Computational Fluid Dynamics) analysis give rise to an accurate treatment, but it is very processor-intensive so that will take extremely long time to calculate the whole compressor operating conditions.

Both the curve fitting method and an analytical model have their shortcomings, since the curve fitting method only constructs curve based on the supplied data set without setting up physical relationships among variables, the extrapolation beyond the region of supplied data may give rise to significant errors. On the other hand, a pure analytical model cannot utilize manufacture turbocharger maps to match the engine performance. Therefore, the combination of a parametric method as well as a curve fitting interpolation could lead to a more accurate solution with the use of manufacture data.

4.2.3 Parametric model

Parametric methods are models to which the model parameters are assigned in order to fit the supplied data. The models are based on equations using theories of physics, gas flow dynamics and fluid mechanics. There are two types of models to map the compressor flow characteristics:

I. Modeling the corrected mass air flow as a function of pressure ratio and corrected speed;

$$\dot{m}_C = f_1(\frac{P_2}{P_1}, N_c) \qquad 4.1$$

II. Modeling pressure ratio as a function of corrected mass air flow and speed.

$$\frac{P_2}{P_1} = f_1(\dot{m}_c, N_c) \qquad 4.2$$

Where $\dot{m}_c = \dfrac{\dot{m}\sqrt{T_1}}{P_1}$

$N_c = \dfrac{N}{\sqrt{T_1}}$

$\dot{m}_c$ is the corrected mass air flow.

N_c is the corrected compressor speed.

Mode II is more straightforward, since the air pressure ratio across the compressor is built up by the air passing through compressor. Morral & Kolmanovsky [17] also suggest that Mode II is superior since it is less sensitive to input errors. Because the gradient of the pressure ratio at low mass flow rate is very small (even zero when it is closed to the surge line), a small variation of pressure ratio could lead to a large change of mass flow.

There are different types of parametric modeling techniques to interpolate and extrapolate the compressor data. However, in-house research [18] shows that the combination of spline functions and the Jesen & Kristensen method provide the best fit for the curve based on the manufacture's data.

Jensen & Kristensen Method

The Jensen & Kristensen (J&K) [19] Method models the characteristics of the compressor using two dimensionless parameters: Ψ and Φ, and the equations are described below:

$$\Psi = \frac{c_p T\left(PR^{\frac{\gamma-1}{\gamma}} - 1\right)}{\frac{1}{2}U_c^{\,2}} \qquad 4.3$$

$$\phi = \frac{\tilde{m}_c}{\frac{\pi}{4}\rho d_c^{\,2} U_c} \qquad 4.4$$

Where

$$\Psi = \frac{k_1 + k_2\phi}{k_3 - \phi}$$

4.5

$$PR = \left(\frac{\frac{1}{2} U_c{}^2 \Psi}{c_p T_a} + 1 \right)^{\frac{\gamma}{\gamma - 1}}$$

4.6

$$U_c = \frac{2\pi}{60} d_c \tilde{N}$$

4.7

$$M = \frac{U_c}{\sqrt{\gamma R T_a}}$$

4.8

$$k_i = k_{i1} + k_{i2} M \quad , \qquad i = 1,2,3$$

4.9

The values of k1, k2 and k3 are found by using a nonlinear regression (known as the Levenberg-Marquardt method). This minimises the error between the values Ψ and Φ calculated from the original data. This yields a function $PR = f(\tilde{m}_c, k_1, k_2, k_3)$ by combining equations (**4.4**), (**4.5**) and (**4.6**), which allows interpolation and extrapolation along speed lines. This can be extended to interpolation and extrapolation between speed lines by finding k_1, k_2 and k_3 for different speeds and applying polynomial regression to equation (**4.9**).

4.2.4 Spline function and compressor data interpolation and extrapolation

In the curve fitting analysis, the spline interpolation is defined as an interpolation method using a special type of piecewise polynomial, which is called spline. Figure 4.5 shows the expression of a cubic spline with four data points which are known as knots (or control points). An equation based on the cubic spline with third order polynomial is expressed as:

$$S_i(x) = a_i x^3 + b_i x^2 + c_i x + d_i$$

In the typical polynomial interpolation, a single cubic (degree 3) polynomial with 4 coefficient can only make a curve with one inflection point. So if a complex curve has more than one deflection points, the order of the polynomial interpolation needs to be higher (e.g. 4th degree polynomial with 5 coefficients has 2 inflection points, 5th polynomial with 6 coefficients has 3 inflection points...). However, curves of polynomial interpolation with higher degree tend to be very sensitive to the knots and do not make smooth shapes Therefore, a piecewise polynomial (spline) has been applied to solve this problem, which each pair of knots represent one segment of the curve and each segment is a cubic polynomial with its own coefficients (Figure 4.5). Since each segment has its own cubic polynomial function and own coefficients, coefficients needs to be calculated based on the data points (knots). For a cubic polynomial with 4 coefficients, four equations are required to be solved. So the example in Figure 4.5 has 4x4=16 coefficients to solve. Hence four conditions are used to calculate these unknown coefficients.

1. Each curve segment needs to pass two control points ($S_i(x_i)$ and $S_i(x_{i+1})$)
2. Curve segments have same slope when they join together ($S'_i(x_{i+1}) = S'_{i+1}(x_{i+1})$)
3. Curve segments have same curvature when they join together

   ($S''_i(x_{i+1}) = S''_{i+1}(x_{i+1})$)

4. Two ends of the whole curve are supplied ($S_0(x_0)$ and $S_n(x_n)$)

Then the coefficients can be solved by the following equation:

$Ma = y$

Where a is the vector of all coefficients, y is the vector of constants, and M is the matrix encoding the above conditions. This calculation is hard to solve by hand but easy to solve in mathematical software (e.g. Matlab) on computer.

This method can be used to provide an interpolation between each point on individual speed line. Since the spline function asks the curve to pass though each data points (knots), extra errors might be generated by the strict curve fitting. So a smoothing spline method, which does not require to pass each points, was applied to solve this problem. However, the extrapolation using spline method shows significant error due to the lack of data points outside the region of data supplied by the manufacture. As suggested by Dowell P., et al [18], a parametric model (J&K) was used to predict the compressor operating data points that the manufacture cannot supply. Figure 4.6 and Figure 4.7 shows that the interpolation/extrapolation based on the spline function and the parametric model provides very good compressor model to cover the whole operating conditions (red: surge region, green: normal region, blue: choke region).

4.3 Turbine model

4.3.1 Turbine maps

Compared with the compressor, the turbine model is more complicated due to the effect of variable geometry nozzle and the pulsating flow from the exhaust side of the engine. The modelling techniques of constructing the pulsating flow simulation will be discussed in the next chapter. However, according to the manufacture's data (Figure 4.8), the turbine map contains even less points than the compressor for each VGT position. It is therefore necessary to increase the density of the data by using

similar approaches as discussed in the previous section. Hence the curve fitting methods and fully analytical simulation to predict the turbine performance will be analysed in this work.

The parametric modelling approach, Jesen & Kristensen method for example, treats the turbine as an adiabatic nozzle to produce the mass flow rate based on the pressure ratio across the nozzle. However, these techniques require a large size of experimental data to fit the curve, especially with an additional variable on the VGT nozzle vane position. Due to the density of data supplied by the manufacture, more experimental data of the turbine are essential to produce a denser turbine map to feed in the lookup tables. Therefore commercial software was applied to interpolate and extrapolate the manufacture's data at each VGT position. Since the Ricardo WAVE is extensively applied in the engine research, and the success has been achieved in the in-house research on modelling turbocharged diesel engine performance [4], Ricardo WAVE is selected as the tool to increase the density of the turbine manufacture's data at each VGT position.

WAVE applies semi-empirical equations to interpolate and extrapolate the data based on the experimental results conducted on a large range of turbines. Firstly, the geometrical shape of the turbine components was adjusted until the specific diameter was matched with the supplied data. Then the points beyond the rage of the supplied data were produced based on the empirical equations. Although the WAVE program predicts the turbine performance very well at the VGT positions provided by the manufacture, the interpolation of the data at other VGT positions where the turbine designer does not supply is only based on linear-interpolation. Hence more sophisticated curve fitting approach was applied to interpolate the data to the unknown VGT positions. Consequently, spline functions were applied to increase the density of the map. Appendix shows the code of the program in Matlab to interpolate and extrapolate the turbine data.

4.3.2 Analytical model

Basics

The turbine analytical model involves modular approaches to predict the turbine performance as a series of discrete components based on the moment of momentum, steady flow energy, mass flow continuity and thermodynamic equations. Although the flow in the turbine is actually three-dimensional, the 3-D solutions, CFD (Computational fluid dynamics) for instance, are very time consuming and processer-intensive. As a result, a simple model with one dimension flow analysis is widely applied in the initial design of turbine components. Hence the one-dimensional analytical turbine model was investigated to predict the turbine performance to increase the size of the data, where the manufacture only provides a few operating points.

Wallace F. J [34, 35] provides an analytical expression for inward radial flow turbines on both the design and off-design conditions, using the one-dimensional gas flow analysis at different stages. The essential feature of the off-design condition in this treatment is the postulate of an irreversible deflection at constant pressure of flow leaving the nozzle to produce a relative velocity vector at entry to the rotor in conformity with the rotor blade angle at entry. Therefore an incidence loss calculation based on the sudden gas flow deflection at the entry of the rotor is introduced in the model. This necessitates the accurate turbine geometry data on both the nozzle positions and rotor shape. Nevertheless, in the absence of the geometry data from the turbine manufacture, controlling parameters were created to vary the modelled turbine geometry for finding the best fit between the modelling results and the manufacture data points.

Although Wallace's treatment was unique at the time of publication in providing a analytical turbine solution for both design and off-design conditions, there are some suggestions that can be made to improve the model prediction for a modern turbocharger with the effect of variable geometry nozzle positions:

a. Adding gas flow analysis in the interspace between the nozzle and the rotor;

b. Replacing the over-all efficiency terms with semi-empirical expressions for the various losses in the system.

c. Adding a gas specific property table for different air-fuel-ratios and temperatures

d. Adding pulsating flow analysis

The latter two suggestions can be achieved as modules in the real-time turbine model, so the gas property table and the pulsating flow analysis will be discussed in chapter 4.4 and 4.5 respectively.

Interspace between the nozzle exit and the rotor tip

In Wallace's turbine model, the gas flow change in the vaneless space between the nozzle and the rotor is not considered, it is therefore necessary to add a calculation of the gas jet velocity and angle at the entry of the rotor. Because the wall friction is ignored, as the vaneless space is very small, the angular momentum is conserved. Consequently, a gas angle turning can be calculated based on the conserved angular momentum and mass flow continuity. Watson & Janota [5] provides an expression of the gas flow angle leaving the interspace (Figure 4.9):

$$\tan\alpha_4 = \frac{r_3 2\pi b_4}{b_2 l_{th2} z_2}\sin\alpha_3 \qquad 4.10$$

Where α is the gas flow angle

b is width of the flow passage;

z_2 is the number of nozzles

l_{th2} is the length of the throat formed by two adjacent nozzle blades

2 denotes nozzle exit throat

4 denotes rotor inlet

Additionally, a pressure gradient is included based on Bernoulli equation for incompressible gas flow. In the vaneless space:

$$\frac{1}{\rho}\frac{dp}{dr} = \frac{C_\theta^2}{r} \qquad 4.11$$

Where p is the pressure

r is the radius

C_θ is the angle of flow against the peripheral vector.

ρ is the density of the flow.

In the following analysis, the suffix:

1 denotes the nozzle exit

2 denotes the rotor inlet

For incompressible flow, the density is constant

$$\rho = \frac{\rho_1 + \rho_2}{2} = const = a$$

Assuming the gas peripheral travelling distance is constant, since the interspace between the nozzle and the rotor is very small.

$$C_\theta r = const'$$

Therefore $C_\theta^2 r^2 = const'^2$

$$\frac{C_\theta^2}{r} = \frac{const'^2}{r^3} = b$$

By integrating the equation **4.11** between stage 1 and stage 2

$$\int_1^2 \frac{1}{a} \cdot dp = \int_1^2 \left(\frac{C_\theta^2}{r} \right) dr = \int_1^2 \frac{b}{r^3} dr$$

Hence the pressure gradient between the nozzle exit and the rotor entry is:

$$[\Delta P] = P_2 - P_1 = -\frac{1}{2} ab \left[\frac{C_{\theta 1}^2 r_1^2}{r^2} \right]_{r_2}^{r_1} = -\frac{1}{2} \left(\frac{\rho_1 + \rho_2}{2} \right) \left[\left(\frac{1}{r_1} \right)^2 - \left(\frac{1}{r_2} \right)^2 \right]$$

4.12

Energy losses model:

In Wallace's turbine analytical model, apart from the incidence loss, no account with regard to various energy losses has been taken in the efficiency calculation. Although, when designing a radial flow turbine, energy losses involved are aimed to be minimised, the actual fluid flow in the radial turbine is extremely complex since it is viscous and highly three-dimensional. Consequently, in the simple one-dimensional analysis, the energy losses calculation in terms of various empirical loss coefficients has been widely applied. Since the coefficients are empirical, they should not be applied to all classes of turbine with any expectation of great accuracy. However the data points from the calculations, especially at off-design conditions, can be useful to increase the data size to fill the lookup tables in the real-time turbine model. The energy losses can be sub-divided into following categories:

g. Nozzle loss

h. Rotor incidence loss

i. Rotor losses in the passage

j. Disc friction loss

k. Clearance loss

l. Bearing loss

The expressions with regard to individual loss calculation will be detailed in the next section.

Turbine analytical model

The aim of this model is to work out the turbine performance at a given operating point, where the turbine VGT position, expansion ratio and speed are specified. An iterative calculation is performed to determine the flow properties and the mass flow rate throughout the stage. The model starts at the inlet of the nozzle, and the flow properties are calculated for each component in turn. The exit conditions from one component become the inlet conditions to the next.

The reliability of the iteration method used to obtain a converged mass flow rate at a given operating point is fundamental to the success of a program of this type. The method to be described is simple, well-tried and ensures a converged solution for all flow conditions. It is based upon an algorithm to determine the interspace pressure between the nozzle and the rotor to reach the mass flow equilibrium. Because the iterative loop of the mass flow calculation at one hypothetic interspace pressure for all the operating points is very time consuming and processor-intensive. The model starts with a simplified assumption of the expansion pressure splitting equally between the nozzle and the rotor (degree of reaction: 0.5), and then the interspace pressure is adjusted to reach the mass flow rate balance.

Since the data supplied by the manufacture is based on the cold flow tests, before starting the modelling, assumptions with regard to the temperature and pressure at stagnation conditions are made the same as the ambient conditions.

$T_{01} = 288K$

$P_{01} = 1bar$

All other measured geometry data are shown in table 4.1 and 4.2

Stage one: Nozzle

With known stagnation temperature (T01=288 K), pressure (P1=1 bar) at the inlet of the nozzle and hypothetical intermediate pressure (P2) at the nozzle outlet, gas velocity exiting the nozzle can be calculated.

$$C_2 = \sqrt{2C_p T_{01}[1-\left(\frac{P_2}{P_{01}}\right)^{\frac{\gamma-1}{\gamma}}]}$$

4.13

The nozzle mass flow rate can be written as:

$$\dot{M}_N = c_2 \sin\alpha_2 \pi d_2 b_2 \rho_{01}\left(\frac{P_2}{P_1}\right)^{\frac{1}{\gamma}}$$

4.14

$$\rho_{01} = \frac{P_{01}}{RT_{01}}$$

Where $c_2 \sin\alpha_2$ is the radial velocity at the rotor entry,

$\pi d_2 b_2$ is the throat area at the rotor entry,

$\rho_{01}\left(\frac{P_2}{P_1}\right)^{\frac{1}{\gamma}}$ is the flow density at the rotor entry.

According to the flow analysis in the interspace between the nozzle and the rotor (equation **4.10**), as well as the energy loss in nozzle, the mass flow rate can be re-written as:

$$\dot{M}_N = \sqrt{2\eta_{nozzle} CpT_{01}\left[1-\left(\frac{P_2}{P_1}\right)^{\frac{\gamma-1}{\gamma}}\right]} \sin\alpha_4 \pi d_2 b_2 \rho_{01}\left(\frac{P_2}{P_1}\right)^{\frac{1}{\gamma}}$$

4.6a

At high pressure ratio, the flow is assumed to be choked at the nozzle throat depending on the operating speed. If the absolute exit velocity is greater than the speed of sound, in other words the Mach number C_2 / a_N is greater than one, the nozzle is under choking condition. Therefore the static nozzle exit pressure is equal to the critical pressure, which is a function of inlet pressure and gas specific heat capacity ratio (eqn 4.15). This is followed by isentropic turning with pressure reduction to interspace pressure P_3 from critical pressure P_N. Therefore the actual pressure in the interspace is smaller than the critical pressure. According to Wallace's analysis (Figure 4.10), the nozzle exit flow velocity changes (eqn 4.17)

$$P_{N2} = P_{01}\left(\frac{2}{\gamma+1}\right)^{\frac{\gamma}{\gamma-1}}$$

4.15

$$C_2 = a_{N2} = \sqrt{\frac{\gamma P_{N2}}{\rho_{N2}}}$$

4.16

$$\frac{\sin^2\alpha_2}{\sin^2\alpha_N} = \left(\frac{\gamma+1}{2}\right)^{\frac{\gamma+1}{2(\gamma-1)}}\left(\frac{2}{\gamma-1}\right)^{1/2}\left(\frac{P_2}{P_{01}}\right)\left[1-\left(\frac{P_2}{P_{01}}\right)^{\frac{\gamma-1}{\gamma}}\right]^{1/2}$$

4.17

Therefore, the nozzle mass flow rate under choking condition is:

$$\dot{M}_N = \dot{M} = a_{N2}\sin\alpha_N \pi d_2 b_2 \rho_{01}\left(\frac{P_2}{P_1}\right)^{\frac{1}{\gamma}}$$

4.6b

Stage two: Interspace between the nozzle and the rotor

An additional flow turning in the vaneless space between the nozzle and the rotor is introduced in the model. Equation **4.10** and **4.12** was applied to calculate the flow angle α_4 and pressure P_4 at the inlet of the rotor.

Stage Three: Rotor Post shock (incidence loss)

Neglecting the temperature change in the interspace, due to the zero work done in the small space, The rotor inlet temperature T_4 is

$$T_4 = T_1\left(\frac{P_4}{P_1}\right)^{\frac{\gamma-1}{\gamma}}$$

4.18

The rotor peripheral velocity is equal to:

$$u_4 = \frac{N\pi d_4}{60}$$

4.19

From the analysis in Wallace's publication [35], the temperature increases after the 'shock' due to the irreversible deflection at constant pressure of flow leaving the nozzle to produce a relative velocity vector at entry to the rotor in conformity with the rotor blade angle at entry. So the temperature after the shock T_4' when flow hit the rotor can be calculated based on the mass flow continuity and energy equation across the 'shock' [35]:

$$(T_4')^2 \frac{c_4^2 \sin^2 \alpha_4^2}{\sin^2 \beta_4 2CpT_4^2} + T_4' - \left[T_4 + \frac{c_4^2 - u_4^2}{2Cp} - \frac{u_4(c_4 \cos\alpha_4 - u_4)}{Cp}\right] = 0$$

4.20

Stage three: Rotor

From the velocity triangle at the rotor exit, the relative rotor exit velocity w_5 can be expressed as:

$$w_5^2 = w_4^{'2} + 2CpT_4^{'}\left[1-\left(\frac{P_5}{P_4}\right)^{\frac{\gamma-1}{\gamma}}\right] + u_5^2 - u_4^2$$

4.21

Where

$$w_4^{'} = c_4 \sin\alpha_4 \frac{T_4^{'}}{T_4} \cos ec\beta_4$$

4.22

The peripheral velocity at the rotor exit is equal to:

$$u_5 = \frac{N\pi d_5}{60}$$

4.23

From velocity triangle, the absolute rotor exit velocity is equal to:

$$c_5^2 = w_5^2 + u_5^2 - 2w_5u_5\cos\beta_5$$

4.24

Where

$$\sin\beta_5 = \frac{j\sin\alpha_4 c_4}{w_5}$$

4.25

$$j = \frac{b_4}{b_5}\left(\frac{d_4}{d_5}\right)\left(\frac{P_4}{P_5}\right)^{\frac{\gamma-1}{\gamma}}$$

4.26

Hence the torque per unit mass, τ , can be deduced as the combination of shock torque τ_s and impeller torque τ_t :

$$\tau = \tau_s + \tau_t = \frac{1}{2}\left(c_2 \sin\alpha_2 - c_2 \sin\alpha_2 \frac{T_2^{'}}{T_2} - u_2 \right) d_2 + \frac{1}{2}\left(c_2^{'} \cos\alpha_2^{'} + \frac{d_3}{d_2} c_3 \cos\alpha_3 \right) d_2$$

4.27

Where $C_2^{'} = u_2 + W_2^{'} \cos\beta_2$

The mass flow rate in the rotor is defined as the flow at the exit of the rotor:

$$\dot{M}_R = \dot{M} = C_5 \sin\alpha_5 \pi d_5 b_5 \rho_4^{'} \left(\frac{P_5}{P_4} \right)^{\frac{1}{\gamma}}$$

4.28

Similar to the analysis in nozzle, if the rotor relative velocity at the exit is greater than the speed of sound, the flow is under choking condition. The physical concept is that the rotor passage dose not permit the establishment of supersonic relative velocities. Consequently, when the mass flow rate rises to reach the limit where the exit relative speed Mach number C_5 / a_{N5} is greater than one, the exit pressure is raised to $P_5^{'}$ to allow the Mach number reduce to unity. This means that there is a pressure discontinuity between the rotor exit and the back pressure ($P_5^{'} \rangle P_5$). Hence, when the choke occurs in the rotor, the governing equations remain identical with the aforementioned equations.

Stage four: efficiency calculation

The turbine isentropic efficiency is defined as the actual work output divided by that work obtained from reversible adiabatic (isentropic / ideal) expansion between the same two pressures. Since there is no use to be made in the kinetic energy leaving a turbine, a more relevant isentropic efficiency could be made based on static exit temperature. So the total to static turbine isentropic efficiency can be expressed as:

$$\eta_{Ts} = \frac{ActualWork}{IdealWork}$$

4.29

If the energy losses are introduced in the efficiency term, the isentropic efficiency is equal to:

$$\eta_{Ts} = 1 - \frac{Losses}{IdealWork}$$

4.30

As discussed in the previous section, the aid of semi-empirical energy loss equations can help the model produce more accurate prediction on the turbine efficiency. The energy losses can be sub-divided into the following categories, and the equations from existing researches are illustrated in equation 4.32, 4.33, 4.34, 4.35, 4.36, 4.37, &4.37.

$$Losses = NozzleLoss + RotorPassageLoss + IncidenceLoss + ClearenceLoss + BearingLoss + ExitLoss$$

4.31

$$NozzleLoss = \frac{1}{2} K_n C_2^{\,2}$$ (NASA Model [97, 98])

4.32

$$RotorPassageLoss = \frac{1}{2} K_p (W_4^{\,2} + W_5^{\,2})$$ (NASA Model [97, 98])

4.33

$$IncidenceLoss = Cp(T_4^{'} - T_4)$$ (Wallace's Model [34 35])

4.34

$$ClearenceLoss = \frac{U_4^{\,5} Z_R}{8\pi}(K_x \varepsilon_x C_x + K_r \varepsilon_r C_r)$$ (Baines' Model [31])

4.35

$$BearingLoss = 0.05\rho(u_4^{\,2}(r_4^2 - r_5^2))$$ (Baines' Model [31])

4.36

$$ExitLoss = \frac{1}{2}C_5{}^2$$

4.37

$$IdealWork = CpT_{01}(1-(\frac{P_5}{P_{01}})^{\frac{\gamma-1}{\gamma}})$$

4.38

Result and analysis

One-dimensional flow analysis across the turbine predicts the turbine performance in a more extended and denser turbine map. Unlike the pure curve fitting (empirical) method, the fully analytical model applies physical equations such as the steady flow energy equation, moment of momentum, continuity equation and thermodynamic equation of state. This allows the turbine map to cover more operating points, especially low speed conditions, without the support of data provided by the manufacture. The above section details a solution based on Wallace's analytical turbine model and semi-empirical energy loss calculations.

Figure 4.11 and Figure 4.12 shows the turbine performance at 100% and 80% nozzle vane openings. The bottom sub-figure demonstrates the relationship between the corrected turbine flow capacity (mass flow rate) and pressure ratio at fixed speed lines. The stars with different colours refer to the manufacture's data at different turbine speed, and the circles represent the turbine model outputs. On the other hand, the top sub-figure illustrates the relationship between the isentropic efficiency and the turbine blade speed ratio (U/C). In the same manner to the mass flow rate figure, the stars represent the manufacture data and the circles are the outputs from the turbine analytical model.

It can be observed in the efficiency map that the peak efficiency appears at low U/C ratio (around 0.5), whereas the efficiency normally peaks at U/C=0.7 in a

conventional turbine. In a conventional turbine wheel, the incidence loss is dominant due to the flow separation at the entry of the rotor. Assuming the ideal flow (design condition/ no incidence loss/ 0.5 degree of reaction) with complete exhaust recovery, the bottom term in the U/C ratio is equal to the isentropic stagnation enthalpy drop. Therefore the optimum efficiency of an ideal radial flow turbine should be at U/C=0.7 (eqn **4.39**)

$$\frac{U_4}{C_s} = \frac{U_4}{\sqrt{2(h_{01} - h_{5ss})}} = \frac{U_4}{\sqrt{2U_4^2}} = \sqrt{\frac{1}{2}} = 0.707$$

4.39

Some research [31, 105, and 106] on mix-flow turbines suggest that the peak efficiency at low U/C ratio will provide better engine transient performance, since the engine acceleration tends to happen at low turbocharger speed. So this phenomenon can be explained by the geometry of the turbine rotor (Figure 4.13). Although it can be observed that the turbine rotor inlet is radial, the rotor channel has a 'bucket' shape. This indicates that the turbine wheel is more like an axial wheel, where the efficiency of the low reaction turbine peaks at low U/C ratio. Figure 4.11 and Figure 4.12 show that the analytical turbine model succeeds to predict this energy flow phenomenon.

In the mass flow analysis (top sub-figure), the one-dimensional model manages to produce the flow relationship against expansion pressure ratio. The choking condition is clear in the curves where at high pressures the corrected mass flow lines becomes asymptotical to the horizontal axis where the supersonic flow speed cannot be established. Moreover the speed difference is shown clearly in the graph, since the choking condition is also dependent upon the turbocharger speed.

Although the one-dimensional analytical turbine model produces good prediction at 100% and 80% nozzle vane openings, there are still some errors at other VGT positions. This can be due to the following factors.

a. Lack of turbine geometry data from the manufacture

b. Need of 3-D analysis in the rotor channel (bucket shape)

c. Lack of nozzle vane position specification

Due to the lack of accurate nozzle vane position specification, it must be emphasized that at tight nozzle positions, the flow exiting the nozzle is no longer directed towards the rotor (Figure 4.14, Figure 4.15 and Figure 4.16), but to the intermediate volume between the stator and the rotor. Thus, the direction of the rotor inlet velocity is not dependent upon the angle of the nozzle blades, but upon the angle of the rotor blades. Therefore the turbine may run under the design condition without an incidence loss (shock loss). Assuming zero swirls at the rotor exit and constant gas flow velocity in the rotor passage, the degree of reaction (D.R) can be assumed to be 0.5. Hence, by knowing the intermediate pressure from D.R, the nozzle mass flow can be calculated. The rotor inlet gas condition changes due to the energy loss in the inter space when the nozzle exit gas hits other nozzle blades. However, this solution requires accurate nozzle position data from the turbine designer.

The analytical turbine treatment in this work demonstrates good predictions at different flow conditions. However, considering the application in the real-time turbine model, further work involving detailed turbine geometry data from the manufacture is essential. Hence, the experimental work using the real-time model to emulate the turbocharger and control the CAHU to test the engine at different operating points will apply the turbine map presented by the commercial software (Ricardo WAVE).

4.4 Turbocharger shaft model

The turbocharger shaft is designed to be mounted to both the turbine wheel and the compressor impeller. Due to requirement of low frictional losses and no serious problem arising at critical speed, the bearing is required to be small, allowing for good

access to the turbine wheel and compressor impeller. In the real-time turbocharger model, the shaft model provides the turbocharger speed based on the power inputs from both the turbine and the compressor models.

The compressor torque and the turbine power are calculated by using the mass flow rates, pressure ratios and isentropic efficiencies from the turbine and compressor maps (eqn **4.40** and **4.41**). Consequently, the turbine and compressor torque can be calculate as the power divided by the shaft rotational speed.

$$\omega_t = \dot{m}_{exh} C_p T_{in} \left[1 - \left(\frac{P_{in}}{P_{out}} \right)^{\frac{\gamma-1}{\gamma}} \right] \eta_t$$

4.40

$$\omega_c = \dot{m}_{air} C_p T_{in} \left[\left(\frac{P_{out}}{P_{in}} \right)^{\frac{\gamma-1}{\gamma}} - 1 \right] / \eta_c$$

4.41

By integrating the sum of the turbine torque (positive), compressor torque (negative), and the drag force due to the frictional loss, the overall instantaneous torque on the shaft can be calculated. According to the Newton's second law, the rotational motion can be described as the overall torque exerted on the body is equal to the mass moment of inertia multiplied by the angular acceleration.

$$\tau = I \dot{\omega}$$

4.42

Where τ is the overall torque on the shaft

I is the inertia of the turbocharger

$\dot{\omega}$ is the angular acceleration

The inertia of the turbocharger is equal to the combination of compressor inertia, turbine inertia and the shaft inertia

$$I = I_{comp} + I_{turb} + I_{shaft}$$

With known inertia of the shaft from the manufacture's data, the shaft acceleration can be calculated. Therefore the turbocharger speed is expressed as output of a feedback loop with a supplied initial speed (Figure 4.17). Hence the speed of the turbocharger is equal to:

$$\omega_{turbo} = \int \dot{\omega} dt$$

4.43

4.5 Gas property model

The specific heat capacity at constant pressure (C_p) and ratio of specific heat (γ) have been widely used on the energy equation, and flow thermodynamic equation in the turbocharger real-time model. The instantaneous expression of C_p and γ are essential to increase the accuracy of the calculation, due to the huge variation of gas property and temperature under different engine operation conditions. The pulsating flow in the exhaust because of the valve opening and closing also requires the accurate calculation of C_p and γ values.

Hence a gas property model (Figure 4.18) is created in the real-time model to derive the instantaneous C_p and γ values based on the gas property (air-fuel ratio) and temperature. In the gas property model, the C_p and γ lookup tables for a given air-fuel ratio and gas temperature are derived from the gas property curve (Figure 4.19).

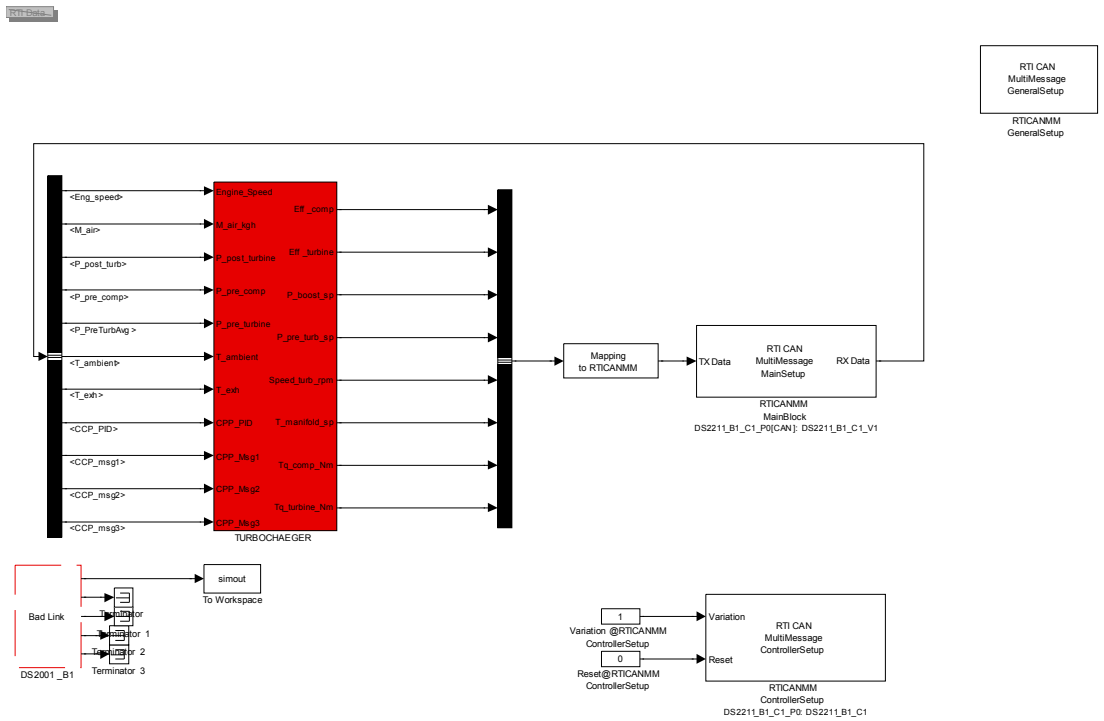

Figure 4.1 Structure of the real-time turbocharger model in Matlab/Simulink

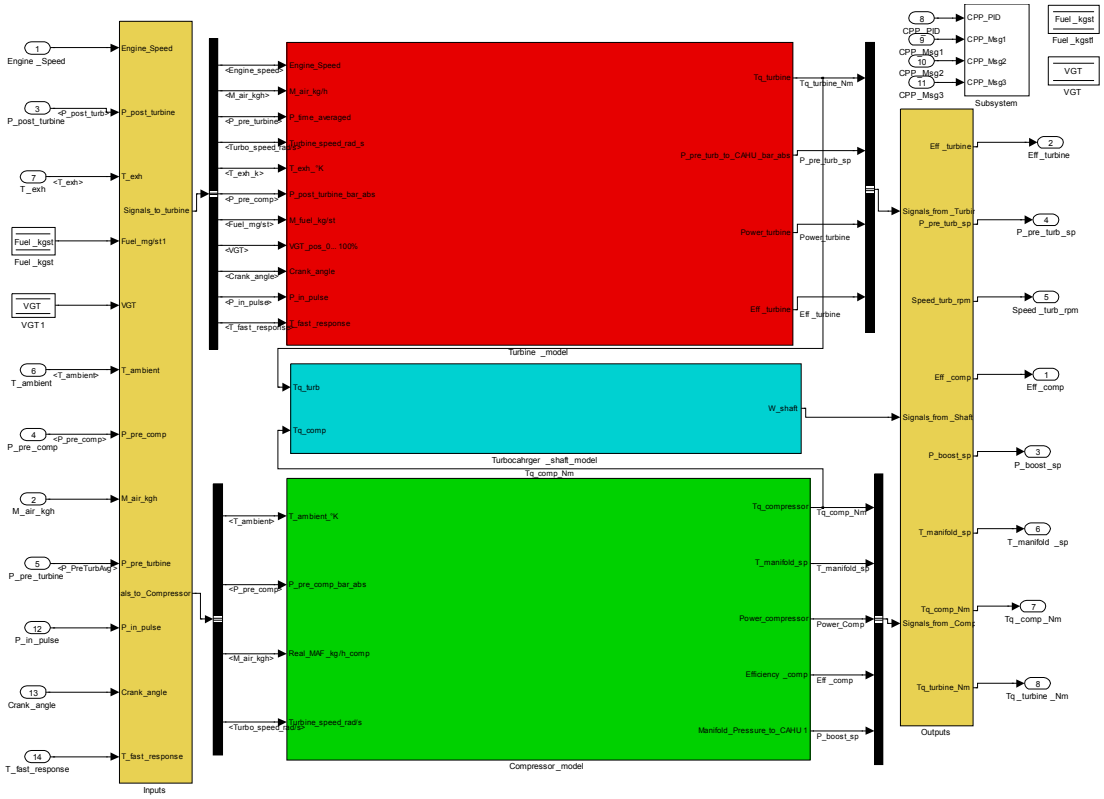

Figure 4.2 The turbocharger real-time model in Simulink

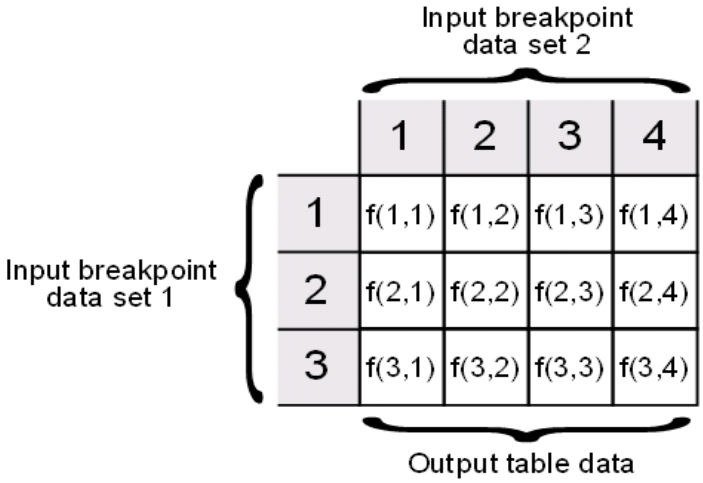

Figure 4.3 Data in a lookup table [96]

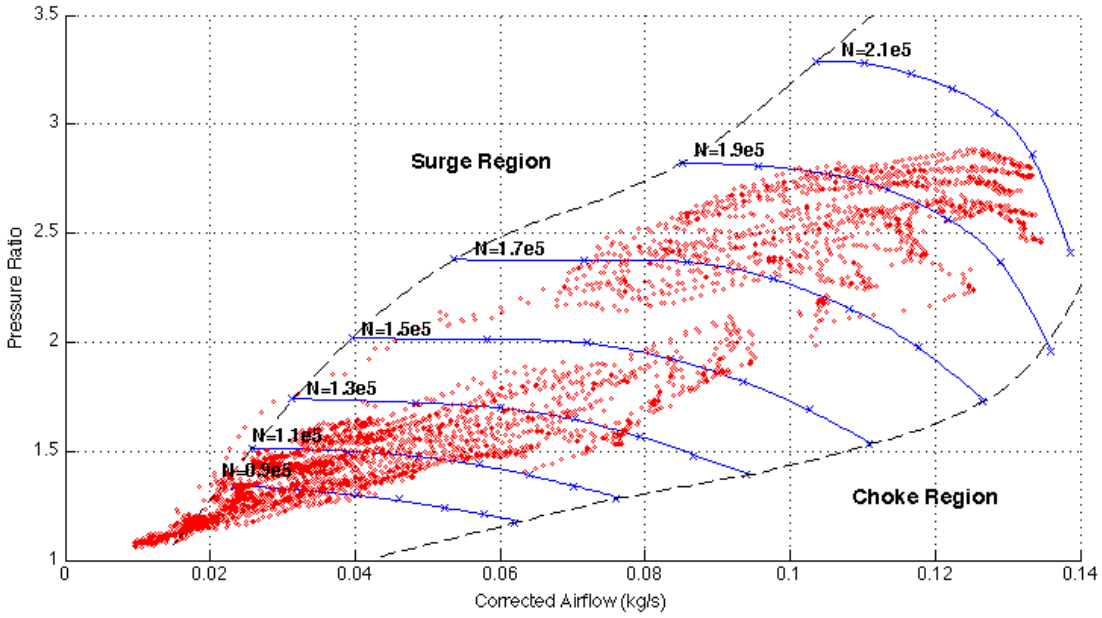

Figure 4.4 Typical Compressor Map With Superimposed Engine Data

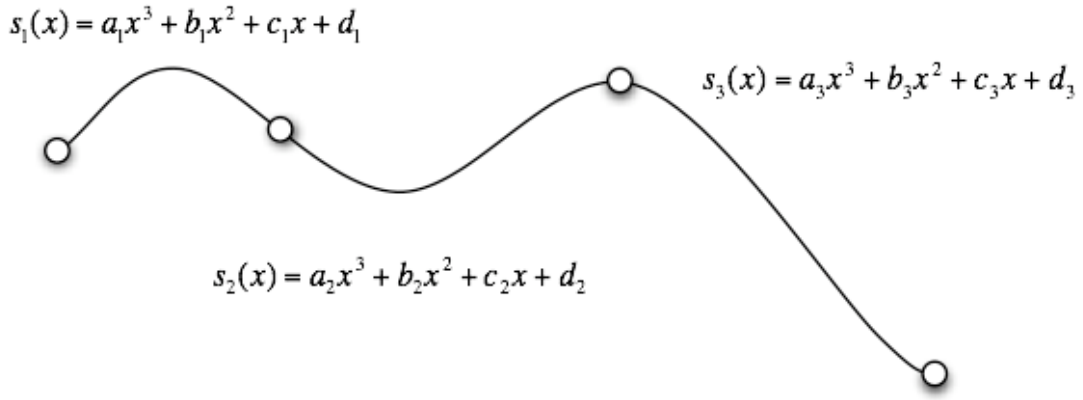

Figure 4.5 Cubic Spline curve with a third order polynomial equation

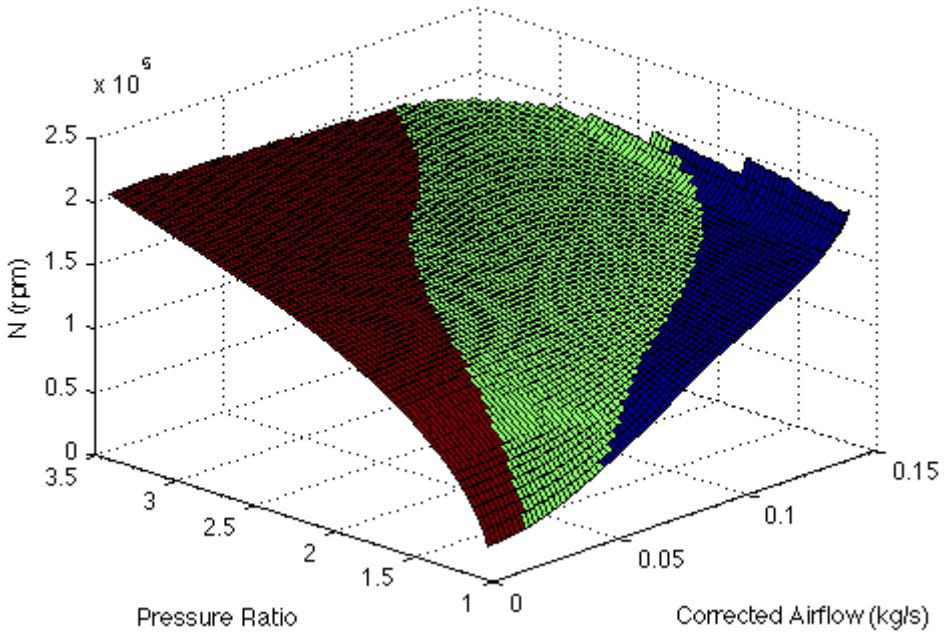

Figure 4.6 Interpolation and extrapolation of compressor data (speed surface)

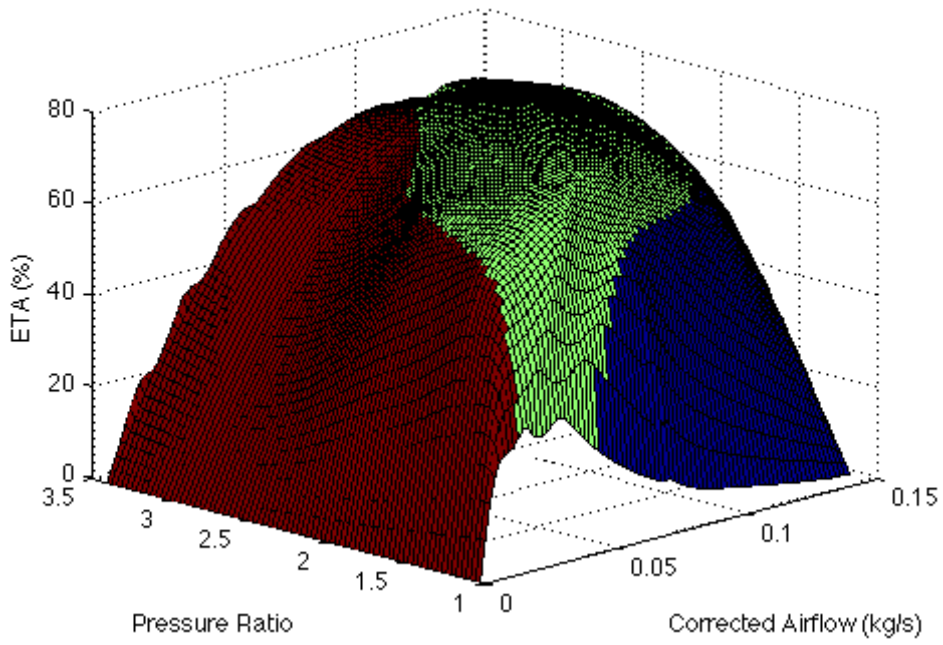

Figure 4.7 Interpolation and extrapolation of compressor data (efficiency surface)

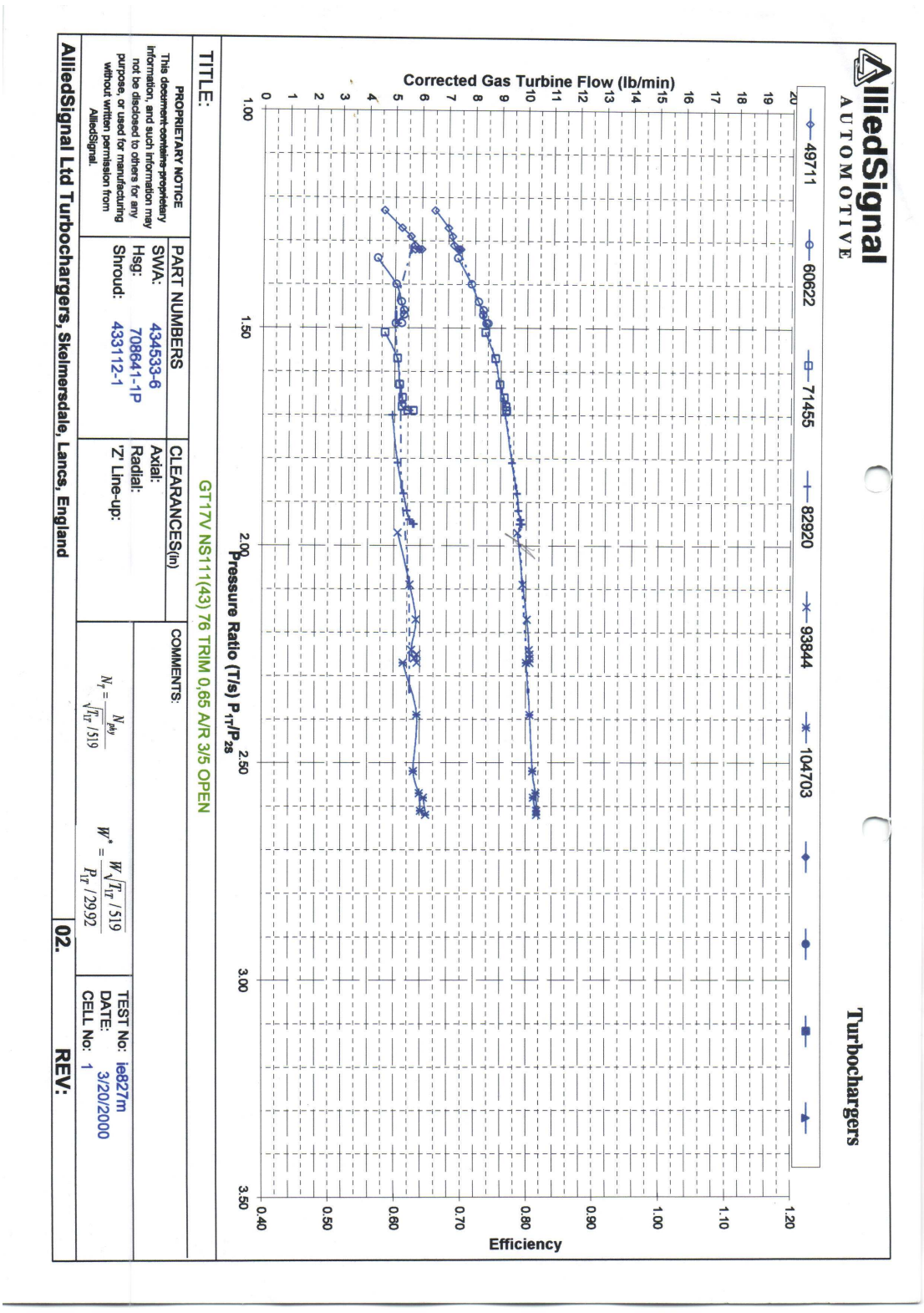

Figure 4.8 Turbine map (60% Opening) supplied by the manufacture

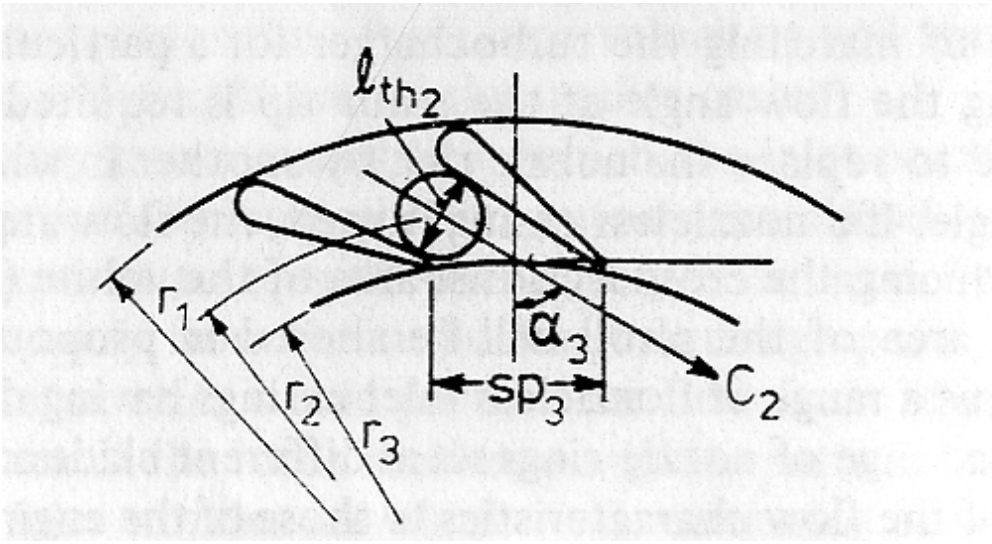

Figure 4.9 Flow velocity at the outlet of nozzle **[5]**

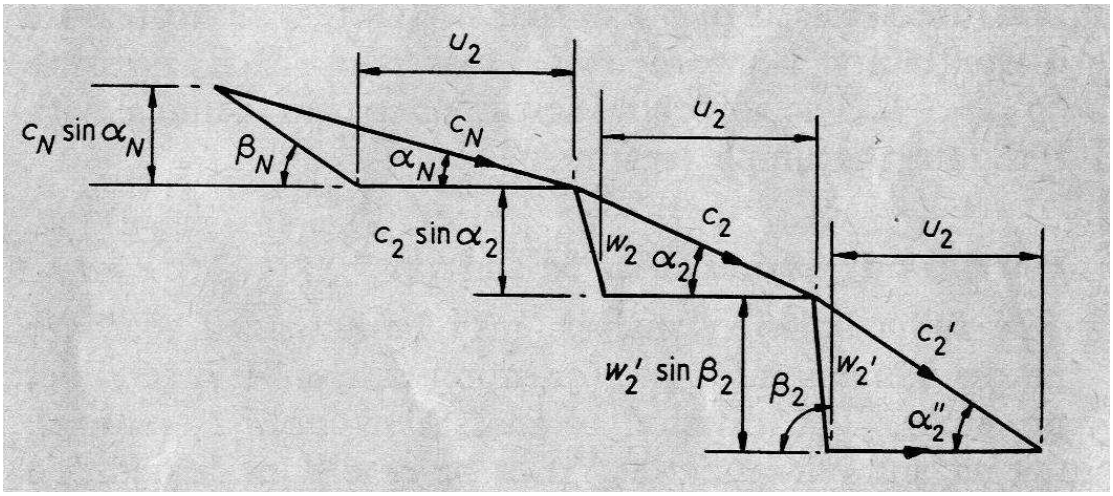

Figure 4.10 Velocity diagram for choked nozzle [35]

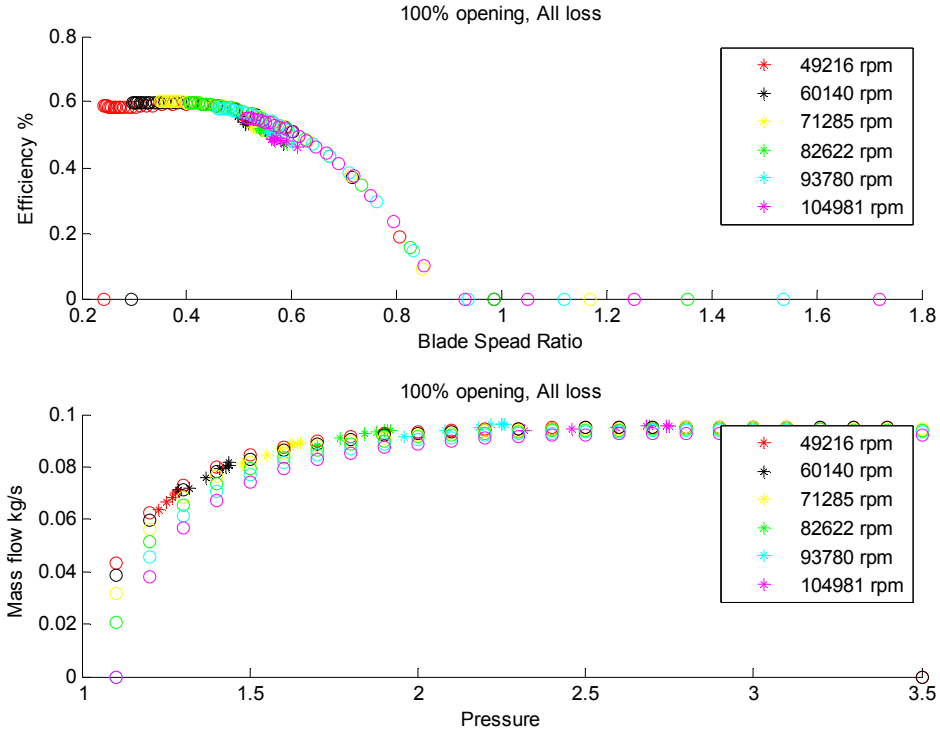

Figure 4.11 Manufacture's data (stars) V.S analytical model (dots) at 100% VGT opening

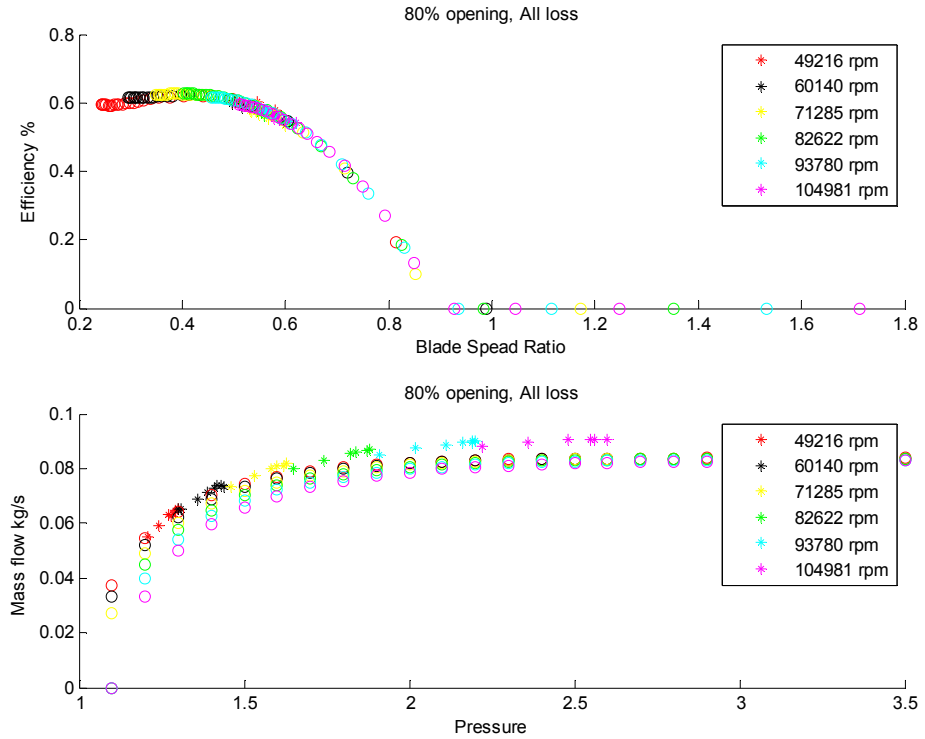

Figure 4.12 Manufacture's data (stars) V.S analytical model (dots) at 80% VGT opening

Figure 4.13 Rotor of the turbine

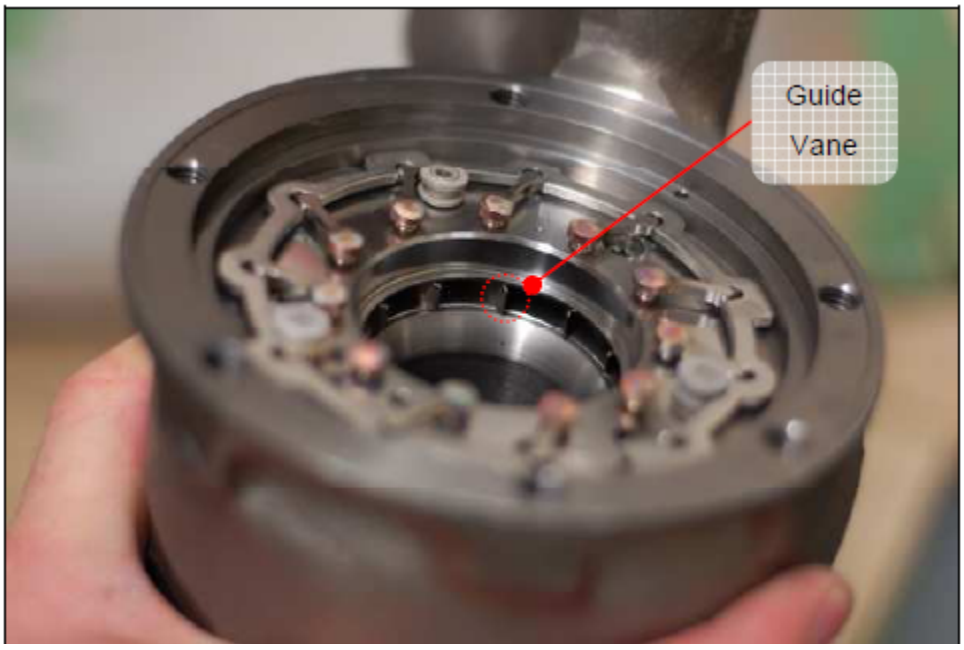

Figure 4.14 Nozzle vanes in the turbine

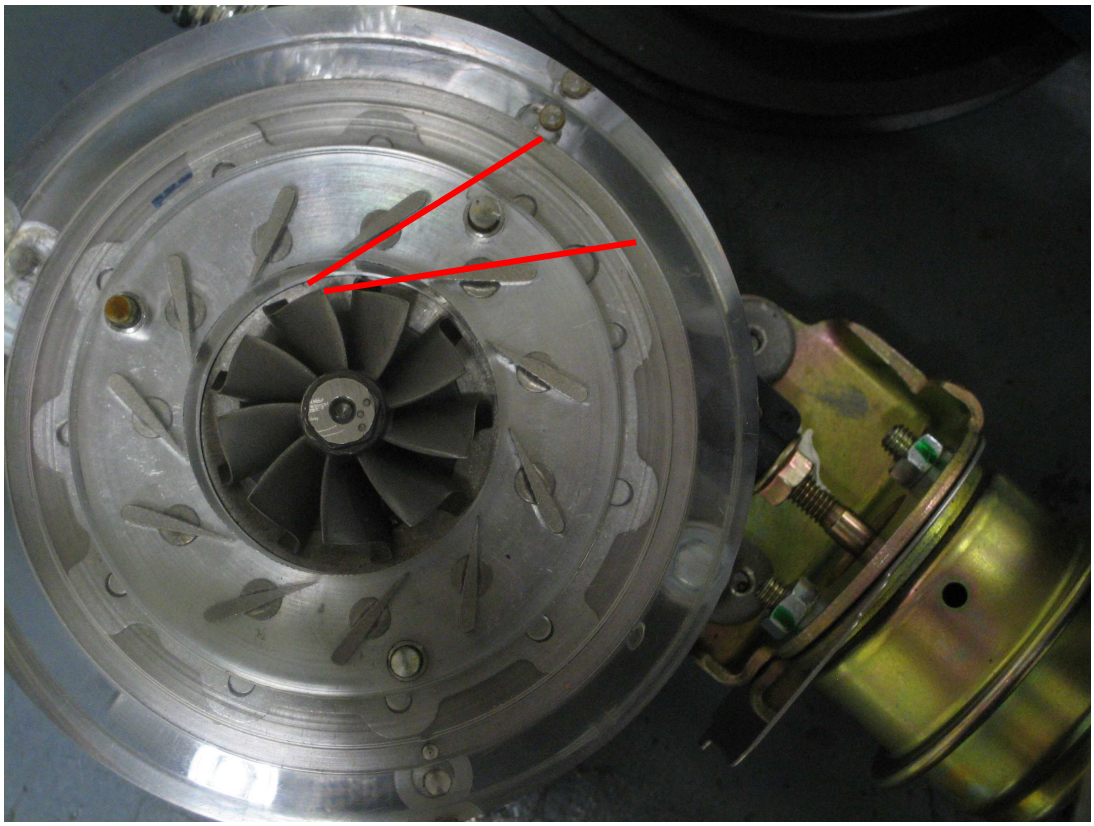

Figure 4.15 Gas flow in turbine at VGT 100 opening

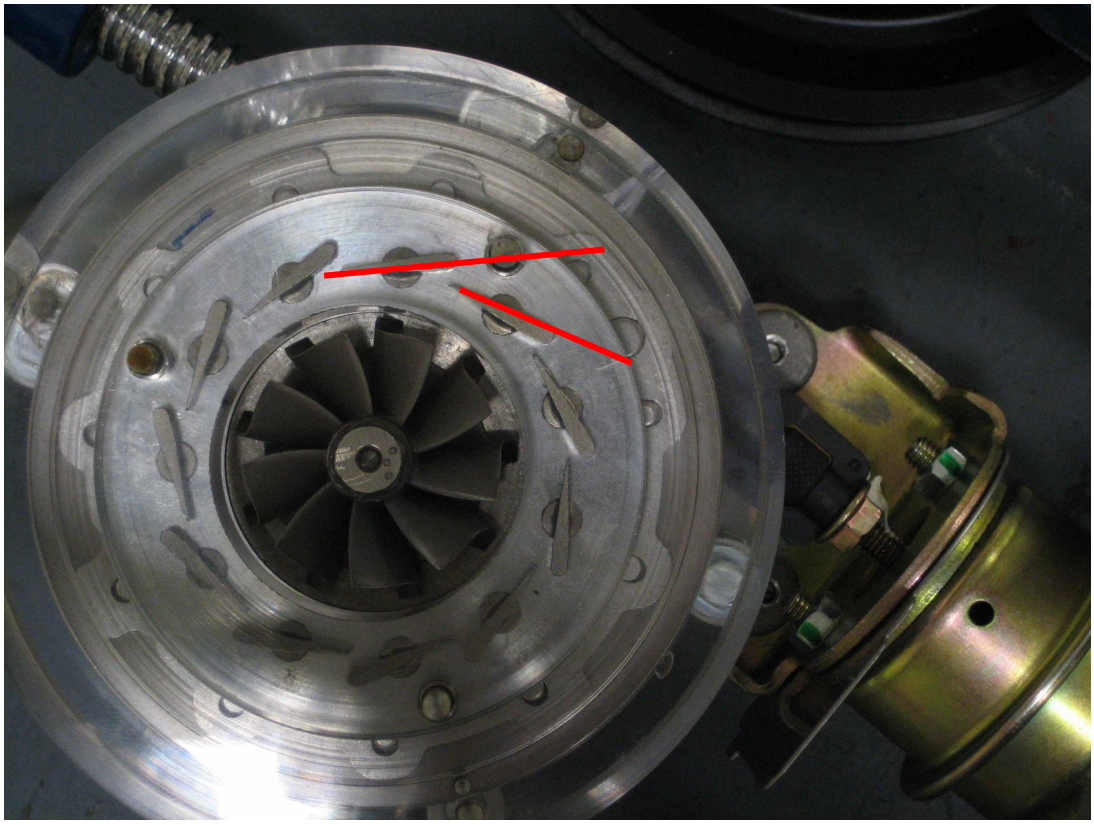

Figure 4.16 Gas flow in turbine at VGT 40 Opening

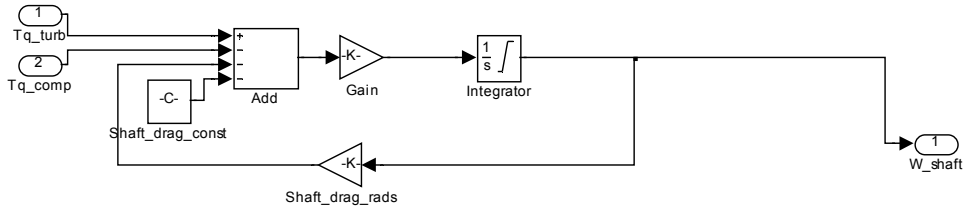

Figure 4.17 Turbocharger shaft model in Simulink

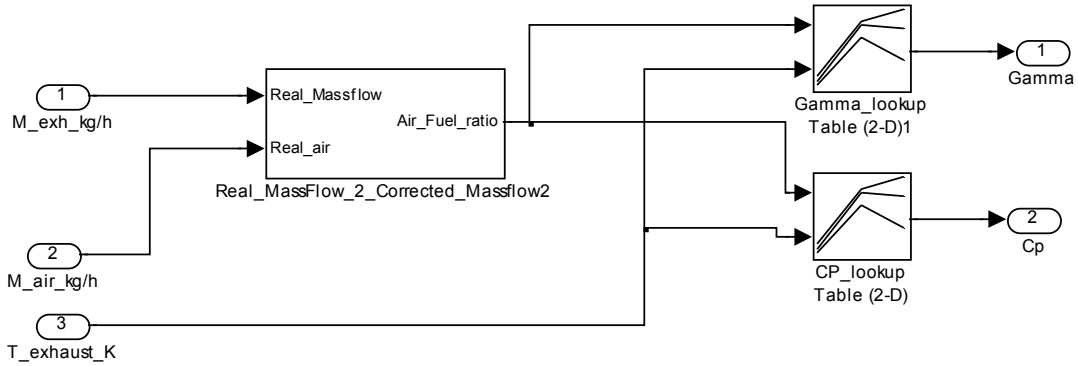

Figure 4.18 Gas property model in Simulink

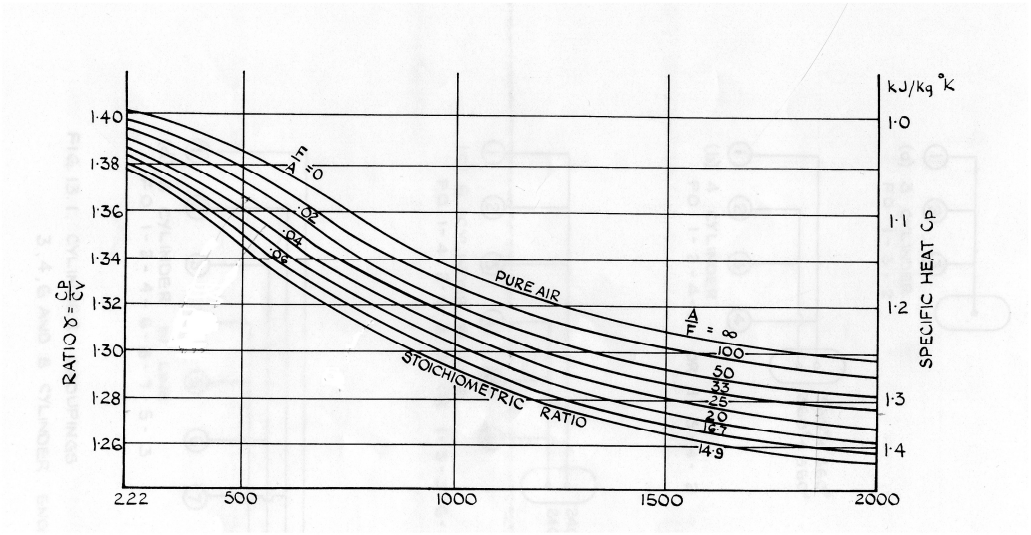

Figure 4.19: Ratio of specific heat $\gamma=C_p/C_v$ and specific heat C_p as a function of temperature and air fuel ratio [115]

Table 4.1Turbine specification

Specification	**Data**	**Specification**	**Data**
Number of nozzle Vane	12	U/C @ peak efficiency	0.55-0.6
Rotor hub diameter d_{5h}	12mm	Nozzle exit depth	5.5mm
Rotor tip diameter d_{5t}	35mm	Rotor inlet depth b_4	5.5mm
Rotor exit depth b_5	14mm	Rotor exit blade angle	24degreeC
Rotor outlet diameter d_5	26mm *	Rotor inlet diameter	41mm

*Rotor inside diameter: $$d_5 = \sqrt{\frac{{d_{5h}}^2 + {d_{5t}}^2}{2}} = \sqrt{\frac{0.012^2 + 0.035^2}{2}} = 0.026m$$

Table 4.2 Throat area at different turbine nozzle vane positions

	100%	**80%**	**60%**	**40%**	**20%**	**10%**
Nozzle Throttle Area (cm2)	4.90	4.30	3.39	2.82	2.00	1.54

Chapter 5 SIMULATING TURBINE CHARACTERISTICS UNDER PULSE CONDITIONS

5.1 Introduction

In chapter 4, the turbocharger real-time model has been discussed based on the constant pressure flow on both the compressor and turbine. However the unsteady flow phenomenon cannot be avoided on the turbine when the turbocharger is located in the exhaust flow of a four-stoke diesel engine. This pulsating flow condition is due to the exhaust pulsations created by the exhaust valve/port opening, and propagation through the manifold.

During the exhaust blow-down period, at the moment the exhaust valve opens, a high pressure is built up due to the high in-cylinder pressure from the combustion and the small volume of the exhaust manifold. If the pressure ratio across the turbine is higher than the critical pressure, the flow in the turbine can be choked. A short period after the exhaust valve/port opening, the pressure drops due to the further expansion of the gas into the exhaust manifold and then to the turbine. At the exhaust valve/port closure, the pressure in the exhaust manifold approaches the atmospheric value. This high pressure pulsating flow caused by the exhaust valve opening potentially provides more energy to the turbine and improves the scavenging and reduces pumping work in a four-stoke engine. However, the flow fluctuation becomes even more complicated in a multi-cylinder engine, which is very common in the automotive applications. Additionally the turbine map from the manufacture is based on the experimental result generally derived from a constant (cold) flow stand. Therefore the model output from the turbine map may not be able to match the result in the real

engine test. Consequently, a new modelling method of constructing the pulsating flow was deemed necessary for improving the accuracy of the turbocharger model, as the model will operate in conjunction with a real engine.

Energy in the pulsating gas flow

It is proposed that the pulsating flow contains more isentropic specific work than a steady flow one with the same cycle averaged pressure ratio. Because the isentropic work can be expressed as the enthalpy difference between the turbine outlet and the inlet, and the enthalpy is equal to:

$$\Delta h = \dot{m} C_p \Delta T$$

A simple energy calculation based on the integration of the product of two sine waves, which represent the pulsating mass flow and pulsating temperature, is shown below:

Assuming two identical sine waves a and b:

$$a = b = A\sin t + \varphi$$

The cycle averaged sine wave over 2π is :

$$\bar{a} = \bar{b} = \frac{\int_0^{2\pi} (A\sin t + \varphi)dt}{2\pi} = \frac{\int_0^{2\pi} (A\sin t)dt}{2\pi} + \frac{\int_0^{2\pi} (\varphi)dt}{2\pi}$$

$$= \frac{-A\cos t\,|_0^{2\pi}}{2\pi} + \frac{\varphi t\,|_0^{2\pi}}{2\pi}$$

$$= 0 + \varphi$$

$$= \varphi$$

So the square of the averaged sine waves is

$$\bar{a} \cdot \bar{b} = \varphi^2 \qquad \text{(a)}$$

On the other hand, the cycle averaged term of the square of two sine waves:

$$\overline{a \cdot b} = \frac{\int_0^{2\pi} (A\sin t + \varphi)^2 \, dt}{2\pi} = \frac{\int_0^{2\pi} (A\sin t)^2 \, dt}{2\pi} + \frac{\int_0^{2\pi} (A\sin t \bullet \varphi) dt}{2\pi} + \frac{\int_0^{2\pi} (\varphi)^2 \, dt}{2\pi}$$

$$= \frac{A^2 \left[\frac{1}{2}(t - t\sin t\cos t) \right]_0^{2\pi} + 2A\varphi[-\cos t]_0^{2\pi} + \varphi^2 t \,|_0^{2\pi}}{2\pi}$$

$$= \frac{A^2 \pi + \varphi^2 \cdot 2\pi}{2\pi}$$

$$= \frac{1}{2}A^2 + \varphi^2$$

(b)

Comparing equation (a) and (b), is it observed that the cycle averaged value of two pulsating terms is greater than the product of two mean values. This shows the pulsating flow tends to contains higher energy than the steady flow. Chen et al. [31] also proves this theory by integrating the stage terminal pressure ratio $\left(\frac{P_{in}}{P_{out}}\right)^{\frac{\gamma-1}{\gamma}}$ over 2π to show that the pulse pressure wave contains more isentropic specific work than a steady flow with the same cycle mean pressure ratio.

The above analysis suggests that the turbine performance under pulsation condition needs to be taken into account in the real-time turbocharger model. It is therefore necessary to construct the mass flow and temperature based on measured pressure pulsation profile from the fast response pressure transducer at the entry of the turbine.

5.2 Calculation of turbine performance under pulse conditions

The pulsation in the turbine is expressible as the pulsating mass flow rate, pressure and temperature:

$\dot{m}_{in} = f_1(\theta)$ ------derived

5.1

$P_{in} = f_2(\theta)$ ------measured

5.2

$T_{in} = f_3(\theta)$ ------derived

5.3

It is proposed that the pulse shape function 5.2 $P_{in} = f_2(\theta)$ should be obtained via high response pressure transducer placed in the compact exhaust manifold and as close as possible to the turbine entry. Function **5.1** $\dot{m}_{in} = f_1(\theta)$ would then be derived by a simple calculation based on a convergent nozzle of throat area A_t (initially assumed) with P_{in} as the measured input, and T_{in} derived from the measured (constant)

Mean temperature $\left(\overline{T}_{in}\right)_{act}$ assumed to occur at the derived time mean pressure $\left(\overline{P}_{in}\right)_{act}$ based on:

$$\left(\overline{P}_{in}\right)_{act} = \frac{\int_0^{4\pi} P_{in} d\theta}{4\pi} = \frac{\int_0^{4\pi} f_2(\theta) d\theta}{4\pi}$$

5.4

The temperature pulse profile can be expressed as:

$$f_3(\theta) = T_{in} = \left(\frac{P_{in}}{\overline{P}_{in}}\right)^{\frac{n-1}{n}} \left(\overline{T}_{in}\right)_{act} = \left[\frac{f_2(\theta)}{\left(\overline{P}_{in}\right)_{act}}\right]^{\frac{n-1}{n}} \left(\overline{T}_{in}\right)_{act}$$

5.5

When n is the assumed polytropic index.

$f_3(\theta)$ is then the required pulse shape for temperature. With P_{in} from eqn (5.2) and T_{in} from eqn (5.5), the mass flow pulse ($f_1(\theta)$) can now be evaluated from the assumed convergent nozzle, replacing the actual turbine, with an initially assumed throat area A_t. The mass flow function can be expressed as:

$$f_1(\theta) = \dot{m}_{in} = \left\{2C_p T_{in}\left[1 - \left(\frac{\overline{P}_{out}}{P_{in}}\right)^{\frac{\gamma-1}{\gamma}}\right]\right\}^{\frac{1}{2}} \left(\frac{\overline{P}_{out}}{P_{in}}\right)^{\frac{1}{\gamma}} \overline{\rho}_{in}(A_t)$$

5.6

Where $\overline{P}_{out}$ and $\overline{\rho}_{in}$ are the turbine outlet pressure and inlet density (assumed constant). The latter term is derived from measurements such as:

$$\overline{\rho}_{in} = \frac{\overline{P}_{in}}{RT_{in}}$$

5.6A

In equation **5.6**, P_{in} and T_{in} correspond to the functions $f_2(\theta)$ and $f_3(\theta)$, respectively. Equation **5.6** is then able to evaluate the time averaged mass flow rate:

$$\left(\overline{\dot{m}}_{in}\right)_{act} = \frac{\int_0^{4\pi} \dot{m}_{in}\, d\theta}{4\pi} = \frac{\int_0^{4\pi} f_1(\theta) d\theta}{4\pi}$$

5.7

In order to make $\left(\overline{\dot{m}}_{in}\right)_{act}$ against the measured turbine mass flow:

$$\left(\overline{\dot{m}_{in}}\right)_{eng} = \left(\overline{\dot{m}_{in}}\right)_{air} + \left(\overline{\dot{m}_{in}}\right)_{fuelt}$$

5.8

Hence the hypothetical throttle area A_t can be iteratively adjusted until equation 5.7 and 5.8 balance.

The turbine work under pulsation conditions can also be evaluated from energy input and output. With $f_1(\theta) = \dot{m}_{in}$ (eqn 5.6) and $f_3(\theta) = T_{in}$ (eqn 5.5), the turbine input energy can be calculated:

$$\dot{E}_{in} = C_p \dot{m}_{in} T_{in} = C_p f_1(\theta) f_3(\theta)$$

5.9

The time averaged value is:

$$\overline{\dot{E}}_{in} = \frac{C_p \int_0^{4\pi} f_1(\theta) f_3(\theta)}{4\pi} = \overline{\dot{m}}_{in} C_p (\overline{T}_{in})_{eff}$$

5.9A

The mass averaged $(\overline{T}_{in})_{eff}$ in eqn 5.9A may be compared with $(\overline{T}_{in})_{act}$, which should be in reasonable agreement with the measured mean inlet temperature. The time averaged turbine work $\left(\overline{\dot{W}}\right)_{turb}$ output is then given by:

$$\left(\overline{\dot{W}}\right)_{turb} = \left[\overline{\dot{m}}_{in} C_p (\overline{T}_{in})_{eff} - \overline{\dot{m}}_{out} C_p \overline{T}_{out}\right] \overline{\eta}_{turb}$$

5.10

where $\overline{\dot{m}}_{out}$ and $\overline{T}_{out}$ are respectively given by $\overline{\dot{m}}_{out} = \overline{\dot{m}}_{in}$ (eqn **5.7**) and by measurement. The assumed turbine mean efficiency $\overline{\eta}_{turb}$ is adjusted so that

$\left(\dot{W}\right)_{turb}$ from eqn **5.10** matches the sum of known compressor work $\left(\dot{W}\right)_{comp}$ and friction work $\dot{W}_f$, i.e.

$$\left(\dot{W}\right)_{turb} = \left(\dot{W}\right)_{comp} + \dot{W}_f \qquad 5.11$$

Where $\left(\dot{W}\right)_{comp} = \dfrac{\dot{m}_{air}\, C_p T_{air\_in}\left[\left(\dfrac{P_{out}}{P_{in}}\right)_{comp}^{\frac{\gamma-1}{\gamma}} - 1\right]}{\eta_{comp}}$ 5.11A

in which $\dot{m}_{air}$, T_{air_in}, $\left(\dfrac{P_{out}}{P_{in}}\right)_{comp}$ are directly measured, and η_{comp} is obtained from the relevant compressor map.

Due to the difficulty from the measurement of the friction work in the bearing and the effect of heat transfer from the turbine side to the compressor side, the turbine work from the calculation needs the calibration based on more detailed turbocharger data. However, the construction of pulsating turbine mass flow and temperature in equation **5.6** and **5.5** respectively gives rise to the turbine performance calculation under pulse conditions in the real-time program. (Figure 5.2)

5.3 Time averaged mass flow

The difficulty in the real-time simulation with regard to the above calculations is the mass flow balance between the time averaged mass flow and the measured mass flow rate (mass air flow + fuel mass flow). The mass air flow and fuel mass flow can be acquired from the measurement and the signal from the engine ECU. However, the calculation of the time averaged value at the crank angle cycle from 0 to 4π is not easy to be set up in real time environment. Because the simulation requires all the calculation based on the real-time inputs, cycle based modules in Simulink cannot be applied, such as the buffer module, memory module, and weighted moving average module.

Furthermore, the actual time span of the crank angle between 0 to 4π varies with different engine speeds. Therefore a crank angle position triggered model to calculate the mean mass flow for variable engine speed conditions is essential. Figure 5.3 shows a new method built up to solve the problem using the calculation of time averaged mass flow rate based on the pulsating mass flow calculation (eqn 5.6) and the crank angle position. The crank angle position is measured from the crank shaft encoder, which shows a square wave representing the crank shaft position.

In this model, the pulsating mass flow rate is integrated by using the crank angle position to trigger the model to recognise the time span of two revolutions. The total mass flow rate is divided by the time to calculate the time averaged mass flow rate. Therefore the throttle area can be derived by using the balance between the calculated time averaged mass flow rate and the actual mass flow rate measured by the mass flow meter.

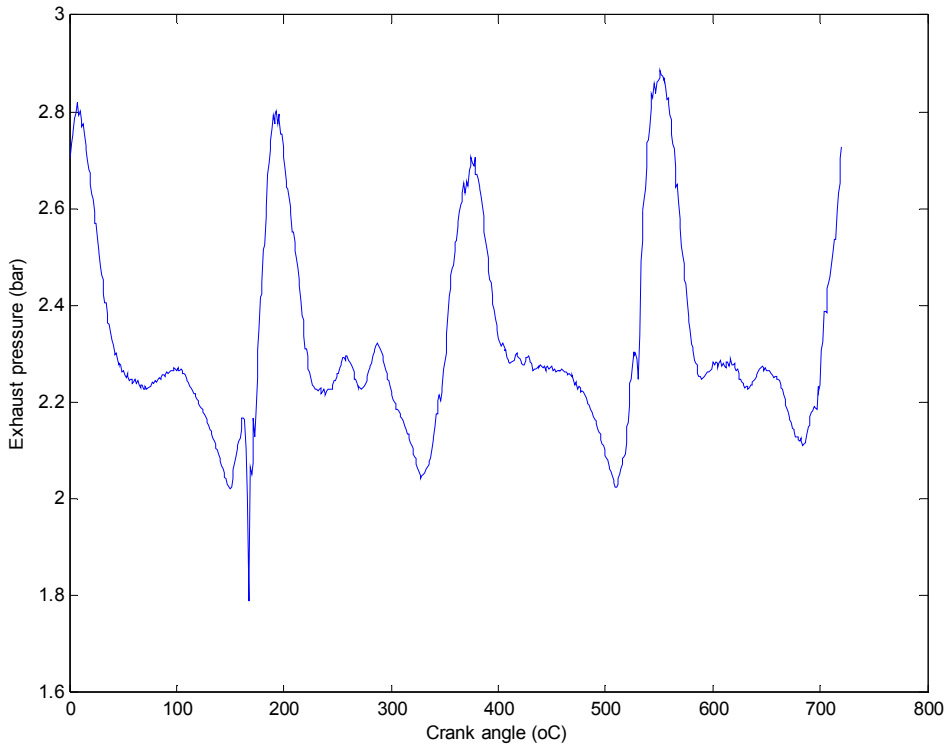

Figure 5.1 Pressure pulsation profile at engine speed 2000rpm

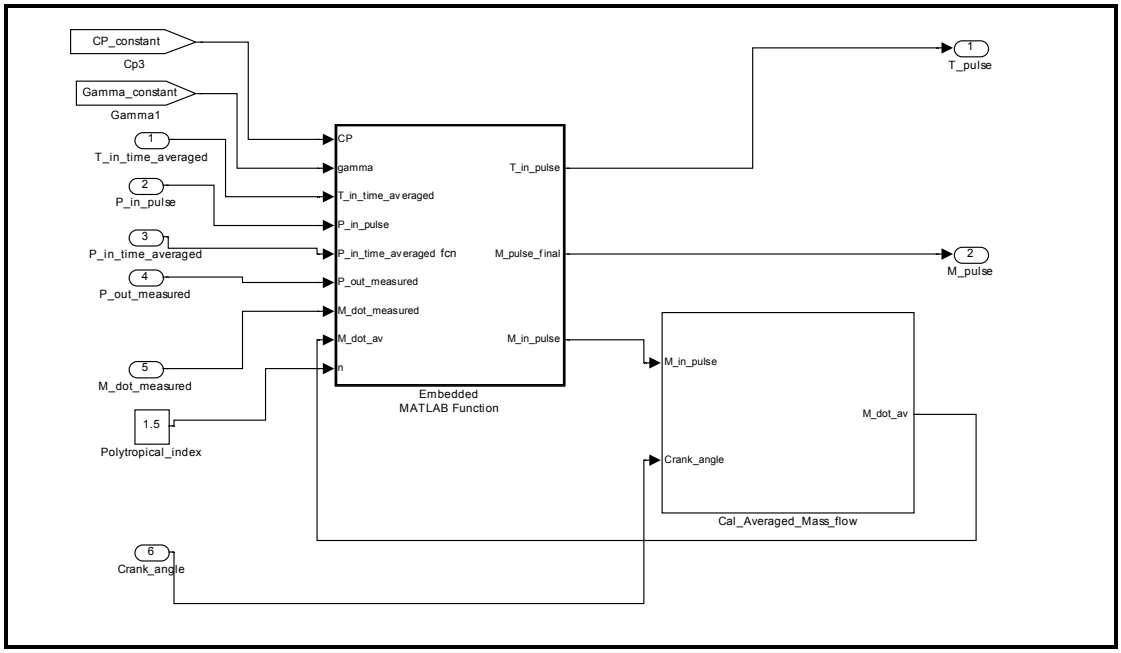

Figure 5.2 Pulsating temperature and mass flow calculation in real-time model

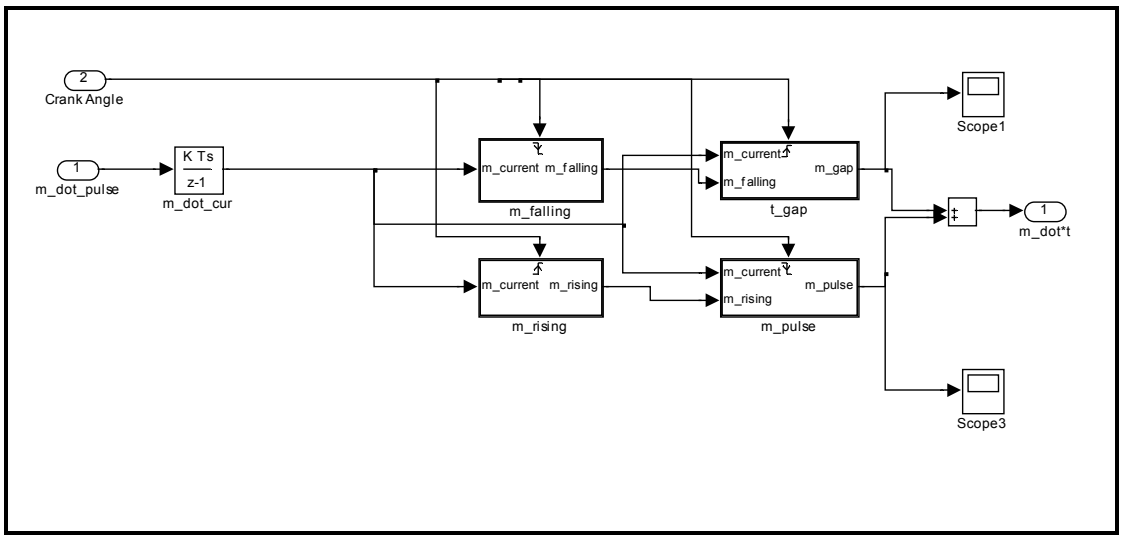

Figure 5.3 Calculation of time averaged mass flow rate

Chapter 6 HARDWARE

Overview

This chapter documents the hardware part of the system including the Charging Air Handling Unit (CAHU), the dSPACE platform and the data communication operating on the CAN bus.

Section 1 details the structure of the CAHU system on both the engine inlet part and the outlet part. The principle of this piece of hardware is discussed and each component in the system is described and the gas flow is analysed.

Section 2 covers the hardware for running the real-time model. A dSPACE platform is presented including the digital signal processor, and various I/O boards.

Section 3 details the communication system among the CAHU control PC, engine test PC, dSPACE control PC, and ECU. The program is shown to intercept, decode and buffer the private message between the engine ECU and its calibration (development) tool.

6.1 Charge air handling unit

Charge air handling unit (CAHU) is a novel testing system in the Powertrain & Vehicle Research Centre (PVRC), which is designed by Dr. Sam Akehurst and manufactured by CP engineering. This hardware has the same effect as the engine air charging device, such as turbocharger, supercharger, e-boost, twin-turbo, and etc. A real-time emulation technique can be applied to control the CAHU to represent the turbocharger, which allows the engine to be tested at different air charging conditions.

Figure 6.1 shows the schematic of the CAHU system. The CAHU consists of two parts: the engine inlet (compressor side) and the engine outlet (turbine side). On the left end of the schematic, the inlet fresh air is supplied by an external industry compressor at 7 bar absolute pressure and 25 °C. Two external industry compressors are available, and each has a flow capacity of 750kg/h. Therefore under extreme conditions, a total mass air flow rate at 1500kg/h can be supplied into the system. When the pressurized air enters the system, a particulate/oil trap ensures clean air, so the engine cannot be damaged by the unwanted particulate and oil. After the filter, the air then passes though a mechanical regulator, which allows the pressure to be reduced to approximately 5 bar. Since even a twin-turbocharger only requires a boost pressure at 4 bar, the pressurized air at 7 bar may cause extra errors when massive amount of air is needed to be dumped. And the 7 bar air would need unnecessary seals downstream to prevent a gas leak. After the regulator, a mass flow sensor (AFM) is placed to measure the total mass air flow by using an orifice plate with differential pressure transducer.

The air then enters the temperature control section, where the air is separated to two paths: one as the cold flow and the other as the hot flow. In the hot flow line, the air is heated by a 15kw electric heater, which allows a temperature rise of 100°C on an air flow of 500kg/hr within 6 seconds. The heater in hot flow is kept at 600°C, an electric/pneumatic valve is applied to mix the hot air and cold air flows and thus converge at the required temperature. A PID system is designed in the CAHU control

system to control the supplied air to reach the required temperature. So a fast response of the air temperature can be achieved via tuning the PID system. Furthermore, the heater circuit is controlled by using an infra red detector, which applies a PWM (Pulse-width modulation) signal to the heater elements based on temperature feedback from the infra red sensor.

After the temperature control section, the air enters the pressure control section to supply the engine air flow at the required pressure. A motorized butterfly valve is placed in the air flow path to control the total flow, so the total air flow, which would likely be used by the engine, can be set in the CAHU control software. Then the pressure of the air flow is controlled by dump valve using a closed loop control system. The mass flow rate in the dumped flow is also measured via a laboratory standard hot wire mass flow meter with an accuracy better than 1%, so the actual mass flow rate enters to the engine can be calculated by the total mass flow rate and the dumped flow rate. Additionally, the dumped flow air is cooled before passing though the mass flow meter for improving the measurement accuracy. In the CAHU control system, the total flow need to be set carefully, since extra errors may be introduced when the fluctuation occurs if a large amount of flow is dumped. Further down to the system, a pressure valve is located at the end of the engine inlet of the CAHU. Therefore the throttle effect can be emulated in the gasoline engine testing.

On the other side of the CAHU system, the engine outlet condition (turbine side) is simulated by a fast response butterfly valve at the exit of the engine exhaust manifold. So an appropriate level of exhaust back pressure can be manipulated to simulate the back pressure which is built up by the engine combustion and the restriction at the turbine entry. A high frequency pressure transducer is placed prior to the back pressure valve, so the exhaust manifold pressure can be measured and transmitted to the real-time model.

The CAHU control system is achieved by connecting with a CP Cadet v12 software on a control PC. So the flow temperature, pressure and mass flow rate can be set up

remotely. The CP Cadet v12 also provides the connection using CAN bus which allows other systems to be incorporated, such as dSPACE platform, engine testing facility control PC, and engine calibration software.

This CAHU system provides the capability of investigating the overall engine performance over a wide range of running conditions which would otherwise be restricted by either engine or turbocharger operation. It also allows the new engine air charging device could be developed, calibrated and validated on engine with the CAHU to emulate the air charging device, before building the prototype hardware. In this case, the CAHU system will be connected with a real-time model to emulate the air charging device, turbocharger model for instance, and the real-time signals are required to be received for the CAHU to manipulate the engine flow in the inlet and exhaust manifolds simultaneously. Therefore, a dSPACE platform is instrumented to run the real-time model and transfer signals and setpoints to the CAHU control unit. The dSPACE hardware will be discussed in the following section.

6.2 dSPACE platform

As mentioned previously in the literature review, the dSPACE is an important piece of hardware in the HIL system. Although the turbocharger model is developed in Matlab/Simulink, the real-time simulation is compiled to C code and finally executed on the dSPACE platform. Figure 6.4 shows the schematic view of the CAHU system and the real-time turbocharger model on the dSPACE platform. The dSPACE platform consists of a digital signal processor (DSP), I/O board, and various application cards.

6.2.1 Digital signal processor

The digital signal processor (DSP) in this dSPACE's modular hardware is DS1006, which is designed to give the computational power for real-time modelling and

interface to the I/O boards and host PC. This DSP features an AMD Opteron processor of 2.6 GHz and a 256 Mb DDR-400 SDRAM local memory and 128 Mb SDR SDRAM global memory are allocated for the dynamic data and hot data exchange with the host PC respectively.

The processor is required to be powerful enough to achieve the real-time operation even with a resolution of 0.1 degree crank angle. In the real-time turbocharger model, the time step is set to 33μs representing 0.1 degree of crank angle at the engine speed of 5000rpm. The interface of the DSP consists of the PHS-Bus interface, serial interface, and host interface to connect with the I/O board, standard RS232 device and the host PC respectively.

6.2.2 I/O board

The I/O board of the system is based on a DS2211 card designed specifically for simulating and measuring automotive signals. The primary task of the I/O is to undertake HIL interfacing with the production engine ECU, therefore the board features an angular processing unit to generate realistic cam shaft and crankshaft signals based on the predicted engine position of the real-time engine model. Additionally, the card enables capture of injection signals, and can simulate a wide range of transducers.

The DS2211 board mainly provides the following features:

a. A/D (analogue to digital) conversion

b. D/A (digital to analogue) conversion

c. Bit I/O (digital signals)

d. CAN support

e. Engine HIL simulation

f. Frequency measurement

g. Pulse generation

The DS2211 board always works with the DSP as a part of the dSPACE modular system. While the DS2211 measures signals directly from sensors (via A/D conversion) or receives signals indirectly from other controller (via bit I/O unit), the DSP performs the calculation of the real-time model. The interface communication between the I/O board and the processor is based on a specified high-speed bus, which is called 'PHS bus'.

Board DS2001

Another I/O board is also integrated into the dSPACE modular system which is the DS2001 board. Compared with DS2211, the DS2001 board provides a higher speed A/D conversion unit with five parallel A/D channels to handle the signal from the fast response transducer in the exhaust manifold of the engine. The faster conversion in the DS2001 board can lower the signal resolution to 4, 8 or 12 bits with smaller time steps, where the DS2211 board needs to perform a full 16 bit cycle based analysis.

6.3 Communication on CAN bus

6.3.1 CAN bus

The communication of the aforementioned HIL system is based on the CAN bus. Controller area network (CAN) is massage based protocol designed especially for the automotive applications, which allows microcontrollers and devices to communicate with each other without a host computer. CAN bus was initially introduced by Robert Bosch GmbH in 1983, and officially released in1986 at the Society of Automotive Engineers (SAE) congress in Detroit, Michigan. In a modern vehicle, there are as many as 70 electronic controllers for various sub-systems [99]. The main processor is the engine control unit, which refers to the ECU. The engine sub-system requires control actuators and feedbacks from various sensors. The communications among the

sensors, actuators and the electronic controllers are essential. Therefore the CAN bus is designed to fill this need.

On the CAN bus, each node (sensor, actuator, or controller) is able to send and receive messages, but not simultaneously. All the nodes are connected on the same CAN bus, and the message is transmitted serially onto the bus. If the bus is free, any node can send message on to the bus. But, if two or more nodes begin sending messages at the same time, the message with higher priority ID will win the 'arbitration', and the message with lower priority will sense this and back off and wait. Eventually (after this arbitration on the ID) only the dominant message can be received by other nodes. Therefore the CAN bus connection provides a high level of security and minimum delay for the messages among each node.

Since the dSPACE board (Ds2211) and the PC with CP Cadet software provide the interface for CAN bus, the CAHU system, real-time model, and the engine test facilities can be connected onto the CAN bus.

Figure 6.5 shows the schematic of the communication for each sub-system on CAN bus.

6.3.2 CCP message on CAN bus

As discussed in the previous section, the engine parameters and measured variables on the testing facilities are able to be transferred via the CAN bus, which is from the PC with CP Cadet software to the real-time turbocharger model operating on the dSPACE platform. However, there are two variables that could not be acquired by the CP Cadet: the VGT position of the turbocharger and the quantity of fuel injection in the engine ECU control strategy. Moreover, for the engine transient test, the VGT position and the Fuelling signals in the engine ECU are required to be transmitted to the real-time turbocharger model as fast as possible.

The CAN messages from the engine ECU only contain the essential signals for controlling the actuators and receiving the feedback from the sensors. So the VGT position and fuelling are the internal variables in the control strategy, which cannot be seen on the ECU CAN messages. However, the variables used in the custom strategy in ECU are still acquired by the calibration tool (e.g. ATI Vision or Kleinknecht Gredi) via the CAN bus for the ECU calibration or diagnostics. Instead of requesting each variable individually, variables are streamed continuously from the ECU to the calibration tool in one CAN message. This conversation between the ECU and the calibration tool is based on the CAN Calibration Protocol, a list of variables that the user wishes to acquire can be defined within the calibration tool and then sends the initial request; once the request is received, the ECU will stream the variables continuously to the calibration tool via the CAN bus.

The CAN Calibration Protocol (CCP) is the software interface protocol between the ECU and its development tool. Normally this interface handles the module calibration, measurement data acquisition, and flash programming activities. The CCP was adopted and enhanced by a European ASAP (Arbeitskreis zur Standardisierung von

Applikationssystemen) association founded by a couple of automotive companies. Figure 6.6 shows the ASAP interface on the CAN bus. The ASAP 1 message is the signal that needs to be intercepted from the conversation between the ECU and the calibration tool.

A typical CCP dialog always uses a master/slave form of conversation. The calibration tool initiates the conversation with a single CAN message (Commond Receive Object (CRO)) and once received, the ECU then starts streaming the requested variables in a single CAN message (Data Acquisition Message (DAQ)). Therefore, in order to intercept the informaction, this CAN message needs to be decoded.

6.3.2.1 DECODING THE CAN MESSAGES

The typical data acquisition message (DAQ) from the ECU to the calibration contains 8 byte of data. This first byte (byte 0) is the package ID (PID) which is used to identify the batch of variables that are contained in each DAQ message. The following six bytes (byte 1-6) are divided into three signals, and each signal has two bytes (16bits). So each signal represents one variable in the 16-bit signed integer form. The last byte (byte 7) is the error code which is normally zero. In this case, only three variables are transferred by one CAN message frame. Therefore the location of these variables is dependent on the request in the calibration tool.

If nine variables have been selected for transmission in the calibration tool, three variables will be sent in a batch. Therefore, 9/3=3 separate CAN frames are going to be sent from the ECU. According to the location of the variables in the calibration tool, variables 1 to 3 arrive in frame 1 with the PID of 0; variables 4 to 6 arrive in the next frame with a PID of 1 and finally variables 7 to 9 arrive in the final frame with a packet ID of 2.

6.3.2.2 Buffer module in Matlab/Simulink

The Simulink module in the real-time turbocharger model handles three tasks:

a. intercept the messages,

b. buffer the message

c. decode signal into engineering units.

Since the dSpace system does not provide hardware buffering the CAN messages, incoming DAQ messages must be dealt with as soon as they arrive, if not they will be overwritten by the next message. Because each message in the batch contains three variables, the message needs to be divided into three separate sections. Figure 6.8 shows the sub-model in Matlab/Simulink. The VGT position and Fuel injection are located in the DAQ message (byte 1-4) with a package ID of 1. Therefore if the first

byte is equal to one, the messages are then stored in a buffer (Figure 6.9). So every time the turbocharger model receives the signals from the buffer, it is kept as the latest message transferred from the ECU.

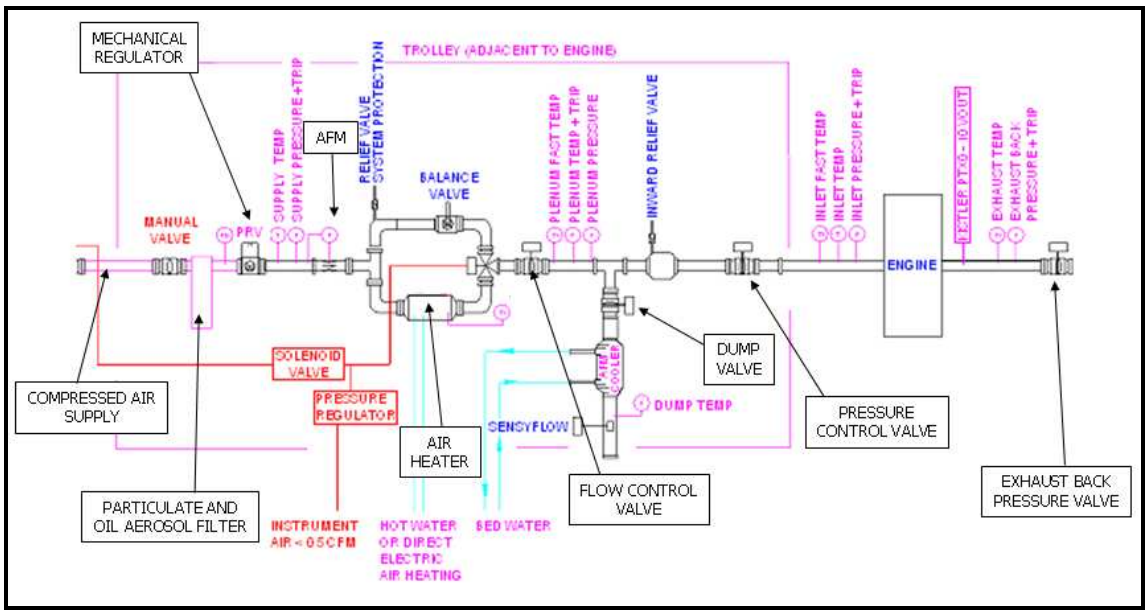

Figure 6.1 Charging air handling unit (CAHU) system Schematic

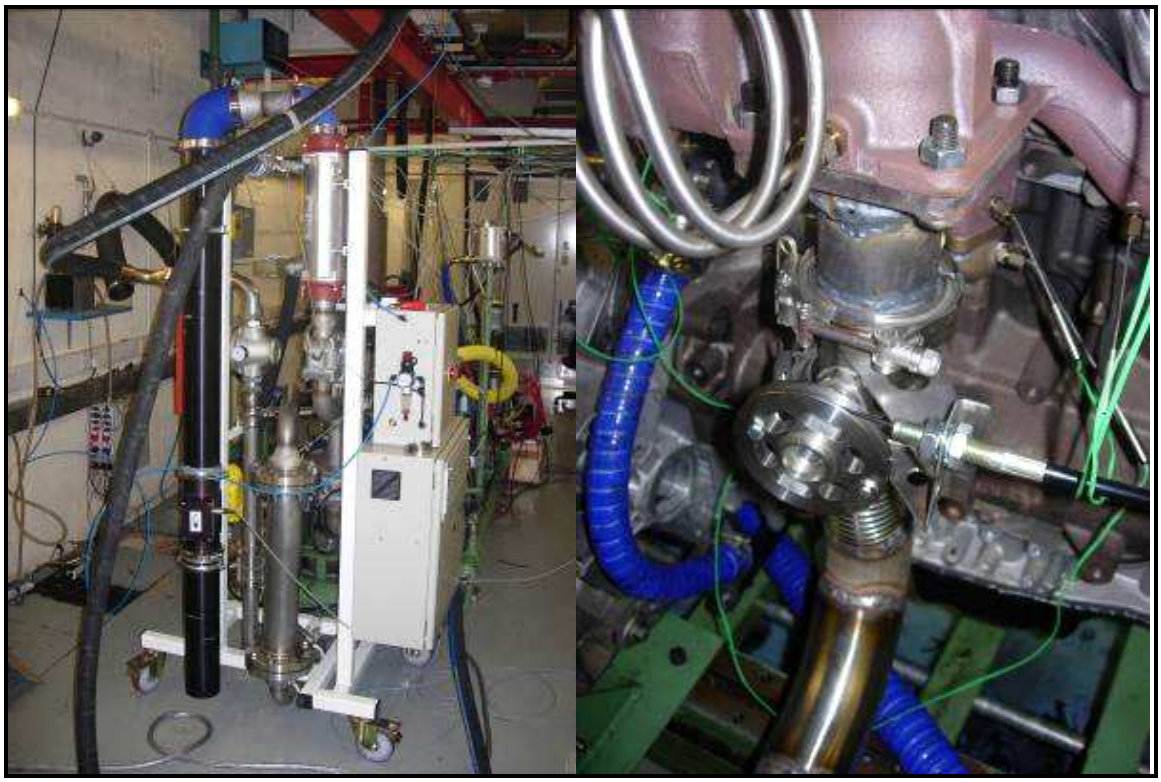

Figure 6.2 CAHU: Engine inlet side & outlet side

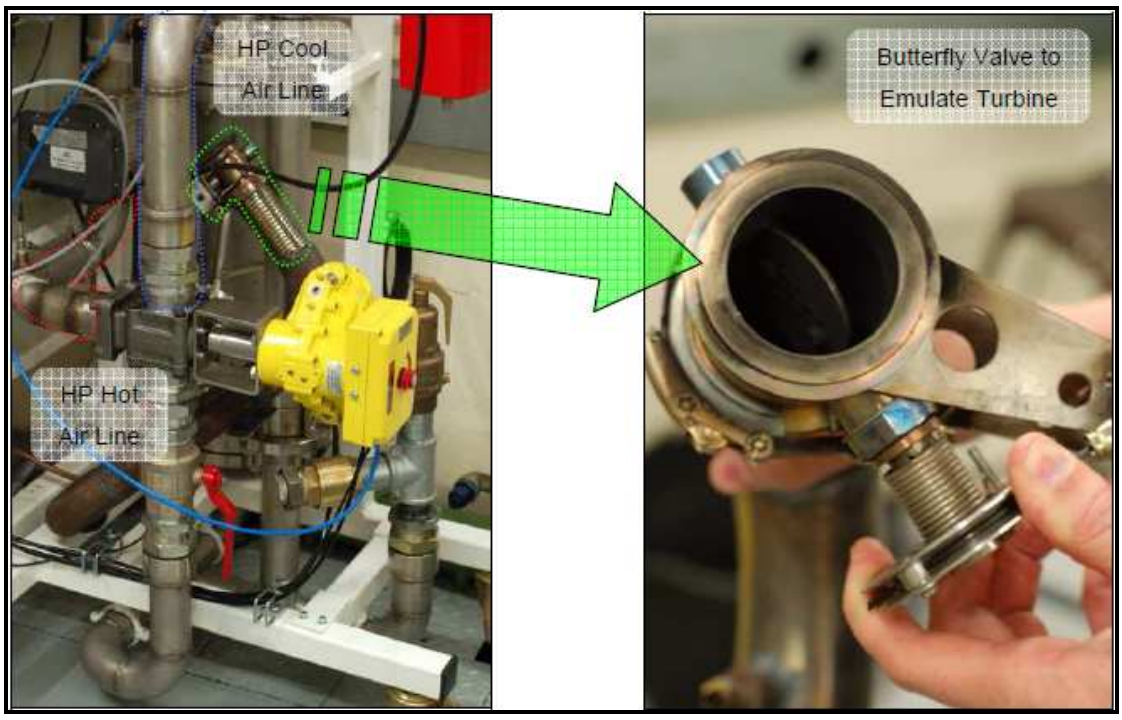

Figure 6.3 Butterfly valve in the CAHU

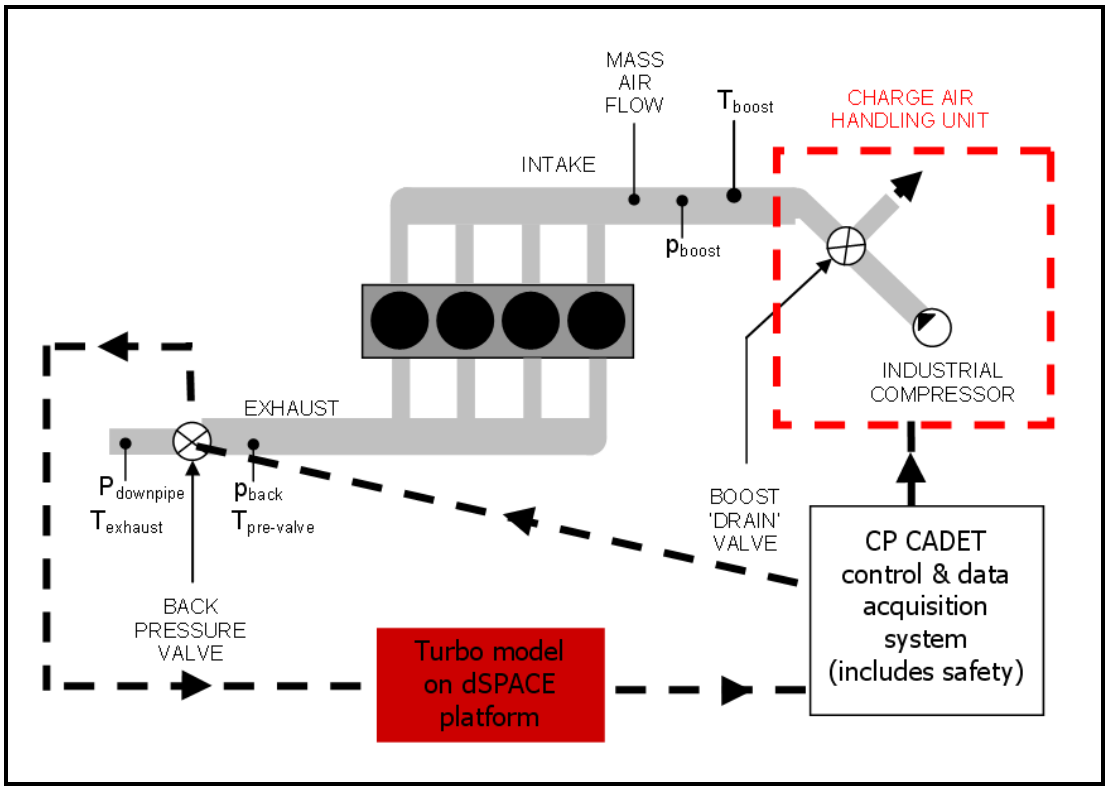

Figure 6.4 CAHU with turbocharger model on dSPACE platform

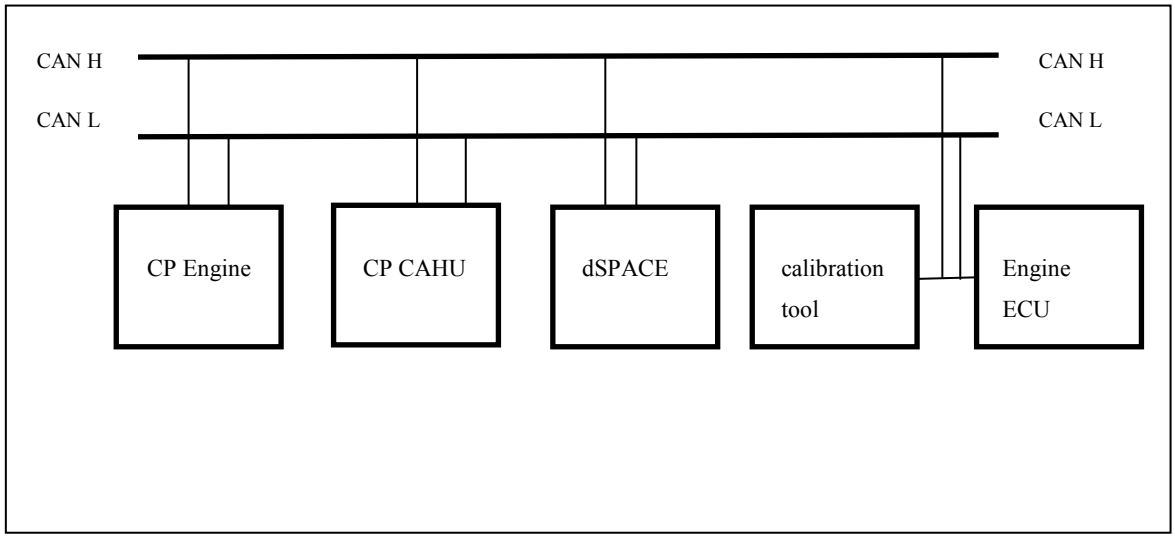

Figure 6.5 Schematic of CAN communication among subsystems

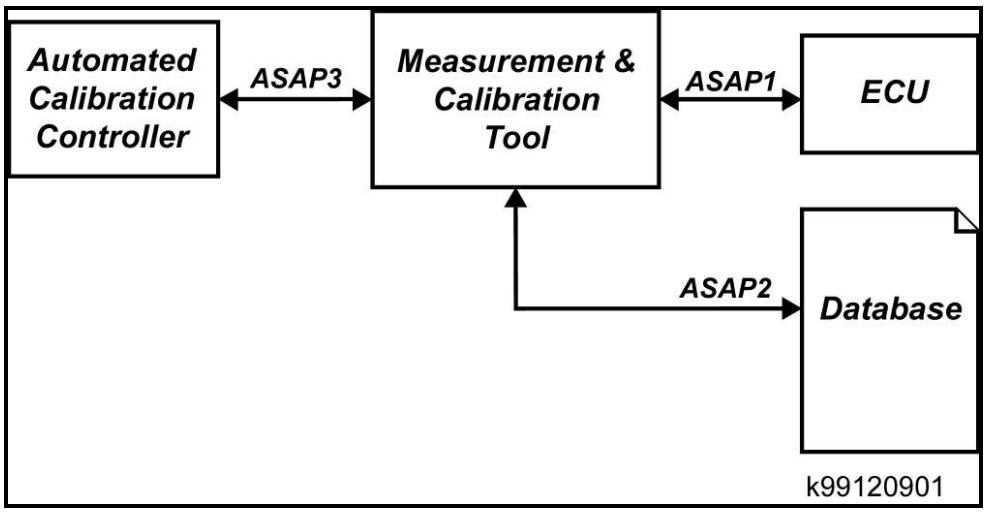

Figure 6.6 The ASAP interface [104]

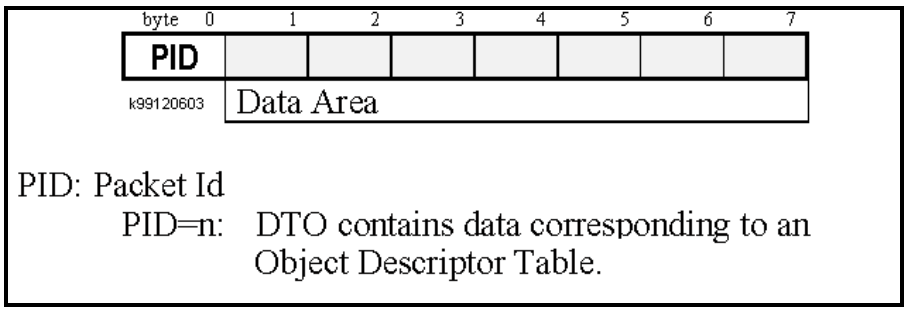

Figure 6.7 Structure of data acquisition message [104]

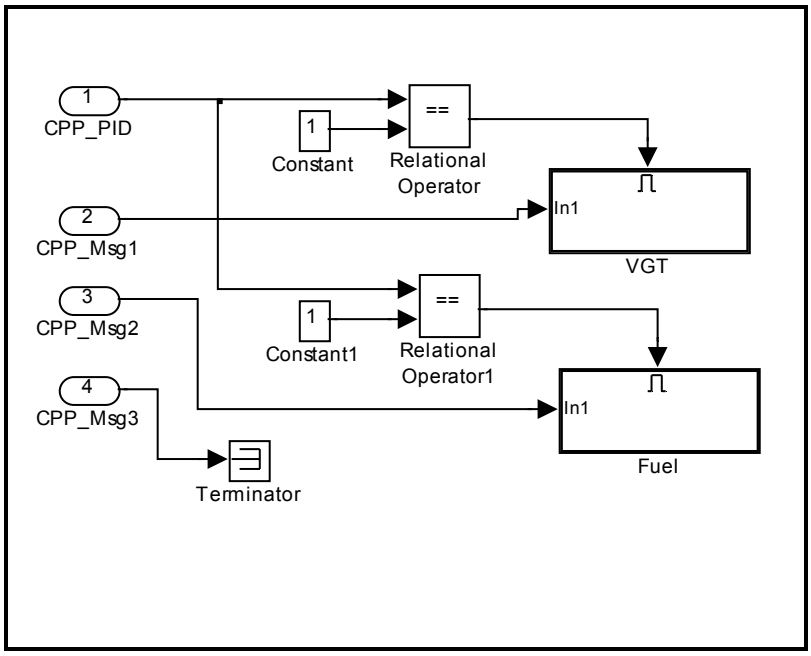

Figure 6.8 CCP message buffer module in Simulink

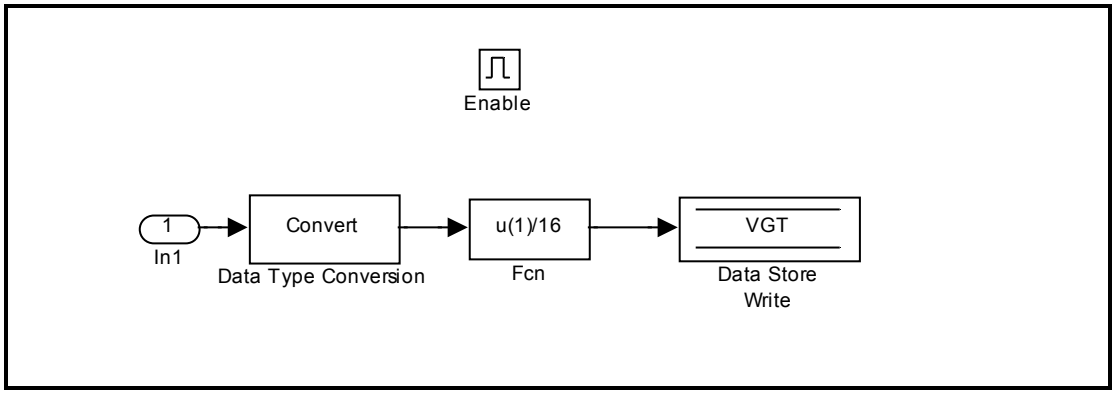

Figure 6.9 Buffer detail in the Simulink

Chapter 7 EXPERIMENTAL FACILITIES

Overview

Chapter 6 focuses on the Charge Air Handling Unit (CAHU); this chapter is concerned with the rest of the experimental facilities utilized in this work. The test rig necessitated the combination of a number of different functions which allows the diesel engine to be operated in conjunction with the Charge Air Handling Unit (CAHU) to simulating the performance of a turbocharged diesel engine and the effect of variable nozzle geometry positions.

This chapter is divided into three sections. The first section details the engine test cell configuration including the diesel engine, engine dynamometer, cooling system, and the temperature and pressure measurements. The second part describes the data capture and acquisition methods, the control system and the communication platform allowing the signals to be transmitted with a high level of security and minimum delay. Section 3 deals especially with the factuality of the rig to work under both steady state and transient test conditions. The challenges during the development of the testing protocols are also discussed.

7.1 Engine

The baseline engine being investigated in the experimental work is a Ford Puma 2.0 litre HPCR diesel engine with a peak torque of 310Nm (Table 7.1), which is used in the Ford vehicles such as the Mondeo and TRANSIT [107]. This engine is equipped with a variable geometry turbocharger (VGT) (Table 7.2) and fitted with a Denso high pressure common rail fuel injection system. The pilot injection scheme and exhaust gas recirculation (EGR) are also installed as common features.

The turbocharger is a Garret GT20 with variable geometry. The effect of variable nozzle positions gives rise to a wider range of operating points for the turbine with regards to the mass flow and the expansion pressure ratio. In line with the test rig development philosophy to cope with high boost conditions, the engine compression ratio is modified from 19:1 to 16.5:1, such that the engine in-cylinder peak pressure can be restricted to a safe level.

During the test procedures, the air charging system of engine was configured to enable two modes of operation:

Mode I: The engine operates with the variable geometry turbocharger and the control scheme from the ECU (Table 7.1)

Mode II: The engine operates with the charge air handling unit and the air charging control signals from HIL real-time model. (Figure 7.2, 7.3, 7.4)

Mode I is the baseline engine configuration which represents a production engine operating, whereas mode II allows the engine to operate with the CAHU. Both of these configurations are utilised to operate under steady state and transient conditions. Therefore the comparison of two sets of experimental results could evaluate the new approach to test engine while developing a new air charging testing

7.2 Engine testing facilities

The engine test cell is equipped with state-of-the-art testing facilities including the engine dynamometer, air mass flow meters, gravimetric fuel meter, external cooling system supplied by a water reservoir, combustion analysis system, and fast response emission analysers (Table 7.3).

7.2.1 Engine dynamometer

A David McClure 215kW AC dynamometer was applied in the engine test cell, which is capable of running to steady state tests, and as well as transient schedules with modelled gear shifts. An engine dynamometer has the benefit of easy accessibility to the major parts of the engine leading to little difficulty over instrumentation and CAHU packaging constraints. Additionally, it provides other added benefits over full chassis rolls testing, which is the reduced variability (no tyre losses etc…) and lower testing costs.

7.2.2 CAS System

The combustion analysis system (CAS) was developed by D2T for internal combustion engine research and design. The crank angle based data capture and acquisition system allows the engine parameters to be measured in real time, such as the cylinder pressure analysis (indicated mean effective pressure, maximum cylinder pressure …), rate of heat release calculation, combustion noise detection, dP/dAlpha up to 5 injections per cycles, mass fraction burned calculation, needle lift, etc. This means that continuous real-time signal transmission between the CAS and the dSPACE is possible. The fast response exhaust pressure data, for example, can be captured and transferred on the HIL system with no time delay. The CAS system is PC based and data can be transferred to other machines for data logging or motoring.

7.2.3 Mass air flow meter

Two types of air flow meters were implemented in the engine test cell: the ABB Sensyflow P gas flowmeter and the Bosch HFM 7 mass air flow sensor. The ABB sensyflow P air flow meter (AFM) applies the 'Hot Film' anemometer principle. The heat transferred form a heated object is measured to calculate the gas mass flow rate, which is directly proportional to the heat loss. The ABB sensyflow air flow meter provides high reproducibility of measurement with high operational reliability and high measuring accuracy, without additional pressure and temperature compensation [110]. The mass air flow meter monitors and records the data at the frequency of 16 kHz. The Bosch air-mass meter HMF 7 is mounted in the air box by the engine manufacture. The signal from the mass meter is transferred to the engine control unit (ECU).

The difference between these two sensors is the operation rage under different pressure conditions. The ABB mass air sensor can work under high pressure conditions i.e. up to 8 bar abs, whereas the MAF (Mass Air Flow) sensor will not tolerant the high pressures and temperatures, which will be experienced as part of this work. Therefore, when the charge air handling unit (CAHU) was connected to replace the turbocharger, the Bosch mass air flow sensor from the manufacture has to be disabled in order to avoid sensing failure under high boost conditions. Subsequently, since the engine control unit (ECU) can not receive any mass air flow signals, the engine ECU may operate in different control strategy and thus send different control signals, such as the quality of fuel demand, the turbocharger nozzle vane position, the EGR throttle position, etc. Hence in order to allow the engine ECU to perform exactly the same as running on a baseline engine with a real turbocharger, the MAF signals measured from the engine ABB MAF sensor are required to be transferred to the engine ECU.

Therefore a new communication that let the ABB MAF sensor transfer signals to the engine ECU was set up using the function of the hardware-in-the-loop system. As discussed in the previous chapter (chapter 6.2). The dSPACE platform is able to send

signals to other controllers through the D/A (digital to analogue) converter. The MAF signal measured from the ABB sensor is acquired initially by the engine test control PC in the CP cadet v12 software, and then the signal will be transferred to the real-time turbocharger model operating on the dSPACE through CAN bus. Finally, after feeding the MAF signals as inputs to a look-up table based model, where the MAF signal is converted to voltage values that the ECU recognises, the MAF signal will be sent to the engine ECU through dSPACE I/O board. This new communication system allows the engine ECU to perform normally without the signal from the conventional MAF sensor.

7.2.4 Pressure measurements

Transducers are the most widely used accurate pressure capturing measurement, due to its high sensitivity and thermal stability. The piezoelectric pressure transducer, for example, is based on quartz crystals (usually silicon dioxide (SiO2)), which provides an electrical charge under various loads. The electrical charge is then converted to voltage signal using an amplifier. The voltage signal can be captured via using an oscilloscope or high speed data acquisition system. The piezoelectric pressure transducer is normally applied to measure in-cylinder pressures due to its fast response, small size, high accuracy and excellent repeatability. The Piezoresistive pressure transducer, on the other hand, applies pizoresistive resistors connected in a wheatstone bridge. The applied pressure unbanlances the bridge and produces a proportional output signal. This type of pressure transducers normally applies to measure the instantaneous exhaust pressure, and injection pressure in the automotive research due to its high frequency response and high linearity.

The applications of pizoresistive pressure transducers in the engine test cell include exhaust manifold, and common-rail fuel injector. Two types of pressure transducers were used including Kistler 4045A, 4065A. Due to the requirement of smaller pressure range and lower cost, engine inlet manifold, the turbine inlet/outlet, and compressor inlet/outlet pressures are measured by strain gauges (Druck 2000, and

249-3959). Table 7.4 shows the specification of the pressure measurements in the engine test cell.

In order to capture the pulsation in the exhaust manifold due to the valve opening/closing events, the Kistler 4045A pressure transducer (Table 7.5, Figure 7.5 and Figure 7.6) was implemented to measure the exhaust manifold pressure. As discussed in the previous chapter (chapter 5), the pulsating exhaust flow appears to have higher energy than the steady flow. The ability to measure the pulsating pressure with resolution to match the crank angle based time interval is essential for the emulating the turbine performance under pulsation conditions. According to the sampling time to measure the pressure at each degree crank angle under high engine speed condition, The pressure transducer needs to capture and response within 1/30,000 second (frequency: 30kHz). Kistler 4045A series transducer has a high natural frequency which is greater than 120 kHz. Table 7.6 shows the requirement of the pressure measurement to catch the pulsation in the exhaust gas.

7.2.5 Temperature Measurement

Temperature is one of the most important measured physical quantities in the engine test cell for the control system. The principle of applying thermocouple to measure the temperature is the electromotive force (emf) being generated by the temperature gradient in an electrical conductor [111]. The output voltage is a measurable signal, since it is a function of the temperature difference along the conductor. Most conducting materials can produce a thermoelectric output. However, only a restricted number of sensible choices can be considered because of the width of temperature range, linearity and repeatability. Type K thermocouple (chromel-alumel) is the most common measurement in the automotive applications because its low cost, simplicity and high reliability [111].

Two kinds of type-K thermocouples (probe diameter 0.75mm and 1.5mm) were used in the engine test cell. The reason to use type K (chromel–alumel) thermocouple is because its high thermo sensitivity and wide temperature range. The temperature range for a typical type K thermocouple is between −200 °C to +1350 °C, which is suitable for engine diagnostics.

In the engine exhaust gas, the slow response of thermocouples (typically 0.1Hz to 5Hz) restricts temperature measurement to be time averaged rather than instantaneous signal [101]. Other thermometers such as the acoustic technique, optical diagnostics and resistance thermometry, are too complicated, difficult to set up and generally expensive. K. Kar et al. [101] suggest the capability to apply normal type K thermocouples to measure the instantaneous exhaust temperature via using thermocouple compensation techniques. This provides the potential to measure the actual exhaust temperature pulsation which needs to be investigated in the future work.

As a result, in the transient engine test, the thermocouple with probe diameter of 0.75mm is implemented in the exhaust manifold, in order to allow real-time model on dSPACE to receive synchronized temperature signals. The reason to choose a thinner thermocouple is because the conduction loss to the probe body would be small.

7.2.6 Testing Facilities Calibration

In order to achieve high accuracy and stability, the testing facilities were calibrated before the commencement of the experimental work. The pressure transducers were calibrated by using a pressure calibration tool to set up six different pressure levels in the CD Cadet v12 software. The mass air flow meter and the thermocouples were calibrated by the manufacture. However the amplifiers were calibrated via using a voltage meter to set up different voltage inputs.

7.3 Data acquisition

7.3.1 CP Cadet V12

In the engine test cell control, two remote PCs apply the CP Cadet V12 software to remotely control the engine testing facilities, as a data acquisition system connecting with the sensors, and also sending signals to communicate with other controller and control the actuators. The software operates in a Windows 2000 based environment. It allows system customization using Visual Basic 6.0 and also contains Real Time multi-tasking direct digital control functions. Its interface supports input from the CAHU, CAN Bus, dynamometer, ECU ASAP3 connection, fuel weighers, sensors and controllers. The CP128 system capture cards are capable of sampling data at rates of up to 80Hz at 16 bit resolution and at up to 160Hz at 8 bit resolution. The hardware interface connection options are serial, IEEE, and Ethernet for a wide range of equipment. The Combustion analysis system (CAS, further details in section 7.2.2) is also connected to CP CADET V12. Additionally, the ECU and its calibration tool (ATI vision), and real-time model on dSPACE are connected with two CP Cadet PCs via the CAN bus. Therefore the data from the engine test facilities, CAHU measurements, ECU and CAS are able to be collected in one CP Cadet PC acquisition system.

7.3.2 ATI Vision

For fast sampling of engine response, data is logged using ATI Vision 2006 sp2. ATI Vision is an integrated calibration and data acquisition tool that collects signals from the ECU and external sources. It is connected to the ECU through a Network Hub interface box. The ATI Network Hub enables the synchronous CAN ICP communication from the ATI vision system to the ECU. The communication between ATI Network Hub and the ECU is via CAN, and between the ATI Network Hub and ATI vision is Universal Series Bus (USB). ATI vision samples engine response such as speed, fuel injection, mass air flow, EGR mass and start of injection timing during a transient at a rate of 50Hz (0.02s). The fuel demand measurement from ATI vision

was calibrated against CP gravimetric fuel weigher for accuracy before the experimental tests.

As shown in Figure 7.2, where the CP Cadet v12 software is installed on the PC marked as the data acquisition and CAHU control. The ATI Vision program is installed on the PC as the calibration tool in the engine test cell. The communication between ATI vision and other control PC is based on the CAN bus. The signals of VGT position and fuelling demand, transferring between the ECU and ATI Vision can also be intercepted by real-time turbocharger model running on the dSPACE platform via the CAN bus. The details of this novel design of the data communication system have been already discussed in chapter 6.

7.4 Test capabilities

7.4.1 Steady state tests

For the steady state tests, it is practice to test each operating point as a thirty times of averaged result to ensure a high level of confidence in repeatability. In the steady state test schedule, the engine was stabilized at least 3 minutes before measurement were taken; the engine data was collected with an averaged 30 seconds result. Also the engine coolant, oil temperatures were controlled to maintain a 5% variation, by using a PID system to control the valves. It can be observed in the results in chapter 8 that the repeatability is very good with little variation. Overall, the steady state performance measurement shows good consistency and repeatability.

7.4.2 Transient tests

The transient tests simulate engine performance during an acceleration or deceleration events. Subsequently, the transient tests were mainly performed at a fixed speed with

varying load steps (tip-in and tip-out). Tip-in tests represent the sudden increase of the load, so that the engine is maintained at low speed, and the paddle position varies from 10% to 100%. To the contrary, tip-out tests refer to the sudden decrease of the load, so the engine speed is fixed and the paddle position varies from 100% to 10%. The reason to choose 10% paddle opening as the start point of the test is because the engine response is quite slow at low rotation speed.

Transient testing requires low rotational inertia of the dynamometer, and high frequency data measurement. In addition to that, the recorded data needs to be synchronised. This requires the CP Cadet PCs, ECU calibration tool (ATI Vision), CAS system, and dSPACE model to transfer and receive signals in a real-time.

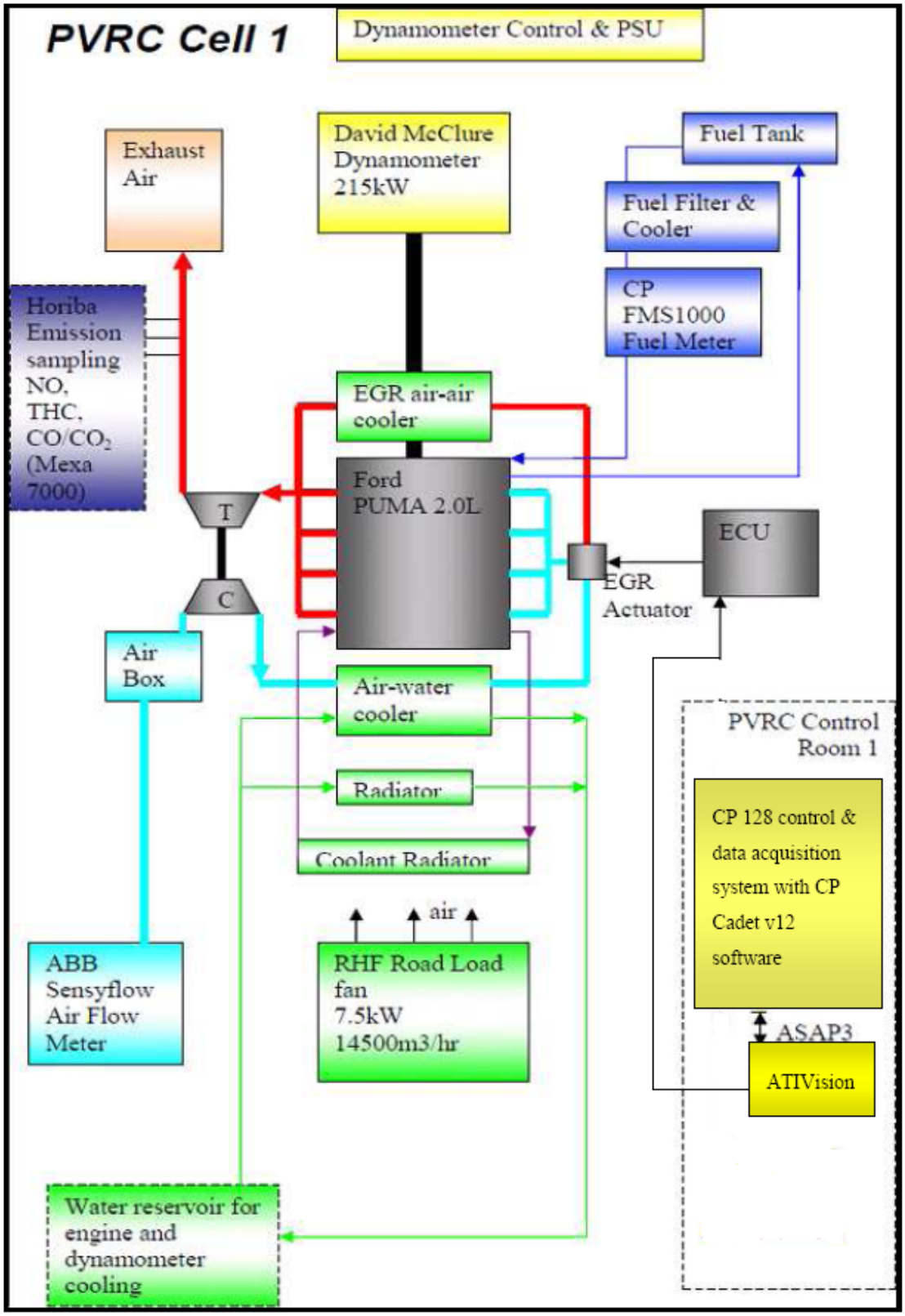

Figure 7.1 Engine test cell 1 facilities

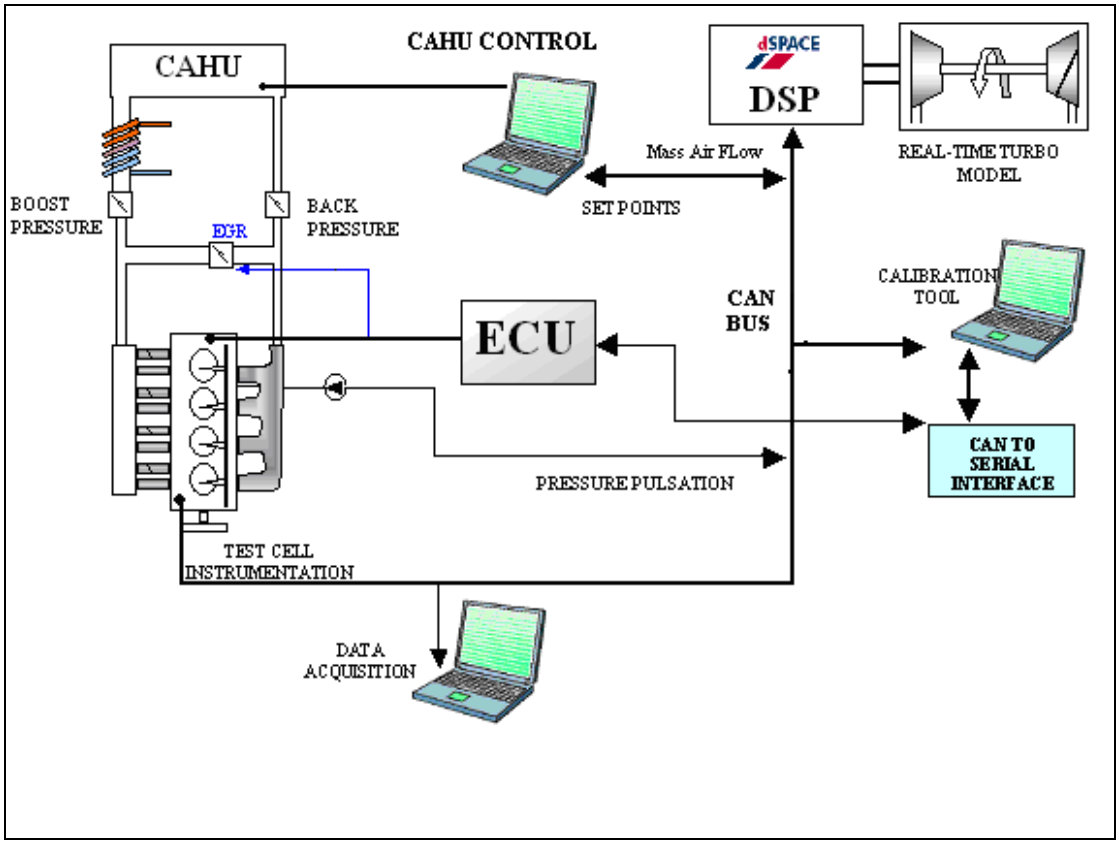

Figure 7.2 Engine test cell 1: Engine with CAHU

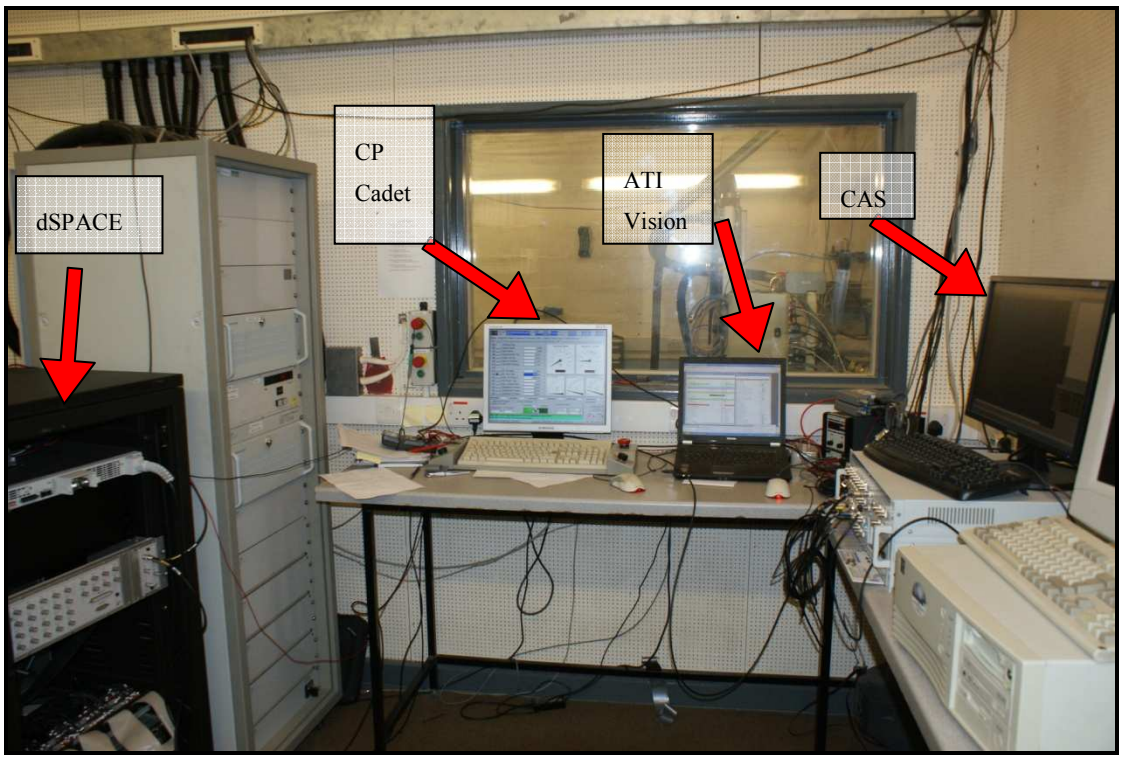

Figure 7.3 Engine test cell one: control room

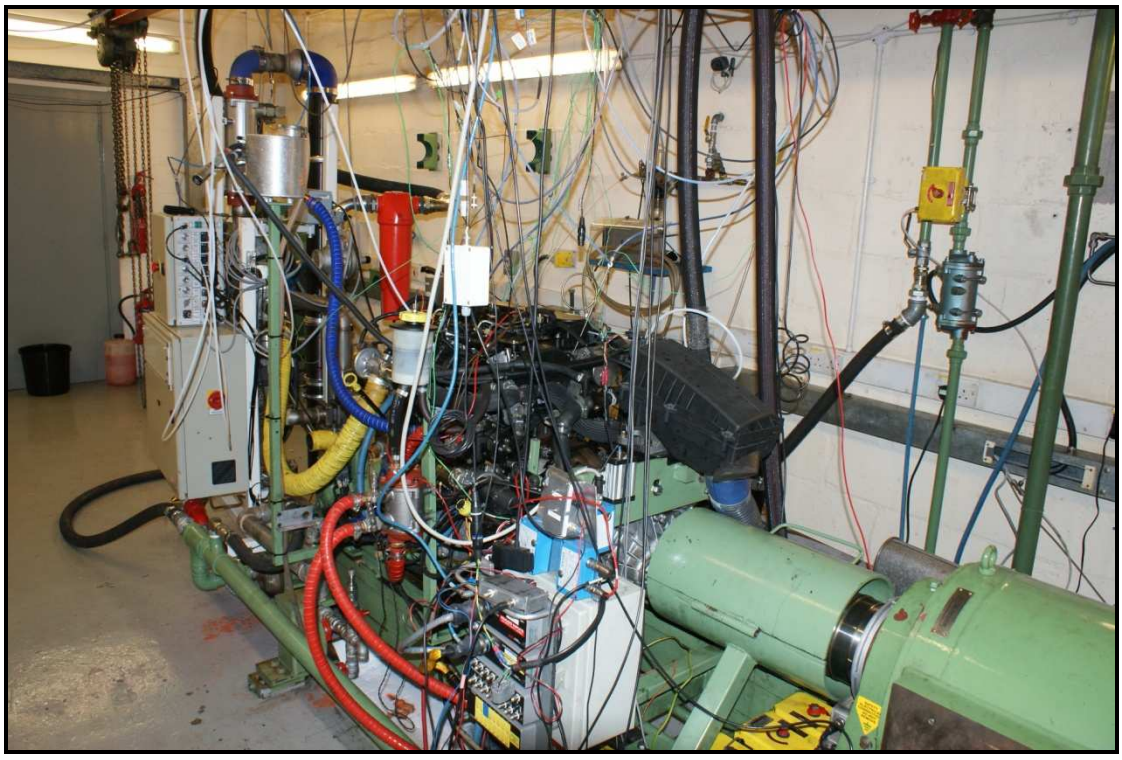

Figure 7.4 Engine test cell one: Engine with CAHU

Figure 7.5 Kistler pressure transducer 4045A

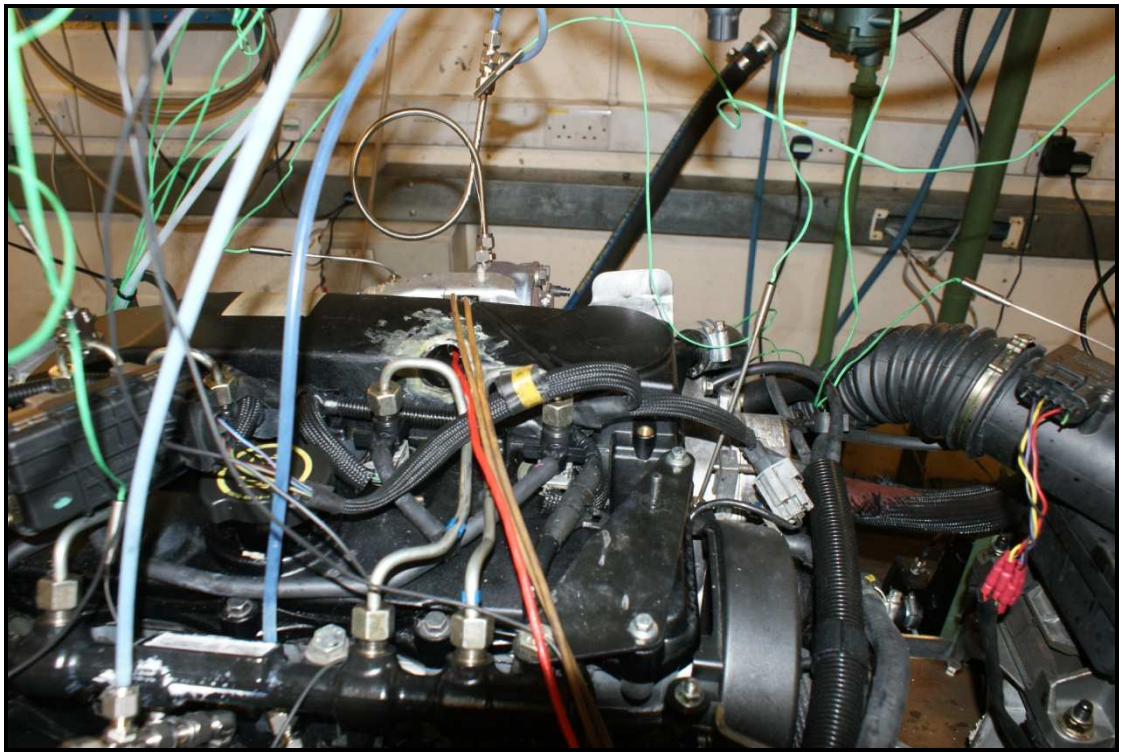

Figure 7.6 Instrumentation of Kistler pressure transducer 4045A

Table 7.1: Engine Specification

Engine Component	**Specification**
Engine Type	Compression Ignition
Stroke	4
Cylinders	4
Fuel Type	Diesel
Fuel Injection	Denso high pressure common rail direct
Compression Ratio	16.5:1
Cylinder Bore (mm)	86
Piston Stroke (mm)	96
Cylinder Volume Displacement (L)	0.500
Connecting Rod Length (mm)	152
Crank Radius (mm)	43
Valve Per Cylinder	4
Valve Timing	Fixed
Combustion TDC	360
IVO	710
IVC	230
EVO	490
EVC	20
EGR	Controlled
Firing Order	1-3-4-2
Turbocharger	Garrett Variable Geometry
Max Torque (Nm) @ Rated Speed (rev/min)	320, 1900
Max Power (kW) @ Rated Speed	95.6, 4000

Table 7.2: Turbocharger Specification

Number of nozzle Vane	11	U/C @ peak efficiency	0.55-0.6
Rotor hub diameter	12mm	Nozzle exit depth	5.5mm
Rotor tip diameter	37mm	Rotor inlet blade angle	90degreeC
Rotor exit depth	14mm	Rotor exit blade angle	24degreeC
Rotor inlet depth	5.5mm		

Table 7.3: Engine Test Cell

Equipment	**Description**
Engine	Ford PUMA 2.0L
Engine Dynamometer	David McClure 215kW AC
Host System	CP128 tower with Cadet v12
In-Cylinder Pressure Measurement	D2T Combustion Analysis System (CAS)
Engine Cooling System	External cooling provided
Test Cell Temperature Control	Road Speed Fan
Temperature Measurement	Slow: K-type
Pressure Measurement	Slow: Druck 2000
Fuel Measurement	CP FMS-1000 Gravimetric
Air Flow Measurement	ABB Sensyflow P Meter
Air Charging Handling Unit	Hardware: In-House
Hardware-in-the-Loop System	dSPACE: board 2211

Table 7.4: Pressure transducers

Brand	Druck	Druck	Kisler	Kisler
Series number	2000	249-3959	6065A	4045A
Pressure range	0…1.6bar	0…6bar	0..2000bar	0…500bar
Temp range	-20…80°C	-20…80°C	-40…140°C	0…140°C
Location	Post catalyst converter, air box, pre compressor	Post compressor, intercooler, inlet manifold, etc	Common rail fuel injection system	Exhaust manifold

Table 7.5: High Speed Pressure Transducer Specification

Specification	**Unit**	**Data**
Sensor Type	-	4045A10
Measuring range	bar	0-10
Overload	bar	25
Sensitivity at lcal	mV/bar	50
Natural frequency	kHz	>120
Operating temperature range	°C	0-140
Cooling type	-	7551
Amplifier type	-	4618A0
Linearity (EP)	±%FSO	<0,3
Thermal zero shift	±%FSO	<0,5
Thermal sensitivity shift	±%	<1,0
Weight	g	33

Table 7.6: Sampling time requirement

Engine speed (rpm)	**Engine speed (rev/s)**	**Engine speed (degree/s)**	**Sample time**	**Frequency**
5000	83.333	30,000	1/30,000	30kHz

Chapter 8 EXPERIMENTAL RESULTS AND ANALYSIS

Overview

This chapter details the experimental work conducted on both the baseline diesel engine with a turbocharger and the engine with the aforementioned advanced air charging test approach, using the CAHU to emulate the turbocharger performance. This work comprehensively details the engine operating performance under both steady state and transient conditions.

Section 1 presents the engine configurations in the tests. As discussed in the previous chapter, two engine configurations are applied in all the tests, and thus the new test approach in mode II can be testified and calibrated against the baseline engine in mode I.

Section 2 details the steady state engine operating points at fixed engine speeds and engine torques. The comparisons of inlet/exhaust manifold pressures, turbocharger speeds, mass air flow rates, and fuel demands between the baseline engine and the engine with CAHU emulation are conducted. An improvement based on the corrected VGT position signals from the engine ECU is also discussed.

Section 3 presents the engine performance under unsteady turbocharger flow model with a fast response pressure transducer to measure the instantaneous exhaust pressure. The difference between the steady flow turbocharger model and unsteady model is

analysed and the improvement of the turbocharger simulating under pulsating condition is highlighted.

Section 4 details the transient tests where the engine was operated at fixed speed and the load was varied in a short time interval. The comparisons of two sets engine configurations are presented as well.

Section 5 details the most important challenge in the testing: system stability due to the oscillation caused by the interaction among the engine, CAHU system and turbocharger model on dSPACE. The instability is analysed by dividing into two areas: hardware and software. A number of different approaches are also discussed to reduce the system oscillation and to allow the CAHU to response rapidly to match the engine transient performance.

8.1 Test configurations

As presented in the previous chapter, during the engine tests, the engine was configured and tested in two modes:

Mode I: Baseline engine with the production turbocharger as the air charging system.

Mode II: Engine in the HIL system with CAHU to emulate the turbocharger in real time.

In mode I, in order to test the engine baseline performance, the engine was implemented in conjunction with a real turbocharger as well as the effect of nozzle variable geometry. It must be mentioned that the EGR (exhaust gas recirculation) valve was also enabled with the control signals from the engine control unit (ECU). So the engine air charge/ discharge performance in the real engine can be evaluated. The experimental data were measured and recorded in the remote automated control PC via using CP Cadet V12 for the data acquisition (see chapter 7).

Mode II allocates the engine in a hardware-in-the-loop testing environment in the absence of a real turbocharger. So the engine is connected with the charging air handling unit (CAHU) as the hardware part of the system, and virtual real-time turbocharger model as the software part of the system on dSPACE to control the CAHU to emulate the turbocharger performance. This means that the real-time simulation on dSPACE allows the CAHU to provide the engine air charge and discharge performance in the absence of a real turbocharger. The tests data were measured and acquired by the CAHU control PC, engine ECU and test control PC, but finally the data are recorded as usual on the remote control PC in the CP Cadet V12 software.

The objective of this chapter is to evaluate the experimental results in the basis of these two configurations, so in order to validate whether the engine with CAHU in mode II can achieve the baseline engine performance in mode I. The experimental results under both the steady state and transient testing conditions are presented and

analysed in the section 8.2 and 8.3. Finally the experimental results between these two configurations offered guidelines to modify the software (real-time model) or the hardware (testing equipments) in order to improve the new testing system in mode II. Hence the system modifications and their improvements will be discussed in section 8.5.

8.2 Steady State Test

8.2.1 Steady state test set up

Steady state refers to the conditions that engine variables gradually decrease or increase until to approach their steady state value. With all the fluctuating variables in the engine due to the chemical reactions, thermodynamic variations and the engine's moving mechanisms, it theoretically takes infinite time to reach a real equilibrium. Consequently, an approximation with regard to the steady state needs to be taken in to account. In this investigation, a certain amount of time (three minutes) of stabilisation and closed loop control schemes on the engine speed, torque and engine coolant/oil temperatures have been set up to reach the steady state conditions.

Before running the engine tests, a test schedule was required to be created in the CP Cadet on the automated control PC. The steady state tests were undertaken by controlling the engine speed and torque to be maintained at fixed values, which represent different engine operating points. For saving the experimental time and to fulfil the need to cover most of the engine operating points, 500 rpm and 20 Nm were selected as the intervals in the index of the engine speed and torque respectively. Additionally a range of engine speed from 1000 to3500 rpm and a range of engine torque from 20Nm to max load were set up to cover the engine operating points (Figure 8.1).

As discussed in the previous chapter, when the engine operates in conjunction with the CAHU emulation, the engine control unit (ECU) cannot receive the MAF signal from the conventional MAF sensor, since it cannot be installed in the air path under high temperature and pressure conditions. Therefore, comparing with the baseline engine operations, the engine ECU may operate at different control set points from the engine control scheme. The engine EGR (exhaust gas recirculation) valve opening position, for instance, was affected due to the lack of MAF signal. Consequently, during the engine test in conjunction with the air charge from CAHU emulation, the EGR valve positions were manually changed according to the recorded baseline engine test results. Another impact due to the lack of MAF signal is that the engine with CAHU emulation cannot achieve the engine limiting torques (full-load condition). Moreover, the accuracy of the real-time turbocharger model may be another contributing factor, since the engine is very sensitive with a different inlet air pressure and temperature. Hence during the steady state test, 20Nm below the limiting torque curve was selected as the maximum torque at each engine speed. Since the engine fault detection operates in a reduced power mode, engine speed was limited to 3500 rpm due to this being the typical range of interest. The engine coolant temperature was also maintained at 85 °C by using a PID closed loop control system.

In the acquisition system, the data were measured at each second and calculated as an average of 30 seconds result to achieve a high level of repeatability. The engine test data were logged on the remote control PC. The recorded engine variables include the engine speed, torque, mass air flow, fuel demand, turbocharger speed, pre/post turbine pressure & temperature, pre/post compressor pressure & temperature, inlet/exhaust manifold pressure & temperature, fuel demand, and the VGT position from the ECU. Table 8.1 shows the acquisition systems for variables. Two sets of tests with two different engine configurations were carried out in the engine test cell, and the results are illustrated and discussed in the next section.

8.2.2 Experimental results and analysis

Turbocharger Speed

The comparison between the actual measured turbocharger speed with the baseline engine and the virtual turbocharger speed in the CAHU emulation is shown in Figure 8.2 and Figure 8.3. Figure 8.2 gives the turbocharger speed at different engine operating points (engine speeds and torques), and Figure 8.3 shows the regression between the actual turbocharger speed and the predicted turbocharger speed in the real-time model emulation. It can be observed from the graph that most of the points locate in the 5% error region near the linear regression line. This means that the accuracy of most turbocharger speed emulations is higher than 95%. The contributing factors of this accurate result in the real-time turbocharger emulation can be summarised as:

Accurate turbine and compressor characteristics maps to predict the isentropic efficiencies, mass flow rates, and pressures.

Real time gas properties calculation to give rise to accurate specific heat capacity (CP) and the ratio of specific heat (γ).

Accurate turbocharger shaft inertia provided by the turbocharger manufacture, good predictions of turbocharger shaft drag force and bearing friction loss.

Precisely measured engine variables including temperatures, pressures, and mass flow rates to feed into the turbocharger model in real-time.

Engine Boost (Inlet Manifold) Pressure

The comparison of engine inlet manifold pressures in two engine configurations is shown in Figure 8.4 and Figure 8.5. Figure 8.4 presents the engine boost pressure at individual engine operating points and Figure 8.5 shows the regression between the actual boost pressure on the baseline engine and the boost pressure from CAHU emulation. In the test of engine with CAHU emulation, rather than the turbocharger speed is the predicted variable in the real-time model, the engine boost pressures were actually measured in the engine inlet manifold, which represent the CAHU response from the turbocharger model output. Compared with the turbocharger speed analysis,

the engine boost pressure shows similar result where the accuracy of the CAHU emulation is around 95% (Figure 8.5). Since the compressor characteristic map in the real-time turbocharger model provides an accurate prediction of the relationship among the compressor speed, mass flow rate and pressure ratio across the compressor, the CAHU can operate with the pressure set points from the model output.

Mass Flow Rate and Fuel Demand

The measured engine air mass flow rate and the recorded fuel demand from the ECU readings are shown in Figure 8.6, Figure 8.7, Figure 8.8 and Figure 8.9. It can be observed that most of the data points of the air mass flow rate and the fuel demand are gravitated in the 5% error zone, which means the accuracy of these two engine parameters is greater than 95%.

Engine Back (Exhaust Manifold) Pressure

During both the steady state and the transient tests, the engine exhaust pressures seemed to be unstable under high engine torque and speed conditions, since this may be caused by the real-time model, CAHU control system, or the engine itself. The reasons and the corresponding modifications on the system to solve the problems will be discussed in section 8.5.

The engine exhaust manifold pressures were measured at each engine operating point (Figure 8.10), and the comparison between the actual back pressure from the baseline engine test and the back pressure from the engine with CAHU emulation is shown in Figure 8.11. It can be observed that most of the errors of the back pressure are greater than 15%. The reasons that cause this inaccuracy of the back pressure data can be categorised as:

Insufficient accuracy of the turbine map to predict the pressure ratio across the turbine.

Non-linear relationship between the VGT signal from the engine ECU and the actual physical nozzle position on the turbine.

Slow response of the pressure control valve at the exhaust manifold.

The accuracy of the turbine map is restricted by the density of the data supplied by the turbine manufacture to feed into the look-up tables. In the future work, in order to improve the accuracy of the turbine model, more experimental data supplied by the manufacture or measured on a turbo-dynamometer is required to increase the density of the look-up tables. Alternatively, a fully analytical turbine model is needed to provide the accurate turbine characteristic among different variables: the turbine speed, gas mass flow rate, the pressure ratio across the turbine and the VGT positions.

The butterfly valve at the exhaust manifold is controlled by a pulley, a single cable and a spring to provide the valve position with the pressure set points supplied by the real-time turbocharger model. So poor stiffness and the low response of the spring may cause the systematic fluctuations, however during the steady state tests, the CAHU control system was stabilized to provide relatively constant measurements. Therefore slow response of the CAHU hardware should not be responsible for the errors of the exhaust pressure data collected during the steady state tests.

It was clear from the results that the relationship between the VGT opening position signals on the engine ECU and the physical nozzle position on the turbocharger needs to be created. Hence, the VGT position correction in the real-time model will be discussed and the comparison of the back pressure between the original result and the improvement will be detailed in the next section.

8.2.3 VGT Position Correction

After the aforementioned analysis about the system possible improvements, a program to calculate the real VGT positions from the ECU signals was required to be added into the turbine model. In order to understand the relationship between the

VGT control signals from the ECU and the real VGT positions on the turbine, an investigation was carried out before entering the stage of the tests. Since the engine baseline test result only contains 64 individual engine operating points, more engine experimental results are needed to be collected before the investigation. Because of the time requirement for a steady state test, a quasi steady state method was selected to investigate more engine operating points. The engine was operated at fixed power curve (5kW, 10kW, 15kW, 20kW, 25kW, 50kW, 75kW and full load) and the engine speed from 1000rpm to 4000rpm with 250 rpm of interval. Hence more than 6000 engine operating points were recorded to compare and validate the VGT correction model.

A program to calculate the actual physical VGT position from the fixed power curve experimental data was created (Figure 8.14). In this program, the turbocharger speed, mass flow rate, and pressure ratio across the turbine were fed into the model to the VGT position based on turbine maps from the manufacture data. Consequently, the comparison between the VGT positions from ECU signal and the VGT positions from the program outputs can be carried out. From Figure 8.15, it is obvious that the two data sets are not linear, which explains some of the errors on the engine back pressure data (Figure 8.12). In order to simplify the model, a linear equation based on the relationship between these two data sets was created. So the VGT position correction was generated to transfer the VGT from the ECU signals to a real VGT position to feed into the turbocharger model (Figure 8.15).

The comparison between the original engine back pressure and the back pressure from the engine tests with the addition of the VGT correction is shown in Figure 8.16. An improvement can be observed in the new engine back pressure regression (Figure 8.13), which shows that most of the data locate in the 10 per cent error region. Compared with the original data regression (Figure 8.12), the addition of VGT position correction in the real-time turbocharger model stabilises the CAHU system and increase the accuracy of the turbine emulation.

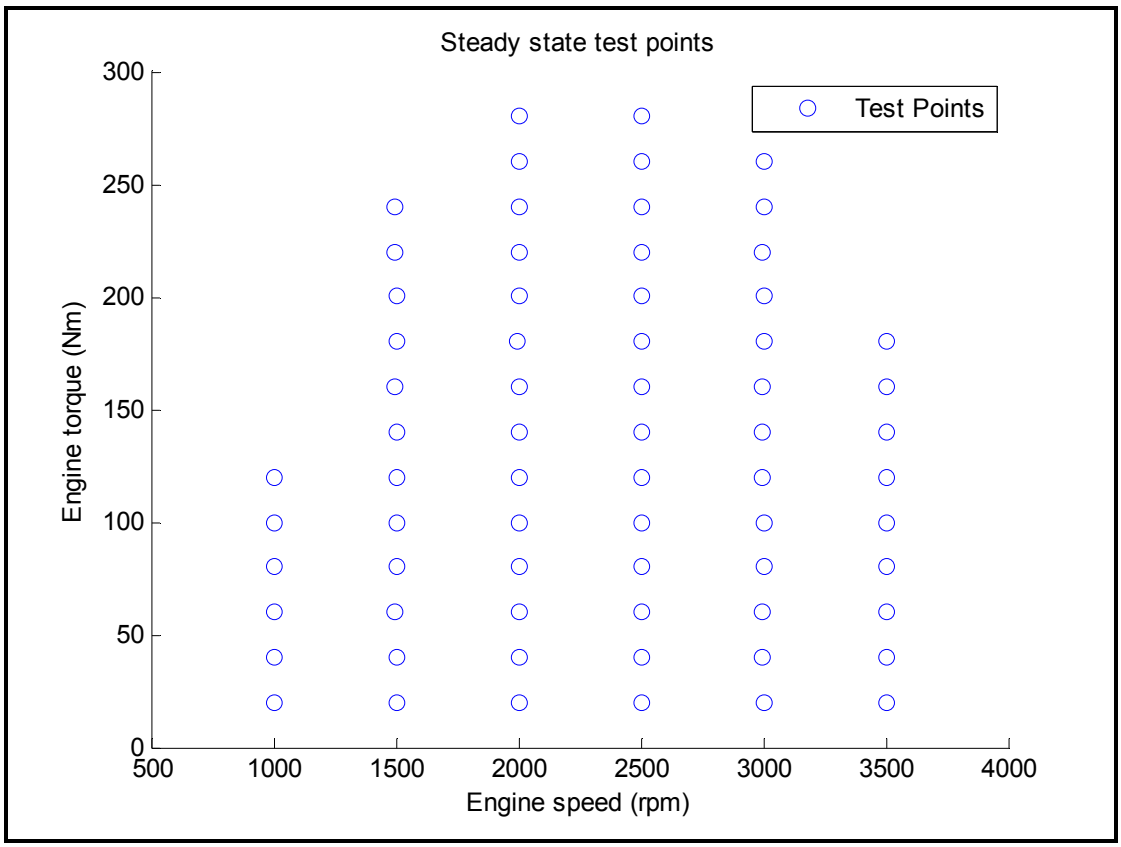

Figure 8.1 Engine steady state test points (49 points)

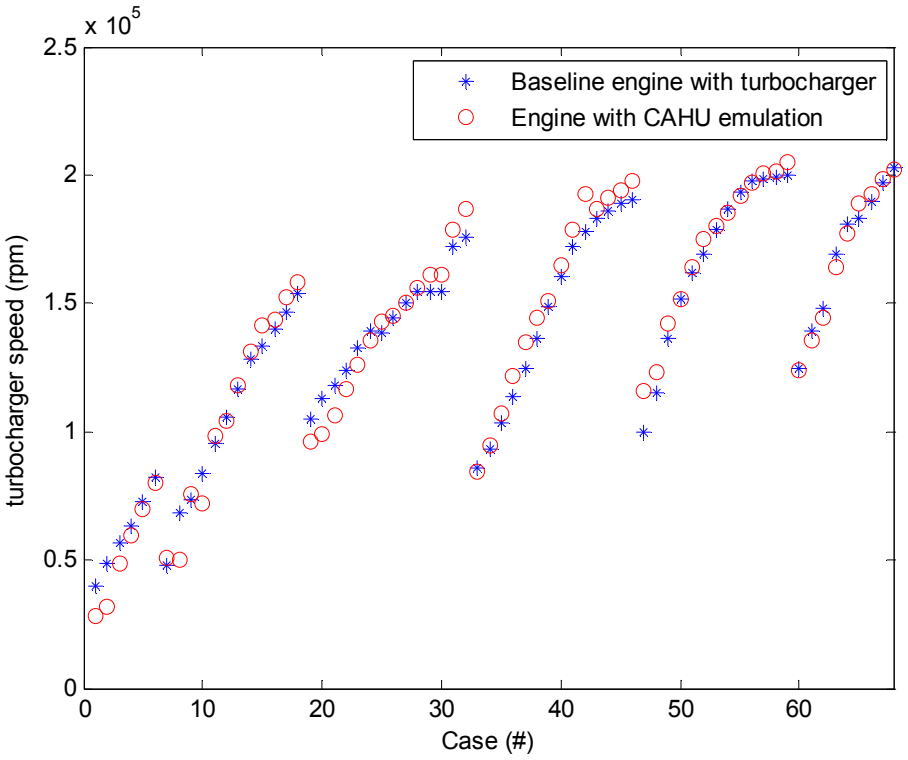

Figure 8.2 Comparison between actual turbocharger speed and emulated turbocharger speed for individual case condition

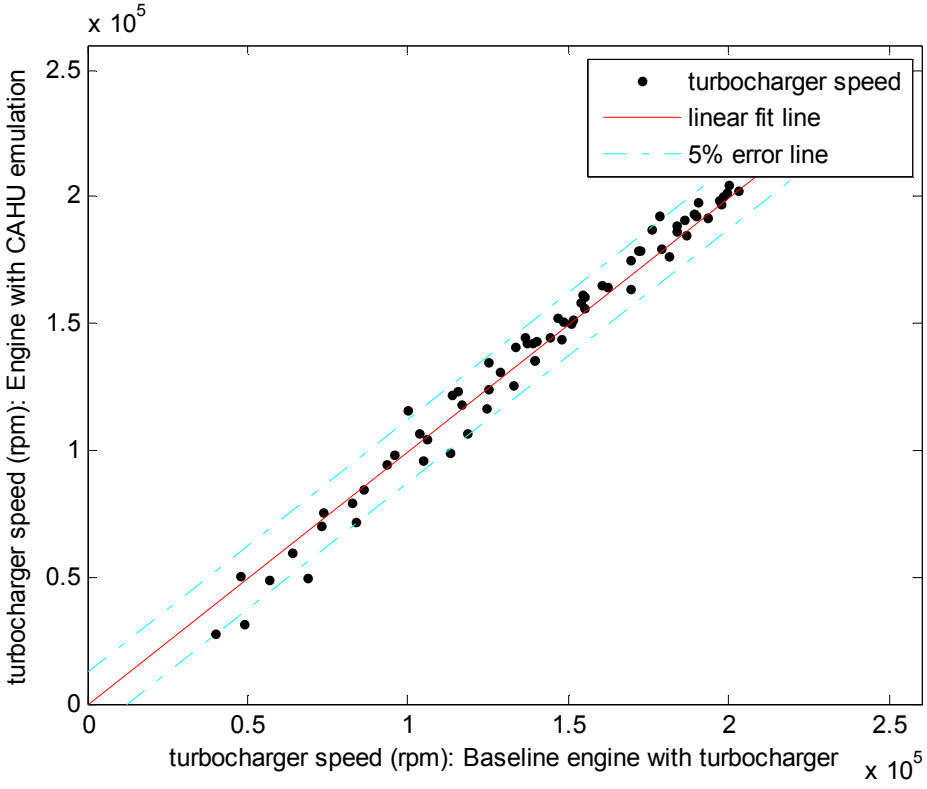

Figure 8.3 Actual turbocharger speed vs. emulated turbocharger speed

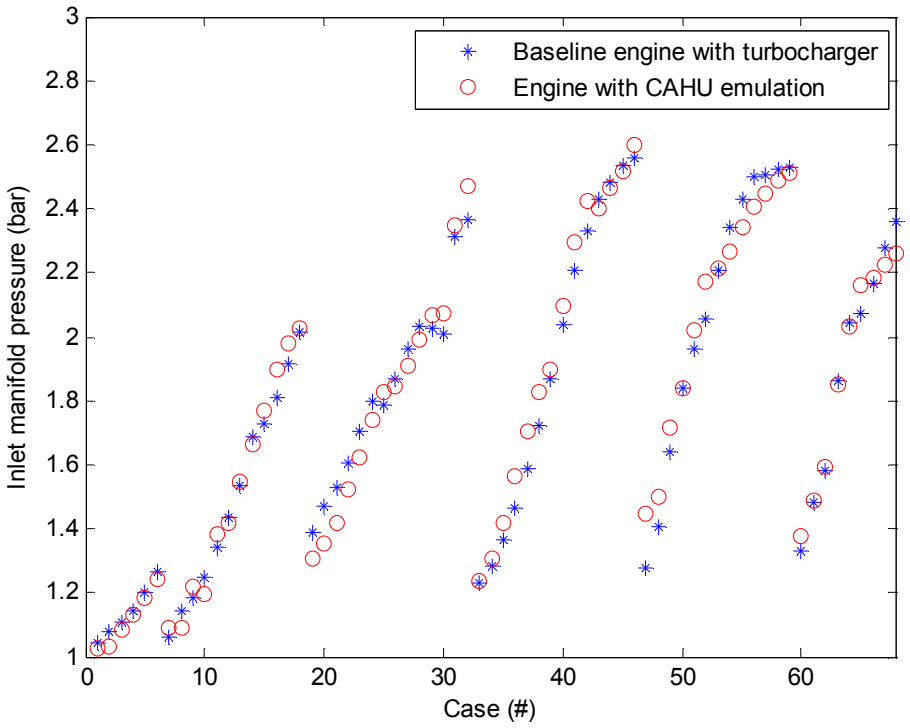

Figure 8.4 Comparison between actual boost pressure and boost pressure with CAHU emulation for individual case condition

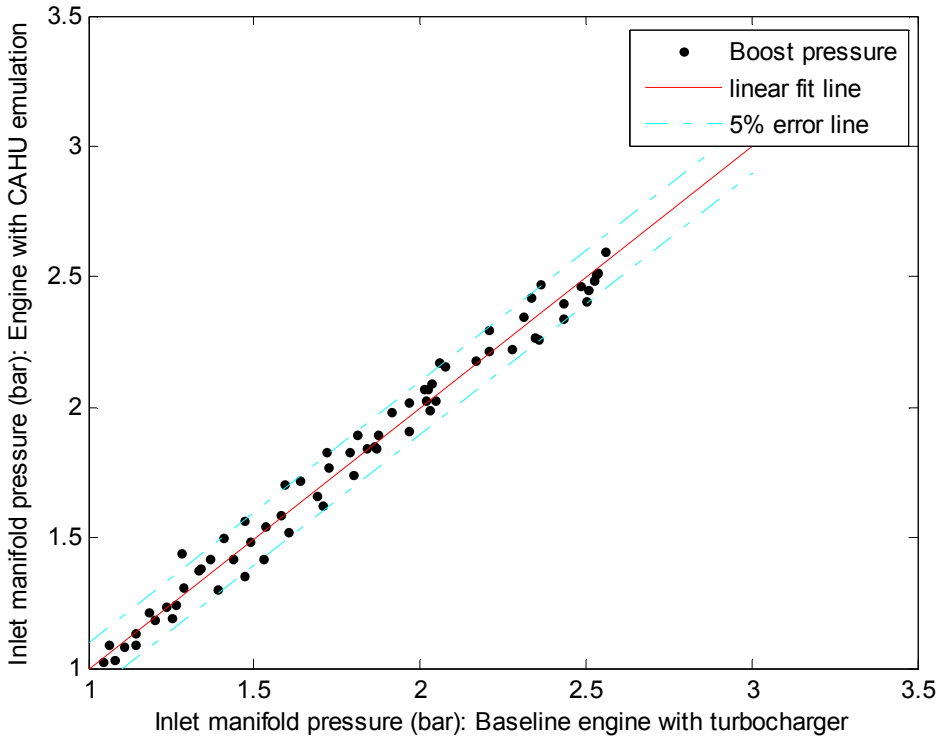

Figure 8.5 Actual boost pressure vs. boost pressure with CAHU emulation

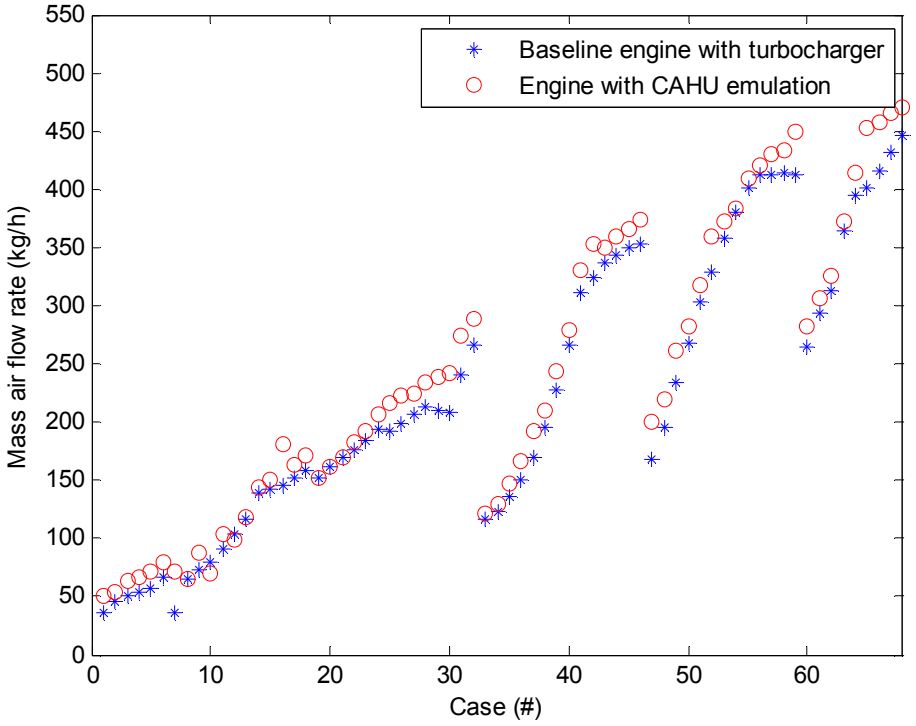

Figure 8.6 Comparison between actual air mass flow rate on the baseline engine and the mass air flow rate with CAHU emulation for individual case condition

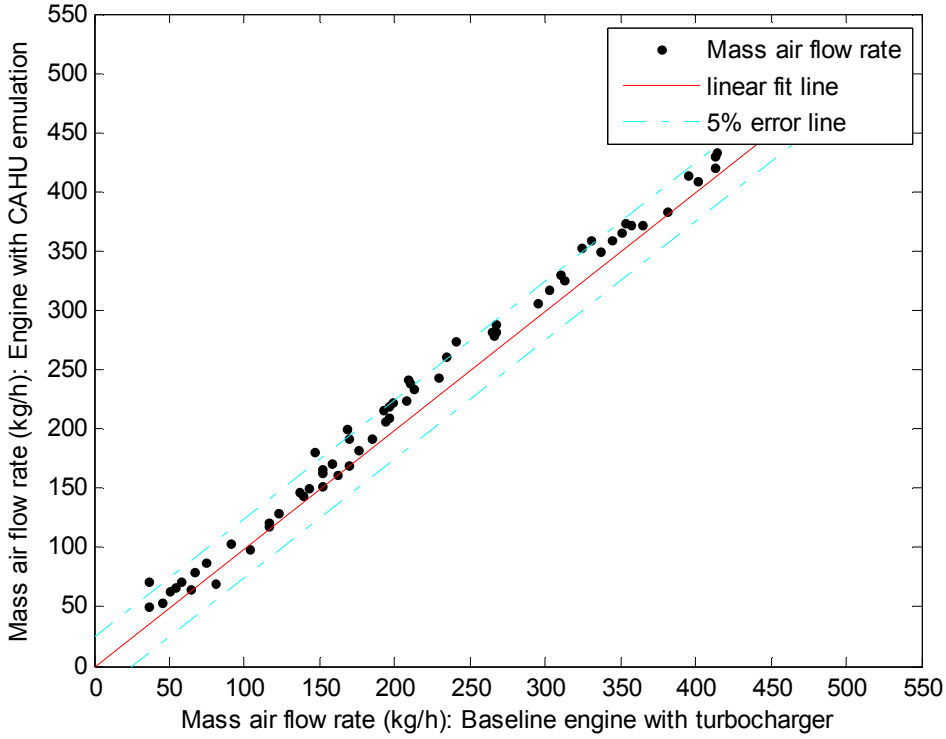

Figure 8.7 Actual air mass flow rate vs. air mass flow rate with CAHU emulation

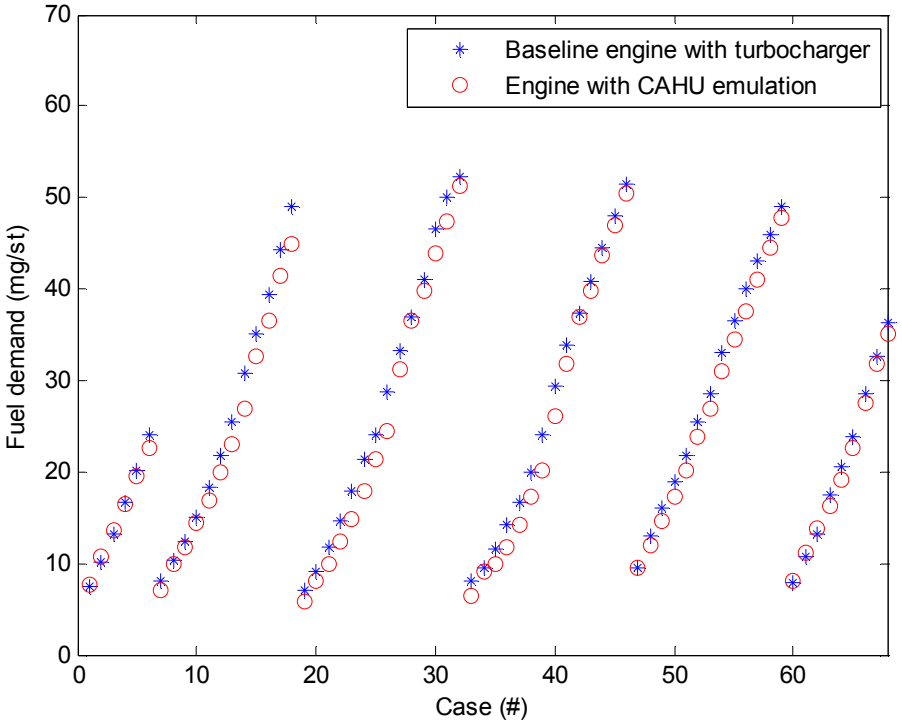

Figure 8.8 Comparison between actual fuel demand on the baseline engine and fuel demand on the engine with CAHU emulation for individual case condition

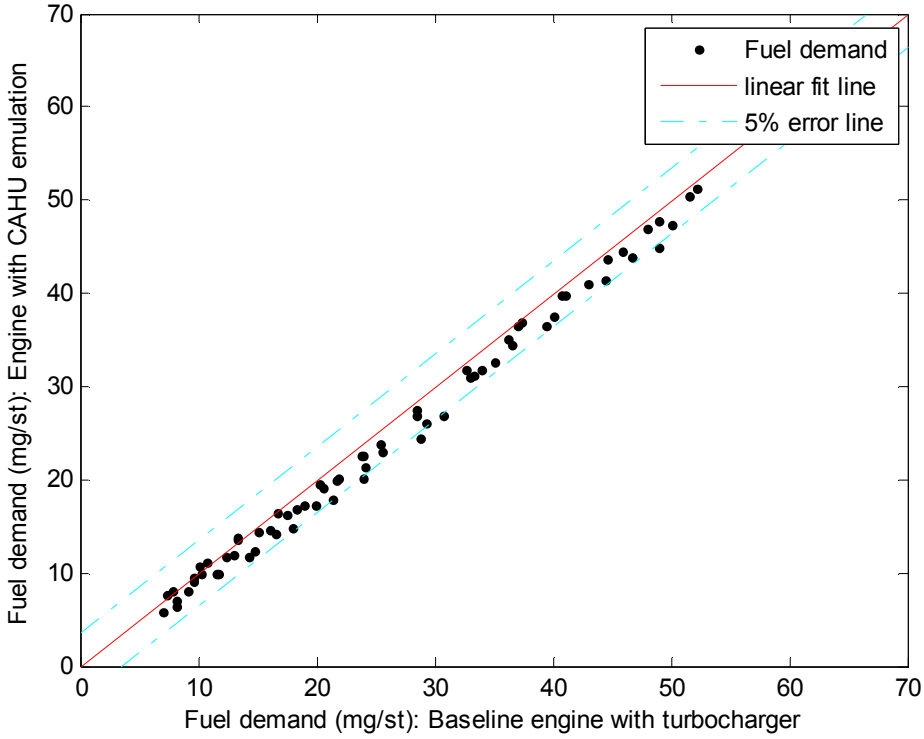

Figure 8.9 Actual fuel demand vs. fuel demand with CAHU emulation

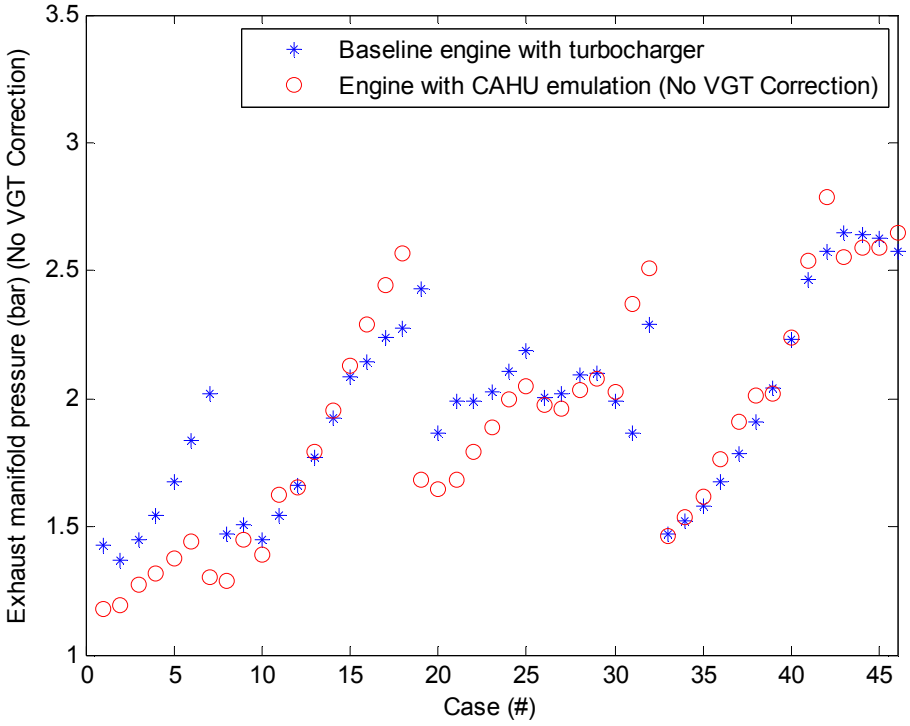

Figure 8.10 Comparison between actual back pressure and back pressure with CAHU emulation for individual case condition (no VGT correction)

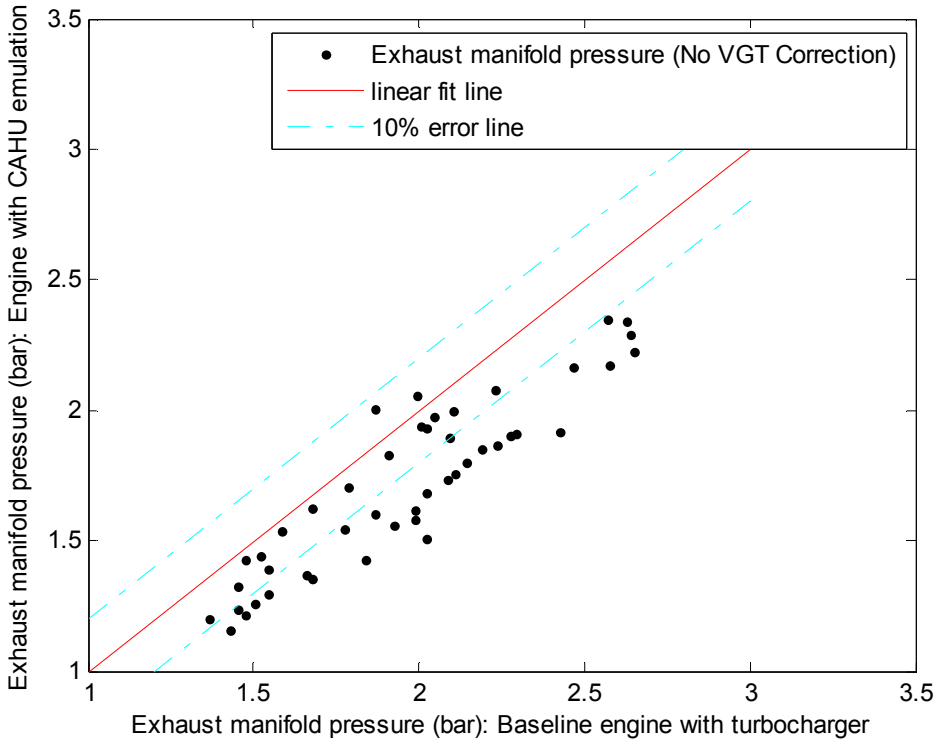

Figure 8.11 Back pressure: Actual vs. CAHU emulation (no VGT correction)

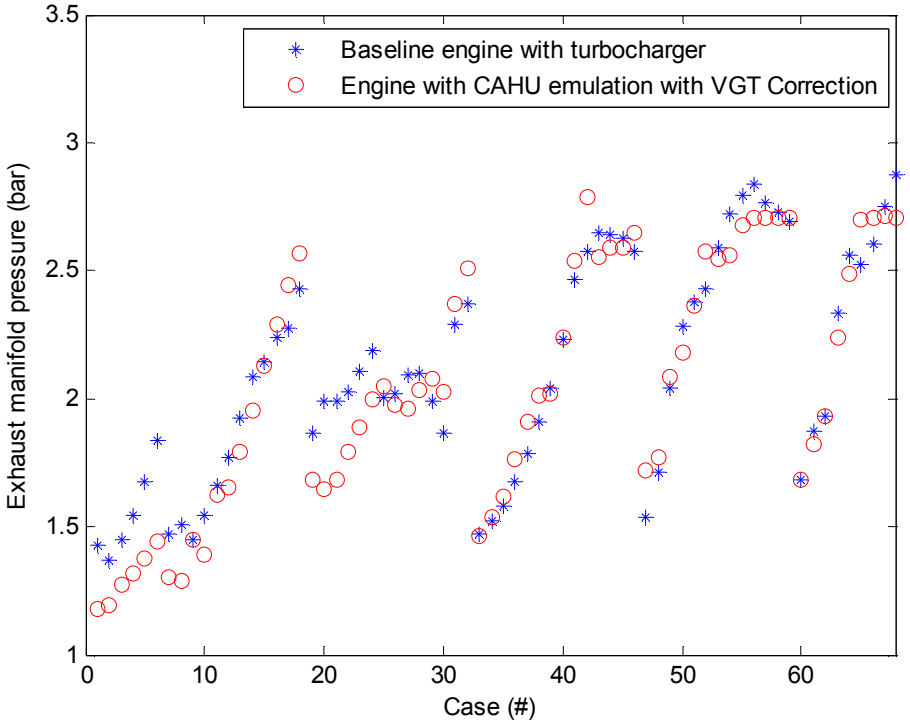

Figure 8.12 Comparison between actual back pressure and back pressure with CAHU emulation for individual case condition (with VGT correction)

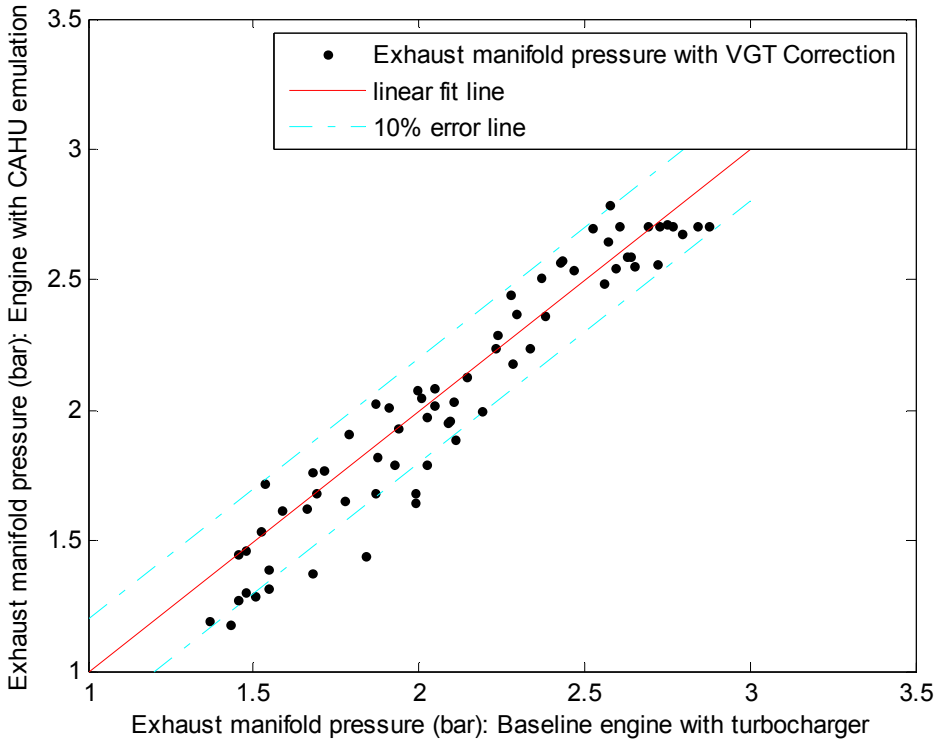

Figure 8.13 Back pressure: actual vs. CAHU emulation (no VGT correction)

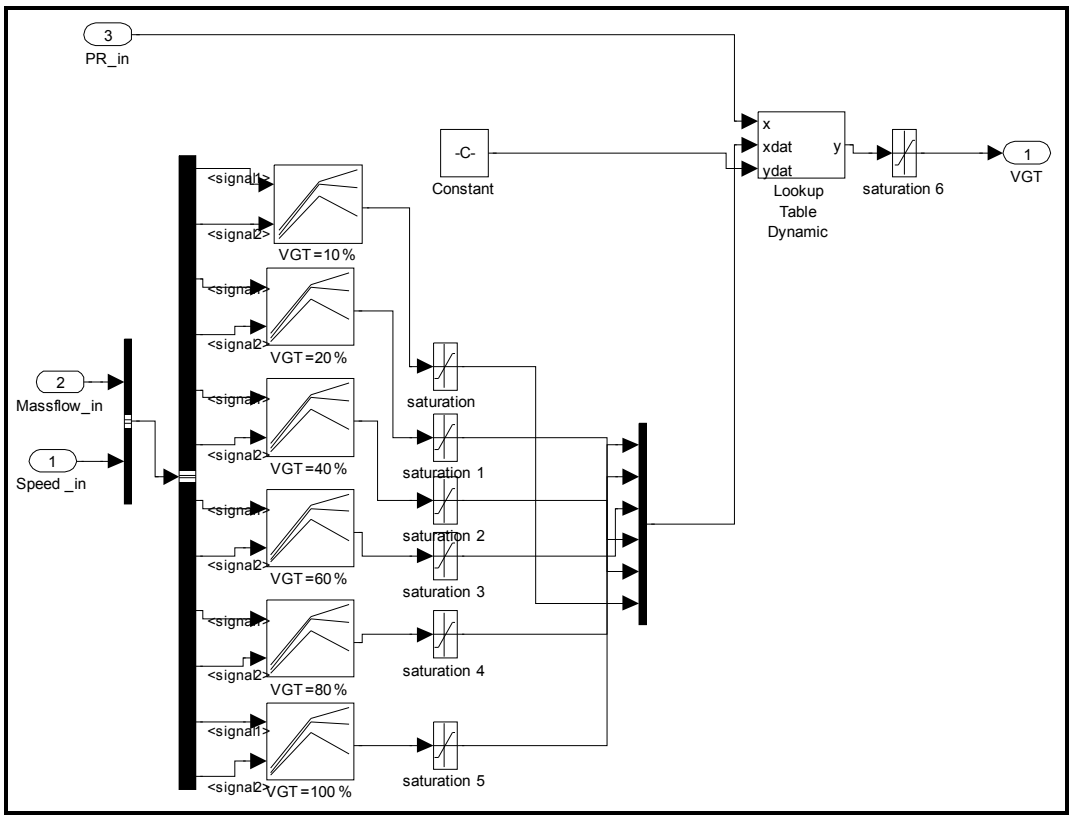

Figure 8.14 Program to calculate the physical VGT positions from engine test data

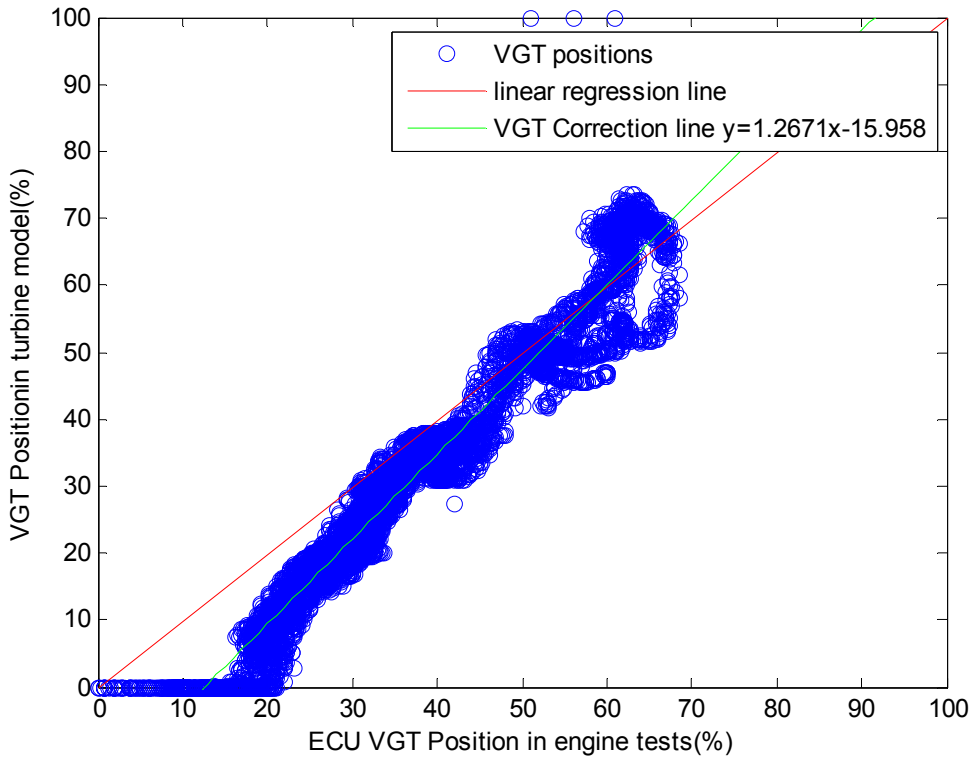

Figure 8.15 VGT in turbine model vs. VGT in ECU

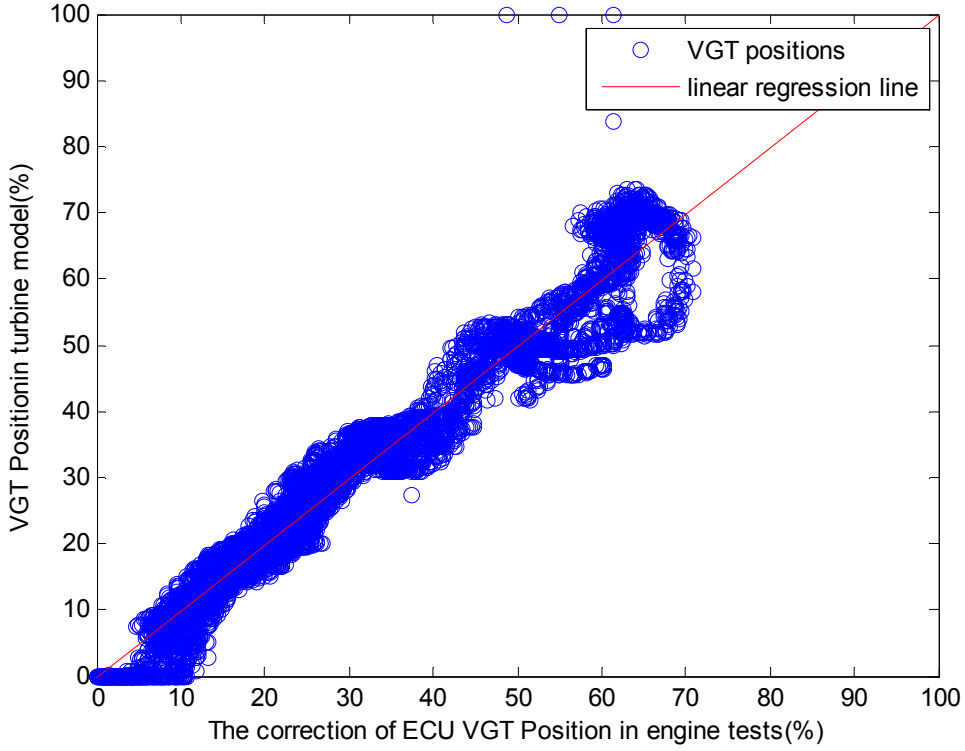

Figure 8.16 VGT in turbine model vs. Corrected VGT in ECU

Table 8.1 Variables in engine acquisition systems

Variable	**Transducer**	**Data acquisition system**	**Frequency**
Exhaust pressure (slow)	Druck 249-3959	CP CAHUt	40Hz
Exhaust pressure (fast)	Kisler 4045A	dSPACE DS2001	0.1° crank angle
Inlet manifold pressure	Druck 249-3959	CP host	40Hz
Exhaust temperature	K-type (slow & fast)	CP host	Slow 4Hz Fast 40Hz
Inlet manifold temperature	K-type	CP host	4Hz
Ambient pressure	Druck 2000	CP host	40Hz
Fuel demand	-	ECU to dSPACE	CAN bus
VGT position	-	ECU to dSPACE	CAN bus
Mass air flow	ABB Sensflow P	CP host	40Hz
Engine speed	Dyno encoder 1024 pulse/rev	CP host	80Hz
Engine torque	HBM torque flange	CP host	80Hz
Turbocharger speed	Speed sensor	CP host	40Hz

8.3 Engine test with pulsating flow simulation

From above figures (Figure 8.10 and Figure 8.11) it can be observed that without the VGT correction the emulated engine back pressure appears to be lower than the actual measured back pressure. However, even with the VGT correction, the figure of engine back pressure (Figure 8.13) shows that the emulated turbine output tends to be lower than the actual result. This difference can be explained by the underestimation from a steady flow turbine model detailed in Chapter 5. In the previous discussion, the model with pulsating flow calculation in the engine exhaust manifold contains more energy than the simplified steady flow calculation. To test this theory, a series of calculations were applied in the turbine model to re-construct the temperature and mass flow rate pulsations in terms of the measured pulsating pressure from the fast response pressure transducer (see chapter 7.2.4). Additionally, the steady state turbine model was retained but disconnect with other parts of the turbocharger model to give rise a direct comparison against the pulsation model (Figure 8.17).

In order to save the time of the experiment, an engine speed in the middle range (2000rpm) and a few different engine loads (100Nm, 120Nm, and 140Nm) were selected to test the turbine performance under pulsation conditions. In Figure 8.18,

Figure 8.19, Figure 8.20, the turbocharger speed difference between the turbine unsteady flow model and steady flow model can be observed. This discrepancy indicates that the turbine in the model with pulsating flow calculations contains more energy than the steady flow model, which testifies the theory in chapter 5.

It is also observed that with a higher engine torque the difference in turbocharger speed is greater. This can be explained that the engine exhaust flow at higher engine load contains higher energy, which results in greater fluctuations in the exhaust pressure, temperature and mass flow rate. It is therefore necessary to add the new approach to improve the accuracy of the real-time turbine model. Additionally, this cutting edge technique to construct the pulsating exhaust temperature and mass flow

rate based on the fast response pressure measurement will benefit the engine transient tests, due to its fast response in the engine gas flows.

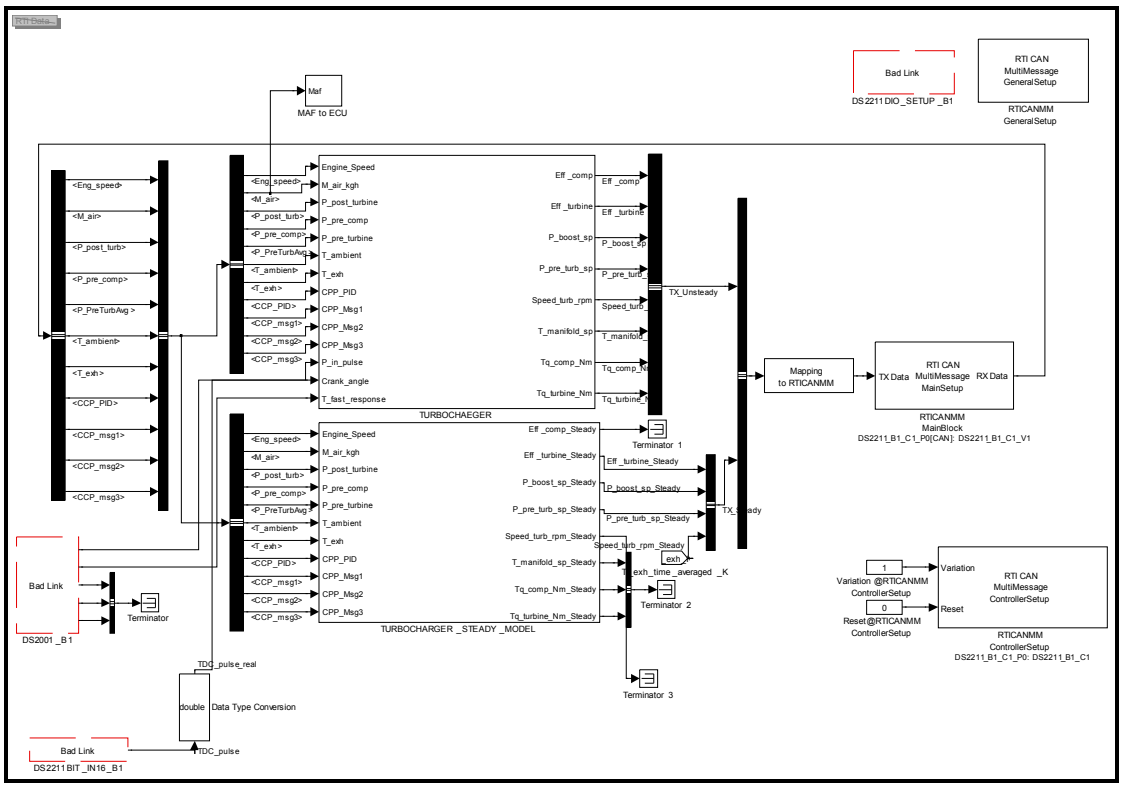

Figure 8.17 Simulink model of the real-time turbine model: steady flow vs. pulsating flow

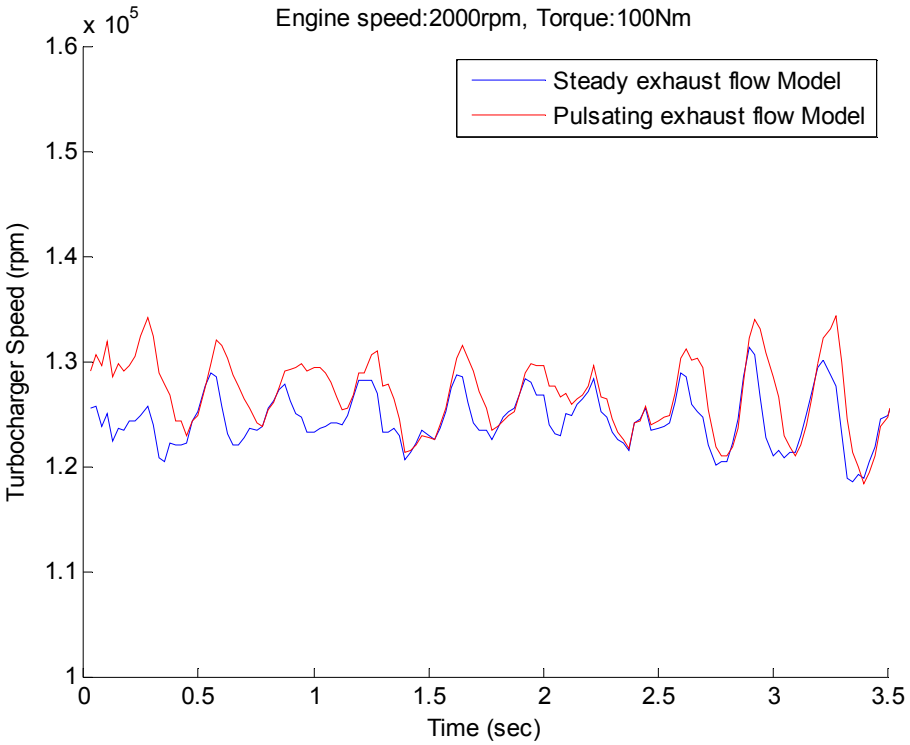

Figure 8.18 Turbocharger speed comparison between steady exhaust flow turbine model and pulsating flow turbine model at 2000rpm and 100Nm

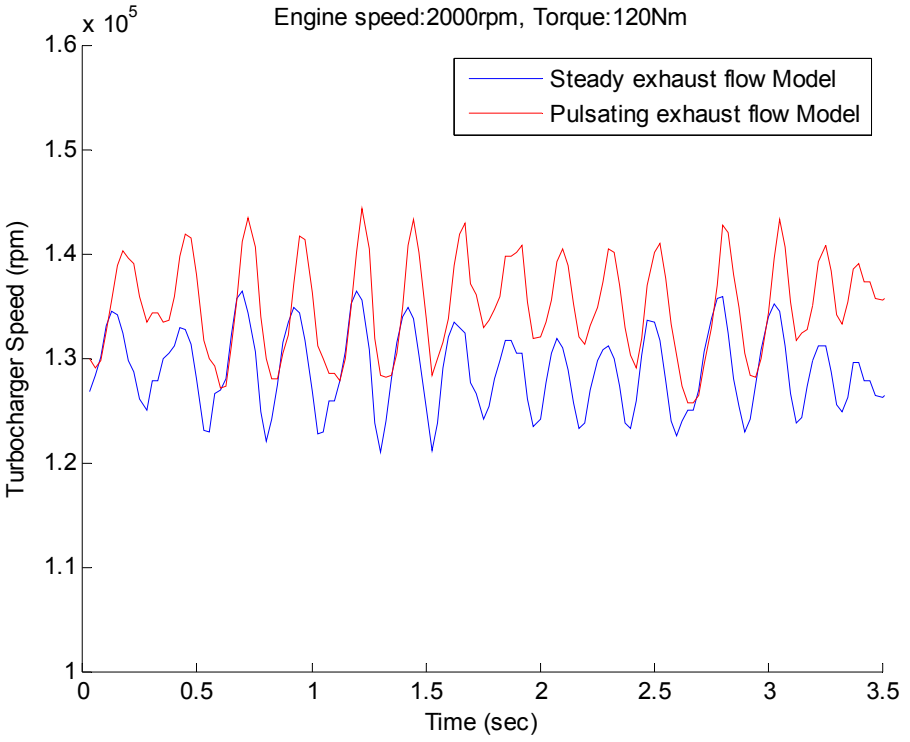

Figure 8.19 Turbocharger speed comparison between steady exhaust flow turbine model and pulsating flow turbine model at 2000rpm and 120Nm

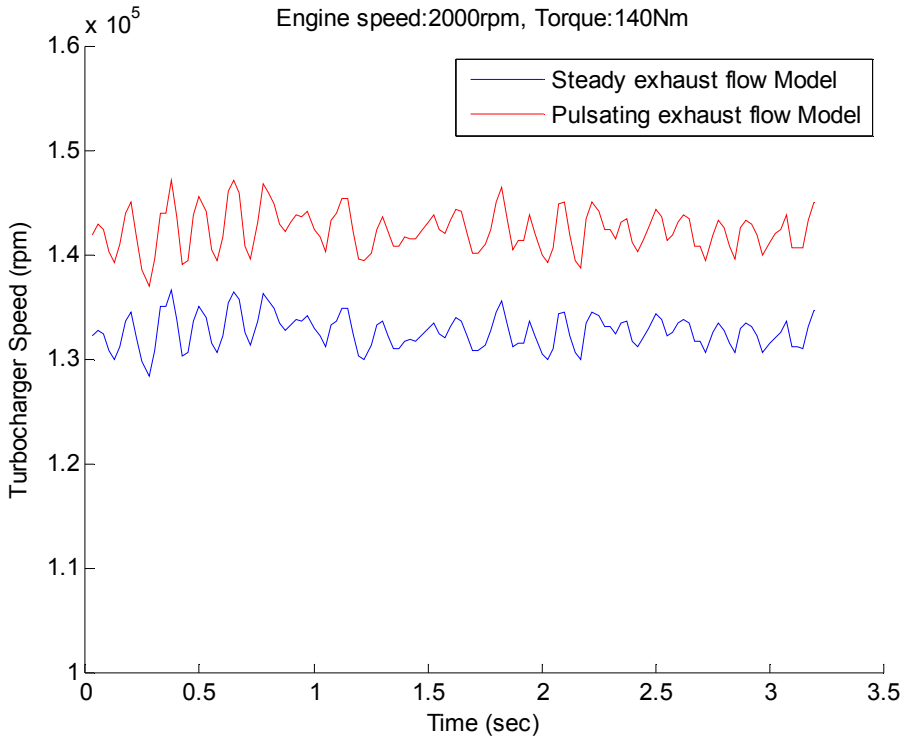

Figure 8.20 Turbocharger speed comparison between steady exhaust flow turbine model and pulsating flow turbine model at 2000rpm and 140Nm

8.4 Transient Test

8.4.1 Transient test set up

The above cases, namely, that of the steady state tests, cannot evaluate the engine transient performance which represents the vehicle responses under a sudden acceleration or a deceleration conditions. Nowadays, the transient performance is more and more important for the turbocharged diesel engine application development to minimise the acceleration delay and hence increase the vehicle drivability. It is therefore necessary to apply the tip-in and tip-out test approaches to investigate the engine performance under the sudden load increment and decrement conditions respectively.

The aim of this transient experiment is to adjust the system to let the CAHU response rapidly enough to simulate the turbocharger performance in response to the engine transient. So the turbine pulsating flow model, which allows the reconstruction of exhaust temperature and mass flow rate in the basis of measured instantaneous exhaust pressure, was applied, rather than the steady flow model.

For enhancing the test repeatability and saving the test time, an automated transient test schedule was required to be created in the CP Cadet V12 software to control the tests based on the schedule. The transient test schedule was programmed to run a tip-in test (from 10% to 100% of pedal position) and then a tip-out test (from 100% to 10% again) at the engine speed of 1500 rpm. The reason to choose low engine speed as the transient test conditions is because the engine transient performance at low engine speed and also low turbocharger speed is more important, as the engine spends significant part of its operating time accelerating from relatively low speeds in response to the vehicle transient. The engine variables such as the engine speed, torque, inlet/exhaust manifold pressures as well as temperatures, turbocharger speed, mass air flow rate, fuel demand, and etc., were recorded in the CP Cadet V12 software with a sampling time of 10 milliseconds. Consequently, it is possible to record the transient performance in a short period of time.

It must be emphasized that the tip-in test which refers to the engine acceleration is more important in the engine transient development, so that the tip-in test results will be mainly discussed in the following sections.

8.4.2 Experimental results and analysis

The engine transient performance is shown in four figures:

a. Engine torque (Figure 8.21)

b. Engine inlet manifold pressure (Figure 8.22)

c. Engine exhaust manifold pressure (Figure 8.23)

d. Turbocharger speed (Figure 8.24)

Figure 8.21shows that the torque of the engine with CAHU emulation respond fast enough to catch torque transient in the baseline engine. Since the tip-in starts from the 2nd second, the 0.5 second after the transient start (2s to 2.5s) is the response of the fuel demand increase from the ECU. It is also observed that there is a small delay on the torque line starting from 2.5s to 4s timeline wise, which is about half second after the good response at start of the transient (2s). This is caused by the boost pressure and back pressure delay at the same time which can be noticed in Figure 8.22 and Figure 8.23. Figure 8.24 also shows the same response on the turbocharger speed curve. This is due to the over correction from the CAHU control system.

When the engine receives the pedal position signal change from 10% to 100%, a sudden increment of fuel demand in the ECU is provided. So a high energy release is generated by the combustion, and it also results in the sudden rise in the back pressure and thus the boost pressure, which is delivered by the turbocharger. However, when the engine is connected with the CAHU to emulate the air charge and discharge from the turbocharger model, the CAHU control system tries to correct this sudden change on both the boost pressure and back pressure by opening the pressure control valve. This pressure correction phenomenon will result in the slow response of the torque

curve due to the lack of boost pressure. It is therefore required to design a new advanced control system in the future to allow the CAHU to improve the performance in the engine transient tests without any overcorrection. Since the current PID control system encounters a trade-off between the fast response which is essential to match the engine transient performance and the problem caused by the overreaction when the engine condition varies. Alternatively, other than re-designing the CAHU control system, other modifications such as a fixed exhaust back pressure valve (EBPV) position or different PID numbers as well as the improvements will be discussed in chapter 8.5.

The back pressure in Figure 8.23 shows a rapid response from CAHU emulation to match the baseline engine back pressure transient. However, in Figure 8.21, a discrepancy on the torque curves after the time of 4^{th} second can also be observed which is due to the lack of power in the turbocharger and hence impacts the engine boost (Figure 8.22 and Figure 8.24). In order to solve this problem, a higher boost pressure via restricting the exhaust pressure valve opening can be achieved to therefore increase the engine torque (figure 8.25, 8.26, and 8.27). Moreover, the turbocharger speed in the CAHU emulation also shows an agreement with the baseline engine result (Figure 8.28). However, the drawback of this method to cause the system instability can also be observed in the boost pressure curve (figure 8.26) Consequently the modifications and the improvements on both the hardware and the software, which allow the system to response rapid enough to match baseline engine transient without sacrificing the system stabilities will be discussed in the next section.

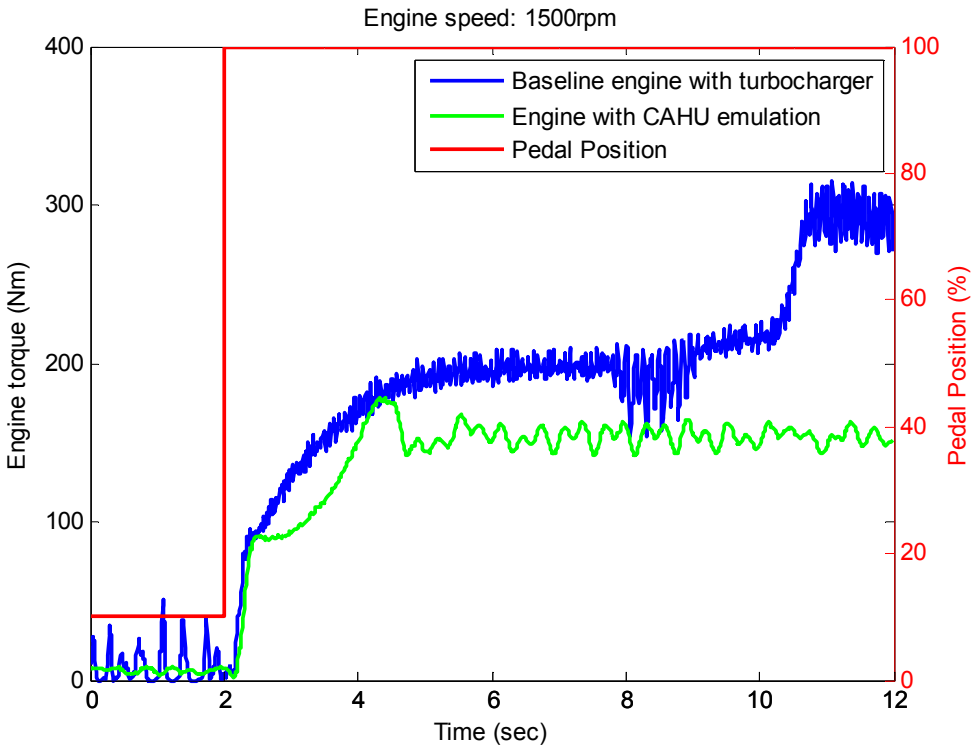

Figure 8.21 Comparison of engine torque between the baseline engine and engine with CAHU emulation in the tip-in test

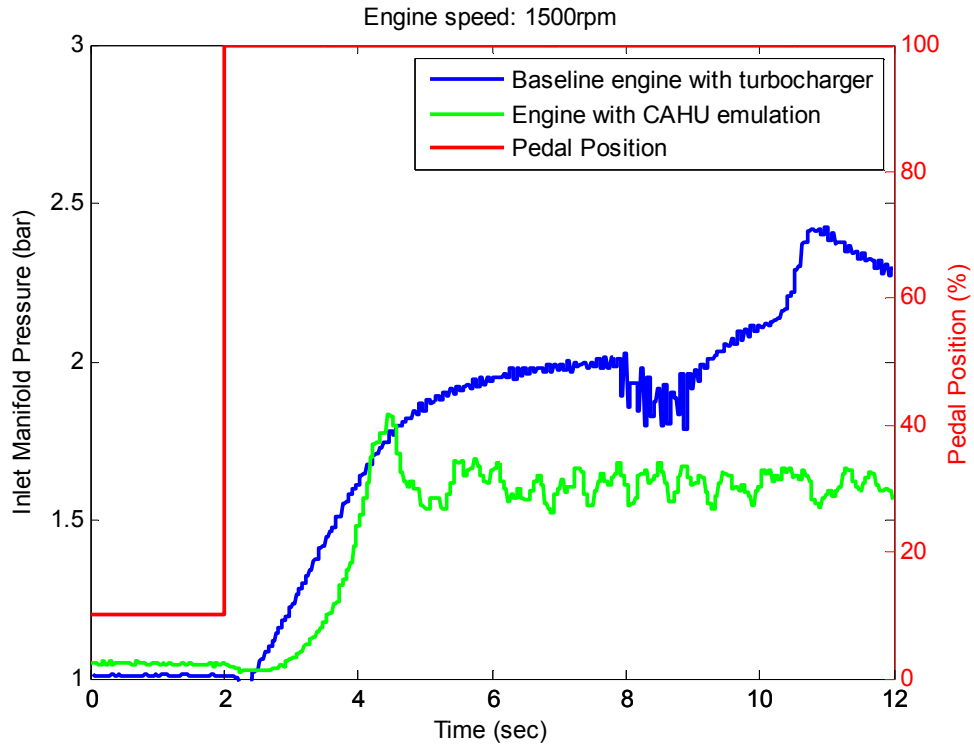

Figure 8.22 Comparison of boost pressure between the baseline engine and engine with CAHU emulation in the tip-in test

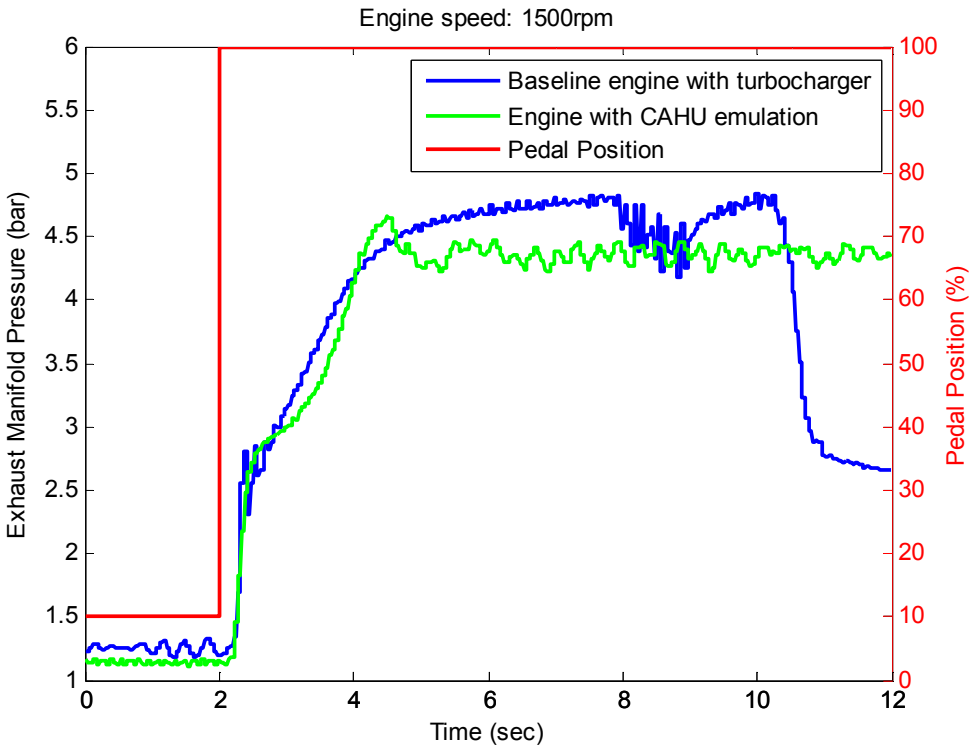

Figure 8.23 Comparison of the exhaust manifold pressure between the baseline engine and engine with CAHU emulation in the tip-in test

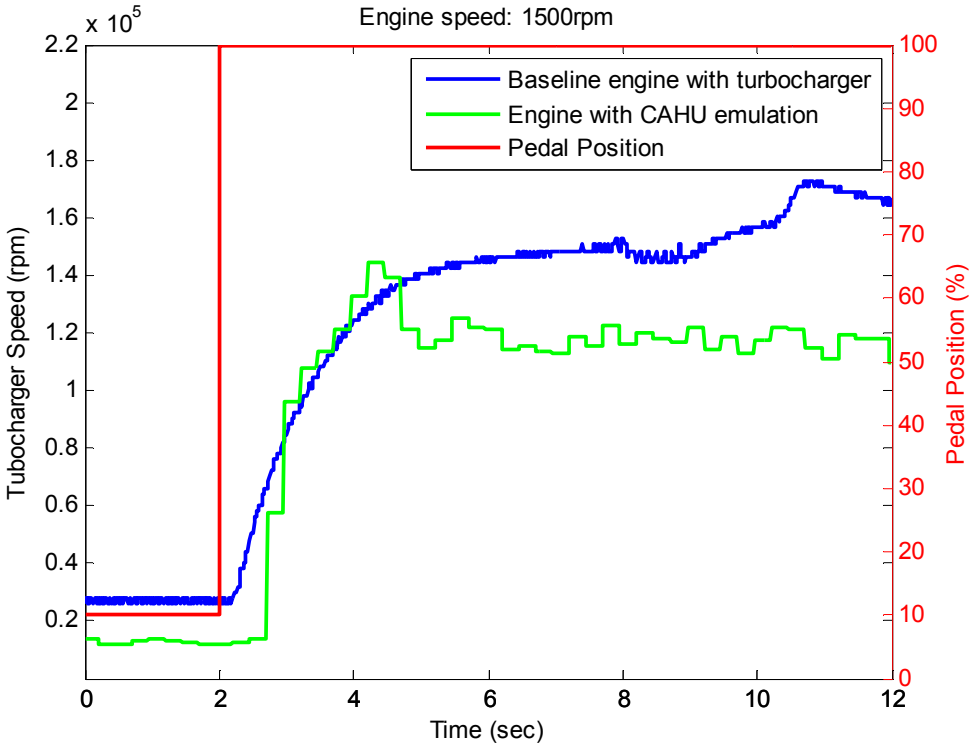

Figure 8.24 Comparison of the turbocharger speed between the baseline engine and engine with CAHU emulation in the tip-in test

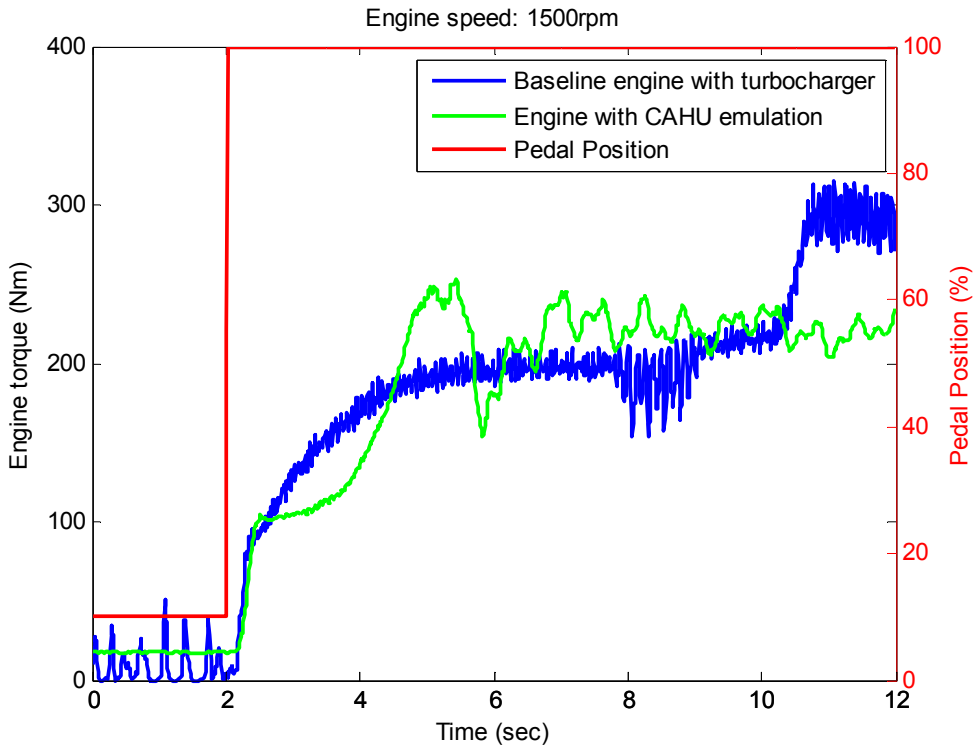

Figure 8.25 Engine torque in transient tests with less EBPV opening

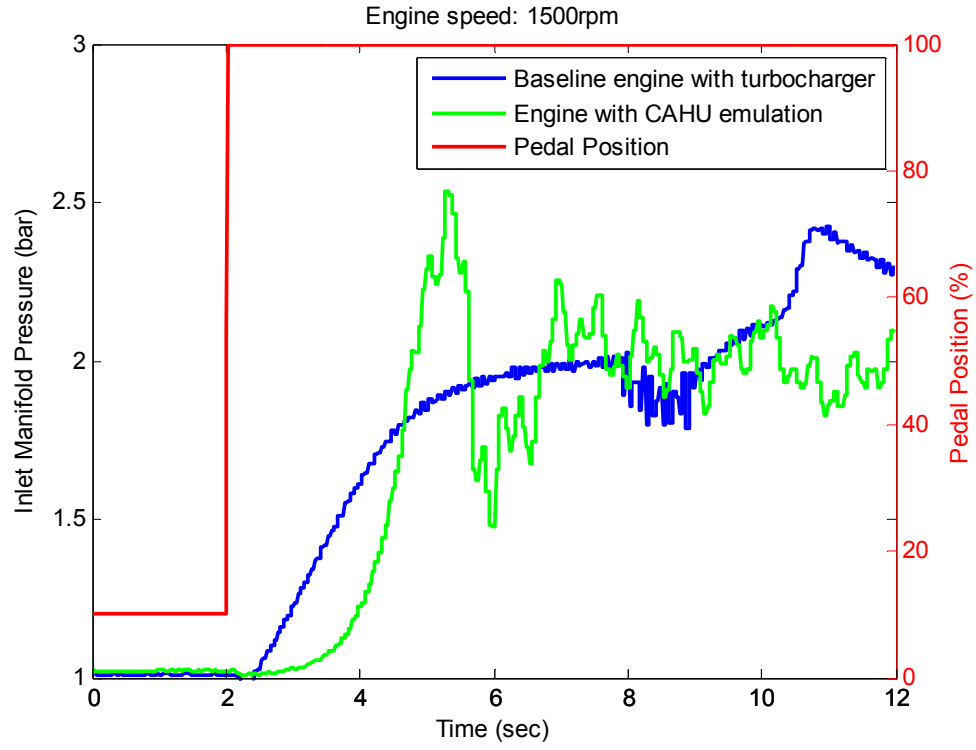

Figure 8.26 Engine boost pressure in transient tests with less EBPV opening

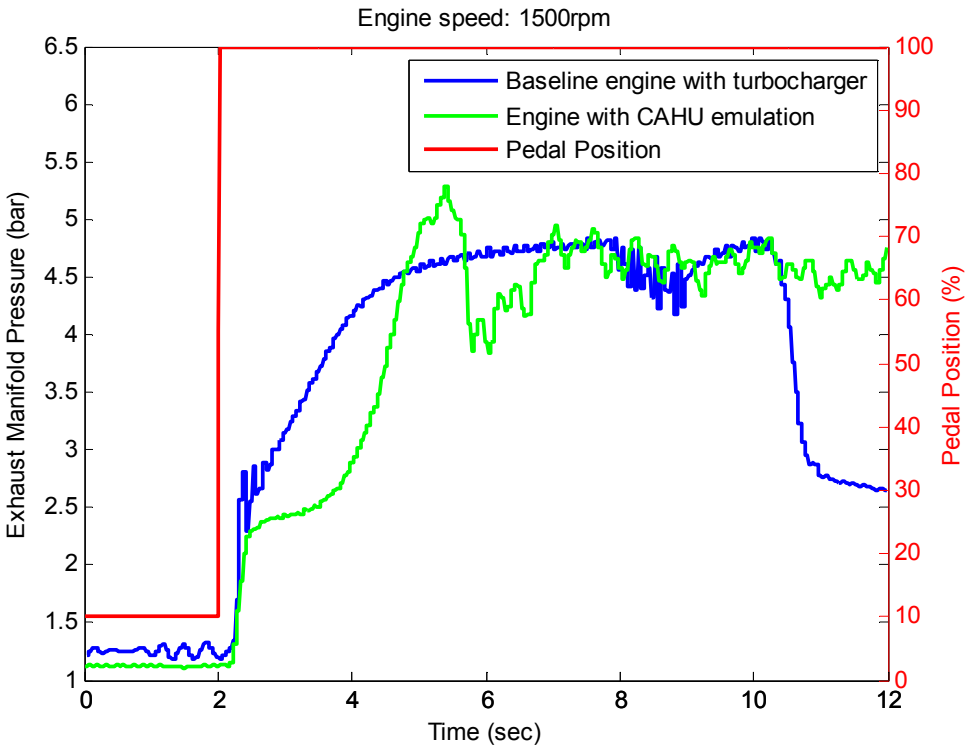

Figure 8.27 Engine back pressure in transient tests with less EBPV opening

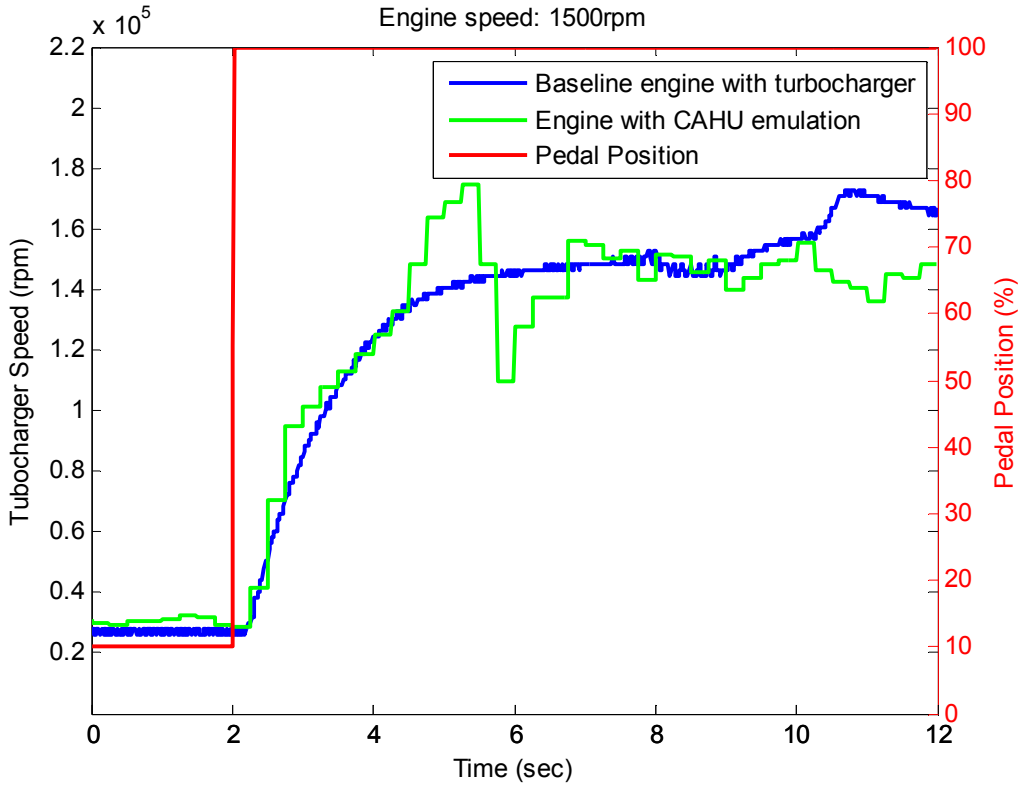

Figure 8.28 Turbocharger speed in the transient tests with less EBPV opening

8.5 System Modifications and improvements

8.5.1 Hardware modifications

By comparing figure 8.10 and figure 8.23, it can be observed that the exhaust pressures in the transient test are much higher than the pressures in the steady state test. There are two possible factors might cause this huge pressure difference:

a. Different VGT position demands from the ECU strategies when the engine operates under the steady state and the transient conditions

b. The rapid energy increment in the exhaust gas that builds up high pressures via passing through a tight nozzle due to the low response at the turbine entry.

Since the aim of the transient tests is to let the CAHU response to catch the engine transient performance, the CAHU system is required to achieve the high back pressures under transient conditions. Subsequently these two factors need to be considered, and the modifications of the hardware or the real-time model should allow the system to operate without adding any extra fluctuations to cause the system instability. However the impact from the first factor needs not be concerned due to the fast VGT position signal transmission from the ECU to the real-time turbocharger model through the CAN bus. The ECU signals can be received with a minimum delay to provide an accurate VGT position in the transient tests. On the other hand, the second factor appears to cause the system instability. Because during the transient tests, when the actual exhaust manifold pressures exceed emulation outputs in the real-time turbine model in terms of the turbine characteristics from the maps, the control system of the CAHU will try to reduce the pressure by opening the pressure control valve, which will cause the system instability from the hardware (exhaust pressure control valve) point of view.

One solution with regard to this problem is to design an advanced control system to let the pressure exceed the limit of the turbine map outputs. However due to the complexity of the control system and the safety issue that the high pressure may

damage the engine exhaust manifold or the turbine blades, a simple solution of reducing the speed of the exhaust pressure control valve response or even fixing the positions of the pressure control valve in some extreme cases was applied during the tip-in tests. It is achieved by adding a rate limiter to limit the valve opening from reducing or manually fixed the exhaust pressure valve position in the CAHU control program (CP Cadet).

The comparison of the engine exhaust pressure between the original system and the modified back pressure control system is shown in Figure 8.29. It is observed that the new system can build up the pressure to the required values without causing extra pressure fluctuations. However, it is also noticed that the system still contains a gas flow fluctuations due to the system instabilities. Hence the improvements from the software point of view are required to be considered, and the system modifications as well as the subsequent experimental results are discussed in the next sections.

Although the change on the exhaust back pressure valve control system is testified to achieve higher pressures, it is also suggested that in the future testing facilities development, a new mechanism of the valve controlling system via a double-cable pulley might improve the accuracy of the back pressure emulation without causing the system instabilities.

8.5.2 Software modifications

In the real-time turbocharger model, the turbine model appears to be more likely to cause the system instabilities. Because in the turbine map, the characteristics between the turbine pressure ratio and the mass flow rate at different VGT positions (Figure 8.31) shows that the pressure ratio gradients are quit small in the high pressure regions, and hence the pressure is very sensitive with the change of mass flow rate. As a result, the turbine model outputs based on the turbine map tends to give rise to a huge variation, when a small change of gas mass flow is sent to the map even due to

the normal measurement fluctuations in the pulsating exhaust flow. On the other hand, the maps in the compressor characteristics show nothing like the trends in the turbine maps. Consequently, the turbine model stability is more important than the compressor's, and it is therefore necessary to add extra mode to stabilize the turbine model without slowing the transient response.

Signal damper

Since the inputs of the real-time turbocharger model are from the measurement, the stability in the inputs needs to be satisfied before feeding to the turbocharger model. Subsequently, signal dampers from the transfer function model in the Simulink toolbox are integrated into the model to prevent the software instabilities (see the red modules in Figure 8.30). This modification would reduce the fluctuation on the model inputs from the measurements such as mass air flow, exhaust manifold pressure, and the boost pressure.

Model output rate limiter

Although the dampers from the Simulink help to improve the system stability, the subsequent drawbacks can be predicted in terms of the delay from the dampers to cause the slow response especially in the transient tests which require the system to response as fast as possible. Therefore, another method to reduce the system fluctuation without sacrificing the speed of the system response is required to be developed.

The rate limiter model in the Matlab/Simulink tool box can block the first derivative of the signal passing through it by setting a rate limit. The rate is calculated in equation 8.1

$$rate = \frac{u(i) - y(i-1)}{t(i) - t(i-1)} \tag{8.1}$$

Where $u(i)$ and $t(i)$ are the current block input and time, and $y(i-1)$ and $t(i-1)$ are the output and time at the previous step.

If the rate of the signal is greater than the specified rising slew rate (R), the output of the rate limiter is calculated as:

$$y(i) = \Delta t \cdot R + y(i-1)$$

On the other hand, if the rate of the signal is lower than the specified falling slew rate (F), the output of the rate limiter is calculated as:

$$y(i) = \Delta t \cdot F + y(i-1)$$

If the rate is between R and F, the output is equal to the input.

$$y(i) = u(i))$$

So during the tip-in tests, the falling slew rate value can be specified in the rate limiter to prevent the pressure drops due to the system fluctuation. On the contrary, a rising slew rate can be set to conduct the tip-out tests. This method allows the system to achieve high back pressure and eliminate the fluctuation generated by the turbine maps.

Fast temperature measurement

In the previous analysis in Chapter 5, the real-time turbocharger model operates in conjunction with a reconstruction of the exhaust temperature and mass flow rate in terms of the measured pressure pulsation. Although the temperature pulsation can be calculated by a given measured temperature, the slow response of the exhaust temperature measurement from a normal thermocouple tends to restrict system to match the baseline engine transient performance (Figure 8.32). A fast response temperature measurement is therefore necessary to be applied in the engine system.

As the fast response thermocouple is detailed in chapter 7.25, the description of the measurement can be neglected and the experimental results to compare the difference

of the system transient performance between the slow and fast temperature measurements.

Mass air flow signal to ECU

The mass air flow signal from the engine embedded MAF sensor is disabled, since the MAF sensor in the air box cannot operate under high boost and high temperature conditions, when the engine is connected with the CAHU. Therefore another mass air flow sensor (ABB Sensyflow P, see chapter 7.2.3) is fitted in the engine inlet manifold to measure the boost pressure and control the CAHU based on the set points from the real-time turbocharger.

Compared with steady state tests, since the engine ECU (engine control unit) can receive the real mass air flow signals, the EGR valve control system was enabled, and the VGT control is more accurate in the transient tests. As a result the CAHU (charge air handling unit) can operate to allow the engine achieve the baseline engine performance with the virtual turbocharger emulation. This can be observed in Figure 8.21, that the engine torques from the transient tests with the CAHU emulation responded fast enough to match the engine torque curve under the baseline transient tests.

New control system on CAHU

In the CAHU system, a PID (proportional–integral–derivative) control algorithm is applied to control the gas pressure and temperature in engine air charging and discharging. A PID controller calculates an "error" value as the difference between a measured process variable and a desired setpoint. The controller attempts to minimize the error by adjusting the process control inputs.

The PID controller calculation (algorithm) involves three separate parameters; the proportional, the integral and derivative values. The proportional value determines the

reaction to the current error, the integral value determines the reaction based on the sum of recent errors, and the derivative value determines the reaction based on the rate at which the error has been changing [101]. By tuning the three constants in the PID controller algorithm, the controller can provide control action designed for different tests to have a minimum error and system oscillation without sacrificing the system responsiveness.

In the transient tests, the PID controllers for the exhaust and boost pressure were tuned to give the best response of the turbocharger in the engine transient. Figure 8.34 gives the comparison of exhaust pressure in the CAHU system for different PID settings. PID-1 controller has a P: 0.016, I: 0.08 & D: 0.0075 and PID-2 controller has a P: 0.005, I: 0.025, & D: 0.0075. It can be observed that PID-1 has a slow response and higher system oscillation. On the other hand PID-2 controller gives a fast response and more stable condition at the engine exhaust gas flow. Although tuning the PID constants' values at different engine conditions can help the CAHU to reduce some system oscillation, an advanced control system for the CAHU to apply for all engine operating points will be necessary to be designed in the future.

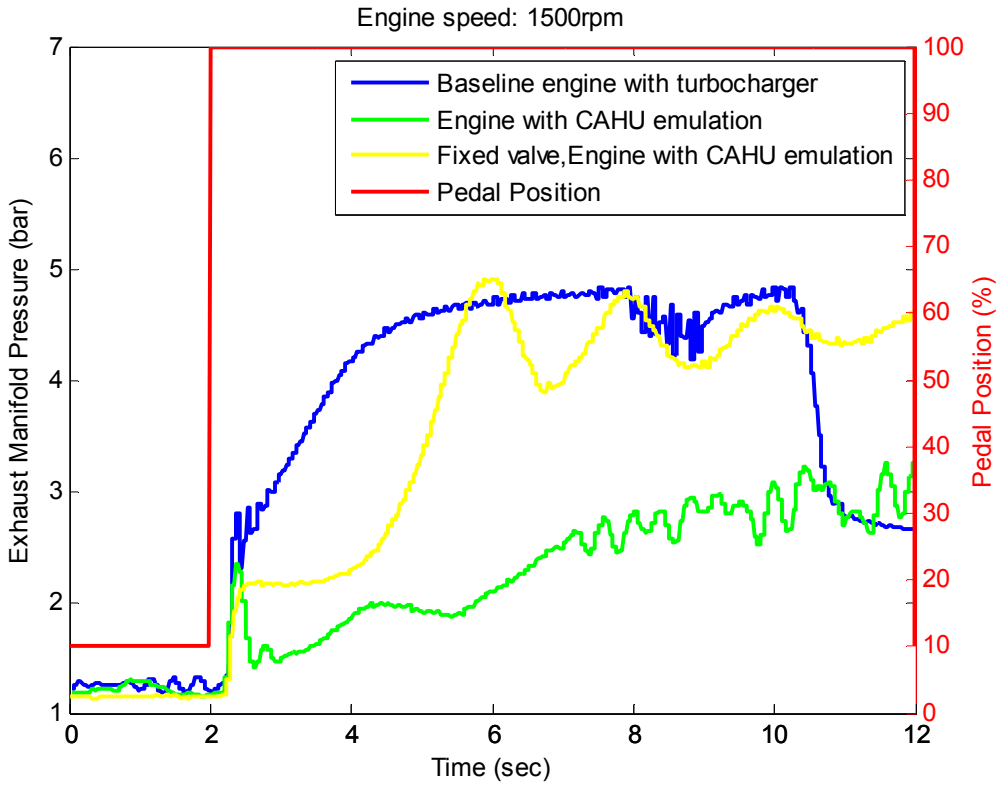

Figure 8.29 Comparison of the exhaust manifold pressure between the fixed exhaust valve position and original model in the tip-in test:

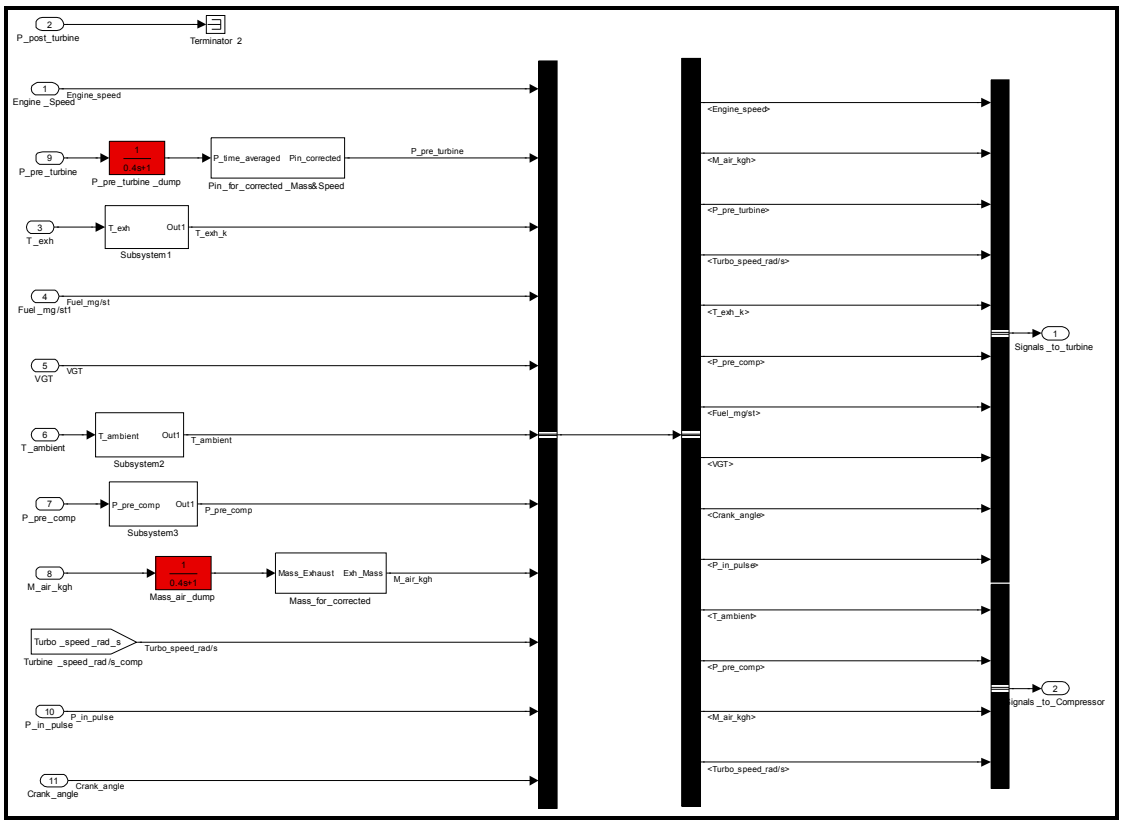

Figure 8.30 Input module in the turbocharger model

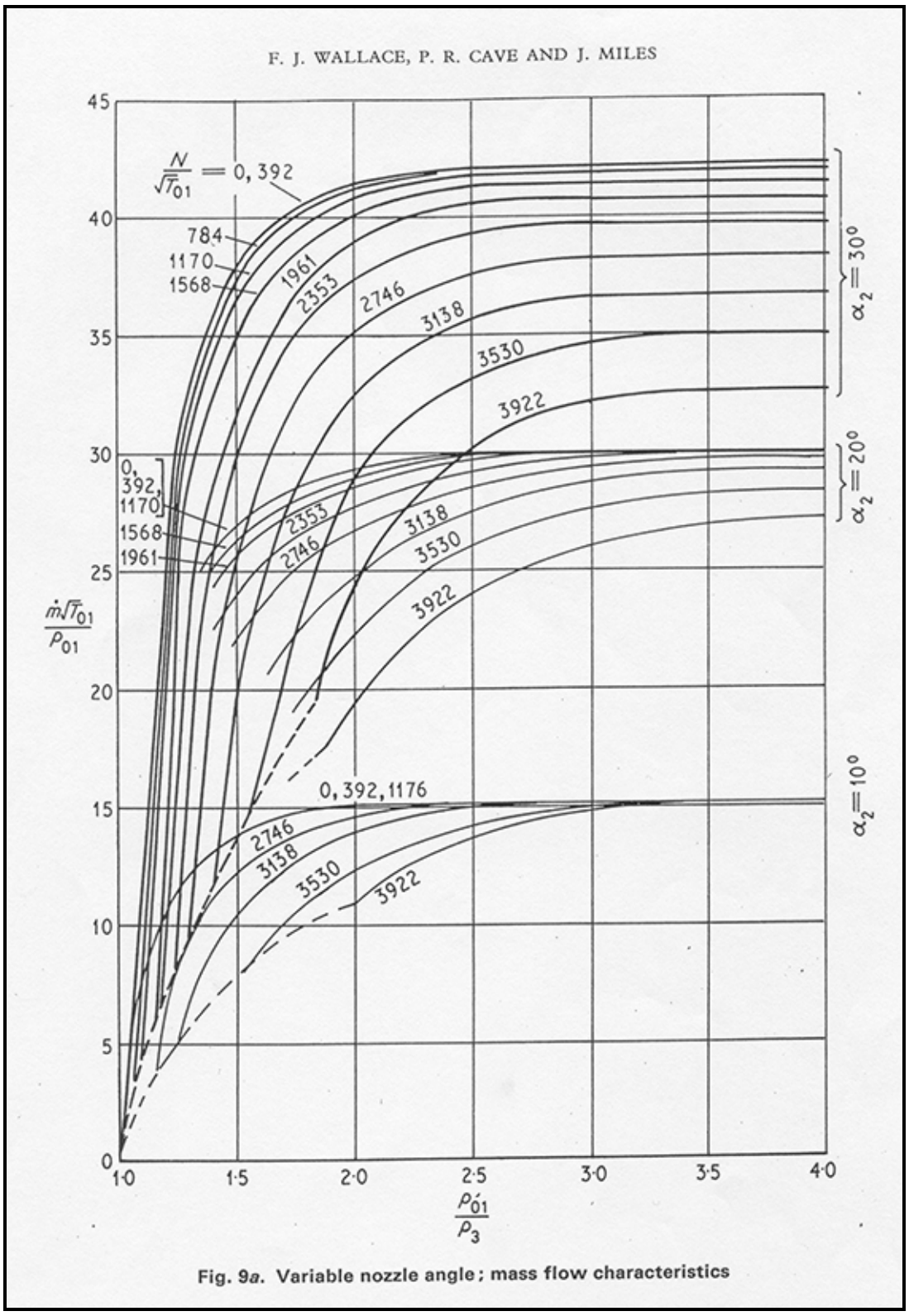

Fig. 9*a*. Variable nozzle angle; mass flow characteristics

Figure 8.31 Turbine characteristics: mass flow rate vs. pressure ratio at different turbocharger speeds [35]

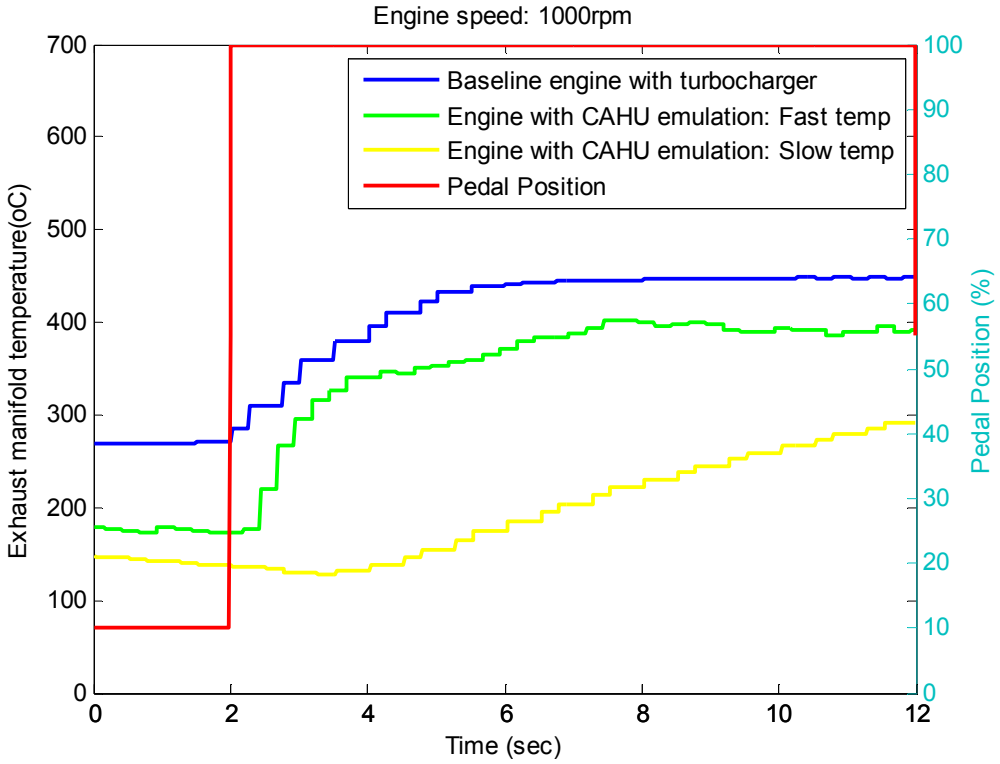

Figure 8.32 Exhaust temperature: fast measurement vs. slow measurement

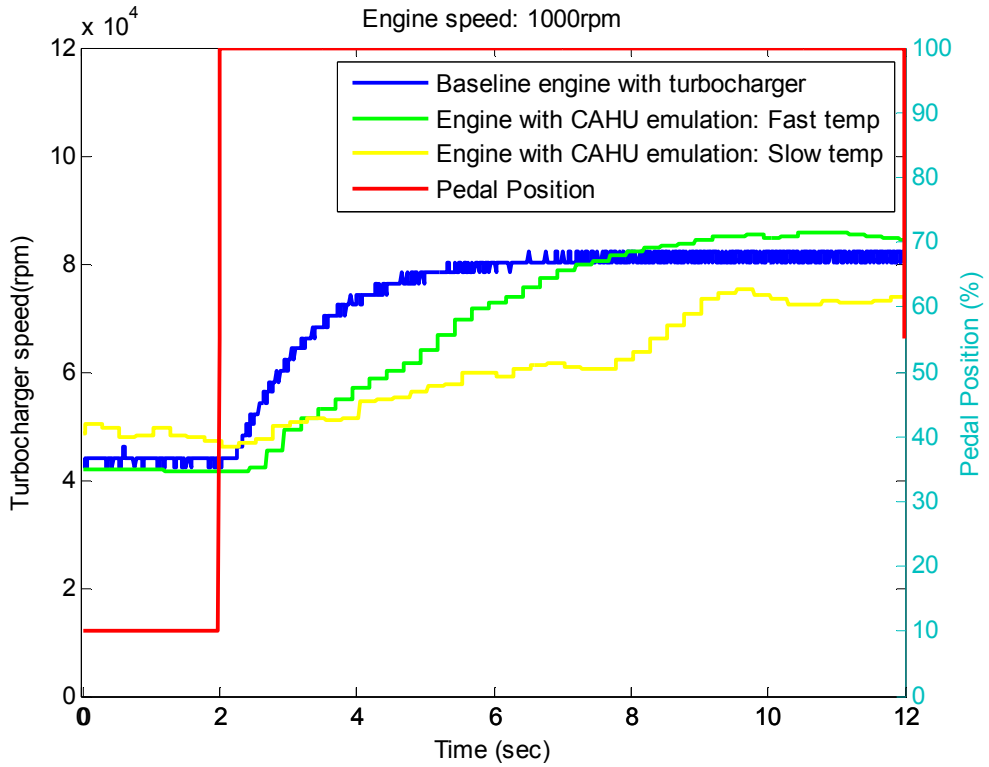

Figure 8.33 Turbocharger speed: fast temperature measurement vs. slow

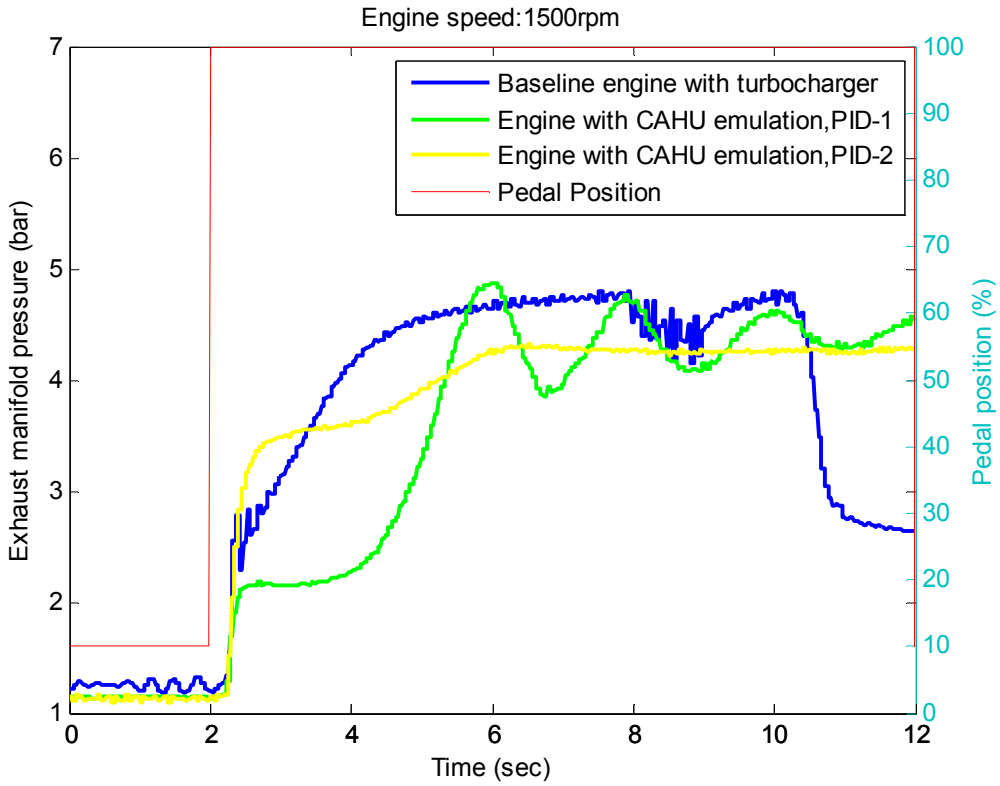

Figure 8.34 Comparison of exhaust pressure in the engine with CAHU at different PID values

Chapter 9 CONCLUSION

9.1 Overall conclusion

The final conclusions of this thesis are discussed in relation with the project aims and objectives as outlined in chapter 1.

1. *"To conduct a literature survey on air charging systems, real time simulation and hardware-in-the-loop systems, with a focus on turbocharger modelling techniques and the benefits of charge air handling systems emulation as appropriate to this study.*"

A comprehensive literature survey has investigated the features and applications of engine air charging technologies, and highlighted the novelty in the applications of a charge air handling unit to emulate prototype boosting systems. The literature survey of turbocharger modelling techniques shows that the empirical model for compressor and turbine may provide good prediction based on a large number of test data supplied by the manufacture when available. However, manufacture's data is normally scarce and low density, therefore an alternative method of using analytical model which represents the processes more fundamentally and hence less reliant on data sourcing is required.

From the literature, it was also noted that the HIL system can significantly improve the engine development process with regard to the development of new control systems. It was also found that the execution speed of the simulation program is critical for the HIL system, as the software requires to be synchronised with hardware in a real time environment. Hence it was suggested that the trade-off between the

execution speed and prediction accuracy of the real time simulation in this work needs to be focused on while developing the turbocharger model to control the CAHU.

2. *"To undertake a detailed investigation of the turbocharger architecture, and numerical and analytical approaches to predict compressor and turbine performance based on data supplied by the turbocharger manufactures."*

The survey of turbocharging systems has identified the features and applications of the turbocharging system and the performance characteristics and identification of the energy flow and gas flow velocity at each stage of the compressor and turbine as the fundamental principle for the real time turbocharger model development. This work has also investigated both the numerical and analytical approaches to predict the compressor and turbine performance; hence denser compressor and turbine maps can be developed for use in the real time turbocharger model, thus reducing model execution time and model error.

3. *"To develop a turbocharger model to operate in a real time environment in conjunction with a hardware-in-the-loop system to control a charge air handling unit (CAHU), which emulates advanced boosting systems."*

In the absence of adequate experimental data supplied by the turbocharger manufacture, a number of numerical and parametrical approaches have been applied to increase the density of the turbine and compressor data. A fully analytical one-dimensional turbine model has also been developed as a series of discrete components based on the conservation of momentum, steady flow energy, mass flow continuity and thermodynamic equations. It was suggested that if detailed turbine geometry data are supplied, the fully analytical turbine solution is capable of predicting the turbine performance at any given operating points, where the turbine VGT position, expansion ratio and speed are specified.

In order to emulate the turbocharger performance and thus control the CAHU for the engine air charging, it is essential to operate the turbocharger model in a real time

environment. For this purpose, the Matlab Simulink based turbocharger model was developed including the compressor model, turbine model, turbocharger shaft model, gas property model and the CAN bus communication system to transfer signals among sub-control systems.

4. *"To carry out a detailed investigation and to design a model to simulate the turbine characteristics under pulse conditions."*

A novel approach to uncover the turbine characteristics under pulsation conditions is described in chapter 5. The pulsating flow due to the engine exhaust valve/port opening/closing and propagation though the exhaust manifold to the turbine is identified as containing higher isentropic energy than the steady flow analysis. Hence it is essential to simulate this phenomenon in the real time turbocharger model. The model reconstructs the pulsating temperature and mass flow rate based on the pulsating pressure profile measured by the fast response pressure transducer at the entry of the turbine. The experimental result to evaluate the model to prove this theory was also demonstrated in chapter 8.

5. "To develop the hardware-in-the-loop system, to be used as a platform to test the engine with the CAHU emulating the turbocharger performance."

A state-of-the-art engine testing approach based on the hardware-in-the-loop system has been applied in this research, including the CAHU (Charging Air Handling Unit) system, engine testing facilities, and the dSPACE platform for operating the real-time model. The CAHU system enables the engine to be tested at different air charging/discharging conditions without connecting to a real turbocharger.

The communication system to allow the signals to transfer among each controller is a significant part of this research, since the messages containing the engine variables and parameters are required to be sent and received as soon as possible which allows the turbocharger model to respond fast enough to synchronise with the hardware in a real time environment. Hence the communication system based on the CAN (Control

Area Network) bus was developed and demonstrated in this work. Variables in the engine ECU control strategy such as the turbocharger vane position and the quality of engine fuel injection are the key parameters for the real time turbocharger model. For this purpose, a new model was developed and demonstrated which could intercept these signals in the conversation between the engine ECU and the calibration tool.

6. *"To undertake an experimental programme of work to validate the new engine testing approach by benchmarking a engine with CAHU to emulate the air charging system against a baseline engine with production turbocharger, under both steady state and transient conditions."*

The experimental work with regard to the comparison of the performance on the engine with CAHU to emulate the turbocharger performance against the baseline engine with a production turbocharger is demonstrated and analysed in chapter 8. The engine performance under steady state conditions has shown an agreement that the new engine testing approach could replace the conventional prototype engine tests which can significantly reduce the cost and time on the development of new engine air charging systems. The accuracies with respect to the boost pressure, turbocharger speed, mass air flow, and fuel consumption in the steady state tests are above 95%. Although the initial result of engine back pressure in the steady state tests has not shown a high level of confidence, the recalibration of VGT positions in the ECU control strategy improves the accuracy to 90%. In engine transient tests, the boost pressure and engine torque have shown fast response similar to that of the baseline engine, which required a fast response thermocouple to measure exhaust temperature. While general transient trends were achieved, some issues were identified with the high speed control of the CAHU interacting with the dSPACE real time turbocharger model. It is proposed that future improvement can be achieved via applying new control algorithms to improve the accuracy and tracking the CAHU control without sacrificing the system stabilities.

9.2 Further work

Certain aspects have come out of this work which follow on and are listed below:

1) It is anticipated further benefits of using denser compressor and turbine maps supplied by the turbocharger manufacture in the real-time turbocharger. This could improve accuracy of the lookup tables in the compressor and turbine models.

2) More turbine experimental data and detailed geometry specification of the turbine could improve the prediction of the fully analytical turbine model, especially for the turbine under tight nozzle vane positions. More turbine experimental data on a turbo-dynamometer would be beneficial for calibrating the parameters in the semi-empirical energy losses' models.

3) To improve the stability of the system without sacrificing the system response under transient test, the PID control system in the CAHU could be replaced by an advanced closed-loop control system.

4) Instead of using a single-cable pulley for controlling the butterfly valve in the CAHU system, a double-cable push-pull pulley arrangement could improve the response and reduce the system oscillation.

5) A new control philosophy for the CAHU system and the real-time model, which controls the mass flow rate in the engine based on the pressure inputs, would eliminate the less sensitive relationship between the pressure ratio and mass flow rate at high pressure region. This would improve the system stability under high back pressure conditions.

Reference

1. 'EPA plain English guide to clean air' http://www.epa.gov/air/caa/peg/
2. 'Official Journal of the European Union, REGULATION (EC) No 715/2007 OF THE EUROPEAN PARLIAMENT AND OF THE COUNCIL, of 20 June 2007 on type approval of motor vehicles with respect to emissions from light passenger and commercial vehicles (Euro 5 and Euro 6)'
3. 'Regulation (EC) No 443/2009 of the European Parliament and of the Council of 23 April 2009 setting emission performance standards for new passenger cars as part of the Community's integrated approach to reduce CO 2 emissions from light-duty vehicles (Text with EEA relevance)' http://eur-lex.europa.eu/LexUriServ/LexUriServ.do?uri=CELEX:32009R0443:EN:NOT
4. **Tan Y**. Automotive Diesel Turbocharger Investigation. PhD Thesis, University of Bath, 2007
5. **Watson N., and Janota M. S.,** Turbocharging the Internal Combustion Engines
6. **Babu G. M.,** Hardware in the Loop Simulation (HIL) for Vehicle Electronics Systems Testing and Validation SAE 2005. Paper No. 2005-26-304
7. BMW Mini Cooper S. http://en.wikipedia.org/wiki/BMW_MINI. (Accessed January 2007).
8. **Fieweger K., Paffrath H. and Schorn N.** Drivability assessment of an HSDI Diesel Engine with electrically assisted boosting systems. IMechE, Conference on turbochargers and turbocharging, paper C602/009/2002, 2002

9. **Shahed S. M.** An Analysis of Assisted Turbocharging with light hybrid powertrain. SAE paper 2006-01-0019, 2006.
10. **Kattwinkel T., Weiss R., and Boeschlin J**. Mechatronic Solution for electric turbocharger. SAE paper 2003-01-0712, 2003.
11. Honeywell Turbo Technologies web page www.honeywell.com/sites/ts/tt/PassengerCars_LightTruks.htm
12. **Hawley J.G., Wallace F.J., Pease A.C., Cox A., Horrocks R.W., Bird G.L.** 'Comparison of variable geometry turbocharging (VGT) over conventional wastegated machines to achieve lower emissions' – SAE Paper 974138. 1997
13. **Wallace F. J. and Cox A.** The ultimate performance potential of compounded diesel engines for heavy duty vehicles. IMechE Conference on turbocharging and air management systems, paper C554/015/98, 1998.
14. **Alain C., Stephane G., Claude L., Patrice H., and** Saulnier S. 'Advanced Diesel Powertrain for reduced fuel consumption and CO2 emissions' – SAE Paper 2004-05-0152 , 2004
15. **Luttermann C., and Mahrle W.,** 'BMW High Precision Fuel Injectionin Conjunction with Twin-Turbo Technology: a Combination for Maximum Dynamic and High Fuel Efficiency' 2007 SAE paper 2007-01-1560, 2007
16. **Arnold S.** 'Single Sequential Turbocharger: A New Boosting Concept for Ultra-Low Emission Diesel Engines' SAE paper 2008-01-0298, 2008
17. **Moraal P., Kolmanovsky I.,** 1999, Turbocharger Modeling for Automotive Control Application, SAE paper 1999-01-0908
18. **Dowell P.G., and Akehurst S.** ' Mapping Techniques for Radial Compressor for use in Real-Time Engine Models' SAE, Paper 2010-01-1227
19. **Jensen J.P., Kristensen A.F., Sorenson S.C.,** Houbak N., 1991, Mean Value Modelling of Small Turbocharged Diesel Engine, SAE, Paper 910070.
20. **Kolmanovsky, I.V., Moraal, P.E., van Nieuwstadt, M.J., Criddle, M., Wood, P.,** "Modeling and identification of a 2.0 l turbocharged DI diesel engine". Ford internal technical report SR-97-039, 1997.

21. **Mueller, M.,** "Mean value modeling of turbocharged spark ignition engines", Master's thesis, DTU, Denmark, 1997.
22. **Nelson, S.A., Filipi, Z.S., Assanis, D.N.,** "The use of neural networks for matching compressors with diesel engines," Spring Technical Conference, volum ICE-26-3, pages 35-42, 1996.
23. **Katsanis T.,** 'Use of arbitrary quasi-orthogonals for calculating flow distribution on a blade to blade surface in a turbomachine' NASA TN-2809, 1965
24. **Barnard M. C. S., and Benson R. S.,** 'Radial gas turbines' Proc. Inst. Mech. Engrs, 183, Pt.3N. 1968/9
25. **Benson R. S., Cartwright W.G., and Woollatt GT.,** 'Calculations of the flow distribution within a radial turbine rotor' Proc. Inst, Mech. Engrs, 184, Pt.36. 1970
26. **Cartwright W. G.,** 'A comparison of calculated flows in radial turbines with experiment.' SAE paper 72-GT-50. 1972
27. **Dawes W. N.,** 'Development of a 3D Navier Stokes solver for application to all types of turbomachinery', ASME Paper 88-GT-70. 1988
28. **Baldwin B., and Lomax H.,** 'Thin layer approximation and algebraic model for separated turbulent flows' AIAA Paper 78-257. 1978
29. **Futral S. M., and Wasserbauer C. A.,** 'Experimental performance evaluation of a 4.59 inch radial inflow turbine with and without splitter blades' NASA TN D-7015.
30. **Wasserbauer C. A., and Glassman A. J.,** 'Fortran program for predicting the off-design performance of radial inflow turbines' NASA TN-8063.

31. **Baines N. C.,** 'A meanline prediction method for radial turbine efficiency' in *Turbochargers and Air management Systems*, Inst Mech Engrs, pp. 45-56
32. **Benson R. S.,** 'A review of methods for assessing loss coefficients in radial gas turbines' Int. J. Mech. Sci. 12, 1970
33. **Chen H., Hakeem I., and Martinez-Botas R.F.,** 'Modelling of a turbocharger turbine under pulsating inlet conditions' Proc. Instn mech. Engrs, vol.210, 1996.
34. **Wallace F. J.,** 'Theoretical assessment of the performance characteristics of inward radial flow turbines', Proc. Instn mech. Engrs 1958 172, 33.
35. **Wallace F. J., Cave P.R., and Miles J.,** 'Performance of inward radial flow turbines under steady flow conditions with special reference to high pressure ratios and partial admission', Proc. Instn mech. Engrs, vol.184, Part 1, Number 56. 1969-70
36. **Akehurst S., and Piddock M.,** ' A Multiple Factor Simulation and Emulation Approach to Investigate Advanced Air Handling System for Future Diesel Engines' SAE paper 2008-01-0297, 2008
37. **Cardanha T.,** Validating Powertrain Controller Systems With the VPACS-HIL Powertrain Simulator SAE 2005. Paper No. 2005-01-1663
38. Tutorial 'Hardware-in-the-loop' PrecisionMBA, LLC. http://www.precisionmba.com/hardware_in_the_loop.htm
39. **Kohl S., and Jegminat D.,** How to Do Hardware-in-the-Loop Simulation Right SAE 2005. Paper No. 2005-01-1657
40. **Park S., Lee J., and Yang S.,** Development of ETC Limp-Home Function Using Test Automation on HILS SAE 2006, Paper No. 2006-01-0610
41. **Kim D., Kim K., Lee W., and Hwang I.,** Development of Mando ESP (Electronic Stability Program SAE 2003. Paper No. 2003-01-0101

42. **Steiber J., Surampudi B., Rosati M., Turbett M., Hansen R., and Tower T.,** Modeling, Simulation and Hardware-in-the-Loop Transmission Test System Software Development SAE2003. Paper No. 2003-01-0673
43. **Shidore N., and Pasquier M.,** Interdependence of System Control and Component Sizing for a Hydrogen-fueled Hybrid Vehicle SAE 2005, Paper No. 2005-01-3457
44. **Wang C., Cardanha T., and Wentzloff D.,** "Development and Implementation of Powertrain Electrical System Simulator with Computer-Controlled Fault Generation SAE 2006, Paper No. 2006-01-1599
45. **Winsel T., Ayeb M., Wilhelm C., Theuerkauf H., J., Pischinger, S., Woermann R., and Schernus C.,** HiL-based ECU-Calibration of SI Engine with Advanced Camshaft Variability SAE 2006, Paper No. 2006-01-0613
46. **Viele M., Stein L., Gillespie M., and Hoekstra G.,** A PC and FPGA Hybrid Approach to Hardware-in-the-Loop Simulation SAE 2004. Paper No. 2004-01-0904
47. **Jin W., and Baracos P.,** A Scalable Hardware-in-the-Loop System for Virtual Engine and Virtual Vehicle Applications SAE 2003. Paper No. 2003-01-1367
48. **Sandiford J., Geusens D., Sourbron R., and Lowrie J.,**Angular Based Event Testing SAE 2004. Paper No. 2004-01-1651
49. **Hunt G., Truscott A., and Noble A.,** An In-Cycle Hardware in the Loop (HIL) Simulator for Future Engine Control Strategy Development SAE 2004 Paper No. 2004-01-0418
50. **Ramaswamy D., McGee R., Sivashankar S., Deshpande A., Allen J., Rzemien K., and Stuart W.,** A Case Study in Hardware-In-the-Loop testing:

Development of an ECU for a Hybri d Electric Vehicle SAE 2004. Paper No. 2004-01-0303

51. 'Real time Computing' http://en.wikipedia.org/wiki/Real-time_computing
52. **Brace C.J.** Transient Modelling of a DI TCI Diesel Engine. PhD Thesis, University of Bath, 1996.
53. **Schulten P. J. M. and Stapersma D.** Mean Value Modelling of the Gas Exchange of a 4-stroke Diesel Engine for Use in Powertrain Application. SAE paper 2003-01-0219, 2003.
54. **Burns J.S., Lamar N., III, Dimick M.O., and Granger S.J.,** Development of the L3: an Efficient, High-power, Clean-Fueled, Parallel-format, Hybrid Vehicle SAE 2000. Paper No. 2000-01-3097.
55. **Winsel T., Ayeb M., Theuerkauf H.J., Pischinger S., Schernus C., and Lutkemeyer G.,** HiL-Calibration of SI Engine Cold Start and Warm-Up Using Neural Real-Time Model SAE 2004. Paper No. 2004-01-1362
56. **Wanpal A., Babu M. G., Kankariya N., Mundhra K., Sundaresan S. A., and Deshpande A. S.,** ECU Testing and Verification using Hardware-in-the-Loop SAE 2006 Paper No. 2006-01-1444
57. **Gehring J., and Schutte H.,** A Hardwar-in-the-loop Test Bench for the Validation of Complex ECU Networks SAE 2002. Paper No. 2002-01-0801
58. **Woermann R.J., Theuerkauf H.J., and Heinrich A.,** A Real-Time Model of a Common Rail Diesel Engine SAE 1999. Paper No. 1999-01-0862
59. **Allen R.W., Rosenthal T.J., Aponso B.L., Klyde D.H., Anderson F.G., Hogue J.R., and Chrstos J.P.,** A Low Cost PC Based Driving Simulator for Prototyping and Hardware-In-The-Loop Applications SAE 1998. Paper No. 980222

60. **Boulat A., Genninasca Y., Charlet a., and Higelin P.,** ECUTEST- A Real-time Engine Simulator for ECU Development and Testing SAE 2001. Paper No. 2001-01-1911.
61. **Ayeb M., Lichtenthaler D., Winsel T., and Theuerkauf H. J.,** SI Engine Modeling Using Neural Networks SAE 1998. Paper No. 980790
62. **Winsel T., Ayeb M., Lichtenthaler D., and Theuerkauf H.J.,** A Neural Estimator for Cylinder Pressure and Engine Torque. SAE 1999. Paper No. 1999-01-1165
63. **Isermann R., Sinsel S., and Schaffnit J.,** Modeling and Real-Time Simulation of Diesel Engines for Control Design SAE 1998. Paper No. 980796
64. **P.Moraal., and L.Kolmanovsky.,** Turbocharger Modelling for Automotive Control Applications. SAE 1999. Paper No. 1999-01-0908
65. **Velardocchia M., and Sorniotti A.,** Hardware-In-the-Loop to Evaluate Active Braking Systems Performance. SAE 2005 Paper No. 2005-01-1580
66. **Wang H., and Xue C.,** Modelling and Simulation of Electric Stability Program for the Passenger Car SAE 2004. Paper No. 2004-01-2090
67. **Castiglione M.S, Stecklein G., Senseney R., and Stark D.,** Development of Transmission Hardware-in-the-Loop Test System SAE 2003. Paper No. 2003-01-1027
68. **Li J., Feng J., Yu F., and Zhang J.,** The Rapid Development of vehicle Electronic Control System by Hardware-in-the-Loop Simulation SAE 2002. Paper No. 2002-01-056

69. **Amato G., and Koster L.,** High Performance Code Generation for Auto, an Automotive uController from Infineon Technologies SAE 2000. Paper No. 2000-01-0393
70. **A. Buchi, Uber Brennkraftmeschinen, Z. Gasturbinenewesen** (1996)
71. **A Whitfield., and N C Baines.,** Design of Radial Turbomachines
72. **Arsie I., Genova D., Pianese C., Sorrentino M., Rizzo G., Caraceni A., Cioffi P., and Flauti G.,** Development and identification of Phenomenological Models for Combustion and Emissions of Common-Rail Multi-Jet Diesel Engines. SAE 2004. Paper No. 2004-01-1877
73. **Zhang J., Gao S., and Jiang F.,** A Diesel Engine Real time Nox Emission Simulation System Based on RTW and VxWorks. SAE 2007. Paper No. 2007-01-0025
74. **Adenmark M., Deter M., and Schulte T.,** Testing Networked ECUs in a HIL Based Integration Lab SAE 2006. Paper No. 2006-01-3495
75. **Yang J., Bauman J., and Beydoun A.,** An Effective Model-Based Development Process Using Simulink/Stateflow for Automotive Body Control Electronics. SAE 2006. Paper No. 2006-01-3501
76. **Fiorani P., Gambarotta A., Tonetti M., and Lanfranco E.,** A Real-Time Model for the Simulation of Transient Behaviour of Automotive Diesel Engines. SAE 2006 Paper No. 2006-01-3007
77. **Shayler P.J., Allen A.J., and Robert A.L.,** Running Real-Time Engine Model Simulation with Hardware-in-the-Loop for Diesel Engine Development. SAE 2005 Paper No. 2005-01-0056
78. **Wang H.,** Hardware-in-the-loop Simulation for Traction Control and Debugs of its Electric Control Unit. SAE 2004 Paper No. 2004-01-2056

79. **Wu Y., Chen B., Hsieh F., Huang M., and Wu Y.,** Development of Hardware-In-the-Loop Simulation for Scooter Engine Control SAE 2006, Paper No. 2006-01-0614

80. **Canova M., Fioranip., Gambarotta A., and Tonetti M**., A real-time model of a small turbocharge Multijet Diesel engine: application and validation SAE 2005, Paper No. 2005-24-065

81. **Philipp O, Buhl M., Diehl S., Huber M., Roehlich S., and Thalhauser J.,** Engine ECU Function Development Using Software-in-the-Loop Methodology SAE 2005. Paper No. 2005-01-0049

82. **Ossyra J., and Ivantysynova M.,** Drive Line Control for Off-Road Vehicles Helps to Save Fuel SAE 2004. Paper No. 2004-01-2673

83. **Cesario N., Muscio C., Farina M., Amato P., and Lavorgna M.,** Modelling the Rate of Heat Release in Common Rail Diesel Engines: a Soft Computing Approach SAE 2004. Paper No. 2004-01-2967

84. **Nabi S., Balike M., Allen J., and Rzemien K.,** An overview of Hardware-In-the-Loop Testing Systems at Visteon SAE 2004. Paper No. 2004-01-1240

85. **Yan Q., Thompson F.C., Paul R.E., and Bielenda J.J**.,Hardware in the Loop for Dynamic Chassis Control Algorithms Test and Validation SAE 2004. Paper No. 2004-01-2059

86. **Krug C., Liebl J., Munk F., Kammer A., and Reuss H**., Physical Modelling and Use of Mordern System Identification for Real-Time Simulation of Spark Ignition Engines in all Phases of Engine Development SAE 2004. Paper No. 2004-01-0421

87. **Caraceni A., Cristofaro F.D., Ferrara F., and Scala S., and Philipp O.,** Benefits of Using a Real-Time Engine Model During Engine ECU Development SAE 2003. Paper No. 2003-01-1049
88. **Kammer A., Liebl J., Krug C., Munk F., and Reuss H.-C.,** Eral-time Engine Models SAE 2003. Paper No. 2003-01-1050
89. **Aaltonen J., and Vilenius M.,** Control and Controllability of Electrohydraulic Valvetrain in High and Medium Speed Diesels SAE 2002. Paper No. 2002-01-2175
90. **Paolo B., Stefano M., Giovanbattista V., and Trifiletti A.,** ECU Development and Testing Through Numerical Optimization and Hardware in the Loop Simulations SAE 2001. Paper No. 2001 01 1865
91. **Lang T., and Schyr C.,** Simulation Aided Process for Developing Powertrains SAE 2000. Paper No. 2000-01-3161
92. **Beaumont J., and Noble A.D., Gebhardt M., Stier G., and Furry S.,** Automation of ECU Software Development: From Concept to Production Level Code SAE 1999. Paper No. 1999-01-1174
93. **Schanne M., and Judt A.,** Application Development for Safty Critical Distributed Embedded Systems with Model verification. SAE 2006. Paper No. 2006-01-1498
94. **Shahbakhti M., Lupul R., and Koch C.R.,** Predicting HCCI Auto-Ignition Timing by Extending a Modified Knock-Integral Method SAE 2007. Paper No. 2007-01-0222
95. **Chow A., and Wyszynski M. L.,** Thermodynamic modelling of complete engine systems – a review IMechE 1999 Vol 213 Part D
96. Matlab Help documentation

97. **Futral S. M., and Wasserbauer C.A.,** 'Off-design performance prediction with experimental verification for a radial-inflow turbine' NASA TN D-2621

98. **Rohlik H. E.,** 'Analytical determination of radial inflow turbine design geometry for maximum efficiency' NASA TN D-4384.

99. http://en.wikipedia.org/wiki/Controller_area_network

100. **Lemon K., Dmuchowski T., and Emaus B.,** Introduction to CAN Calibration Protocol. SAE 2000, Paper number 2000-01-0389

101. **Kar K., Roberts S., Stone R., and Oldfield M.,** Instantaneous Exhaust Temperature Measurements Using Thermocouple Compensation Techniques. SAE 2004, Paper number 2004-01-1418

102. http://en.wikipedia.org/wiki/PID_controller

103. **Bains N** 'Developments in Turbocharger Simulation' Webniar by Concepts NREC, 20100304 1501-1

104. **Lemon K., Dmuchowski T., and Emaus B.,** 'Introduction to CAN Calibration Protocol', 2000, SAE paper No. 2000-01-0389

105. **Baines, N.C., Wallace, F.J. and Whitfield, A.** 'Computer Aided Design of Mixed Flow Turbines for Turbochargers' Transc. ASME, July 1979 Vol 101 440-449.

106. **Rajoo S., and Martinez-Botas,** 'Experimental study on the performance of a variable gemotry mixed flow turbine for automotive turbocharger' 8th International conference on turbochargers and turbocharging, 2006, page 183-192.

107. Ford Motor Company UK. http://www.ford.co.uk. (Accessed October 2005).

108. **House D. H.,** 'Spline curves' Clemson University

109. **Ariga I., Masuda S., and Ookita A.,** Inducer Stall in a Compressor with Inlet Distortion. 1987 Trans ASME Journal of Turbomachinery 190:27-35

110. http://www05.abb.com/global/scot/scot211.nsf/veritydisplay/57264ec82b40b7bac125744100300156/$File/50_14-05-EN-RevD-04_2008.pdf

111. 'Guide to thermocouple and resistance thermometry' issue 6.0

112. BorgWarner Turbo Systems. http://www.turbos.bwauto.com/en/products/technology.asp

113. **Saulnier S. and Guilain S.** 'Computation Study of Diesel Engine Downsizing Using Two-Stage Turbocharging.' SAE paper 2004-01-0929, 2004.

114. **Piddock M**. Engine Optimization for Downsizing by Experiment and Simulation. PhD Thesis, University of Bath, 2010

115. **Wallace F**., 'Turbocharger-Engine Matching: The Derivation and Use of Compressor and Turbine Maps' Presentation, University of Bath

116. **Merola S. S., Vaglieco B. M., Formisano G., Lucignano G., and Mastrangelo G., '**Flame Diagnostics in the Combustion Chamber of Boosted PFI SI Engine' SAE Paper 2007-24-0003, 2007

117. **Johnson T.V.,** 'Review of Diesel Emissions and Control' SAE Paper 2010-01-0301, 2010

118. **Rajoo S., and Martinez-Botas R.F., '**Improving Energy Extraction from Pulsating Exhaust Flow by Active Operation of a Turbocharger Turbine' SAE Paper 2007-01-1557, 2007

119. **Tange H., Ikeya N., Takanashi M., and Hokari T.,** 'Variable Geometry Diffuser of Turbocharger Compressor for Passenger Vehicles' SAE Paper 2003-01-0051, 2003

120. Wijetunge R., 'Transient Optimisation of a Diesel Engine' PhD Thesis, University of Bath, 2001

Appendix

```
%Modification
%23/04/2009
%Add slip factor from Meitner.,P.J & Glassman.,A.J. to take account
for the effects of back sweep at the entry of the blade. The
incidence angle can be calculated from slip factor.
%
%

%  close all
 clear all

 clc



 Turb=0;
 error_final=0;
 error_per=0;
 BSR_result=0;

 VGT=100;



% for a=1:42

    figure ()

Turbine_ManufactureData()



        Turbine_data_100

        BETA2B

        VGT=100;

        Turbine_data_100
```

```
Turb_speed_index =
unique(RawData_turb_100_Speed(logical(RawData_turb_100_Speed(:))),'fi
rst');



h1=subplot(3,3,1);

hold on

plot(BSR(1:7),RawData_turb_100_Eff(1:7),'r*')

plot(BSR(8:14),RawData_turb_100_Eff(8:14),'k*')

plot(BSR(15:21),RawData_turb_100_Eff(15:21),'y*')

plot(BSR(22:28),RawData_turb_100_Eff(22:28),'g*')

plot(BSR(29:35),RawData_turb_100_Eff(29:35),'c*')

plot(BSR(36:42),RawData_turb_100_Eff(36:42),'m*')

xlabel('Blade Spead Ratio')

 ylabel('Efficiency %')

 title('100% opening, All loss')

% legend(h1,'49216 rpm','60140 rpm','71285 rpm','82622 rpm','93780
rpm','104981 rpm',6);




h2=subplot(3,3,2);

hold on


plot(RawData_turb_100_PR(1:7),RawData_turb_100_Mass(1:7),'r*')

plot(RawData_turb_100_PR(8:14),RawData_turb_100_Mass(8:14),'k*')

plot(RawData_turb_100_PR(15:21),RawData_turb_100_Mass(15:21),'y*')

plot(RawData_turb_100_PR(22:28),RawData_turb_100_Mass(22:28),'g*')

plot(RawData_turb_100_PR(29:35),RawData_turb_100_Mass(29:35),'c*')

plot(RawData_turb_100_PR(36:42),RawData_turb_100_Mass(36:42),'m*')
```

```
xlabel('Pressure')

 ylabel('Mass flow kg/s ')

 title('100% opening, All loss')

% % legend(h2,'49216 rpm','60140 rpm','71285 rpm','82622 rpm','93780
rpm','104981 rpm',6);



% for VGT=60:2:100

if VGT>=0

 for v=6:6



for j=11:35


save('Turb_sim_result_100','Turb*','error_final','error_per','BSR_res
ult','beta2b','iopt','beta2b_new','DC_Speed','DC_BSR','Turb_speed_ind
ex')

    save ('v_s','v','VGT','j')

    clear all



    load v_s

    load Turb_sim_result_100

        Turbine_data_100



% str_column=(v-6000)/4000;

% str_page=VGT/2-29;

str_column=v;




     Speed_index=Turb_speed_index;
```

```
     Speed_rpm=Speed_index(v);


    Speed_color={'ro' 'ko' 'yo' 'go' 'co' 'mo'};


    u2=Speed_rpm*pi*dr/60;
    u3=Speed_rpm*pi*d3/60;


    str=j-10;
    Pr=j/10; % pressure ratio vary from 1 to 3
    P1=1.02; %P01=1 bar
    P3=P1/Pr;
    Pn_critical=P1*(2/(gamma+1)).^(gamma/(gamma-1)); % critical
pressure is 0.5278


 BSR_final=(Speed_rpm*pi*dr/60)./((2*Cp*T1*(1-(1./Pr).^((gamma-
1)/gamma))).^0.5);


 beta3=beta3_initial+0.05*(BSR_final-DC_BSR).^2;


density=P1*1e5/R/T1;




%-------------------------------------------------------------------
------
error=1; % just to get first iteration going
%  first_guess=Pr-((Pr-1))/4; % first guess assumes 50:50 pressure
drop ratio
```

```
 first_guess=Pr; % first guess assumes 50:50 pressure drop ratio


gain=0;

 gain_a=0;

 while (error>0.0001 || error <-0.0001)


    first_guess=first_guess-error*gain*gain_a;

    gain_a=1;


    Pr_nozzle=first_guess;

    if Pr_nozzle<1 || Pr_nozzle>Pr




        break



    else



    P2=P1/Pr_nozzle;

    density2_nozzle=density*(P2/P1).^(1/gamma);

     P2_space=P2+0.5*density2_nozzle*((2/dn).^2-(2/dr).^2)*1E-5;

%    P2_space=P2;

    density2=density*(P2_space/P1).^(1/gamma);


 if P2>=Pn_critical %Nozzle is not choking
```

```
    T2=T1*(P2_space/P1).^((gamma-1)/gamma);

    C2=(2*Efficiency_nozzle*Cp*T1*(1-(P2/P1).^((gamma-
1)/gamma))).^0.5;




    W2_square=u2.^2+C2.^2-2*u2*C2*cos(Ar);

    W2=W2_square.^0.5;



    % for T2_postshock=T1:1400

    %Derived by combinning energy equation across 'shock' with
allowance for

    %work done, with continuity across the shock.  From EQN 5 in
'Wallace, Cave

    %&Miles'

    f2=@(y)(y*C2*sin(Ar)/(sin(beta2b_new)*T2)).^2/(2*Cp)+y-
(T2+(C2.^2-u2.^2)/(2*Cp)-u2*(C2*cos(Ar)-u2)/Cp);



    T2_postshock=fzero(f2, T2);




        density2_postshock=density2*T2/T2_postshock;

        density3=density2_postshock*(P3/P2_space).^(1/gamma); %Assume
the flow in the rotor is isentropic

        W2_postshock=C2*sin(Ar)*(T2_postshock/T2)*csc(beta2b_new);


W3_square=W2_postshock.^2+2*Cp*T2_postshock*Efficiency_rotor*(1-
(P3/P2_space).^((gamma-1)/gamma))+(u3.^2)-(u2.^2);
```

```
        W3=abs(W3_square).^0.5;
%
        sonic_speed3=(gamma*P3*1e5/density3).^0.5;


        Mach_W3=W3/sonic_speed3;


        if Mach_W3>1
            Mach_W3=1;
            W3_new=sonic_speed3;
            f3=@(y)W3_new.^2-
(W2_postshock.^2+2*Cp*T2_postshock*Efficiency_rotor*(1-
(y/P2_space).^((gamma-1)/gamma))+(u3.^2)-(u2.^2));
            P3_new=fzero(f3,P3);
        else W3_new=W3;
            P3_new=P3;




        end
%
%       gain_s=0.001;
%
% while (Mach_W3>1)
%         P3=P3+gain_s;
%         if P3>P2_space
%             triger=1;
%             break
```

```
%          else
%          density3=density2_postshock*(P3/P2_space).^(1/gamma);
%          sonic_speed3_new=(gamma*P3*1e5/density3).^0.5;
%
W3_square=W2_postshock.^2+2*Cp*T2_postshock*Efficiency_rotor*(1-
(P3/P2_space).^((gamma-1)/gamma))+(u3.^2)-(u2.^2);
%          W3=abs(W3_square).^0.5;
%          Mach_W3=W3/sonic_speed3_new;
%          end
% end



          C3=(W3_new.^2+u3.^2-2*W3_new*u3*cos(beta3)).^0.5;
          sinA3=W3*sin(beta3)/C3;
          A3=asin(sinA3); %rotor exit angle
          Mass_nozzle=(2*Efficiency_nozzle*Cp*T1*(1-(P2/P1).^((gamma-
1)/gamma))).^0.5*Area_nozzle2*density*((P2/P1).^(1/gamma));
          Cd_square=2*Cp*T1*(1-(P3_new/P1).^((gamma-1)/gamma));







     Cm4=C2*sin(Ar);
     Cm5=W3_new*sin(beta3);
     Cx=(1-(r5t/r4))/(Cm4*b4);
     Cr=(r5t/r4)*(z-b4)/(Cm5*(d3/2)*b5);
     Lc=(u2.^3*Zr/(8*pi))*(0.4*clearance_x*Cx+0.75*clearance_r*Cr-
0.3*((clearance_x*clearance_r*Cx*Cr).^0.5));
```

```
      beta2=abs(atan((u2-C2*cos(Ar))/(C2*sin(Ar))));

      beta=atan(0.5*(abs(tan(beta2))+tan(beta3)));

      c=z/cos(beta);

       Lp=Kp*((LH/DH)+(0.68*(1-(d3/dr).^2)*cos(pi/2-beta3)/(b5/c)));




      %Watson & Jenota Method

%       i=atan(abs(C2*cos(Ar)-u2)/(C2*sin(Ar)))-beta2b;

%       AR=cos(i)-sin(i)*tan(beta2b);

%       T2_T1=(-1+(1+4*((gamma-1)/2)*(M1.^2)*(AR.^2)*(1+(gamma-
1)/2*(M1.^2))).^0.5)/(2*(AR.^2)*(M1.^2)*(gamma-1)/2);

%       Entrop_drop=gamma*R/(gamma-1)*log(T2_T1);




 %
Loss_Passage=2*Lp*(W3_new.^2+W2.^2*(cos(atan(abs(C2*cos(Ar)-
u2)/(C2*sin(Ar)))-beta2b)).^2)/Cd_square;


Loss_Passage=2*Lp*(W3_new.^2+W2.^2)/Cd_square;

                if Loss_Passage>0.4

                   Loss_Passage=0.4

                 end


Loss_Nozzle=0.5*(P3_new/P2).^((gamma-1)/gamma)*C2.^2/Cd_square;

                 if Loss_Nozzle>0.3

                     Loss_Nozzle=0.3;

                     end


              Loss_Exit=0.5*C3.^2/Cd_square;
```

```
%               Loss_Shock=2*(P3_new/P2).^((gamma-
1)/gamma)*Cp*(T2_postshock-T2)./Cd_square;

%

              if (beta2-beta2b-iopt)<=pi/4




           Loss_Shock=(W2*sin(beta2-beta2b-iopt)).^2./Cd_square;

                 else

         Loss_Shock=W2.^2*abs(0.5+beta2-beta2b-iopt-pi/4)./Cd_square;

                   end


              if Loss_Shock>0.4

                 Loss_Shock=0.4;

               end




Loss_Bearing=2*0.05*density*((Speed_rpm*pi/30).^2)*(r4.^2-
(d3/2).^2)/Cd_square;

 Loss_Clearence=0.05*Lc/Cd_square;



Mass_rotor=W3_new*sin(beta3)*Area_rotor*density2_postshock*(P3_new/P2
_space).^(1/gamma); %assume the flow is imcompressable.


Efficiency_overall=(1-Loss_Shock-Loss_Passage-Loss_Nozzle-
Loss_Clearence-Loss_Exit)*0.9;
```

```
%       Efficiency_overall=(1-Loss_Shock)*0.6;



BSR_final=(Speed_rpm*pi*dr/60)./((2*Cp*T1*(1-(P3_new/P1).^((gamma-
1)/gamma))).^0.5);




%-------------------------------------------------------------------
------

%-----If Nozzle is choking, an isentropic turning with pressure
reduction

%to the interspace pressure P2 from Pn is introduced


 else



            T2=T1*(P2_space/P1).^((gamma-1)/gamma);

%             C2=(2*Efficiency_nozzle*Cp*T1*(1-(P2/P1).^((gamma-
1)/gamma))).^0.5;

            density2_Pn=density*(Pn_critical).^(1/gamma);

            C2=(gamma*Pn_critical*1e5/density2_Pn).^0.5;

            sin_Ar_choke_square=((gamma+1)/2).^((gamma+1)/(2*(gamma-
1)))*(2/(gamma-1)).^0.5*P2_space/P1*(1-(P2_space/P1).^((gamma-
1)/gamma)).^0.5*(sin(pi/2-A2).^2);

            sin_Ar_choke=(abs(sin_Ar_choke_square)).^0.5;

            Ar_choke=asin(sin_Ar_choke);




            W2_square=u2.^2+C2.^2-2*u2*C2*cos(Ar_choke);
```

```
            W2=W2_square.^0.5;









f2=@(y)(y*C2*sin_Ar_choke/(sin(beta2b_new)*T2)).^2/(2*Cp)+y-
(T2+(C2.^2-u2.^2)/(2*Cp)-u2*(C2*cos(Ar_choke)-u2)/Cp);

            T2_postshock=fzero(f2, T2);

%             if (T2_postshock>T1 || T2_postshock<T2), error=0.0002;
continue, end







%          density2=density*(P2/P1).^(1/gamma);


         density2_postshock=density2*T2/T2_postshock;

W2_postshock=C2*sin_Ar_choke*(T2_postshock/T2)*csc(beta2b_new);

W3_square=W2_postshock.^2+2*Cp*T2_postshock*Efficiency_rotor*(1-
(P3/P2_space).^((gamma-1)/gamma))+(u3.^2)-(u2.^2);


         W3=abs(W3_square).^0.5;
%


         density3=density2_postshock*(P3/P2_space).^(1/gamma); %Assume
the flow in the rotor is isentropic


         sonic_speed3=(gamma*P3*1e5/density3).^0.5;
```

```
%         sonic_speed3=(gamma*P2_space*1e5/density2_postshock).^0.5;
% Sonic speed at the exit of the rotor.

%          density2_Pn=density*(Pn_critical).^(1/gamma);              %
density at the exit of the nozzle, when the nozzle is choking.

         sonic_speed2=(gamma*Pn_critical*1e5/density2_Pn).^0.5;  % the
sonic speed at the inlet of the rotor.




         Mach_W3=W3/sonic_speed3;









         if Mach_W3>1

             Mach_W3=1;

             W3_new=sonic_speed3;

             f3=@(y)W3_new.^2-
(W2_postshock.^2+2*Cp*T2_postshock*Efficiency_rotor*(1-
(y/P2_space).^((gamma-1)/gamma))+(u3.^2)-(u2.^2));

             P3_new=fzero(f3,P3);

         else

             W3_new=W3;

             P3_new=P3;



         end



%          gain_s=0.001;

%  while Mach_W3>1
```

```
%          P3=P3+gain_s;
%          if P3>P2_space
%              break
%          end
%          density3=density2_postshock*(P3/P2_space).^(1/gamma);
%          sonic_speed3_new=(gamma*P3*1e5/density3).^0.5;
%
W3_square=W2_postshock.^2+2*Cp*T2_postshock*Efficiency_rotor*(1-
(P3/P2_space).^((gamma-1)/gamma))+(u3.^2)-(u2.^2);
%          W3=abs(W3_square).^0.5;
%          Mach_W3=W3/sonic_speed3_new;
%  end


                C3=(W3_new.^2+u3.^2-2*W3_new*u3*cos(beta3)).^0.5;



                 sinA3=W3_new*sin(beta3)/C3;
                 A3=asin(sinA3); %rotor exit angle


%                 Area_nozzle2=n*lth2*bn_new

Mass_nozzle=sonic_speed2*Area_nozzle2*density*((Pn_critical).^(1/gamm
a));
                                 Cd_square=2*Cp*T1*(1-
(P3_new/P1).^((gamma-1)/gamma));
    Cm4=C2*sin(Ar);
    Cm5=W3_new*sin(beta3);
    Cx=(1-(r5t/r4))/(Cm4*b4);
    Cr=(r5t/r4)*(z-b4)/(Cm5*(d3/2)*b5);
```

```
    Lc=(u2.^3*Zr/(8*pi))*(0.2*clearance_x*Cx+0.4*clearance_r*Cr-
0.3*((clearance_x*clearance_r*Cx*Cr).^0.5));



     beta2=abs(atan(u2-C2*cos(Ar))/(C2*sin(Ar)));

     beta=atan(0.5*(abs(tan(beta2))+tan(beta3)));

     c=z/cos(beta);

      Lp=Kp*((LH/DH)+(0.68*(1-(d3/dr).^2)*cos(pi/2-beta3)/(b5/c)));



Loss_Passage=2*Lp*(W3_new.^2+W2.^2)/Cd_square;

                                    %
Loss_Passage=2*Lp*(W3_new.^2+W2.^2*(cos(atan(abs(C2*cos(Ar)-
u2)/(C2*sin(Ar)))-beta2b)).^2)/Cd_square;

             if Loss_Passage>0.5

                Loss_Passage=0.5;

             end


Loss_Nozzle=0.5*(P3_new/P2).^((gamma-
1)/gamma)*sonic_speed2.^2/Cd_square;

               if Loss_Nozzle>0.3

                  Loss_Nozzle=0.3;

               end

                                    Loss_Exit=0.5*C3.^2/Cd_square;
%
Loss_Shock=2*(P3_new/P2).^((gamma-1)/gamma)*Cp*(T2_postshock-
T2)./Cd_square;



               if (beta2-beta2b-iopt)<=pi/4

                Loss_Shock=(W2*sin(beta2-beta2b-iopt)).^2./Cd_square;
```

```
                else
    Loss_Shock=W2.^2*abs(0.5+beta2-beta2b-iopt-pi/4)./Cd_square;
                 end


                if Loss_Shock>0.5
                   Loss_Shock=0.5;
                end

Loss_Bearing=2*0.05*density*((Speed_rpm*pi/30).^2)*(r4.^2-
(d3/2).^2)/Cd_square;


     Loss_Clearence=0.05*Lc/Cd_square;

Mass_rotor=W3_new*sin(beta3)*Area_rotor*density2_postshock*(P3_new/P2
_space).^(1/gamma); %assume the flow is imcompressable.


Efficiency_overall=(1-Loss_Shock-Loss_Passage-Loss_Nozzle-
Loss_Clearence-Loss_Exit)*0.9;
%                                  Efficiency_overall=(1-
Loss_Shock)*0.6;


 BSR_final=(Speed_rpm*pi*dr/60)./((2*Cp*T1*(1-(P3_new/P1).^((gamma-
1)/gamma))).^0.5);


 end


    end
    error=Mass_nozzle-Mass_rotor;
           gain=gain+0.01;
```

```
 end
subplot(3,3,1);
plot(BSR_final,Efficiency_overall,char(Speed_color(v)));
% plot(BSR_final,Efficiency_overall,'ro');




subplot(3,3,2);
 plot(Pr,Mass_nozzle,char(Speed_color(v)));
% plot(Pr,Mass_nozzle,'ro');
%
subplot(3,3,3);
hold on
plot(BSR_final,Loss_Passage,char(Speed_color(v)));
 ylabel('Passage Loss %')
subplot(3,3,4);
hold on
plot(BSR_final,Loss_Nozzle,char(Speed_color(v)));
 ylabel('Nozzle Loss %')
% subplot(3,3,5);
% hold on
% plot(BSR_final,Loss_Exit,char(Speed_color(v)));
subplot(3,3,5);
hold on
plot(BSR_final,Loss_Shock,char(Speed_color(v)));
ylabel('Shock Loss %')
subplot(3,3,6);
hold on
plot(BSR_final,W2,char(Speed_color(v)));
```

```
ylabel('W2  m/s')

subplot(3,3,7);

hold on

plot(BSR_final,P2,char(Speed_color(v)));

ylabel('P2 ')

subplot(3,3,8);

hold on

plot(BSR_final,Loss_Exit,char(Speed_color(v)));

 ylabel('Exit Loss ')

subplot(3,3,9);

hold on

plot(BSR_final,Loss_Clearence,char(Speed_color(v)));

 ylabel('Clearence Loss ')




eval(['Turb_mass(' num2str(str) ',' num2str(str_column)
')=Mass_nozzle;']);

eval(['Turb_pr(' num2str(str) ',' num2str(str_column)  ')=Pr;']);

eval(['Turb_efficiency(' num2str(str) ',' num2str(str_column)
')=Efficiency_overall;']);

eval(['Turb_Loss_Passage(' num2str(str) ',' num2str(str_column)
')=Loss_Passage;']);

eval(['Turb_Loss_Nozzle(' num2str(str) ',' num2str(str_column)
')=Loss_Nozzle;']);

eval(['Turb_Loss_Exit(' num2str(str) ',' num2str(str_column)
')=Loss_Exit;']);

eval(['Turb_Loss_Shock(' num2str(str) ',' num2str(str_column)
')=Loss_Shock;']);

eval(['Turb_Loss_Clearence(' num2str(str) ',' num2str(str_column)
')=Loss_Clearence;']);
```

```
eval(['Turb_Loss_Bearing(' num2str(str) ',' num2str(str_column)
')=Loss_Bearing;']);



eval(['Turb_speed(' num2str(str) ',' num2str(str_column)
')=Speed_rpm;']);

eval(['Turb_BSR(' num2str(str) ',' num2str(str_column)
')=BSR_final;']);




save('Turb_sim_result_100','Turb*')

 end


end

%-------------------------------------------------------------------
------


else


    Turb_model_below40


end
```